TU DELFT

MASTER THESIS

Rail Wear in Curves at the Tramway of Amsterdam

Author:
Noa Peteroff

Supervisors:
Dr. A.A. Nunez Vicencio
Prof.dr. Z. Li
Dr. ir. Y. Yang
ir. Janneke Tax

A thesis submitted in fulfillment of the requirements for the degree: Master of Science

December 24, 2021

Abstract

Noa Peteroff

Rail Wear in Curves at the Tramway of Amsterdam

Rail wear in curves at the tramway of Amsterdam is a considerable problem since it consumes a significant part of the maintenance budget. The wear mechanism is not fully understood because some curves could suffer much more than others, while the cause for the difference is unknown. GVB, the public transport operator of Amsterdam, wants to obtain better insight into this problem to optimise maintenance processes and reduce maintenance costs.

First, a literature review was conducted to assess knowledge on this issue and analyse methods to model train-track systems. Next, based on the literature review, parameters were identified which could influence the rail wear process, e.g. tram velocity, primary yaw stiffness or rail hardness. An evaluation of available data on those parameters at GVB was made. Data that was available and deemed essential was aligned and later used as input for a rail wear prediction model for the tramway of Amsterdam. The essential data analyses are the velocity analysis and wheel qR decay analysis. A tool was developed to obtain a detailed profile of driven velocities at the tram network, based on massive daily data from all the trams. Wheel measurement data from all the trams in the network were analysed to assess the wear of the tram wheels. Statistics were obtained over six years of wheel measurement data measured twice per year per tram. Besides, the usage data processed for inclusion in the model are tonnage, vehicle type distribution, amount of coupled vehicles and average vehicle loading.

Furthermore, more than six hundred simulations were performed at DEKRA rail with GVB tram models in VAMPIRE, to obtain more insight into tram curving behaviour. Based on the simulation outcomes, relationships between energy dissipation (T_γ) and radius, velocity, flange angle, vehicle loading and -type were derived. Those relationships were obtained per wheel and aggregated per tram passage. Finally, a rail wear model was made, which combines the relationships derived from the simulations, track characteristics and usage data about the curves. The energy dissipation (T_γ) was used as a wear indicator by the prediction model.

From the velocity analysis, trams generally keep to the speed limits, but trams drive too fast at specific curves. The wheel analysis showed qR at the tram's front wheels decays considerably faster than other wheels. Combino tram type's wheel decay was poorer than the older BN tram type. From the simulations, wheel wear has the most adverse effect on rail wear in curves. Increased vehicle velocity or amount of passengers also has a considerable negative influence on rail wear. The expected wear rises exponentially if the curve radius decreases. Also, the dependency on velocity increases exponentially when the curve radius decreases.

The model was used to estimate energy dissipation for all the curves in the network. Four of those curves were selected for detailed analysis. Further, a comparison between rail wear measurements and the wear prediction model was conducted for two hundred curves. The estimations of the whole network were shown to GVB employees in charge of maintenance, who indicated the general estimation complies with their observations. Particularly, curves that were predicted with a higher energy dissipation were the ones that, in practice, are experiencing the most severe wear process. The detailed analysis of four curves showed correlations between model estimations and measured wear. However, the model could not explain some increased wear rates. The comparison with two hundred curves indicated differences in measured wear and the energy estimation. No general coefficient could be found which directly relates them both. Therefore, more research is needed to obtain an accurate model of railway wear and the expected energy dissipation. The more accurate model should revisit assumptions made in the vehicle model, such as a better inclusion of the longitudinal force interaction.

Finally, it is recommended that GVB ranks the curves using both the developed model and wear measurements. Curves with significant deviations in both rankings could be subject to further investigation to uncover critical parameters which might cause increased wear. Furthermore, the usage of other wear indicators can be considered if they have the potential to facilitate maintenance decisions, for example, power dissipation. As the wheel condition showed to be a critical factor for rail wear, condition-based wheel re-profiling should be implemented. Particularly, the wheel re-profiling policy should consider the higher deterioration rates of the front tram wheels.

Acknowledgements

The result and smooth research process were not possible without the help of the daily supervisor's Alfredo Nunez Vicencio (TU Delft) and Janneke Tax (GVB). Furthermore, much help was obtained from a broad range of GVB employees, DEKRA rail and the TU Delft thesis committee. Much thanks to everybody who has aided this research. Special thanks to the other members of the TU Delft committee: Zili Li and Yuguang Yang. Furthermore, the other employees at Tram Asset Management of GVB, Steef Rosseboom, Gert Loogman and Onno Herscheit, did a great job giving the right advice and providing a pleasant working environment. At last, the simulations were not possible without the help of Martin Hiensch and Mark Linders from DEKRA rail in Utrecht.

Contents

Abstract i

Acknowledgements iii

1 Introduction 1
- 1.1 Problem Statement . . . 1
- 1.2 Introduction to GVB . . . 1
- 1.3 Research Questions . . . 3
- 1.4 Scope . . . 3
- 1.5 Research Methodology . . . 3
  - 1.5.1 Literature Research . . . 4
  - 1.5.2 Available Data Exploration . . . 4
  - 1.5.3 Data Quality and Usability Investigation . . . 4
  - 1.5.4 Rail Wear Simulations . . . 4
  - 1.5.5 Predictive Model Design . . . 4
  - 1.5.6 Model Validation . . . 4
- 1.6 Tram Network Characterization . . . 4
  - 1.6.1 General Description . . . 5
  - 1.6.2 Rolling Stock . . . 5
  - 1.6.3 Network Characteristics . . . 5

2 Literature Review and Background Information 7
- 2.1 Background Information . . . 7
  - 2.1.1 Overview Tramway . . . 7
  - 2.1.2 General Concepts of Tramway Curve Negotiation . . . 7
  - 2.1.3 Modelling Vehicle Dynamics . . . 11
  - 2.1.4 Modelling Wheel-Rail Contact . . . 14
  - 2.1.5 Wear . . . 17
  - 2.1.6 Energy Dissipation and Frictional Work . . . 19
  - 2.1.7 Further Reading . . . 20
- 2.2 Literature Review . . . 21
  - 2.2.1 Tram Railways Compared to Heavy Railways . . . 21
  - 2.2.2 Track Modelling Techniques . . . 22
  - 2.2.3 Monitoring . . . 24

3 Data Availability and Quality 26
- 3.1 Rail and Wheel Measurements . . . 26
  - 3.1.1 Rail Geometry Data (Railcloud) . . . 26
  - 3.1.2 Strukton Photo Measurements . . . 28
  - 3.1.3 Sensornet . . . 29
  - 3.1.4 Wheel Wear Measurements . . . 30
- 3.2 Exploitation Data and Measurements . . . 30

3.2.1 Vehicle Type Distribution . . . 30
3.2.2 Coupled Vehicles . . . 31
3.2.3 Vehicle Occupation . . . 31
3.2.4 VECOM (Vehicle Communication) . . . 31
3.2.5 DBPU Dashboard . . . 31
3.2.6 Tram Log Data . . . 32
3.2.7 Kibana . . . 32
3.3 Track Characteristics . . . 33
3.3.1 SAP Database . . . 33
3.3.2 Lubrication Devices . . . 33
3.4 Maintenance Data . . . 34
3.5 Conclusion . . . 35

4 Velocity Analysis **37**
4.1 Introduction . . . 37
4.2 Results . . . 37
4.2.1 Input . . . 37
4.2.2 Output Examples . . . 38
Output per Trackpoint . . . 38
Output per Tracknumber . . . 38
4.2.3 Findings Velocity Analysis . . . 41
Detailed Analysis Curve 1 . . . 44
Detailed Analysis Curve 2 . . . 45
4.3 Validity . . . 45
4.3.1 Verification by Employees . . . 45
4.3.2 Validity Check Detailed Analysis . . . 45
4.3.3 Validity Check Plotted Loggings . . . 47
4.3.4 Comparison with Another Week . . . 48
4.3.5 Acceleration Analysis . . . 48
4.4 Conclusion Velocity Analysis . . . 48

5 Wheel Analysis **50**
5.1 Introduction . . . 50
5.1.1 Objective of the Analysis . . . 50
5.1.2 General Analysis Description . . . 50
5.1.3 Analysis Input Description . . . 51
5.1.4 Analysis Output Description . . . 51
5.2 Detailed Analysis Description . . . 51
5.3 Results . . . 52
5.3.1 Average qR on the network . . . 53
5.3.2 qR Decay per Wheel . . . 55
5.4 Validity and Discussion . . . 55
5.5 Conclusion . . . 57

6 Wear Simulation in Tramway Curves **58**
6.1 Introduction . . . 58
6.2 Simulation Analysis: Three Curves . . . 58
6.2.1 Introduction . . . 58
6.2.2 Curve Description and Input Values . . . 59
6.2.3 Results Three Curves Simulations . . . 59
Tight Curve Simulation Results and Verification . . . 60
Medium Curve Simulation Results and Verification . . . 74

Gentle Curve Simulation Results and Verification . . . 79
6.2.4 Simulation Variants . . . 80
Braking . . . 81
Loaded Vehicle . . . 82
No Flange Lubrication . . . 83
Worn Wheels . . . 84
Worn Rails . . . 86
Increased Velocity . . . 88
CAF Urbos 100 . . . 88
Settlement After Bridge . . . 88
6.3 Parametric Simulations . . . 89
6.3.1 Introduction Parametric Simulations . . . 89
6.3.2 Simulation Sets . . . 89
Basis per Simulation Set . . . 90
6.3.3 Parametric Simulation Results . . . 90
6.4 Conclusion Simulations . . . 94

7 Energy Estimation Model **95**
7.1 Introduction . . . 95
7.1.1 Model Aim . . . 95
7.1.2 General Model Description . . . 95
7.1.3 Model Input Description . . . 96
7.1.4 Model Output Description . . . 96
7.2 Model Description . . . 97
7.2.1 Introduction . . . 98
7.2.2 Energy Dictionary Generation . . . 98
7.2.3 Loading of Curve Characteristics . . . 98
7.2.4 Initial Energy Value Assignment . . . 99
7.2.5 Interpolation Based on Wheel Wear Distribution . . . 99
7.2.6 Interpolation Based on Average Loading . . . 99
7.2.7 Factoring Based on Vehicle and Velocity Distribution . . . 101
7.2.8 Yearly Dissipated Energy Calculation . . . 101
7.3 Results . . . 102
7.3.1 Result Examples . . . 102
7.3.2 Energy Estimation . . . 102
7.4 Comparison Energy Estimation with Profile Measurements . . . 103
7.4.1 Curve 1 - Verbindingsdam/Ertskade . . . 103
7.4.2 Curve 2 - J. Evertsenstraat/J.Tooropstraat . . . 105
7.4.3 Comparison Curve 1 and Curve 2 . . . 105
7.4.4 Curve 3 - Raadhuisstraat/Nwz. Voorburgwal . . . 105
7.4.5 Curve 4 - W. de Zwijgerlaan/A. de Ruijterweg . . . 106
7.4.6 Comparison Curve 3 and Curve 4 . . . 106
7.4.7 Comparison All Curves . . . 106
7.4.8 Comparison with Large Group of Curves . . . 108
7.5 Conclusion . . . 110

8 Conclusion and Discussion **111**
8.1 Conclusion . . . 111
8.2 Recommendations . . . 113
8.3 Discussion . . . 114

A Tram Network Characterization **116**

A.1 Overview . . . 116
A.2 Rolling Stock . . . 116
A.2.1 Siemens Combino . . . 117
A.2.2 CAF Urbos 100 . . . 118
A.3 Public Transport Network Amsterdam . . . 118
A.4 Infrastructure Characteristics . . . 122
A.5 Network Usage . . . 126

B Comparison Measurements and Estimation Results **134**

C Velocity Coupling Model Description **139**
C.1 Introduction to the Velocity Coupling Method . . . 139
C.1.1 Tracknumbers . . . 139
C.1.2 Trackpoints . . . 139
C.1.3 Routecodes . . . 140
C.2 General Description of the Analyzing Process . . . 140
C.3 Step 1 : Loading of Input Data . . . 141
C.3.1 General Input: Grid and Day Range . . . 141
C.3.2 Tram Logdata . . . 141
C.3.3 Tram Routedata . . . 141
C.3.4 Infra Routedata . . . 143
C.3.5 Track Points . . . 143
C.4 Step 2A: Determine Route and Trackpoints . . . 143
C.4.1 Obtain Route . . . 143
C.4.2 Obtain Trackpoints . . . 145
C.5 Step 2B: Obtain Nearest Valid Trackpoint . . . 145
C.6 Step 3: Velocity per Trackpoint Analysis . . . 145
C.6.1 Acceleration Analysis . . . 145
C.6.2 Statistical Analysis per Tracknumber . . . 148
C.7 Step 4: Output . . . 149

D Simulation Method and Models **150**
D.1 VAMPIRE Software . . . 150
D.2 Simulation Models . . . 150
Vehicle Models . . . 151
D.2.1 Wheel-rail Contact Models . . . 151
D.2.2 Track Models . . . 154
D.3 Integration Method . . . 154
D.4 Post Processing Method . . . 155
D.4.1 Post Processing Method Parametric Simulations . . . 158
Parametric Simulation Post Processing Code Description . . . 159

Bibliography **161**

List of Figures

1.1 Wear zones. 2
1.2 Tram vehicles used at the tram network in Amsterdam. 2
1.3 Overview on the research methodology. 3
1.4 Simplified overview of the urban public transport network of greater Amsterdam. 5
1.5 Location of tight curves (radius < 30 meter). 6

2.1 Grooved rail encased in concrete. 8
2.2 Cross sections of tramway rail and wheel (Group, 2021). 8
2.3 Overview of important movement directions for tram curve negotiation (Arman, 2021). 8
2.4 Flange contact during curve negotiation (Siemens, 2016). 9
2.5 Schematic overview of the steering forces on a tram bogie. 10
2.6 Conventional bogie (older type). 11
2.7 Bogie with independent wheels. 12
2.8 Possible simulation model for a car body. 12
2.9 Possible simulation model for a bogie. l = length, k/d = stiffness/damping. . 13
2.10 Typical shape of the wheel-rail contact surface (contact patch). 13
2.11 Possible contact situations new wheels (one point contact). 14
2.12 Possible contact situations worn wheels (two point contact). 14
2.13 Contact patch adhesion state, depending on the friction coefficient, normal force and creepage (Yang, 2020). 16
2.14 Dimensions for spin creepage (Yang, 2020). 17
2.15 Wear map of steel (Williams, 1999). 18
2.16 Relation between the dissipated energy and the occurrence of rolling contact fatique and wear (Burstow, 2003). 19

3.1 Geometry measurements in the city centre of Amsterdam. 27
3.2 Longitudinal overview of vertical wear for a selected track part in Railcloud. The red line represents vertical wear at the left side and blue line on the right. 27
3.3 Example of measured cross section vs original cross section. 27
3.4 Photo made and used by Strukton to derive the rail geometry. 28
3.5 Measured way side vibrations at the Lelylaan. The vehicle numbers are shown in each circle. 29
3.6 Measured squeal noise levels by two trams equipped with noise sensors of Sensornet. Measurement period: October-November 2021. 29
3.7 Schematic overview of tram wheel re-profiling. black = original shape; red = worn shape; green = re-profiled shape. 30
3.8 Examples of exploitation data. 32
3.9 Spatially displayed aggregated notifications of the CAF Urbos 100 tram. . . . 33

3.10 Horizontal welding: in red is the worn rail profile, in blue is the line which is needed to restore the original profile and in yellow is the material which should be removed first to enable welding (approximate dimensions). . . . 34
3.11 Available measurement data. . . . 35
3.12 Available exploitation data. . . . 36
3.13 Available track characteristics data. . . . 36

4.1 Average velocities at the tram network. . . . 38
4.2 Average velocities near Leidseplein. . . . 39
4.3 Example analysis of the mean driven velocity in the inner right curve. . . . 39
4.4 Average velocities per tracknumber, the table on the left shows the velocity distribution for the inner right curve as example. . . . 40
4.5 Velocity differences per tracknumber, a measure for the amount of acceleration per tracknumber. . . . 40
4.6 Average velocity driven on the tram network: yellow: <30 kph; orange 30-50 kph; red >50 kph. . . . 41
4.7 Red points: curves, crossings and switches with radius smaller than 30m where at least 20% drives faster than 20 kph. . . . 42
4.8 Examples of track parts with a radius smaller than 30m where 20% of the vehicles are passing above 20 kph. . . . 42
4.9 Example analysis of a curve (R=25) where vehicles are passing at high velocity (Plesmanlaan/Johan Huizingalaan). . . . 43
4.10 Velocity distributions Plesmanlaan/Johan Huizingalaan. . . . 43
4.11 Example analysis of a curve (R=25) where vehicles are passing at high velocity (Verbindingsdam/Ertskade). . . . 44
4.12 Detailed velocity analysis at the Burgemeester Röellstraat/Burgemeester Rendorpstraat junction. . . . 46
4.13 Detailed velocity analysis at the Sportlaan stop in Amstelveen. . . . 46
4.14 Raw Logdata plotted at the Raadhuisstraat/Nieuwezijds Voorburgwal Intersection. . . . 47
4.15 Difference in mean velocity week 33 2021 compared to 20-29 June 2021. Blue dot = > 5kph decrease, red = > 5kph increase. Road works done in week 33 at the Paulus Potterstraat (blue stretch) are clearly visible. . . . 49

5.1 qR measure for the flange steepness. . . . 51
5.2 Wheel wear categories, based on the steepness of the flange expressed in qR. 51
5.3 Example of the used method for one wheel. . . . 52
5.4 Derived qR probability distribution for the left wheels of the Combino. . . . 53
5.5 Derived qR probability distribution for the right wheels of the Combino. . . . 54
5.6 Derived qR probability distribution for the left wheels of the BN tram. . . . 54
5.7 Derived qR probability distribution for the right wheels of the BN tram. . . . 55
5.8 Average qR decay rate per wheel per vehicle type. . . . 56

6.1 Footage of the 3 selected curves. . . . 59
6.2 Input data for the principal simulations of the 3 curves. . . . 60
6.3 Aggregated results for the simulation at the outer rail representing a Combino negotiating a tight curve. . . . 61
6.4 Aggregated results for the simulation at the inner rail representing a Combino negotiating a tight curve. . . . 61
6.5 Schematic overview of the steering forces on bogie 1. . . . 62
6.6 Creep forces at the first bogie, L = inner rail, R = outer rail. . . . 63

6.7 Creep forces at the second bogie, L = inner rail, R = outer rail. 64
6.8 Schematic overview of the steering forces on bogie 2. 65
6.9 Creep forces at the third bogie, L = inner rail, R = outer rail. 66
6.10 Schematic overview of the steering forces on bogie 3. 67
6.11 Energy dissipation on the flanges of the wheels of bogie 1. L = inner rail, R = outer rail. 68
6.12 Energy dissipation on the treads of the wheels of bogie 1. L = inner rail, R = outer rail. 68
6.13 Energy dissipation on the treads of the wheels of bogie 2. L = inner rail, R = outer rail. 69
6.14 Zoomed in at the creep force along the curve from Figure 6.6 and 6.7. 69
6.15 Energy dissipation on the flanges of the wheels of bogie 3. L = inner rail, R = outer rail. 70
6.16 Energy dissipation on the tread of the wheels of bogie 3. L = inner rail, R = outer rail. 70
6.17 Measurement of the vertical wear along the outer curve at the 's Gravenzandestraat - Sarphatistraat intersection in 2020 71
6.18 Measurement of the vertical wear along the outer curve at the 's Gravenzandestraat - Sarphatistraat intersection in 2021 71
6.19 Average decay in flange angle per month for the right side of the Combino. . 73
6.20 Average decay in flange angle per month for the left side of the Combino. . . 73
6.21 Average decay in flange angle per month per expected energy intake per wheel for the current curve: r25, v10, new profiles. y axis: decay per energy intake [delta qR/(month*(kJ/m))], x axis: axles. 74
6.22 Aggregated results for the simulation at the outer rail representing a Combino negotiating a medium curve. 75
6.23 Aggregated results for the simulation at the inner rail representing a Combino negotiating a medium curve. 75
6.24 Creep forces of bogie 3 in the medium curve. 76
6.25 Schematic representation of bogie 2 and 3 at the middle curve. 77
6.26 Aggregated results for the simulation at the outer rail representing a Combino negotiating a gentle curve. 79
6.27 Aggregated results for the simulation at the inner rail representing a Combino negotiating a gentle curve. 80
6.28 Tram vehicle and global wheel - rail contact forces, in yellow the extra pitch moment added to simulate the braking. 81
6.29 Aggregated results for the simulation at the outer rail representing a loaded Combino negotiating a tight curve. 82
6.30 Aggregated results for the simulation at the inner rail representing a loaded Combino negotiating a tight curve. 83
6.31 Aggregated results for the simulation at the outer rail representing a Combino negotiating a tight curve. 84
6.32 Aggregated results for the simulation at the outer rail representing a Combino with worn wheels negotiating a tight curve. 85
6.33 Aggregated results for the simulation at the inner rail representing a Combino negotiating a tight curve. 85
6.34 Aggregated results for the simulation at the inner rail representing a Combino with worn wheels negotiating a tight curve. 86
6.35 Aggregated results for the simulation at the outer rail representing a Combino with worn rails negotiating a tight curve. 87

6.36 Aggregated results for the simulation at the inner rail representing a Combino with worn rails negotiating a tight curve. 87
6.37 Aggregated results for an empty Combino outer rail flange. 91
6.38 Aggregated results for an empty Combino outer rail tread. 91
6.39 Aggregated results for an empty Combino inner rail flange. 92
6.40 Aggregated results for an empty Combino inner rail tread. 92
6.41 Aggregated results for an empty Combino with worn wheels outer rail flange. 93
6.42 Aggregated results for an empty Combino with worn wheels outer rail tread. 93

7.1 Input for the energy estimation model, general usage data taken from 23-09-2021, wheel wear data taken from tram wheel measurements from 2014 until 2020 (see Chapter 5), velocity data taken from 20-29 June 2021 (see Chapter 4). 96
7.2 Output of the energy estimation model for one example curve. 97
7.3 Wheel wear categories, based on the steepness of the flange expressed in qR. 97
7.4 Flow chart of the energy estimation model. 98
7.5 The T_γ dictionary which green boxes are filled per curve. H = outer rail, L = inner rail, F = Flange, T = Tread. 98
7.6 Initial T_γ value selection using interpolation based on the curve radius. . . . 100
7.7 T_γ interpolation per wheel wear category. 100
7.8 T_γ factoring to arrive at a statistical passage value. HT = tread at outer rail. . 101
7.9 Energy dissipation categories for one statistical tram passage (SP) and the yearly amount of energy intake (TW). The colours are used in the figures which show the energy estimations on the map. 102
7.10 Example of the energy dissipation estimation model output, for curve 1110 at the Nieuwezijds Voorburgwal - Raadhuisstraat intersection. See Figure 7.9 for the color references. H = outer rail, L = inner rail, F = Flange, T = Tread. . 102
7.11 Example overview of the network wide yearly expected energy dissipation values in curves. See Figure 7.9 for the color references. 103
7.12 Legend of the velocities per trackpoint, resulting from the analysis described in Chapter 4 104
7.13 Example validation of curve 33030. Green = start, red = end. Velocity legend: Figure 7.12. The profile measurements along the curve show the vertical wear in mm (left = red, right = blue). 104
7.14 Example validation of curve 48910. Green = start, red = end. Velocity legend: Figure 7.12. The profile measurements along the curve show the vertical wear in mm (left = red, right = blue). 105
7.15 Example validation of curve 1110. Green = start, red = end. Velocity legend: Figure 7.12. The profile measurements along the curve show the vertical wear in mm (left = red, right = blue). 106
7.16 Example validation of curve 43790. Green = start, red = end. Velocity legend: Figure 7.12. The profile measurements along the curve show the vertical wear in mm (left = red, right = blue). 107
7.17 Comparison yearly expected energy dissipation and measured wear for the 4 selected curves. 107
7.18 Example of extreme worn rail (left) and faulty rail profile measurements (right). 108
7.19 Scatter plot of the yearly estimated energy dissipation and measured wear of the outer rail tread. 109
7.20 Scatter plot of the estimated energy per passage and yearly measured wear of the outer rail tread. 109

A.1 Overview of the tram tracks, -depots and -workshops in Amsterdam. 117

A.2 Technical drawing of the Siemens Combino for Amsterdam Siemens, 2007. . 117
A.3 Tram vehicles used at the tram network in Amsterdam. 118
A.4 Simplified overview of the urban public transport network of greater Amsterdam. 119
A.5 Typical tram track lay-outs in the larger city center. 119
A.6 GVB Combino op lijn 13 bij de halte Jan van Galenstraat (Eelco, 2021). . . . 120
A.7 To coupled Urbos trams on line 25, here the line was being tested after the renovation (Dubbelman, 2020). 121
A.8 Two coupled Siemens Combino's at line 26 (EenRailSpotter, 2020). 121
A.9 Equipment division on the network, numbers between parenthesis are the number of equipment objects per category. 122
A.10 Curve radius distribution [m]. 123
A.11 Last track renewal year. 123
A.12 General last renewal year of parts on the tram network. 124
A.13 Last renewal year of tight curves (radius < 30 meter). 124
A.14 Location of tight curves (radius < 30 meter). 125
A.15 General usage by other traffic. 125
A.16 Usage by other traffic tight curves only (radius < 30 meter). 126
A.17 General railtype. 128
A.18 Tight curves railtype. 128
A.19 General steel sort. 129
A.20 Tight curves steel sort. 129
A.21 General rail fastening system. 130
A.22 Tight curves rail fastening system. 130
A.23 General hardening type. 131
A.24 Tight curves hardening type. 131
A.25 Tram passages per track segment. 132
A.26 Average loading per vehicle per track segment. 132
A.27 Total volume of passengers per track segment. 133

B.1 Scatter plot of the yearly estimated energy dissipation and measured wear of the outer rail tread. 135
B.2 Scatter plot of the yearly estimated energy dissipation and measured wear of the outer rail flange. 135
B.3 Scatter plot of the yearly estimated energy dissipation and measured wear of the inner rail tread. 136
B.4 Scatter plot of the yearly estimated energy dissipation and measured wear of the inner flange. 136
B.5 Scatter plot of the estimated energy per passage and yearly measured wear of the outer rail tread. 137
B.6 Scatter plot of the estimated energy per passage and yearly measured wear of the outer rail flange. 137
B.7 Scatter plot of the estimated energy per passage and yearly measured wear of the inner rail tread. 138
B.8 Scatter plot of the estimated energy per passage and yearly measured wear of the inner rail flange. 138

C.1 Each piece of track has its own tracknumber, on the left the tracknumber ('AN') is visible for the curve part encircled in red. 139
C.2 Trackpoints used in the velocity analysis. 140
C.3 Data attached to each trackpoint. 140

C.4 Step 1 of the analyzing process: loading of input data. 142
C.5 Velocity loggings, directly plotted in QGIS. 143
C.6 Step 2A of the analyzing process: determine the tram route. 144
C.7 Step 2B of the analyzing process: determine the nearest valid trackpoint. . . 146
C.8 Step 3 of the analyzing process: velocity per trackpoint analysis. 147
C.9 Step 4 of the analyzing process: output. 148

D.1 Siemens Combino vehicle model. 151
D.2 Wheel-rail contact model with new 60R2 rails and new wheels. The red line represents the rail profile, green line is the wheel profile and the red ellipse is the contact patch (Hertzian model). 152
D.3 Wheel-rail contact model with worn rails and new wheels. The red line represents the rail profile, green line is the wheel profile and the red ellipse is the contact patch (Hertzian model). 152
D.4 Wheel-rail contact model with new 60R2 rails and worn wheels. The red line represents the rail profile, green line is the wheel profile and the red ellipse is the contact patch (Hertzian model). 153
D.5 Dissipated energy at the wheels of the first bogie at the flange contact surface. 156
D.6 Dissipated energy at the wheels of the first bogie at the tread contact surface. 157

Chapter 1

Introduction

This research focuses on wear in tramway curves. Chapter 1 provides an introduction to the investigation. The problem statement argues the need for this research, followed by an introduction to GVB, the public transport company of Amsterdam. After that, the research questions, scope and research methodology are provided. The chapter concludes with an overview of the tramway of Amsterdam.

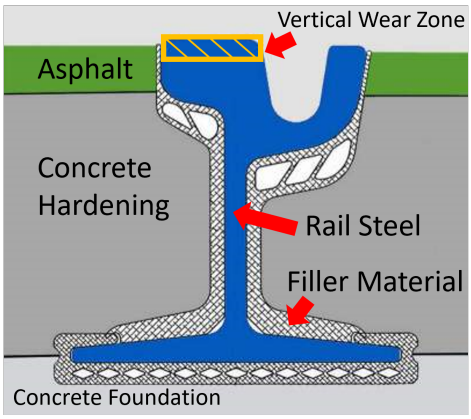
1.1 Problem Statement

GVB wants to obtain more insight into the rail degradation processes of tramways, to enhance maintenance planning. This research focuses on vertical and horizontal rail wear in curves, one of the leading causes of necessary maintenance. The wheel and rail contact induces both vertical and horizontal wear on rails. Vertical wear causes the railhead to become thinner. Another problem caused by vertical wear is the increase of rail irregularities. Since the wear will not occur at the same rate along the rail, the rail surface will become uneven. This causes a less comfortable ride and faster rail and vehicle equipment deterioration because of dynamic loading. Horizontal wear entails the same but then in the horizontal direction. On the contrary to vertical wear, horizontal wear could be removed by adding welding material to the side of the railhead. Figure 1.1a shows the global location on the railhead where vertical wear occurs, Figure 1.1b shows the same for horizontal wear.

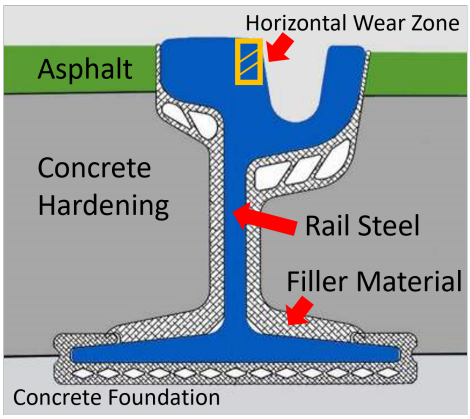
The problem itself lies in the complexity of such wear processes. At some particular curves, the wear rate is much higher than in other curves, without proven reasons. This causes problems with maintenance planning. GVB would like to obtain a better overview of data at its disposal today, which might help make a better prediction for the rail wear rate for the future.

1.2 Introduction to GVB

GVB provides metro, tram, bus and ferry services in the metropolitan area of Amsterdam. The company and predecessors have transported people in Amsterdam for more than 120 years. In 2019 GVB transported nearly a million travellers on an average working day. Around 5000 employees are working at GVB (GVB, 2021). Figure 1.2a and 1.2b show the two used vehicles on the tramway.



(A) Vertical wear zone Trading, 2021.



(B) Horizontal wear zone Trading, 2021.

FIGURE 1.1: Wear zones.



(A) A Siemens Combino at line 14 in Amsterdam Simons, 2019.



(B) A CAF Urbos in GVB livery at line 5 at the Marnixstraat/Rozengracht intersection Martin, 2021.

FIGURE 1.2: Tram vehicles used at the tram network in Amsterdam.

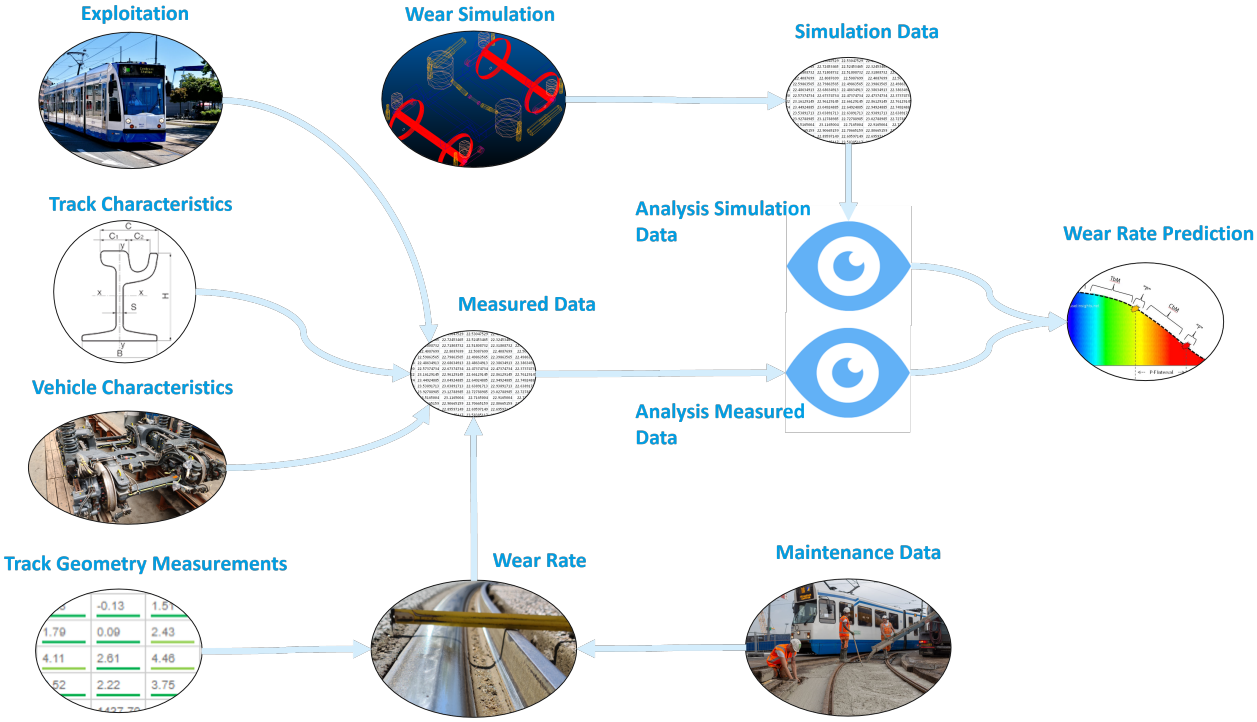


FIGURE 1.3: Overview on the research methodology.

1.3 Research Questions

With the problem statement in mind, the following research questions are formulated. Main question: **How can tram rail wear in curves at GVB be better predicted?**

- 1 - What is state of the art regarding tram railways in the fields of maintenance, track modelling and monitoring?
- 2 - Based on the measurement data and information available at GVB, which data and track parameters should be considered to predict tram rail wear?
- 3 - Which processes are responsible for the occurrence of rail wear, and what are the most influential parameters?
- 4 - How could the rail wear process in specific curves and in general be simulated?
- 5 - How could a wear prediction model be developed which predicts the wear for all curves on the tramway of the whole city of Amsterdam?

1.4 Scope

The model development is limited to vertical and horizontal wear in curves at the tram network in Amsterdam. This scope is chosen because wear in sharp curves takes much maintenance effort. Furthermore, the wear rate in curves is complex compared to other degradation processes, increasing the problem size.

1.5 Research Methodology

Each step of the methodology is described separately. Figure 1.3 provides an overview of the research methodology.

1.5.1 Literature Research

The literature research aims to provide an overview of simulation models and monitoring techniques for tram railways. The study also gives particularities for tram railways compared to conventional railways and information about rail wear. The literature research forms a basis for this whole thesis.

1.5.2 Available Data Exploration

Data is gathered by researching which information is available within GVB and what could be used in the wear prediction model. The collected data falls into four main categories: measurement, usage, asset, and external data. Measurement data includes data to assess the rail condition, for example, rail geometry measurements. Usage data consist of a broad range of data, pointing to how the track asset is used, for example, the daily load on a particular curve. Asset information contains, for example, the steel hardness or rail type. The last category, external data, includes data linked to the environment of the asset, for example, the vicinity of a stop or usage by other traffic modes.

1.5.3 Data Quality and Usability Investigation

The available data is assessed based on quality and usability for the wear model. At first, the information needs to be reliable enough to be included in the model. Second, data should be able to be handled by e.g. Python code, so the proposed solution can be implemented in the whole tramway. During this investigation, the limitation and assumptions embedded in the data are retrieved. The data selected to be included in the remainder of the research is further analyzed and adapted to make it feasible for inclusion in the wear prediction models.

1.5.4 Rail Wear Simulations

Simulations are performed to assess which parameters are most influential in rail wear. For example, the influence of the curve radius and tram velocity was analyzed. The wear simulations are performed parametrically, using a fictive curve and changing only one parameter stepwise at a time per run.

1.5.5 Predictive Model Design

Based on the outcomes of the simulations, a wear prediction model was developed, which predicts the wear per curve on the tramway based on the chosen input data relevant for rail wear.

1.5.6 Model Validation

The wear model is validated by predicting the wear for a group of curves with the model. The expected wear is evaluated by comparing it with the actually measured wear on those curves.

1.6 Tram Network Characterization

The following subsections provide a short overview of the tram network of Amsterdam. First, a general description is given, followed by information on the rolling stock and network characteristics. Appendix A contains an extended tram network description.



FIGURE 1.4: Simplified overview of the urban public transport network of greater Amsterdam.

1.6.1 General Description

The tram network in the city centre has high usage. The tramway serves the outside districts New-West, Amstelveen and Diemen; other neighbourhoods are only done by metro, buses and ferries. Maintenance is very costly since track works lead to significant traffic disruptions. Figure 1.4 shows an overview of the rail public transport network in Amsterdam.

1.6.2 Rolling Stock

The rolling stock consists of 70-80% of the Siemens Combino, a low floor tram. In 2021 an older tram type (BN) was retired and replaced by the low floor CAF Urbos 100. Both the Combino and Urbos 100 have a maximum velocity of 70 kph.

1.6.3 Network Characteristics

The track network consists of about 200 km rails and 500 stops. The maximum velocity is 70 kph, but trams often drive not faster than 50 kph or even 30 kph in practice. Although trams have gone through Amsterdam for over a century, most parts of the network are not that old since tracks are renewed from time to time. The majority of the network has been revived in the last 20 years. The vast majority of the network is not older than 30 years. An essential characteristic of the tram network in Amsterdam is a large number of tight curves. 24% of all curves has a radius smaller than 30 meters. Most of these tight curves are located at junctions, which are primarily found in the city centre (Figure 1.5). Often, tracks are shared with general other traffic or buses and taxis, especially in the city centre. The infrastructure consists mainly of 60R2 grooved rail (78% in general and 90% in tight curves), made of R200 steel.

For further reading, Appendix A contains an more detailed and extended tram network description.

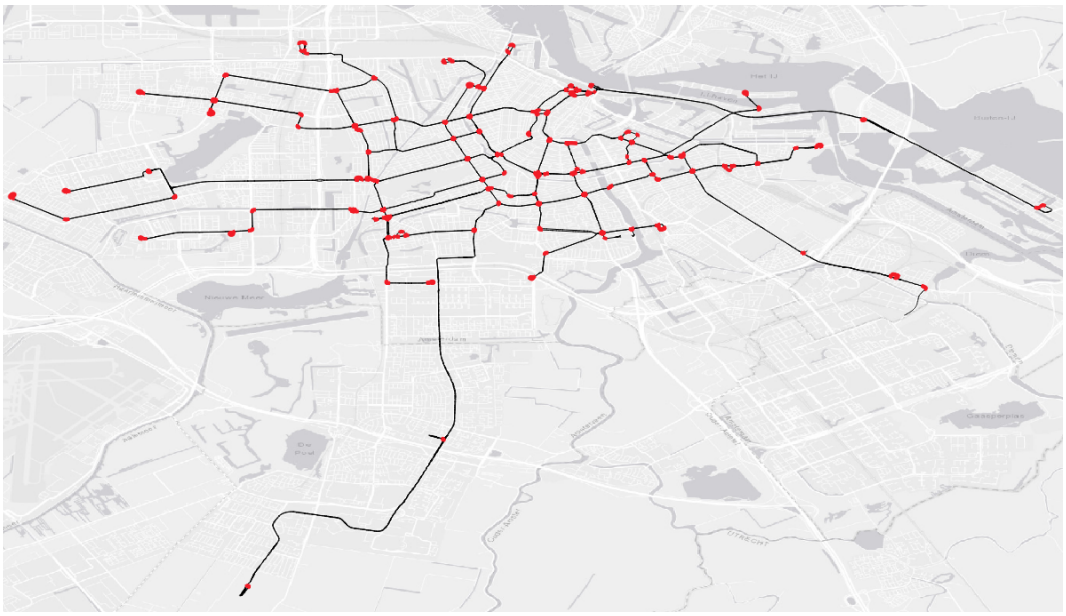


FIGURE 1.5: Location of tight curves (radius < 30 meter).

Chapter 2

Literature Review and Background Information

The following sections provide background information and compare a set of scientific articles.

2.1 Background Information

This section provides background information regarding curving negotiation of tramway vehicles and wear simulation.

2.1.1 Overview Tramway

This subsection provides a basic overview of the tram railway and vehicle structure with related terminology.

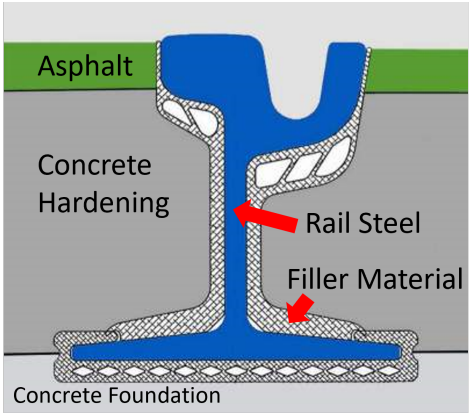
Regarding the track structure, different kinds are used for tramways. In Amsterdam, grooved rails encased in concrete (see Figure 2.1a) is mainly used. At some stretches, vignole rail is used. This type of rail is the standard for heavy rail (e.g. trains). However, the tracks with sharp curves are mainly built with grooved rail encased in concrete. Therefore, the remainder of the background information and research focuses on the grooved rail in the concrete structure; Figure 2.1b shows this structure.

Figure 2.8 shows a simplified overview of a tramway vehicle. Trams consist of wheels that are mounted to bogie frames. These bogies are connected to the body of the vehicle. Two sets of wheels are mounted to one bogie frame in most cases. Suspension and damping are provided between the wheels, bogies, and body to overcome damage and vibrations from the wheel-rail contact. The suspension between the wheels and bogie is called primary suspension. Between the bogie and body, it is called secondary suspension. In trams, commonly the rubber between the wheel body and wheel tyre provides suspension. The wheel tyre is replaced periodically since it wears off during operation.

Figure 2.2a and 2.7 show the cross-sections of a grooved rail and a tram wheel on grooved rail. The terms in these figures will be used throughout this thesis.

2.1.2 General Concepts of Tramway Curve Negotiation

The following degrees of freedom of the vehicle are important: longitudinal movement (along the track), lateral movement (sideways) and yaw movement (along the vertical axis). Figure 2.3 shows these movements.

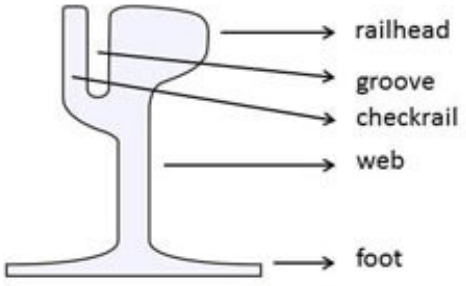


(A) Tramway track structure cross section (Trading, 2021).

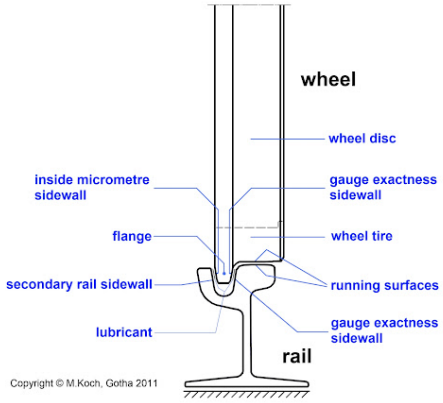


(B) Track reconstruction in the Jordaan neighborhood.

FIGURE 2.1: Grooved rail encased in concrete.



(A) Grooved rail cross section.



(B) Wheel on grooved rail cross section.

FIGURE 2.2: Cross sections of tramway rail and wheel (Group, 2021).

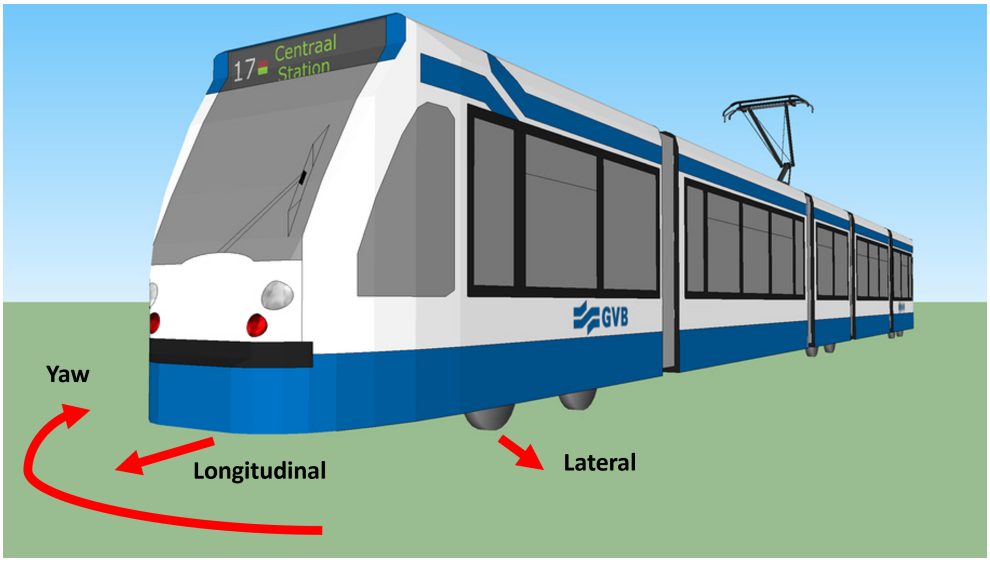


FIGURE 2.3: Overview of important movement directions for tram curve negotiation (Arman, 2021).

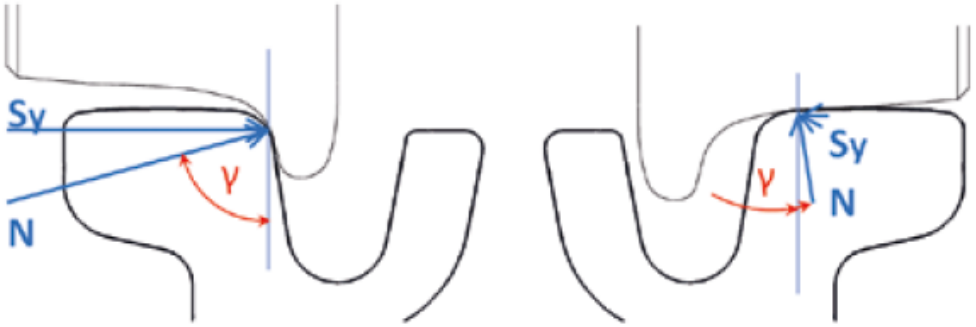


FIGURE 2.4: Flange contact during curve negotiation (Siemens, 2016).

When a tram runs through a curve, lateral centrifugal forces push the vehicle towards the outer rail. The wheel flange on the outer side can make contact with the rail (2.4)in this case. The amplitude of the centrifugal force depends on the vehicle's mass, velocity and curve radius, according to the following equation:

$$F_C = \frac{mV^2}{R} \tag{2.1}$$

With:

F_C = centrifugal force
m = vehicle mass
V = vehicle velocity
R = curve radius

At the tramway of Amsterdam, no or only little (1-2 mm) cant is applied, which enlarges the lateral movement because of the centrifugal force. Cant is usually applied in railway curves by twisting the track. Tangential friction forces oppose the centrifugal forces at the wheel-rail contact interface in the lateral direction. When the wheel flange comes into contact with the railhead, also normal forces oppose the centrifugal forces. Those reaction forces guide the bogie through the curve (2.5).

A tram wheel cannot line up perfectly with the curve since the wheel is attached to the bogie, which cannot provide full flexibility. This leads to an *angle of attack* (2.5). Each wheel has a small yaw displacement compared to the running line of the track. To allow the position of the axles to adapt according to the curvature, wheels are conical. Suspension is installed in the boogie to smooth this movement to increase comfort. Stiff suspension results in more comfort for the passengers but a lower ability to guide the wheels. Therefore it causes larger wheel-rail contact forces, which results in a faster wheel and rail degradation.

The guiding principle works well for curve radii larger than about 80 meters. However, tram infrastructure often has much smaller radii, resulting in insufficient wheels' steering. This issue causes the wheels to slip, which causes wear. To solve this problem, independent steering wheels are developed for trams. Those independent wheels are not mounted to a common axle, lifting the condition that both wheels have the same rolling velocity. This technique enables the tram to steer with reduced slip through smaller curves. However, the running behaviour is less stable with independent wheels at higher velocities. Left and right wheels could still be electrically coupled when attached to the same engine.

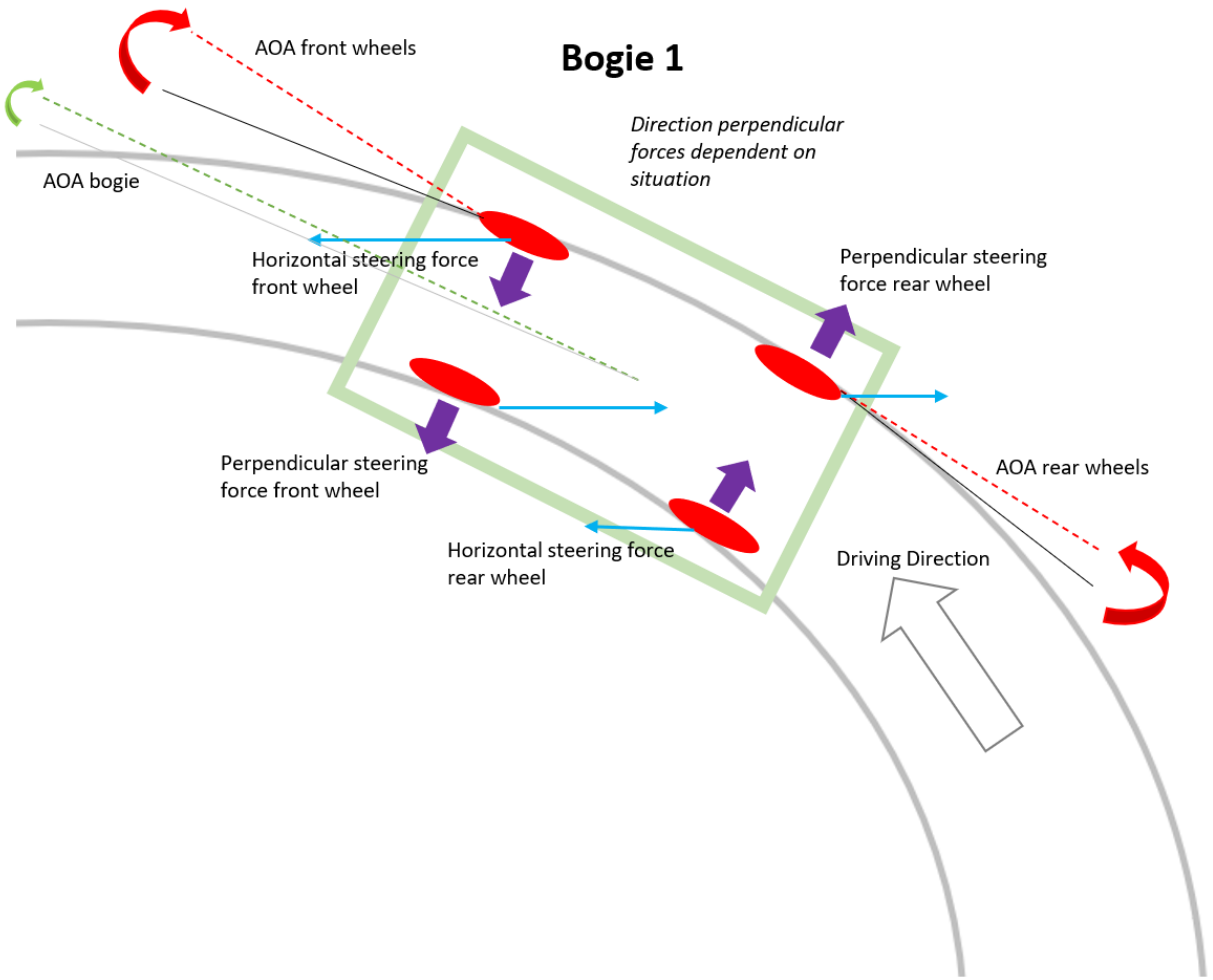


FIGURE 2.5: Schematic overview of the steering forces on a tram bogie.



FIGURE 2.6: Conventional bogie (older type).

Figure 2.6 and **??** show the difference between the conventional 2 axle bogie and the bogie with independent wheels. More information on independent wheels could be found in (Siemens, 2016).

2.1.3 Modelling Vehicle Dynamics

Section 2.2.2 provides an overview of modelling techniques available for railway applications. This section explains vehicle modelling by multi-body models. This technique is also used in the simulations described in Chapter 6.

Vehicle dynamics are often modelled by a multi-body model of the track and vehicle. The vehicle is modelled by multiple bodies interconnected by springs and dampers. The car body, bogie frame and wheels could all be discretised in bodies with a specific mass and moment of inertia. Then, the stiffness and damping effects between the bodies can be modelled with specific spring stiffnesses and damping ratios. Multi-body models are often solved using computational software, although simple problems could be solved by hand.

When the models are defined, the next step is to describe coordinate systems. Interlinking those coordinate systems with goniometry enables us to interpret global and local displacements and forces. Equations of motion define the forces and displacements for each element, given an initial force or displacement from the previous timestep. Those equations are then solved per timestep with a mathematical integration scheme. This method enables the simulation of a running vehicle along a track.

Figure 2.8 shows a possible multi-body model for a tramway vehicle. Figure 2.9 shows a possible multi-body model for a tramway bogie with both wheels fixed to the same axle.

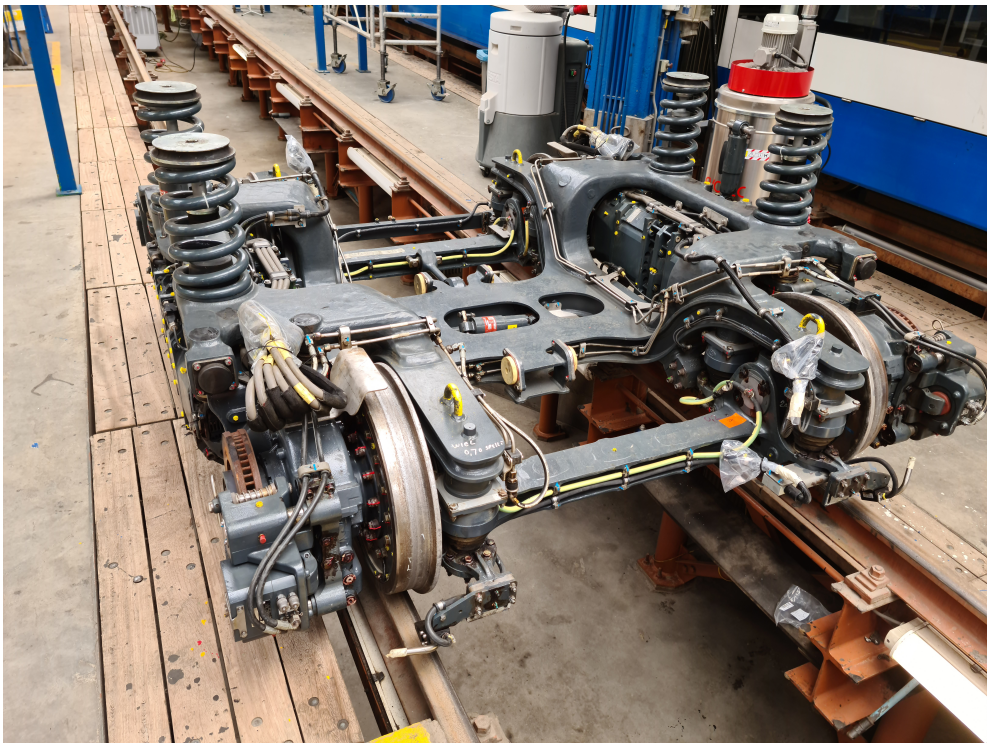


FIGURE 2.7: Bogie with independent wheels.

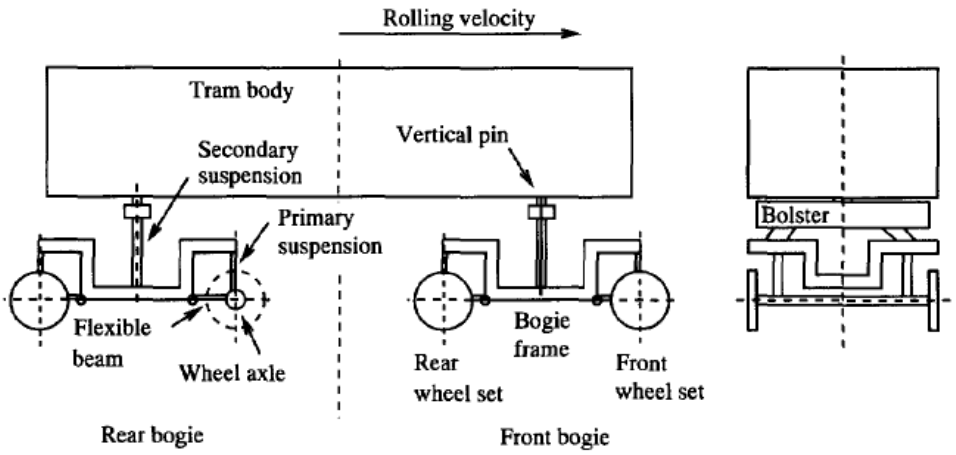


FIGURE 2.8: Possible simulation model for a car body.

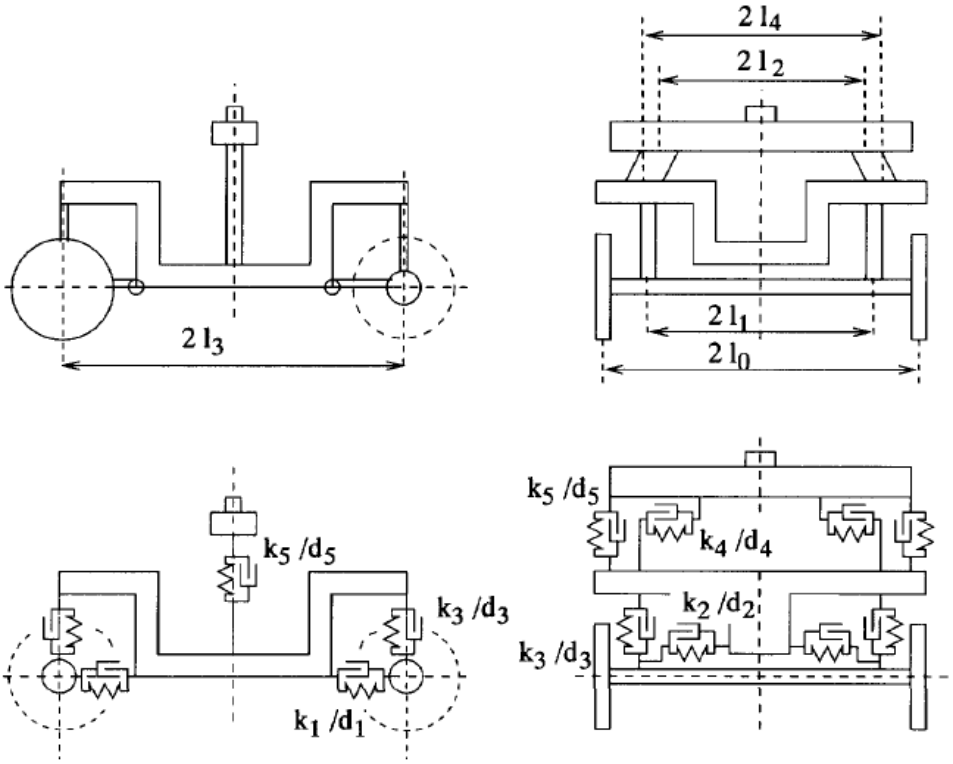


FIGURE 2.9: Possible simulation model for a bogie. l = length, k/d = stiffness/damping.

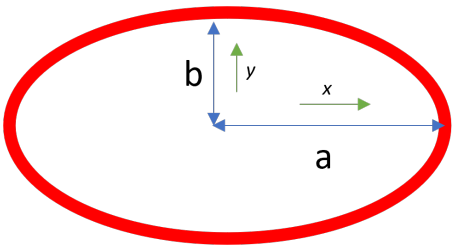


FIGURE 2.10: Typical shape of the wheel-rail contact surface (contact patch).

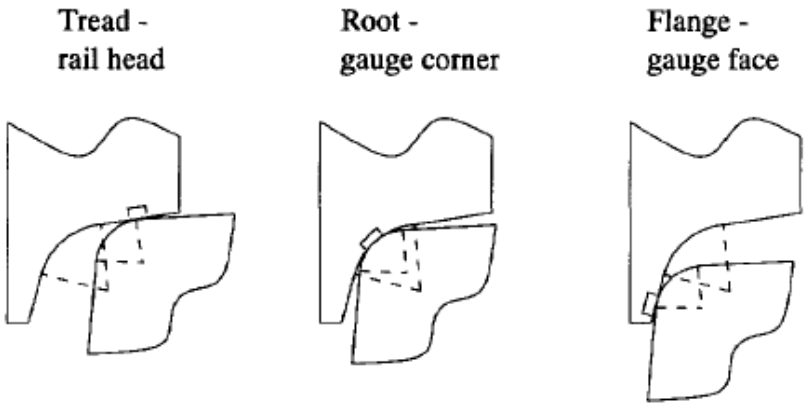


FIGURE 2.11: Possible contact situations new wheels (one point contact).

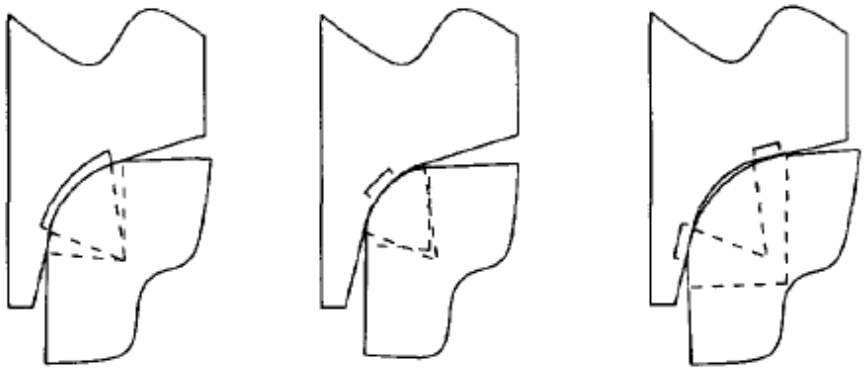


FIGURE 2.12: Possible contact situations worn wheels (two point contact).

2.1.4 Modelling Wheel-Rail Contact

The surface where wheel and rail make contact (contact patch) is usually relatively small (1 square centimetre)(2.10). Because of this, contact stresses could rise to 1 GPA. One point contact (2.11) is the default case for regular operation on a straight track with unworn wheels. Two-point contact (2.12) can occur in curves when the flange makes contact with the rail. In this case both the wheel flange and tread have one contact point with the rail. The chance of two-point contact increases with worn wheels. During conformal contact, the wheel and rail make contact over a large surface. This conformal contact can occur when wheel and rail geometries converge to each other because of wear.

The relation between normal force, size of the contact zone and compression stress in the contact zone can be modelled by the Hertz theory (Hertz, 1882). This theory is only applicable under the assumption of linear elastic material, non-conforming contact, bodies that are half-spaces and frictionless surfaces. The following relation for the normal compression stress of two bodies in contact was derived by Hertz:

$$p_0 = \frac{3N}{2\pi ab} \tag{2.2}$$

$$p_{x,y} = p_0 \sqrt{1 - \frac{x^2}{a} - \frac{y^2}{b}} \tag{2.3}$$

With:

$p_{x,y}$ = normal contact stress at x,y (see Figure 2.10)
p_0 = maximum normal contact stress at midpoint contact patch
N = normal contact force

a and b represent the dimension of the contact patch (2.10). a and b can be calculated based on the principal radii of wheel and rail, Young's modulus and Poisson coefficients. K.L.Johnson, 1985 could be consulted for more information on contact theory.

Tangential forces also have a significant role in rail wheel contact. Amonton (Amontons, 1699) and Coulomb (Coulomb, 1773) provided three frictional laws, which help to understand the influence of friction on rolling contact:

- The force of friction is directly proportional to the applied load.
- The force of friction is independent of the apparent area of contact.
- Kinetic friction is independent of sliding velocity.

This implies the following relation:

$$\mu_T = \frac{Q}{P} \leq \mu \tag{2.4}$$

With:

μ_T = traction coefficient
Q = tangential creep force
P = normal force
μ = coefficient of friction

The creep force is limited to:

$$Q_{max} = \mu P \tag{2.5}$$

A body will start to slide when the maximum creep force is applied to that body. Then, the whole contact patch is in slip. This theory also applies to wheels on rails. When no creep force is present, e.g. at (theoretical) frictionless rolling motion, the whole contact patch is in stick. If the creep force is between zero and maximum, part of the contact patch is in slip and part in stick. This process is illustrated in Figure 2.13.

As mentioned before, the wheels could not line up perfectly with the rails in curves. To correct this misallignment, the wheels have to make slip motions, causing part of the contact patch to slip. Furthermore, the wheel's rolling mostly produces some frictional force since the wheel and rail surfaces are not perfectly smooth.

By comparing the forward velocity of the vehicle to the rolling velocity of the wheels, it is possible to compute the velocity produced by the slip. The ratio between the slip velocity and forward velocity is called *longitudinal creepage*. During driving, tram vehicles

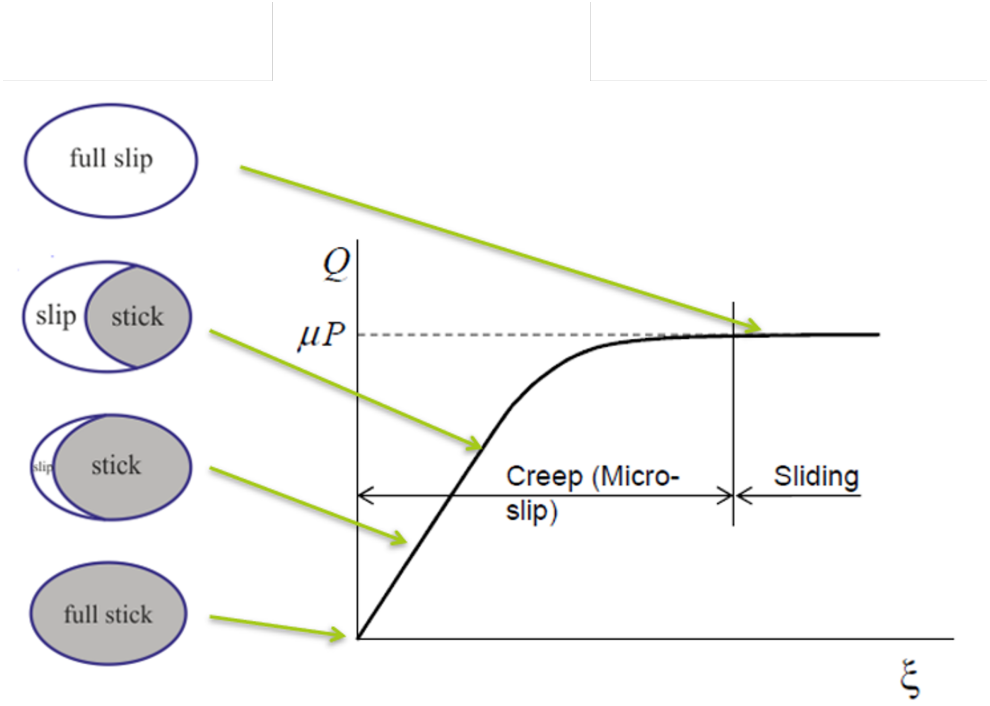


FIGURE 2.13: Contact patch adhesion state, depending on the friction coefficient, normal force and creepage (Yang, 2020).

also move in the lateral direction. The ratio between net lateral movement and lateral slip velocity is the *lateral creepage*. The lateral creepage is equal to the yaw angle of the wheel. Both longitudinal and lateral creepages are non-dimensional. The *spin creepage* is dependent on the wheel dimensions and expressed in rad/m or 1/m (see Figure 2.14).

The following equations define the creepages.

Longitudinal creepage:

$$\xi_x = \frac{(|V| - |c|_x)}{v} \tag{2.6}$$

With:

ξ_x = longitudinal creepage
$|V|$ = rigid velocity in longitudinal direction
$|c|_x$ = rolling velocity in longitudinal direction
v = forward velocity (longitudinal direction)

Lateral creepage:

$$\xi_y = \alpha \tag{2.7}$$

With:

ξ_y = lateral creepage
α = yaw angle wheel

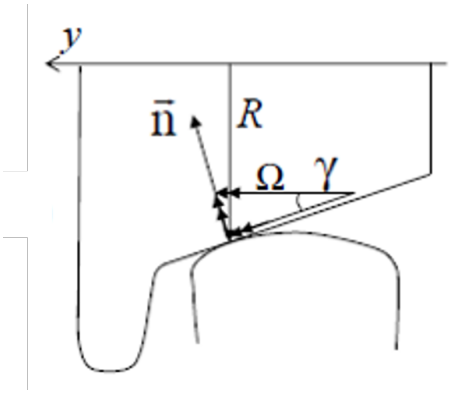


FIGURE 2.14: Dimensions for spin creepage (Yang, 2020).

Spin creepage:

$$\phi = \frac{\Omega sin\gamma}{v} = \frac{sin\gamma}{R_{wheel}} \approx \frac{\gamma}{R_{wheel}} \tag{2.8}$$

Figure 2.14 provides the parameters for the spin creepage calculation.

The Finite Element Method (FEM) provides the ultimate solution to simulate creepages. A drawback of this approach is long calculation times. Therefore, the finite element approach limits the possibility of simulating longer stretches of a track or multiple situations. Carter developed in 1926 (Carter, 1926) the first analytical relation between non-dimensional creep force and creepage. This anlysis was done by combining the Hertz contact theory Hertz, 1882 and the Amonton-Coulomb frictional laws (Amontons, 1699,Coulomb, 1773). Kalker (J.J.Kalker, 1967) developed a model to simulate forces and creepages during wheel-rail contact based on the work of Carter. This model is still widely used today. A drawback of analytical models compared to FEM is the disability to model complex contact geometries, conformal contact and dynamic effects.

2.1.5 Wear

The friction and related creepages lead to the removal of surface material, and this process is called wear (Bolton and Clayton, 1984). In wheel-rail contact, wear can occur in different directions, depending on the resultant sliding movements of the wheel. The rail wear increases when slip becomes more dominant at the contact patch, for example during acceleration, braking and curve negotiation.

A main starting point to understand the wear process is Archard wear equation (Williams, 1999):

$$V = \frac{kWL}{H} \tag{2.9}$$

With:

V = wear volume
k = non dimensional constant
W = normal force
L = sliding distance

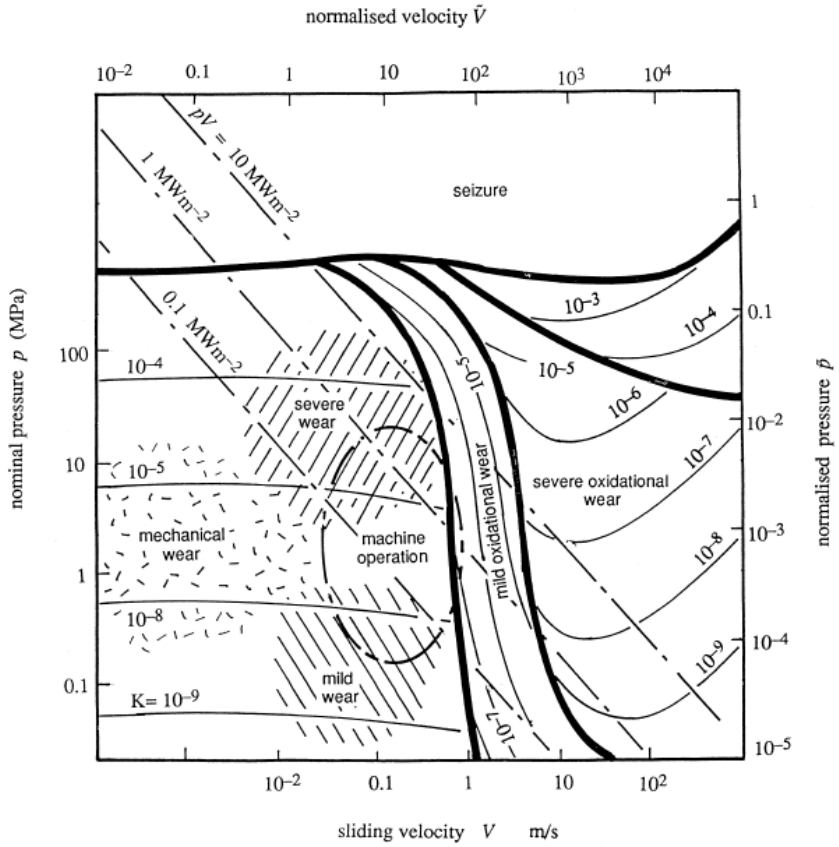


FIGURE 2.15: Wear map of steel (Williams, 1999).

H = hardness softest surface

It is challenging to model wear, which makes wear prediction also challenging. This difficulty is the large number of factors that influence wear. Also, the wear process itself is non-linear (Williams, 1999). The following factors influence the wear process: normal load, relative sliding speed, geometry, initial temperature, local environment and thermal-, mechanical- and chemical properties of the materials involved. Third bodies, for example lubrication, dirt or debris also influence the wear process.

To improve understanding of the wear process per material, wear maps are developed to visualise the non-linear characteristics. Figure 2.15 shows an example of such a wear map. The sliding velocity and pressure indicate the wear coefficients to be expected. The wear map in Figure 2.15 shows the characteristics of medium carbon steel based on pin-and-disc data. A typical aspect is a deviation in mild and severe wear. A slight increase in loading or velocity could trigger the transition from mild wear to a severe wear regime. Mild wear gives flat flakes as debris and is acceptable in most engineering applications. Severe wear results in larger chunks of materials separated from the material and often unacceptable.

Full-scale experiments have been done for railways to understand wear with roller wheels on rails. An artificial creepage was applied to the wheels to obtain the wear rates per creepage. Those experiments are described in (Bolton and Clayton, 1984). This study found three wear types. Type 1 wear was independent of the material composition and creepage. In this case, the dominant wear modes were oxidation and flake formations dictated

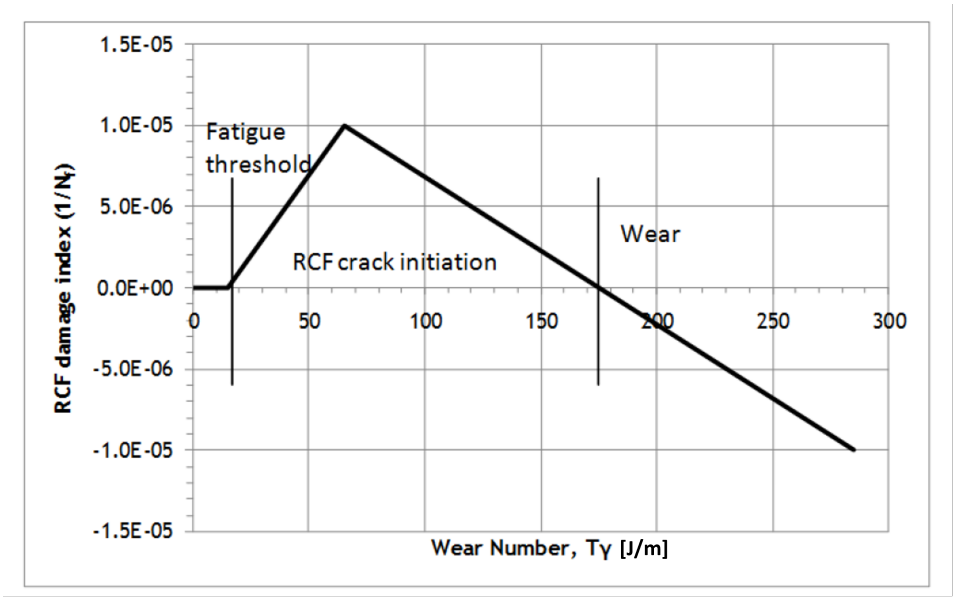


FIGURE 2.16: Relation between the dissipated energy and the occurrence of rolling contact fatique and wear (Burstow, 2003).

by the tangential force. Type 2 wear was dependent on material properties, contact pressure and creepage. This wear type gave flakes and was found on the running band. Type 3 wear was found on the gauge side of the rail and the flanges. The range of debris particles was wider, and the rough, cracked surface was similar to pure sliding tests.

2.1.6 Energy Dissipation and Frictional Work

Energy dissipation (T_γ), the expended energy per unit distance in frictional rolling contact, can be used as wear estimator RGL, 2018. The expended energy per unit distance is the product of creep force and creepage. To obtain the total energy dissipation, the expended energy in longitudinal, lateral and spin direction is summed, according to the following formula:

$$T_\gamma = Q_x \xi_x + Q_y \xi_y + M\phi \tag{2.10}$$

With:

T_γ = expended energy per unit distance
Q = tangential (creep) force
ξ = creepage
M = spin moment
ϕ = spin creepage

T_γ is expressed in Joule/meter. The tangential force is also often denoted with a capital T. The creepage can also be denoted by a γ. This difference explains the naming of T_γ.

Figure 2.16 from (DEKRA, 2020) shows the general influence of the dissipated energy on the rail. Until levels around 20 J/m, no damage is done. Above this level, cracks will appear in the rails, which causes rolling contact fatigue (RCF). The rolling contact fatigue peaks around 65 N, where approximately 100 000 load cycles are needed (y-axis) to create visible

cracks. If T_γ increases further, the wear will increase, which removes the initiating cracks. This mechanism has a positive influence on the occurrence of RCF. Above approximately 175 J/m, no cracks will occur, and then there is only material removal by wear. According to DEKRA, 2020, it was found that above 300 J/m non-lubricated R260 rail will enter a state of abrasive wear.

The wear can also be indicated by dissipated power as a result of frictional work (G. Alarcón, 2015). In this case, the dissipated power is calculated by the following formula:

$$P_{friction} = (Q_x \xi_x + Q_y \xi_y + M\phi)V \tag{2.11}$$

With:

V = vehicle velocity

The dissipated power is expressed in Nm/s (work per second).

Both energy and power dissipation indicators can be used to estimate wear. No evidence was found that one of both indicators outperforms the other in terms of accuracy. However, as stated in (Williams, 1999), no wear indicator is available which has total accuracy.

According to Archard's wear equation (see section 2.15), wear volume is dependent on a constant, normal force, sliding distance and material hardness. The creep force (friction force) is directly proportional to the normal force (see section 2.1.4). The creepage is the ratio of velocity generated by slip versus total velocity. Therefore, the energy dissipation indicator indirectly takes the normal force and friction coefficient into account, scaled by the velocity portion caused by slip. The power dissipation is the energy dissipation multiplied by the vehicle velocity. While creepage is non-dimensional except for the spin creepage, velocity measures distance per time unit. Therefore, the power dissipation wear indicator also considers sliding distance, besides normal force. It can now be argued the power dissipation indicator is suspected to be more accurate.

To estimate volumetric wear, both indicators should be corrected by the material hardness. Furthermore, still some factors are left which could influence the wear process: rail and wheel surface geometry, temperature, thermal- and chemical properties of the materials involved and third bodies at the contact interface, e.g. dirt or debris. Those factors could be embedded in the non-dimensional constant of Archard's wear equation. However, no method was found that successfully embed those factors in a constant. It would also be challenging to compute correct values for all those variables for situations in practice. In conclusion, the discussed wear indicators can provide general wear estimations. However, it is challenging to obtain an accurate estimation of volumetric wear.

2.1.7 Further Reading

(K.L.Johnson, 1985) provides an overview of elementary contact theories, which form the basis for contact modelling methods. To obtain more information on general railway theory and modelling approaches of tram railways, (Periard, 1998) gives broad and in-depth information on the modelling of a tram railway system. (Shevtsov, 2008) also provides a broader overview of modelling to optimise wheel and rail profiles. (Williams, 1999) describes wear theory, modelling approaches and provides further references for more understanding on wear.

2.2 Literature Review

This section contains the literature review. At first, the differences between heavy railways and tram railways are highlighted. Second common track modelling approaches are compared, and at last common monitoring techniques are described.

2.2.1 Tram Railways Compared to Heavy Railways

In comparison to heavy rail, little research has been done into tram railways and other light rail infrastructure (Higgins and Liu, 2018). Tram tracks are less standardised compared to heavy railways and might differ from city to city (Łuczak et al., 2020). This lack of standardisation makes knowledge transfer on tram railways more complex compared to heavy rail (Vinko, 2016b). The risk of severe accidents increases with higher velocity, leading to stricter safety standards for heavy railways. This more increased safety standard results in more need for research into heavy railway infrastructure compared to tramways (Vinko, 2016a).

Some characteristics of tramways differ from conventional railways: the curve radii are smaller due to the proximity of buildings and other roads. Also, tram vehicles are smaller. Modern trams do have a lower floor to smooth passenger loading. The low floor disables a joint axle for both wheels. Therefore, the bogies then have independently rotating wheels. The rails mainly consist of groove rail, but this varies per city. Regarding operations, not only the lower speed in general but also the higher amount of accelerations leads to differences in track degradation patterns compared to conventional railways (Ahac and Lakušić, 2017).

Considering tram vehicle characteristics more closely, it is worth mentioning that trams have a lower conicity tread to be compatible with a flat crown. Furthermore, flanges are steep to oppose derailment in tight curves, and the flange tip is flat to support flange tip running at crossings. Also, the flange distance and size is minimised to limit the groove width while still providing the minimum dimensions for curve negotiation (Crosbee, Allen, and Carroll, 2017).

Wear and rail irregularities in the horizontal and vertical direction are commonly seen tramway failure mechanisms (Vinko, 2016b). Also, rail corrugation and fatigue damage were commonly seen failure mechanisms because of dynamic loading at joining tracks. Also, deterioration of rubber filler profiles or filling bitumen which causes drainage failures and breakage of the pavement layer are common seen failure mechanisms. During simulations with the multi-body analysis program VAMPIRE it has been concluded tram wheels suffer more flange and headwear compared to train wheels (Crosbee, Allen, and Carroll, 2017), causing wheel flats which in turn could damage the rail (Kouroussis, Vogiatzis, and Connolly, 2017).

Furthermore, vibration and noise often cause problems in tram infrastructure. Not only because of the vicinity of buildings, but also the nature of the tram track makes it vulnerable to noise and vibration problems. Especially curves are sensible, construction methods and misalignments play a significant role (Vinko and Bocz, 2018). During a case study at the tramway in Grenoble regarding squeal noise in curves, microphones and sensors were mounted on the wheels to measure the angle of attack, velocity, lateral displacement and sound levels. It was found that the lateral creep of the wheels is the governing factor in noise pollution (Vincent et al., 2006).

A case study in Brussels (Kouroussis, Vogiatzis, and Connolly, 2017; Kouroussis, Verlinden, and Conti, 2010) concluded that regarding excessive vibrations, the length and height of

the track defects govern the velocity of the vehicle. The severity of vibrations decreased when the measurement point was moved further away from the track. The study was performed by estimating the dynamic forces at the track with numerical analysis, based on a multi-body model of the vehicle and the track. The vibrations were predicted by linking the estimated force to ground transmissions measured on-site with a falling mass machine. Afterwards, vibrations at the selected site were measured, it turned out that the estimated vibrations were quite accurate compared to the predicted vibrations.

Multiple techniques exist to oppose typical tram railway problems. For example, the case study in Grenoble (Vincent et al., 2006) found that resilient wheels could reduce squeal noise. Other options were altering the friction at the wheel-rail interface by adding lubrication, softening the primary suspension or adding a welded strip to the rail. However, a case study at the tram railway in Zagreb (Ahac and Lakušić, 2017) showed many solutions are not able to deal with occurring problems fully. The study found that the track degradation rate and effectiveness of solutions and maintenance often differ per location and instance, without clear reasons. It is also challenging to establish a clear relation between traffic loads and deterioration rates, as has been found during the case study in Budapest (Vinko and Bocz, 2018), although a positive correlation is widely assumed.

In conclusion, tram railways have more differences than heavy railways, leading to a wider range of track and vehicle characteristics, which leads to specific problems per tramway. It is challenging to perform sound scientific research on tram railways, taking this wide range of possible characteristics and the often mutable urban environment into account.

2.2.2 Track Modelling Techniques

This section evaluates different track modelling techniques available in the literature. Since the amount of literature focussing on tram railways is relatively small, models used for conventional track modelling are also assessed, which might serve as an example for tramway track modelling. Two common track modelling approaches could be distinguished: physical models aided with numerical methods to provide solutions and analytical models which rely on statistical methods. Also, combinations of both models have been found.

In general, physical models require sophisticated computational software and are used to model specific physical problems, for example, vibration or wear simulation. In general, statistic models are used in a more holistic view attempting to find the weight of different parameters in multiple degradation mechanisms. Statistic models are also used to optimise maintenance and inspection costs based on past data.

Limitations exist both for stochastic and physical modelling approaches. The authors of a review on general track models presented in the literature (Melo et al., 2020), concluded models based on a stochastic system and data from the past often lack validation. Physical models, especially combined with experiments, provide more reliable results than stochastic models. However, physical models are often limited to single components and degradation mechanisms (Melo et al., 2020). Hybrid models taking a physical approach calibrated and validated with experiments are in general considered to be most reliable (Melo et al., 2020).

An example of a physical model is described in (Łuczak et al., 2020): the purpose of this model was to simulate tram wheel flange wear in curves and on a straight track. This model combined a multibody model of the vehicle to simulate forces acting at the rail and a finite element model of the wheel-rail interface to compute resulting rail wear. For curve negotiation simulation, the multi-body simulation used the curve radius, line velocity and the suspension properties of the researched vehicle to calculate the vertical forces

and angle of attack. Considering the material hardness and lateral creepage, the finite element model computed the volumetric material loss at the wheels. This model assumed that slip inherent to the creepage is the only significant contributor to wear. The set-up of this model allowed many parameters and circumstances to be included. However, with this amount of parameters, simplifications were also needed, and computational times of about 10 hours were recorded. The simulation results of this model were verified with actual measurements in the field. Basic agreement between simulation and measurements was visible, but the operation conditions proved too variable and complex to provide a helpful prediction model.

The previously described case study at the tramway in Brussels (Kouroussis, Vogiatzis, and Connolly, 2017) is another example of a physical model. The authors mention issues with numerical models: the vast amount of input parameters needed and the long computation time. An advantage of a physical, e.g. finite element model, is the amount of insight obtained in underlying mechanical processes. Still, it is often difficult to capture multiple situations in one finite element model.

The previously mentioned case study at the tram railway in Zagreb (Ahac and Lakušić, 2017) is an example of a stochastic model. The following parameters were involved: rail geometry, segment information, usage information (e.g. velocity, the tonnage) and spatial information (e.g. vicinity of stations). In the modelling process, the mean values and standard deviations of the rail geometry were used to represent the condition of the track. A regression analysis was used to derive the influences of track parameters on rail geometry data. This study concluded that horizontal wear is largest in open track sections with tight curves. Furthermore, wear is highly dependent on vehicle velocity, curve radius and rail fastening stiffness. Also, the rail tensile strength and the arrangement of tram stops influence the wear process.

The research at a Swedish heavy railway (Soleimanmeigouni et al., 2020) describes a more general track degradation model, which was aimed to provide help with asset management instead of understanding underlying principles. Data of 10 years of maintenance and geometry measurements were collected to calibrate a mathematical model which models track degradation. In this model, the track condition was a non-physical parameter resulting from a weighted contribution of quality indicators. The standard deviation of the longitudinal level and occurrence of isolated defects on the longitudinal level were used as quality indicators. The authors have mentioned the following results: more inspection intervals decrease the percentage of time a particular track segment spends in deteriorated condition. The decrease of track condition accelerates itself, making early intervention favourable. This conclusion is shared by the authors of (Kasraei, Zakeri, and Bakhtiaryi, 2020), where a comparable model is described, which used K-means clustering and Monte Carlo simulations to predict the total expected costs from corrective and preventive maintenance.

In conclusion, literature often describes two modelling approaches to model track degradation. Each method has some particular problems, limiting usability for revenue purposes. A common problem is the lack of validation of the described models in the literature (Melo et al., 2020). Tram and light rail infrastructure networks are often too complex and diverse to model correctly since the information needed is not available. However, usable insights could be obtained from physical models which focus on a particular problem.

2.2.3 Monitoring

Track degradation models could be combined with track monitoring, where the monitoring serves as continuous input for the models. In essence, all monitoring techniques described in the consulted literature aim to obtain information on the current track state. In combination with a model, this data is used to predict the condition of the track in the future. Two different approaches of track monitoring could be distinguished: the first method relies on acceleration sensors mounted on the vehicle, the second method relies on geometrical measurements obtained with laser systems.

Acceleration based monitoring methods provide accelerations in the three principal directions. With the help of frequency analysis, extraordinary vibrations could be detected and often linked to a particular kind of track defect. The placement of the acceleration sensors is an important issue to consider. (Weston et al., 2015) discusses possible places for the acceleration sensors. In general, the sensors could best be placed on the boogie frame or axle. If long wave irregularities are of interest, sensors at the car body are also needed. The resulting vibrations from the vehicle itself need to be filtered to obtain the vibrations generated by track defects (Higgins and Liu, 2018). The obtained vehicle acceleration data needs to be linked to a specific location along the track. Often GPS is used since the use of odometers, or the vehicle's velocity, has too much error which builds up over long segments of measurements (Weston et al., 2015).

The post-processing procedure of acceleration measurements contains filtering of noise and frequency analysis. In (Vinko, 2016a), a Kalman filter was used to separate the noise from track defect induced vibrations. Applying the filtering process resulted in measurements independent of the vehicle's velocity, this enabled comparison with measurements from other vehicles. In (Vinko and Bocz, 2018), the spectral density of the acceleration measurements was obtained using the Fourier transform. Since different track defects often resulted in particular acceleration frequencies, the measurements could already be linked to defect categories.

In the beforementioned study in Budapest (Vinko and Bocz, 2018), the results of the acceleration measurements were validated with geometry measurements and inspection results. This study concluded that a combination of both dynamic and geometry measurements is preferred, because some dynamic defects are hard to measure with geometry measurements and vice versa. Furthermore, besides the tonnage, the specific kind of vehicle turned out to be a significant factor. During this study, acceleration measurements on selected track segments were performed, to assess the possibility to monitor the condition of the track using in-service vehicles. In (Xie et al., 2018), an approach was described, which combines acoustic measurements, wheel slip data and weather information to support maintenance decisions.

Looking at the advantages and disadvantages of acceleration based measurements, (Weston et al., 2015) concludes especially vertical and lateral irregularities could be assessed based on acceleration. For corrugation detection, a microphone could help. When measured regularly, the propagation of defects and influence of maintenance could also be assessed with the help of acceleration measurements. (Weston et al., 2015) also describes some challenges encountered with acceleration-based measurements. In practice, it is challenging to obtain a sufficiently accurate estimation of the vehicle's current location and velocity. A Global Navigation Satellite System is often used to overcome the previously mentioned problems, but inconsistencies in mapping could raise difficulties when linking measurements to a particular location.

The second approach to assess the track condition involves using geometrical measurements, measured with laser technology. Lasers could measure the rails' entire geometry, cant, twist, superelevation, gauge, and corrugation. A full 3d model of the rails could be measured by laser systems (Wegdam, n.d.). The measured 3d model can then be reviewed in, e.g. Autocad to assess possible local track defects or to derive rail wear. Furthermore, this process could be automated by the use of computer algorithms. Depending on the nature of the calculated differences, specific types and magnitudes of local track degradation can then be assigned to the measured rails. In this approach, the standard deviation of the rail geometry can be used as a measure for track quality (Vinko, 2016b).

A related monitoring option is the use of optical (photo) measurements. An advantage of photo measurements is the visibility of the rail surface, which makes it easier for humans to detect certain kinds of track damage. Also, the context of the defect could be revealed by a photo. However, it is challenging for a computer to estimate rail geometry and related defects from images. Also, the lens should be cleaned continuously, which is a major main difficulty with photo measurements (Weston et al., 2015). Therefore, a combination of laser and photo measurements seems to be the best option in terms of post-processing possibilities. Since then, a computer could compute locations with damage based on laser measurements. A human could assess the photos of these locations to verify the defects computed by the computer.

In conclusion, monitoring techniques could be separated into acceleration-, laser- and photo measurements. Combining all three methods is the most promising since then benefits could be taken from all advantages.

Chapter 3

Data Availability and Quality

This chapter describes the data sets providing usable data for the master thesis research. The first section explains the available rail measurement data for wear in curves. Secondly, data originating from the tramway exploitation are discussed. The third section explains track characteristics data. The concluding section discusses the shortage of maintenance data.

3.1 Rail and Wheel Measurements

This section explains the rail and wheel measurement data available at GVB, which could be used for wear predictions.

3.1.1 Rail Geometry Data (Railcloud)

GVB digitally measures the geometry of the rails for several years, but the measurement times and methods have not been consistent. The data is available from yearly infrastructure measurements in 2017, 2018, 2019, 2020 and 2021 of the whole tramway. The measurements in 2019 were performed during the winter season. All other measurements were performed during the summer season. In 2017 and 2018, the company *Deutzer Technische Kohle* (DTK) performed the measurements. The measurements of 2019, 2020 and 2021 were performed with the MW3000 machine by the company Autech.

The main set-up of the Autech measurements consists of an excavator with both road and rail wheels. This vehicle pushes a brushing unit at the front and pulls the MW3000 measurement unit at the back (see 3.1a. The MW3000 machine measures the rail geometry with a laser. The check rail serves as a reference point to overlay the measured profile with the original one. An odometer measures the travelled distance. Therefore, profile measurements could be taken every 1/3 cm and assigned to the accurate location along the track. GPS is often not accurate enough to couple measurements to the precise location, due to the vicinity of buildings at many measurement locations. The whole measurement set-up moves at a speed of 20 kph during the measuring. Figure 3.1b shows the measurement display on the measurement vehicle. The measured geometry is displayed with an angle because the lasers measure under an angle. This angle is corrected directly by automatic post-processing in the measurement vehicle.

The reliability of a measurement at a particular location could be verified by considering the longitudinal and cross-sectional drawing of the measurement (3.2 and 3.3). Figure 3.2 displays an example track section in Railcloud. The rail horizontal and vertical wear in longitudinal view is shown on the left. The right shows the cross-sections from where the wear values are deduced.



(A) Rail measurement set-up.



(B) Rail measurement display.

FIGURE 3.1: Geometry measurements in the city centre of Amsterdam.

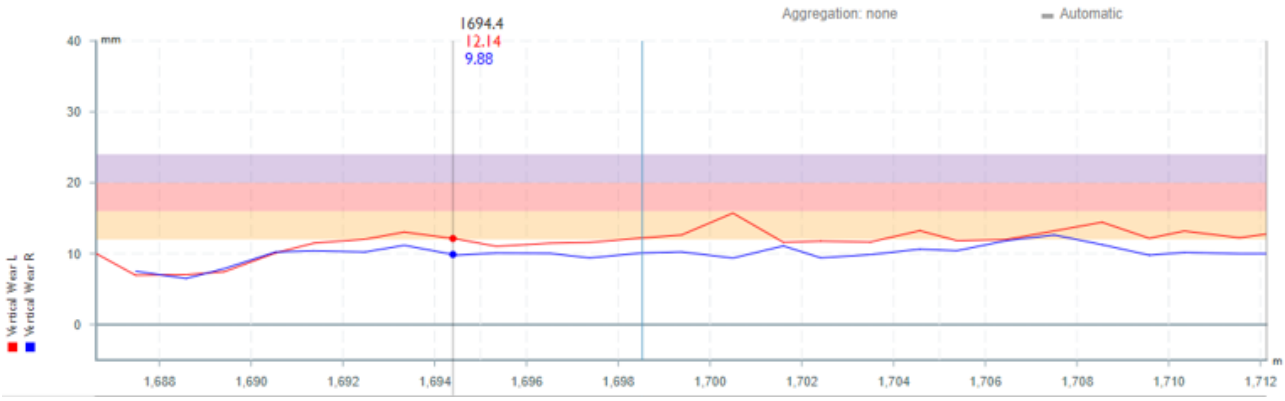


FIGURE 3.2: Longitudinal overview of vertical wear for a selected track part in Railcloud. The red line represents vertical wear at the left side and blue line on the right.

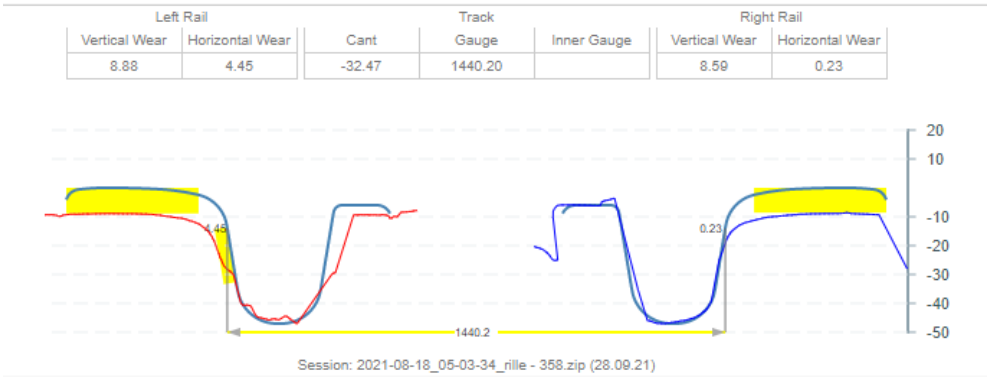


FIGURE 3.3: Example of measured cross section vs original cross section.

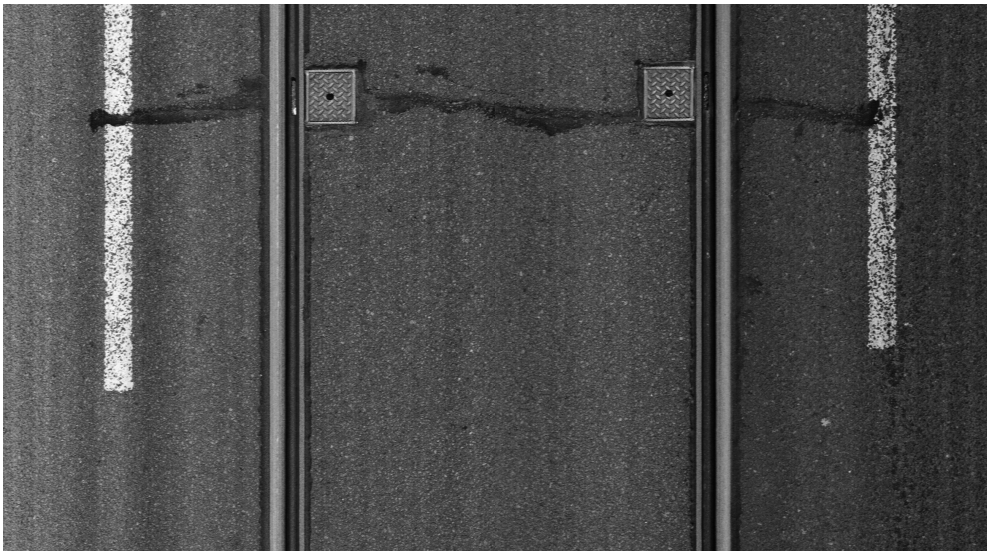


FIGURE 3.4: Photo made and used by Strukton to derive the rail geometry.

The horizontal and vertical wear is automatically calculated per track segment from the rail profile measurements and the original rail profiles. Algorithms compare the measured and original rail profiles to compute the wear. The top of the rail is the reference point for vertical wear. Horizontally the reference point is 14 mm below the original height of the rail. The automatic wear calculation can also be verified by considering the cross-sections shown in Figure **??**. For GVB, these yearly measurements give an overview of the tramway wide rail condition. Based on this, long term maintenance is planned.

The rail profile measurements of 2021 came available late in this research. Only 2020 and 2021 measurements were reliable enough to deduce approximate wear rates on a large scale. Therefore, large scale wear rates could only be used for the validation of the energy estimation model in Chapter 7. Furthermore, the error rate in those wear rates is still high because of inaccurate measurements and missing maintenance data. Rail profile measurement data was also used to validate the simulations in Chapter 6.

3.1.2 Strukton Photo Measurements

Strukton performed rail measurements by taking top view photos of the track with their dedicated vehicle. An algorithm analysed those photos to estimate the track width and other relevant measures. Those analysis results were used to assess the condition of the rail to enhance maintenance planning. An advantage of the 'photo approach' is the track's visibility on the photo. This insight can verify the measurements or deduce damages types from the images. The measurements were performed in the summer of 2020, although a limited part of the network was covered. Figure 3.4 shows an example of these photo's on a straight track.

The reliability of the measurements by the photos in curves is not very high since, during the post-processing method, difficulties arose when analysing curves. The images could still be helpful to verify other measurements or for inspection tasks. The options for the usage of this data in the current research are limited, since the part of the network covered is small and because of the reliability of the measurements in curves. If track photos at the time of measurements were available at a larger scale, those photos could be helpful for measurement verification and validation. Inside defects are not visible on the pictures,

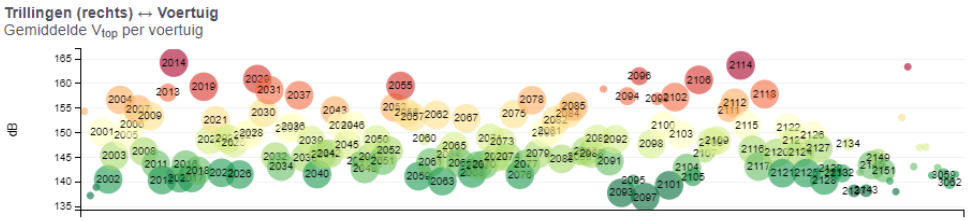


FIGURE 3.5: Measured way side vibrations at the Lelylaan. The vehicle numbers are shown in each circle.



FIGURE 3.6: Measured squeal noise levels by two trams equipped with noise sensors of Sensornet. Measurement period: October-November 2021.

but the images can give the context of rail measurements. The data is not suited to use automatically in a wear prediction model in its current form.

3.1.3 Sensornet

For the tram network of GVB, Sensornet performs wayside measurements and measurements on the pantograph of a selected vehicle. This measurement campaign started in October 2021. The measurements are performed to obtain more insight into noise and vibration levels. The data could be used to detect locations with a possible catenary-, pantograph, or rail damage. The wayside track measurements could indicate tram defects since subsequent passing vehicles could be compared (see 3.5). Since the data is only measured per second, it would be challenging to deduce specific track defects by frequency range analysis.

The data from the Sensornet noise measurements could not be used to directly detect rail wear in curves. However, noise levels could be compared to measured rail wear to assess the possible relation between noise and wear. Also, noise levels under different humidity circumstances could be evaluated. This analysis could link wear levels and humidity if a connection between noise and wear is established first. This research does not elaborate on those possible relations, but it recommends further study into this topic. Figure 3.6 shows measured curve squeal noise, measured by two trams equipped with Sensornet sensors.

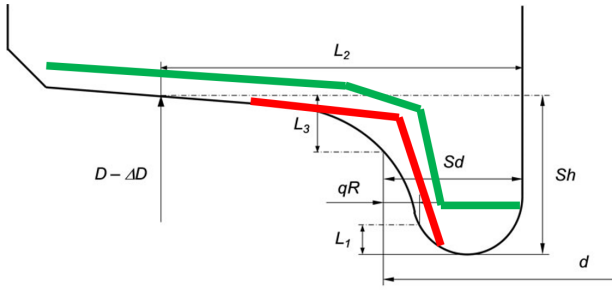


FIGURE 3.7: Schematic overview of tram wheel re-profiling. black = original shape; red = worn shape; green = re-profiled shape.

3.1.4 Wheel Wear Measurements

Tram wheels need re-profiling every five months to equal wheel irregularities and obtain the desired flange thickness. This re-profiling is done by milling the tram wheels till they are smooth again and the desired flange thickness is restored.

During usage, the flange wears in the horizontal and vertical directions. Horizontal wear will make the flange thinner and the inner side of the flange steeper, which is shown by the red line in Figure 3.7. The steepness (qR) of the flange is an essential measure since a steeper flange will harm the vehicle behaviour during curving. The original wheel profile (green line in 3.7) is restored by wheel milling. After milling, the wheel diameter decreases. When the wheel diameter is reduced to 520 mm (original = 600 mm), the wheel band must be replaced.

The milling installation measures the wheel profiles before and after grinding. The data is processed by hand, so small mistakes are included in the data. However, it is expected this error will not be significant with a large amount of data. The average wheel wear and wear rate per vehicle could be assessed from the data. When certain vehicles do have unusually high wear, possible causes could be researched. It is difficult to couple wheel wear rates directly to particular lines since most vehicles travel on a wide range of different lines. This data was used to analyse how wheel wear rates vary per vehicle and establish an average wheel wear value for the whole network.

3.2 Exploitation Data and Measurements

This section explains the exploitation data used in the research. This data type is used as input in the prediction model. The exploitation data contains the distribution of vehicle types and coupled vehicles, the vehicle occupation, tram notifications and log data and at last, the vehicle paths. The following subsections explain the exploitation data in more detail.

3.2.1 Vehicle Type Distribution

The vehicle type distribution gives the number of tram vehicles, specified per type passed on a segment between two stops. This data provides insight into network usage, since more heavy used segments and segments primarily used by one particular tram type are revealed. This data could help find the cause for more intense wear on specific segments. The information is retrieved from the 23rd of September, 2021. The vehicle type distribution could change over months but not very often over only days. Therefore, it was deemed

sufficient to pick data from just one day to represent the vehicle type distribution. No correction was needed for COVID19 related measures since trams were not affected.

This data can derive other quantities besides the number of different vehicles that passed a particular segment. The load per axle is known per vehicle type, the empty weight and the number of axles. This information enables the computation of the number of axles and weight (tonnage) which passes between two stops. Figure 3.8a gives an example of the data representation in GIS.

3.2.2 Coupled Vehicles

Coupled vehicles double the number of axles and (empty) weight per tram passage. Therefore, it is worth taking this data into account. Also, coupled compositions might cause a different wear pattern since the velocity profile when passing a curve could change. The measured quantity is the amount of coupled and single vehicles per track segment between two stations. The data format is comparable to the *vehicle type distribution* data set.

3.2.3 Vehicle Occupation

GVB also provided data about the vehicle occupation per track segment; the passenger numbers per day are given. This data can result in a more sophisticated estimation of the average vehicle weight per segment. Passengers could add on average 2-3 extra tonnes per vehicle, which is significant on a vehicle with an empty weight between 35 and 40 tonnes. The data is provided from a day in September 2021. Those data are not corrected for decreased passenger numbers because of COVID19, since the number of passengers was almost equal to normal levels at that time.

The data is assumed to be reliable for this purpose, with a maximum error of 10 per cent. Since the magnitude of this error is supposed to be evenly distributed over the network, curves could still be compared.

3.2.4 VECOM (Vehicle Communication)

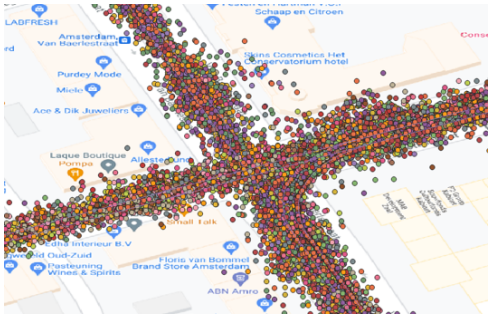
VECOMS (Vehicle Communication) are tram detection devices mounted on the track. Those devices detect a tram and also its vehicle number. This measurement is used to divert switches in the proper direction. As a result, those devices are mainly found at the front of active switches, dividing the track into two tracks. Per VECOM, the number of vehicle passages and corresponding vehicle numbers is recorded. This data can result in the number of vehicles and types, derived from the vehicle number per track segment. This data can be used to verify the *Vehicle Type Distribution* data.

3.2.5 DBPU Dashboard

The operational department of GVB uses the DBPU dashboard to track operational statistics: e.g. average delay on the network or occurrence of disruptions. Via this dashboard, it is possible to assess the routes driven per vehicle number in the past. This data could be used for a variety of analyses. It is possible to link vehicles to routes at a known time, and it is possible to use this information while analysing driven velocities on the network. Unfortunately, it is not possible to research the influence of different routes on wheel wear, since vehicles are not used on specific routes but run over the whole network.



(A) Distribution of different vehicle types, Siemens Combino (green) is clearly the main vehicle in this part of the city.



(B) Tram log locations directly plotted in GIS, each color resembles a different tram, in total 5.5M log locations are considered.

FIGURE 3.8: Examples of exploitation data.

3.2.6 Tram Log Data

Combino and Urbos 100 tram vehicles in operation send every 10 seconds an update, which contains the GPS location, current velocity, vehicle number and current route of the tram. A data set of 10 days (20-30 June 2021) for all Combino and Urbos 100 trams was obtained to investigate. The GPS locations are measured from the front end of the tram. The GPS locations of the data could be several meters off. However, the large quantity of data is assumed to provide redundancy to overcome this problem. The velocities, vehicle numbers and routes are verified in GIS and proved accurate. Section 4.3 further elaborates on the validity of this data set.

Figure 3.8b shows an example of the log data points directly plotted in GIS. Each colour represents a different tram. The figure reveals the locations should be not challenging to couple to a line, but there are challenges for coupling at track intersections. Also, coupling the log data to a specific track direction is challenging. Chapter 4 further elaborates on the post-processing method and challenges.

The route data enables the coupling of a log to a specific track since it is known which tracks lay on a particular route. When post-processing challenges are overcome, velocity distributions could be made along the track with this log data. Velocity distributions could influence wear patterns. Therefore it is interesting to know the actually driven velocities along the track.

3.2.7 Kibana

Kibana is a dashboard that displays a wide range of data originating from CAF Urbos 100 trams in operation. The data contains real-time vehicle locations and log data from the trams. The most relevant log data in this research are the activation of the sander, low adhesion warning and overspeed notifications. It can reveal locations with adhesion problems, sand on the rail which might cause more wear and places where drivers often drive above the speed limit. Linking specific curves to adhesion, sanding or velocity issues is very interesting for the current research. However, the data is only available for the CAF Urbos 100 trams, gradually introduced into service since late 2020 on specific lines. As a result, the information is not available for the whole network but only lines where the

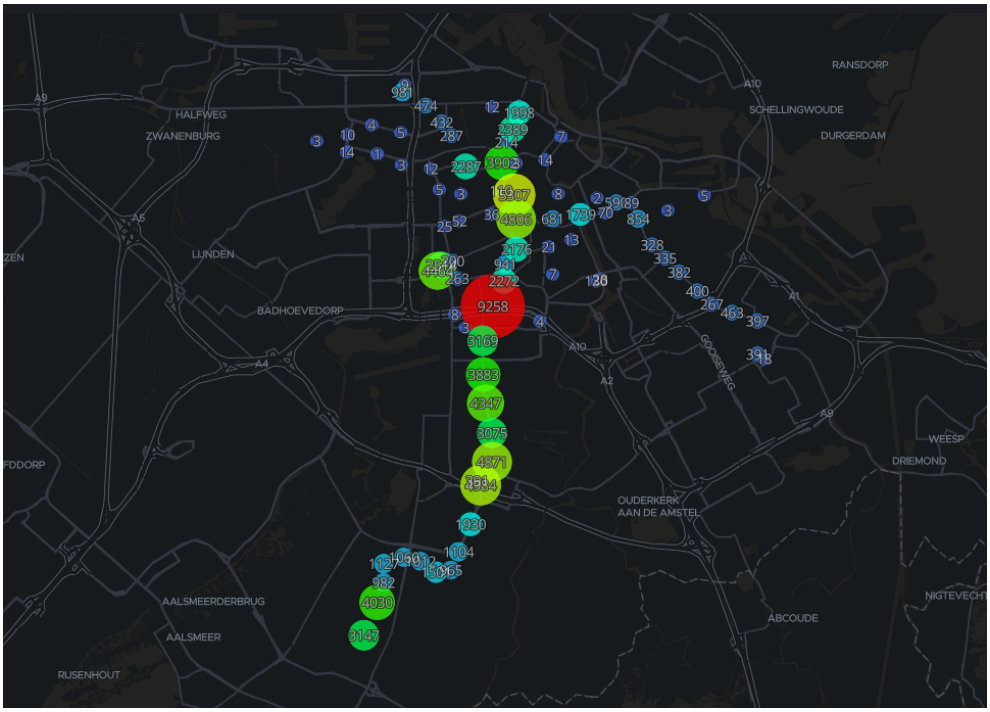


FIGURE 3.9: Spatially displayed aggregated notifications of the CAF Urbos 100 tram.

new trams have driven regularly. Figure 3.9 shows the aggregated notifications for the CAF Urbos 100 trams on the map of Amsterdam.

3.3 Track Characteristics

This data category includes track characteristics, e.g. rail type and hardness. The most relevant database for track characteristics is the SAP database. Wayside lubrication installations are described separately.

3.3.1 SAP Database

Track characteristics are stored in the SAP database. The equipment number is often a single curve or straight, the lowest entity where features are assigned to. The most important characteristics for this research are rail type, steel sort, curve length and curve radius. The reliability of the database is high since employees of the asset management team continuously monitor, use and improve the database if necessary. The data can be used to deduce the influence of track characteristics on wear occurrence, given the availability of wear rates along the track. The data can also serve as input to predict wear using a wear model based on data analysis or simulations.

3.3.2 Lubrication Devices

GVB has several wayside lubrication devices provided by Rail Partner Holland. Those devices deposit a lubricant to the wheels. The wheels pick up this lubricant and spread to curves after the lubrication device. The lubrication agent used is RPS 02, provided by Rail Partner Schweiz AG. It is a liquid acid to treat the side and head of the rail. Friction characteristics are optimised for wear and noise production. The lubricant forms an intermediate layer between the rails and the wheels, which lowers the frictional coefficient

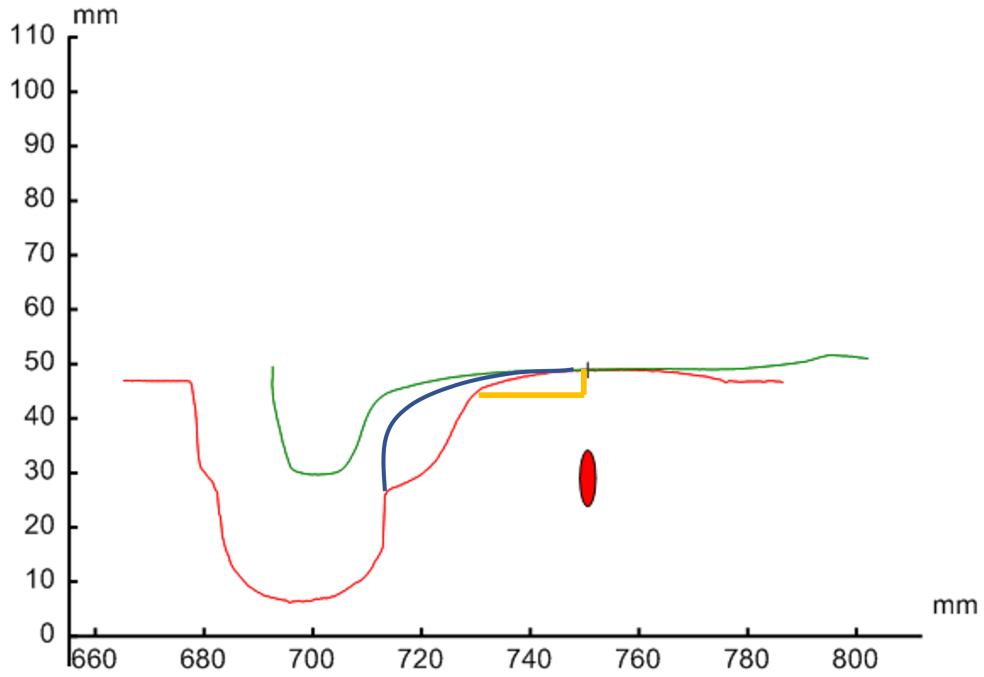


FIGURE 3.10: Horizontal welding: in red is the worn rail profile, in blue is the line which is needed to restore the original profile and in yellow is the material which should be removed first to enable welding (approximate dimensions).

at the wheel and rail contact. This lubrication provides a smoother curve passing by the tram and less noise pollution.

Wayside lubrication devices are often placed before turning loops at endpoints and other sharp and noisy curves. When correctly done, the lubrication will last for several curves but only in the direction which matches the lubricated side. The lubricant wears off from the wheels quickly on a straight track because of the sinusoidal movement, which is characteristic for railway vehicles moving on a straight track. It is important to know which curves are lubricated by wayside rail lubrication to assess the wear behaviour and influential parameters. Therefore, with the exact locations of the devices and the lubricated sides, it is possible to estimate which curves are affected by the lubrication.

3.4 Maintenance Data

To determine wear rates, rail geometry measurements alone are insufficient. Two important maintenance actions influence the wear rate: grinding and welding. During grinding, the upper vertical 0.1 mm of the railhead is removed, during welding, material is added at the inner side of the rail. Figure 3.10 provides a schematic overview of these track maintenance actions on a tram railway cross-section. In red is the worn rail profile, in blue is the line needed to restore the original shape, and in yellow is the material which should be removed first to enable welding.

Data Name	Data Source	Data Content	Possible Usage	Usage by Research
Track profile measurements	Railcloud / Autech	- (worn) Track geometry	- Computation track wear rates - Validation model results	- Computation track wear rates - Validation model results
Strukton photo measurements	Strukton	- (worn) Track geometry - Track photos	- Verification other profile measurements	- No usage
Noise/Vibrations	Sensornet	- Wayside noise and vibrations	- Identification of track defects	- No usage
Wheel wear	GVB (re profile machine)	- (worn) Wheel geometry	- Computation wear rate wheels - Validation model results	- Computation wear rate wheels - Validation model results

FIGURE 3.11: Available measurement data.

In conclusion, maintenance actions also influence the measured wear rate. To obtain actual wear rates, maintenance actions should be considered when considering profile measurements. Unfortunately, no maintenance database is available at the GVB.

Figure 3.11, 3.12 and 3.13 provide an overview of the available measurement, exploitation and track characteristics data. The figures indicate data source, content, possible usage and final data usage by the research.

3.5 Conclusion

The primary data sources used in this research are presented, which concludes the second research question: *Based on the measurement data available and information available at GVB, which data could help to predict tram rail wear?* On several parts, an abundance of data is available to understand and predict track degradation. However, the lack of maintenance data makes it challenging to establish reliable wear rates, which is needed to validate a wear prediction model. Also, the data is spread over multiple databases and departments that are not always informed about the existence of data at other departments. A centralised platform for data collection could enlarge the available data usage possibilities.

Data Name	Data Source	Data Content	Possible Usage	Usage by Research
Vehicle amount	GVB - exploitation	- Number of vehicle passages per track segment	- Computation tonnage	- Computation tonnage
Vehicle type distribution	GVB - exploitation	- Vehicle type distribution per track segment	- Input wear prediction model	- Input wear prediction model
Coupled vehicles distribution	GVB - exploitation	- Distribution of coupled vehicles per track segments	- Input wear prediction model - Tonnage	- Input wear prediction model - Tonnage
Passenger numbers	GVB - exploitation	- Number of passengers per track segment	- Input wear prediction model	- Input wear prediction model
VECOMS	GVB - electrical systems	- Turnout passages with vehicle number	- Computation vehicle routes - Tonnage	- No usage
DBPU dashboard	GVB - vehicles	- Route per vehicle number	- Computation vehicle routes	- No usage
Tram log data	GVB - exploitation	- Route per vehicle number - Velocity every 10s per vehicle number	- Computation vehicle routes - Computation velocity on network	- Computation vehicle routes - Computation velocity on network
Kibana	GVB - vehicles (Urbos)	- Sander usage - Low adhesion notifications - Overspeed notifications	- Input wear prediction model	- No usage

FIGURE 3.12: Available exploitation data.

Data Name	Data Source	Data Content	Possible Usage	Usage by Research
SAP database	GVB - general	Per track segment: - Rail type - Steel sort - Curve length - Curve radius - Rail fastening system	- Input wear prediction model	- Curve radius is taken as input - No usage of other parameters
Lubrication devices	GVB - asset management	- Locations of lubrication devices	- Input wear prediction model	- No usage

FIGURE 3.13: Available track characteristics data.

Chapter 4

Velocity Analysis

The origin of interest for the velocities lies in the assumption that the velocity at which a tram vehicle negotiates a curve plays a significant role in wear generation. This assumption will be verified during the simulation phase, described in Chapter 6. The method of the velocity analysis is described in Appendix C. This chapter describes the main results of the investigation. Chapter 7 describes how the outcomes of the velocity analysis are used in the energy estimation model.

4.1 Introduction

Modern tram vehicles record all vital information during operation, including a general update every 10 seconds containing the current location, time, velocity and vehicle number. They also sent an update when a tram is set up and ready for a new route at route end- and start points. This information was used to obtain a detailed overview of driven velocities on the whole tramway. One week already contains 6 million tram updates which should be assigned to the track the tram vehicle was most likely driving on.

The GPS locations sent by trams have an accuracy of 1-2 meters, with some outliers laying up to 10 meters from the track. This accuracy is sufficient to assign logging to a specific point along the route, but insufficient to give the point to the left or right track. The route updates provided a solution to this problem since it can be determined per specific vehicle on what route, in which direction it was driving at a particular time. Therefore, each logging could be coupled to one particular track. Since the amount of data was huge, a Python script was written to perform this for all updates sent by every tram in operation every 10 seconds over one week. Appendix C elaborates on the analysis model in Python. This chapter presents the results and validity.

4.2 Results

This section presents the results of the velocity coupling model. The overall aim is to explain which data is used as input for the energy estimation model. At first, the input data is described, second, examples of the output are shown. Third, the usage possibilities are described and last, the findings of the analysis are described. The method of this analysis is defined under Appendix C.

4.2.1 Input

The input data used in the thesis project was all the tram log and route data from 20 till 29 June 2021 (ten days). It was assumed those ten days would give a reliable presentation of the driven velocities on the network. Later, a validation run was done for the week from 16

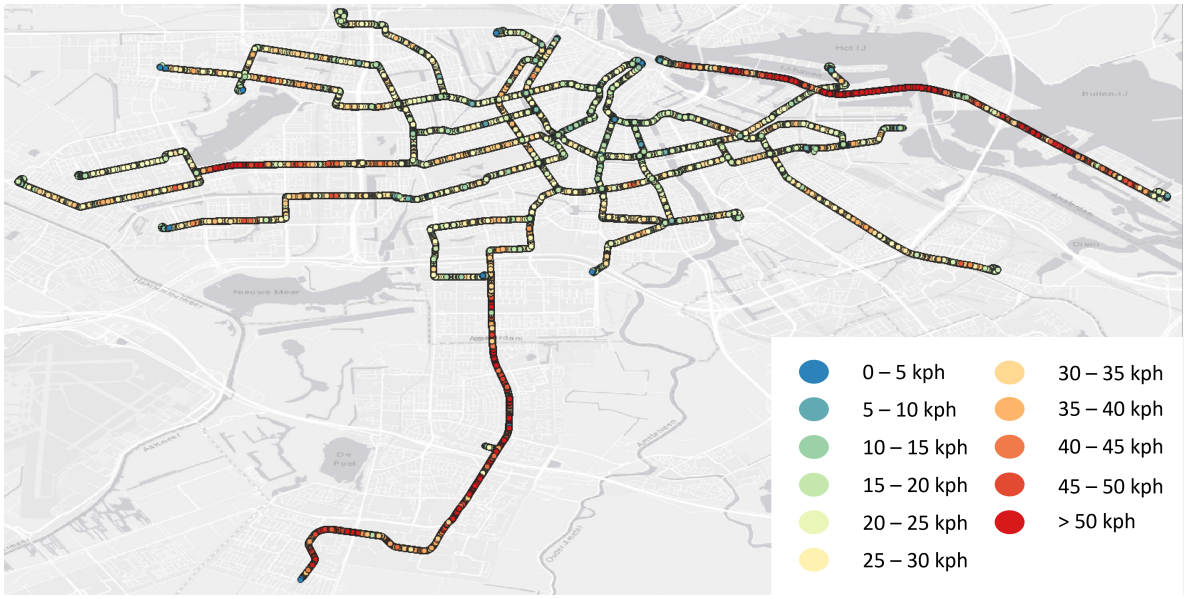


FIGURE 4.1: Average velocities at the tram network.

till 22 August to assess possible influences of the chosen day range and period. It turned out those influences were negligible for this research. See Section 4.2 for more information on the validation.

4.2.2 Output Examples

This subsection is divided into the output per trackpoint and the output per tracknumber. Trackpoints contain imaginary points plotted every about one meter along the track. Tracknumbers include specific curves or straights as a whole.

Output per Trackpoint

The output per trackpoint is meant for detailed analysis of tram driving behaviour. Detailed average velocities on the whole tramway are available. Figure 4.1 shows the outcome of the analysis for the whole tramway. Figure 4.2 is the same picture as 4.1 but then zoomed in at the Leidseplein. Figure 4.3 shows an example of an analysis of the inner right curve.

Output per Tracknumber

This output contains the velocity distributions per tracknumber (4.4 for an example near Leidseplein. As shown in the figure, the distribution shows the amount of logging's captured per velocity category with a step size of 5 kph. Standstill (v0.0) forms a separate category, In this case, a tram was standing still. Based on the number of loggings per velocity category, percentages are calculated per velocity category. These percentages per curve are the most critical outputs since it serves as input for the energy estimation model.

Since the GPS locations could have some offset, it is important to take care while drawing conclusions based on velocity categories with less than 20 hits. A velocity category with just a few hits could only consist of inaccurate loggings. Consult section 4.2 for more information on the validation.

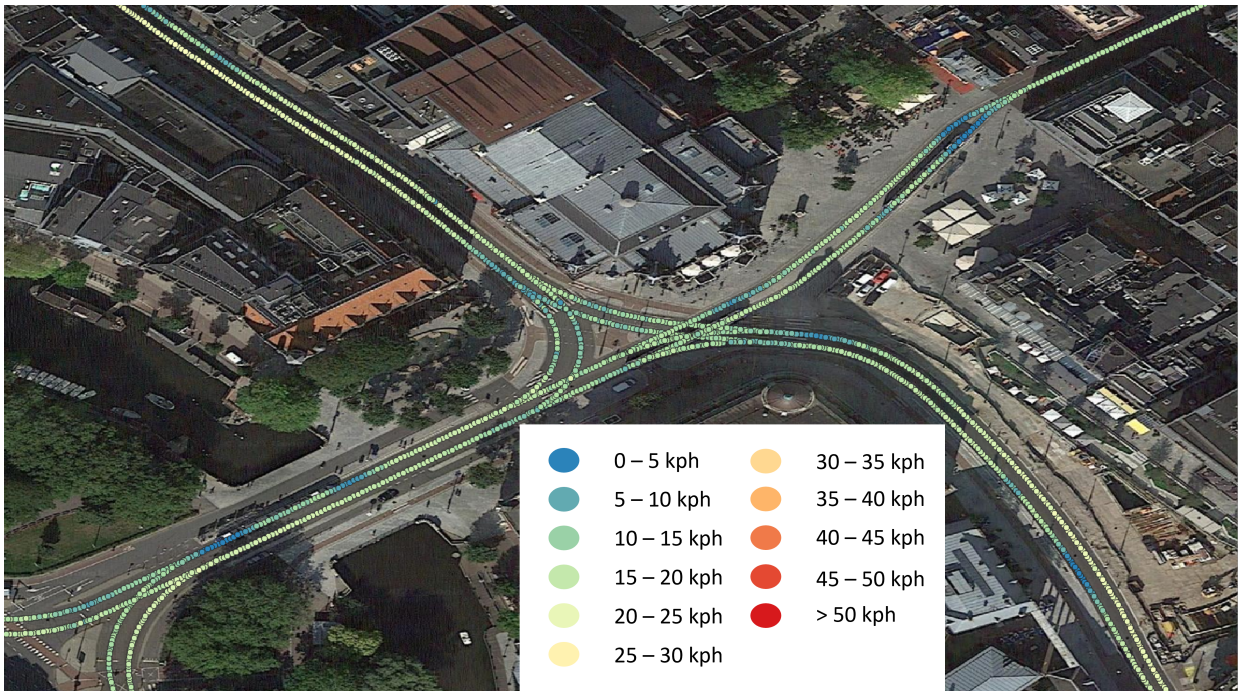


FIGURE 4.2: Average velocities near Leidseplein.

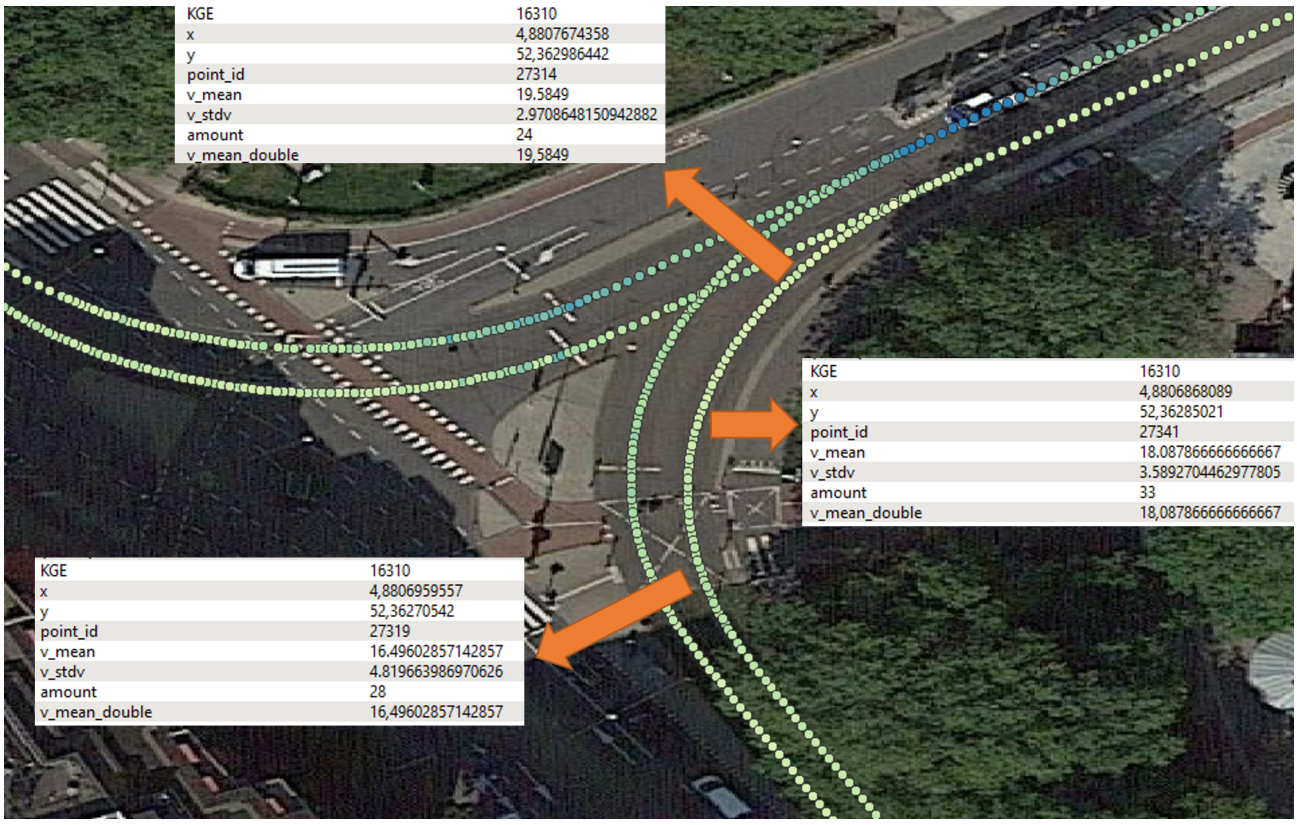


FIGURE 4.3: Example analysis of the mean driven velocity in the inner right curve.

AN	16310
TP	Boog
KGE	L0260-16310
Bg r=	42
Wisselnumm	NULL
Halte	NULL
KGE_2	16310
V_mean	17,660372413793105
%0.0	1
%0-5	1
%5-10	1
%10-15	12
%15-20	61
%20-25	24
%25-30	0
%30-35	0
%35-40	0
%40-45	0
%45-50	0
%50-55	0
%55-60	0
%60-65	0
%65-70	0
V_stdev	3,705061972768917
v_diff	1,2867970370370365
n0.0	19
n0-5	17
n5-10	20
n10-15	198
n15-20	1018
n20-25	408
n25-30	2
n30-35	0
n35-40	0
n40-45	0
n45-50	0
n50-55	0
n55-60	0
n60-65	0
n65-70	0

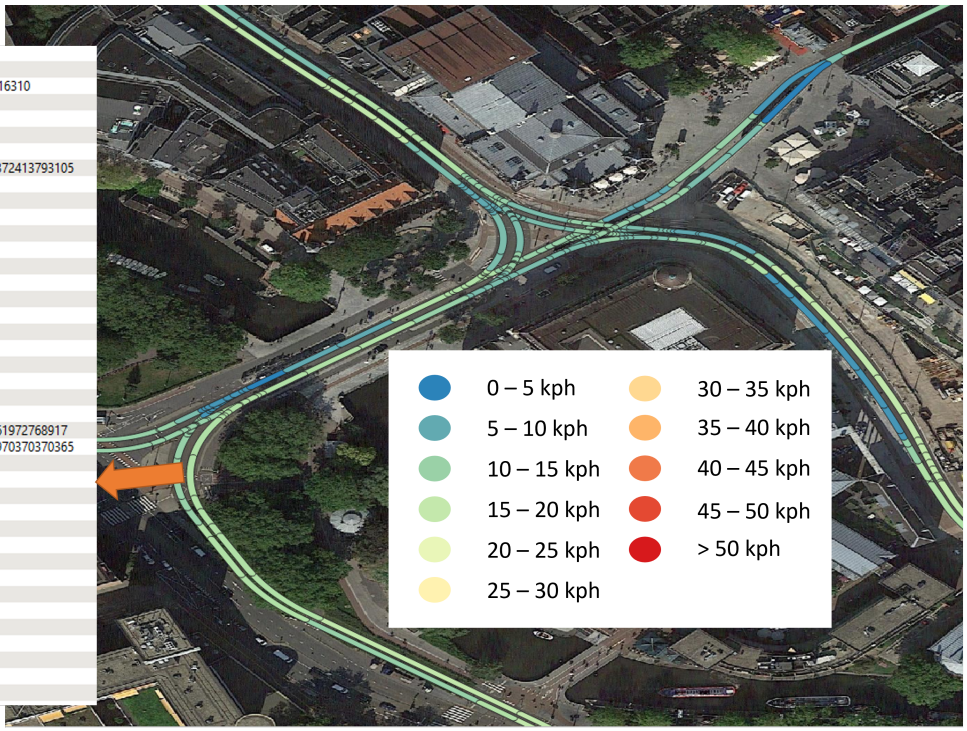


FIGURE 4.4: Average velocities per tracknumber, the table on the left shows the velocity distribution for the inner right curve as example.

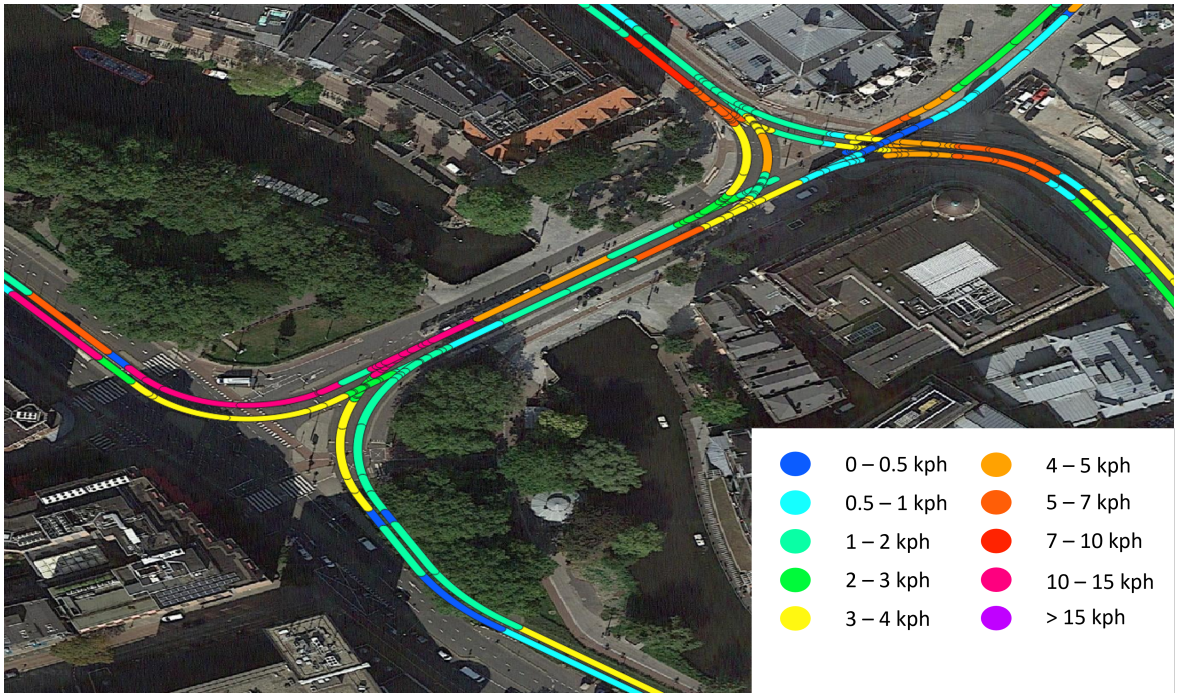


FIGURE 4.5: Velocity differences per tracknumber, a measure for the amount of acceleration per tracknumber.

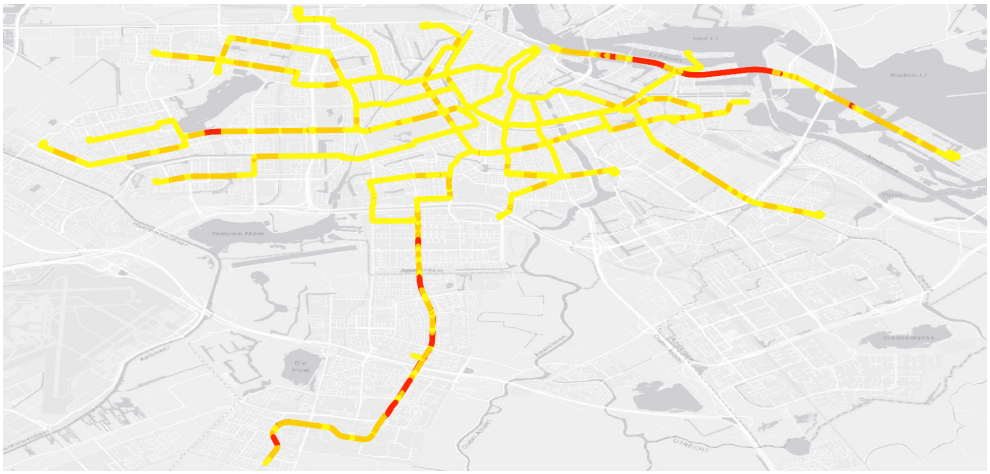


FIGURE 4.6: Average velocity driven on the tram network: yellow: <30 kph; orange 30-50 kph; red >50 kph.

Figure 4.5 shows an example of the outcome of the acceleration analysis. The results are less accurate than the velocities, since it is based on an algorithm that only takes the outer trackpoints of the tracknumber into account. Because of the decrease in accuracy and the difficulty in simulating the effect of accelerating vehicles (see Chapter 6), it was decided not to take acceleration into account in the energy estimation model. However, in later research, acceleration could be an explaining factor for unexpected high wear rates.

4.2.3 Findings Velocity Analysis

This subsection presents the findings of the velocity analysis. In this case, the focus is on driven velocities and tram driving patterns in curves. First some examples will be given on how the results can be used. Thereafter, some general findings will be presented from the velocity analysis. Those results might help declare why certain curves suffer more from wear than other curves.

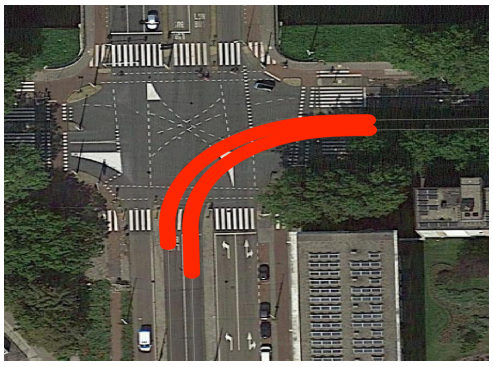
In the Netherlands, the general speed limit within the city limits is 30 or 50 kph; figure 4.6 depicts the average velocity driven by tram vehicles. From this figure, it is clear that, in general, the driven velocities by trams are pretty low, and general speed limits are not violated often. The average velocity on the whole network is 20.5 kph. This includes trams stopping at traffic lights and regular stops. In the city centre, all average velocities are below 30 kph. On longer stretches outside the city centre, average velocities between 30 and 50 kph are measured. The velocity tends to increase at branches stretching to outside neighbourhoods.

Besides general speed limits that are valid for all traffic, trams have to comply with specific speed limits. Switches, crossings and tight curves (Radius <= 30) have to be passed with a velocity of 10 kph, all tough in practice. A somewhat higher velocity of 15 kph is, in general, accepted. An important question from GVB was to assess where vehicles are passing too fast, since this might contribute to increased rail wear. Figure 4.7 shows those points in red where at least 20% of the drivers drove faster than 20 kph. This result reveals quite some points where trams pass more quickly than prescribed. Those points are mainly found at road crossings, which is not an enormous surprise since tight curves are primarily located at intersections.

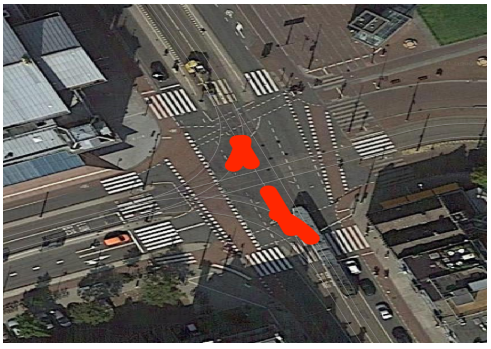
Figure 4.8a and 4.8b show zooms towards two particular points in Figure 4.7. Research under tram drivers can reveal why trams drive significant fast on those track parts.



FIGURE 4.7: Red points: curves, crossings and switches with radius smaller than 30m where at least 20% drives faster than 20 kph.



(A) Example of curves with high velocities Plesmanlaan/Johan Huizingalaan.



(B) Example of crossings with high velocities Concertgebouwplein/Van Baerlestraat.

FIGURE 4.8: Examples of track parts with a radius smaller than 30m where 20% of the vehicles are passing above 20 kph.

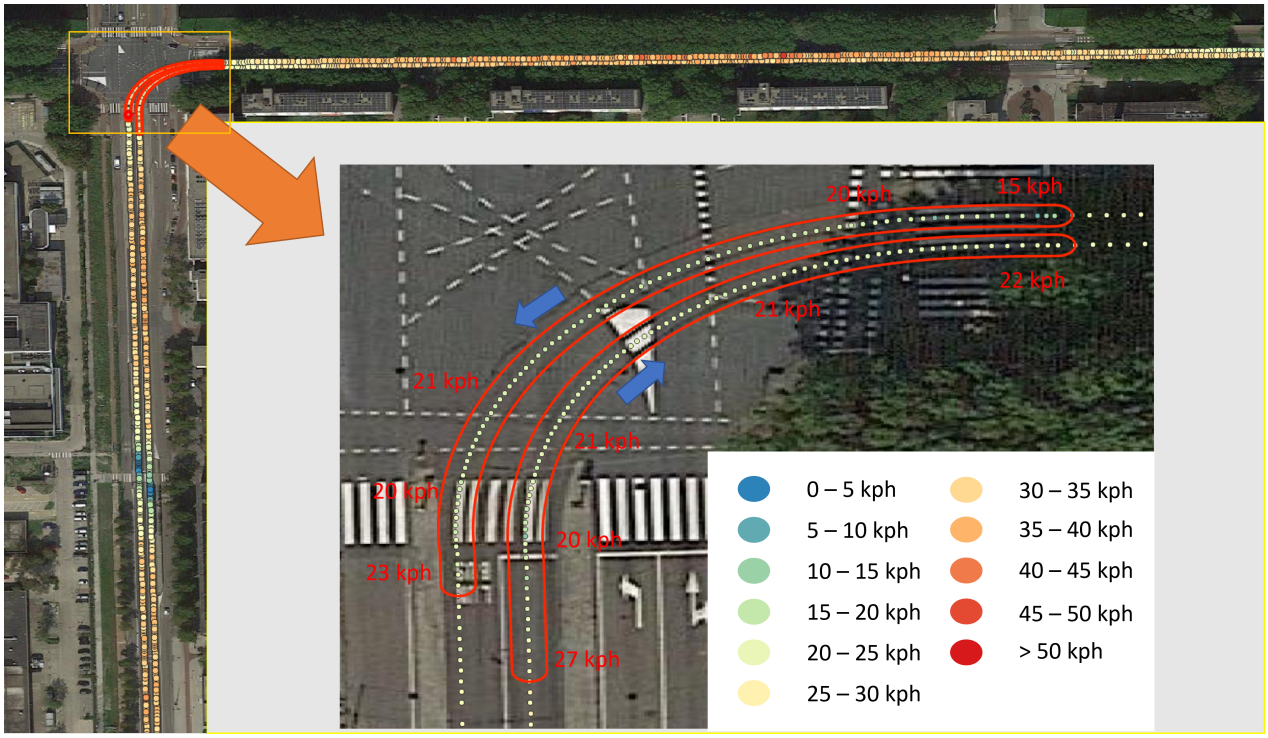


FIGURE 4.9: Example analysis of a curve (R=25) where vehicles are passing at high velocity (Plesmanlaan/Johan Huizingalaan).

V_mean	20,01068629148629
%0.0	3
%0-5	1
%5-10	1
%10-15	1
%15-20	35
%20-25	54
%25-30	6
%30-35	0
%35-40	0
%40-45	0
%45-50	0
%50-55	0
%55-60	0
%60-65	0
%65-70	0

(A) Velocity distribution inner curve.

V_mean	21,513304031209362
%0.0	3
%0-5	1
%5-10	1
%10-15	1
%15-20	16
%20-25	62
%25-30	16
%30-35	1
%35-40	0
%40-45	0
%45-50	0
%50-55	0
%55-60	0
%60-65	0
%65-70	0

(B) Velocity distribution outer curve.

FIGURE 4.10: Velocity distributions Plesmanlaan/Johan Huizingalaan.

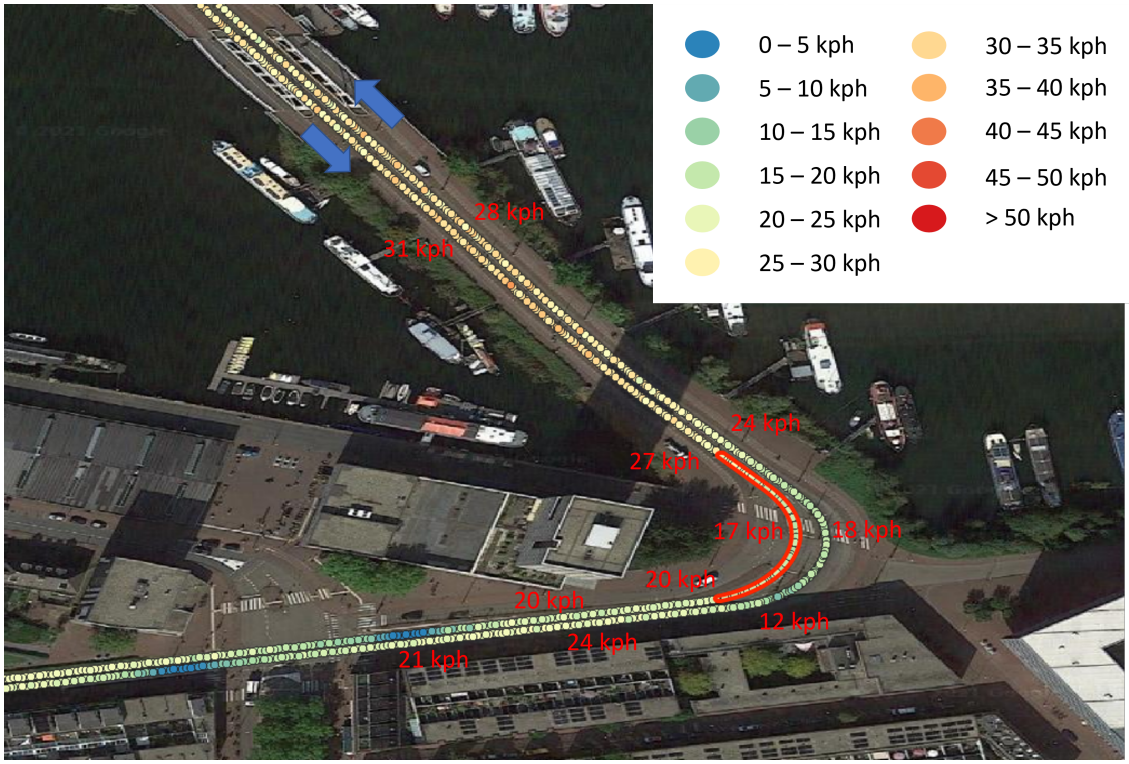


FIGURE 4.11: Example analysis of a curve (R=25) where vehicles are passing at high velocity (Verbindingsdam/Ertskade).

Detailed Analysis Curve 1

An example will now be given on how a curve where trams drive too fast could be analyzed. This analysis is shown in Figure 4.9. The figure shows the situation at the Plesmanlaan/Johan Huizingalaan intersection. For this small radius, trams go notoriously fast since the average velocities shown in red are above 20 kph, while a velocity of 15 kph would be the acceptable upper boundary in this case.

One could argue that the inner curve has a non-accurate mean velocity since the straight part at the start counts as a curve, while no axles are still in the actual curve at that point. Figure 4.10a and 4.10b show the calculated velocity distributions in both curves. Indeed, the mean velocity is higher in the inner curve. The mean velocity in the inner curve is 1.5 kph higher, and also the representation of the 20-25 kph and 25-30 kph velocity category is 8-10% larger. It is recommended that GVB improve the spatial curve definition to improve curve velocity estimations.

The reason for the high overall velocity in those two curves could be declared by the relative high velocity at the long straights adjacent to this curve (shown in 4.9). The human perception of speed is subjective. Drivers that drive at first at high velocity and then brake could underestimate their velocity after braking. The results show that drivers generally tend to decrease the velocity by about 10 kph when entering a tight curve. Therefore, curves surrounded by straight tracks where drivers could speed up are more prone to speed limit violations. However, this hypothetical reasoning should be proved by research among e.g. tram drivers.

Detailed Analysis Curve 2

The influence of surrounding straights could also be shown in another example, at the Verbindingsdam/Ertskade junction. This curve has a small radius of 25 meters, and turns more than 90 degrees. Nevertheless, trams go also notoriously fast on this curve. Figure 4.11 gives an overview of the situation. Here, the inner curve is marked as a curve where trams tend to go too fast, while the outer curve is not. As in the previous case, this could be declared by the velocity before the curve's actual start, which is higher at the inner curve. However, in both cases, the speed limit is violated, as seen in the detailed analysis, since the upper acceptable velocity limit is 15 kph.

The inner curve lays after a long straight where trams could reach a relatively high velocity, which seems to tempt drivers to decrease speed but not sufficiently. The outer curve is preceded by a junction and a shorter straight where drivers do not reach a relatively high velocity. In this case, trams decrease the speed to an acceptable level but accelerate too early, which causes especially the rear axles to negotiate at a too high velocity. The pedestrian crossing is also likely to influence, since the view for trams coming on the outer curve is partially blocked while trams coming on the inner curve have better visibility. This hypothesis could also be proven by further research.

To conclude this result section, multiple factors can influence the driven velocity in curves, the most apparent ones: radius, adjacent straights, visibility, surrounding passenger stops and surrounding junctions. Overall, trams stick to the prescribed velocities. On several specific curves, the average velocity is above the speed limit. On a more extensive selection of curves and crossings, only a portion of trams goes too fast. Wear rates on those particular curves can be compared to wear rates where trams comply with the speed limit to assess the influence of velocity on wear. This research step is not undertaken in the current research since the needed profile measurements were not available on time for this purpose.

4.3 Validity

The validity of the analysis is assessed by different means: consulting employees, looking at the trackpoints, considering the raw log data, and comparing with another week.

4.3.1 Verification by Employees

In total, three employees in charge of inspection and maintenance were asked. The employees considered the results of the velocity analysis to check if they matched the expectations. This check cannot validate the results numerically, and the employees could be biased. Overall, the driven velocities according to the analysis were lower than the expectations but still feasible in the opinion of GVB employees.

4.3.2 Validity Check Detailed Analysis

The spatial accuracy of the detailed analysis was checked by considering the results near tram stops. Figure 4.12 show a junction with a tram stop at each side. The figure proves the location and velocities are based on the position of the front cab. Since in this case, the minimum velocity is expected at the horizontal stripe, where trams stop and wait for the traffic light. This kind of analysis was done on multiple locations. It was concluded that the spatial allocation of velocities was accurate enough to deduce the driven velocities. Therefore, the detailed analysis would also be suitable to identify brake zones where sanders are often activated. Sand in the rails could also influence the wear process.

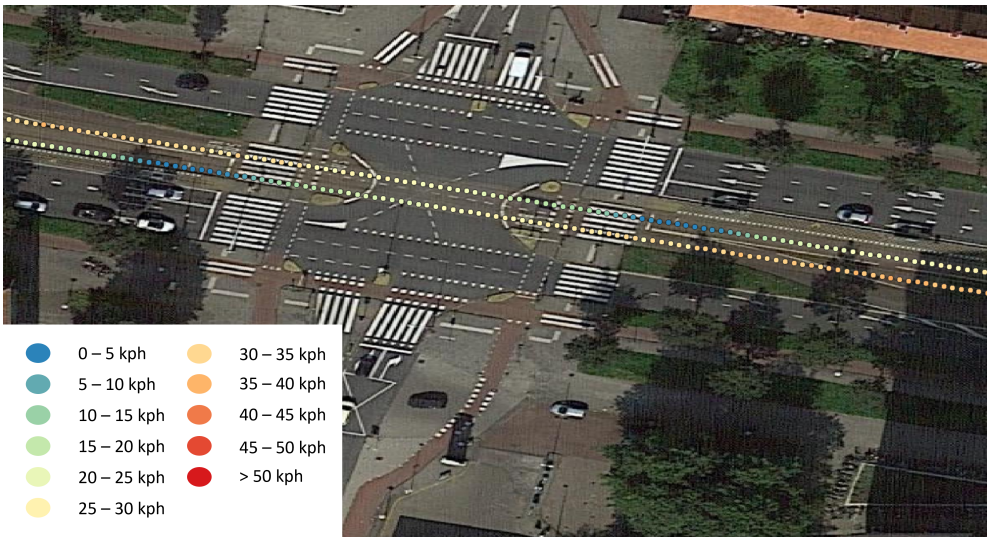


FIGURE 4.12: Detailed velocity analysis at the Burgemeester Röellstraat/Burgemeester Rendorpstraat junction.

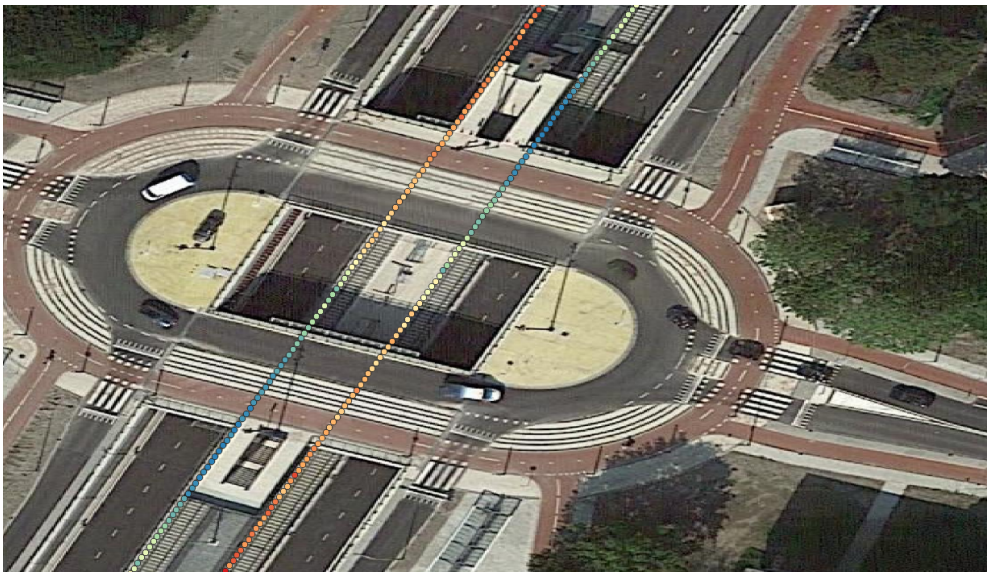


FIGURE 4.13: Detailed velocity analysis at the Sportlaan stop in Amstelveen.



FIGURE 4.14: Raw Logdata plotted at the Raadhuisstraat/Nieuwezijds Voorburgwal Intersection.

An issue remains with trams with cabs at both ends, Figure 4.13 shows the analysis at the Sportlaan Station in Amstelveen. This station is part of line 25, where only Urbos 100 trams are in operation, which can drive bi-directional. Also, in this case, the zone of low speed only occurs at the end of the platforms where trams usually stop. This result indicates that the front cab reports the location.

4.3.3 Validity Check Plotted Loggings

Figure 4.14 shows the raw log data plotted at one of the most adverse locations for accurate GPS measurements because of large buildings next to the relative small streets. In this negative case, most loggings lay in a bandwidth of 12 meters around the tracks. By looking at the horizontal offset of loggings from the track, it is possible to deduce an average inaccuracy. The average offset is 3-4 meters and a maximum of 6 meters. Most cases provide better GPS accuracy with bandwidths generally around 6 meters, leading to around an average inaccuracy of 2 meters. No evidence was found that the bandwidth increases significantly at stretches where trams drive faster, so it is assumed that loggings at higher velocity will not be more scattered than loggings at lower speed.

Considering the average location offset of 3-4 till 6 meters in extreme cases, it should be concluded that this offset could cause coupled velocities to wrong tracknumbers. This chance of error increases near the border of tracknumbers. Since at least 100 loggings are connected per tracknumber in most cases, it is assumed that redundancy in the number of available loggings will balance this disturbance. However, velocity categories with only a few (<20) loggings assigned should be taken with care since that might be loggings from a neighbouring track part.

The final factor to consider is the overhang of the cab, which is close to 3 meters. The exact location of the GPS device is not known, but it is in the front cab of the trams. This overhang means that the actual location of the first axle could have a maximum lack of 3

meters behind the deduced velocity location. This factor is not considered further but can influence the velocity distributions at specific locations.

A statistical factor affecting accuracy is trams that go faster will leave fewer loggings per unit distance, since a logging is sent every 10 seconds. As a result, trams driving at a lower velocity are more often *seen* at a curve which could decrease the calculated average velocity compared to reality. The resulting decrease is expected to be minor because of the relatively low speeds, e.g. if 50 per cent of the trams would drive 20 kph and the other 50 per cent 30 kph, the calculated average velocity per stretch would be 24 kph. In reality, it would be 25 kph. A velocity based compensation factor can compensate trams providing fewer data points due to higher speeds. No correction was made for this influence factor, but it could be subject to future improved analysis.

4.3.4 Comparison with Another Week

To assess the influence of using data from another time frame, week 33 from 2021 was also analyzed. The differences were calculated per trackpoint to evaluate differences in mean velocities. This analysis can be used to establish a margin for error. Figure 4.15 shows the result of this comparison. The vast majority of dots are green which means that the difference is within 5 kph. On the Paulus Potterstraat (blue stretch), maintenance was going on in week 33, while trams were still allowed to drive.

4.3.5 Acceleration Analysis

The acceleration analysis was validated by considering the visible average acceleration from the trackpoints. In most cases, the results were satisfying, although the level of accuracy is not as high as the velocity analysis. This higher inaccuracy is because only the average values on the outer trackpoints of a tracknumber are compared. Therefore, the acceleration analysis can only be used as primary guidance to discover track parts with high accelerations, but it should always be verified with the detailed velocity analysis.

4.4 Conclusion Velocity Analysis

Tram velocity records were coupled with Python code to specific tram segments over the whole tramway. The tram driving directions were derived based on the tram route records. This analysis revealed tram driving behaviour for the entire tramway. The results could be validated and further used in this research. Furthermore, it could be helpful for GVB.

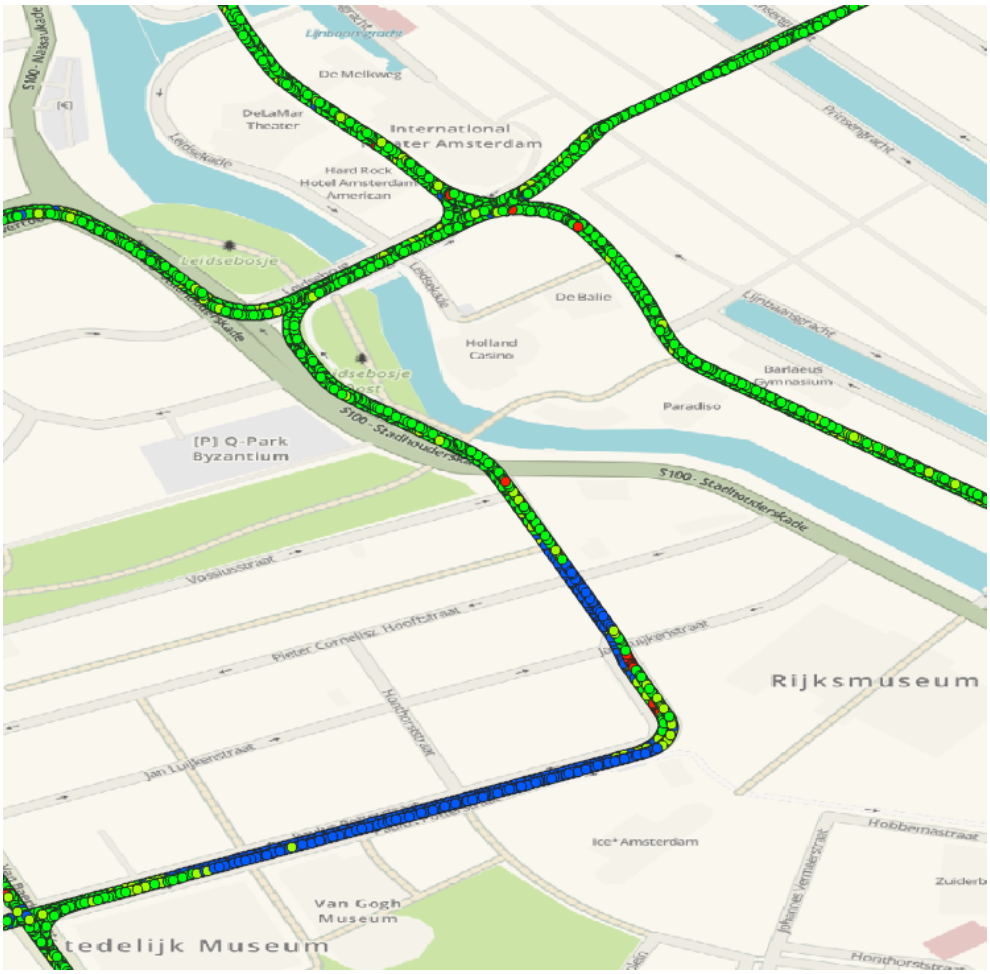


FIGURE 4.15: Difference in mean velocity week 33 2021 compared to 20-29 June 2021. Blue dot = > 5kph decrease, red = > 5kph increase. Road works done in week 33 at the Paulus Potterstraat (blue stretch) are clearly visible.

Chapter 5

Wheel Analysis

5.1 Introduction

Wheel profile measurements were obtained over six years. Those measurements were analyzed to determine the average wheel conditions of trams. The results are used as input for the energy estimation model, described in Chapter 7. This introduction provides an overview of the analysis. After that, the *Detailed Analysis Description* provides more in-depth information. This chapter is concluded with the results and a discussion on the validity of the analysis.

5.1.1 Objective of the Analysis

The main objective of the analysis is to obtain insight into the wheel wear of trams on the tramway. Since worn wheels have a considerable adverse effect on rail wear (Chapter 6), it was decided to have a closer look at the state of the tram wheels on the network. To understand the wear process, it is helpful to know the percentage of wheels in bad condition and wheels in good condition at a given time instance. A wheel wear distribution for the whole network, or better, per curve, could help estimate the wear per curve. Furthermore, a distribution of wear rates per wheel per vehicle type could also help understand the wear process at the wheel-rail contact.

5.1.2 General Analysis Description

Wheel measurement data was obtained from the old BN trams (Brugeoise et Nivelles) and the Combino trams from mid-2014 until mid-2020. Unfortunately, no Urbos trams were already in service before mid-2020. The wheels of each tram vehicle are re-profiled every approximately five months. Before and after re-profiling the wheel dimensions are measured. One of those dimensions is the qR, or the flange steepness, in other words. Figure 5.1 shows the qR on a cross-section of a wheel. For simplification reasons, the flange steepness was chosen as a single identifier for the wear state of the wheel, since it was the most critical measure, according to GVB. During usage of the wheels, the round transition between the flange and the tread (see Figure 5.1) becomes more angular, which harms wheel wear (simulated in Chapter 6). A lower qR means a more angular flange/tread transition, Figure 5.2 shows the wheel wear category classification based on the possible qR ranges.

The qR decay rates are calculated based on the measurements and time differences after subsequent re-profiling sessions for all wheels. The qR of each wheel per month is simulated with those measurements, based on the linear decay assumption. This simulation results in a monthly derived qR for each wheel in the tram fleet between 2014 and 2020.

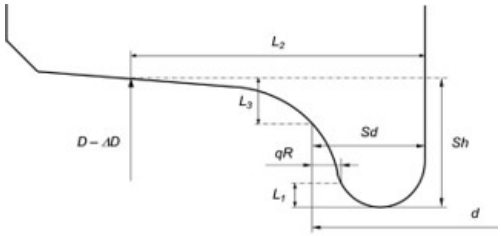


FIGURE 5.1: qR measure for the flange steepness.

qR Range	Wear Category
> 4.5	No Wear
4.0 – 4.5	Slight Wear
3.5 – 4.0	Light Wear
3.0 – 3.5	Moderate Wear
2.5 – 3.0	High Wear
< 2.5	Very High Wear

FIGURE 5.2: Wheel wear categories, based on the steepness of the flange expressed in qR.

All those monthly values are assembled in a distribution that estimates the average state of wheel wear on the tramway.

5.1.3 Analysis Input Description

The analysis has the following input per re-profile session:

- qR per re-profiled wheel before re-profiling.
- qR per re-profiled wheel after re-profiling.
- re-profile date.
- vehicle number (refers to a specific vehicle).

5.1.4 Analysis Output Description

The analysis delivers the following output:

- Average qR on the network per tram type, based on monthly interpolation derived from measurements
- qR decay distribution per wheel per tram type, based on decay rates from measurements

5.2 Detailed Analysis Description

The analysis is coded in Python to handle the over 20 000 different measurements at once. It reads the input files per re-profile session. The input files are in XML (Extensible Markup Language) format. Employees at the re-profile machine need to fill each measurement file

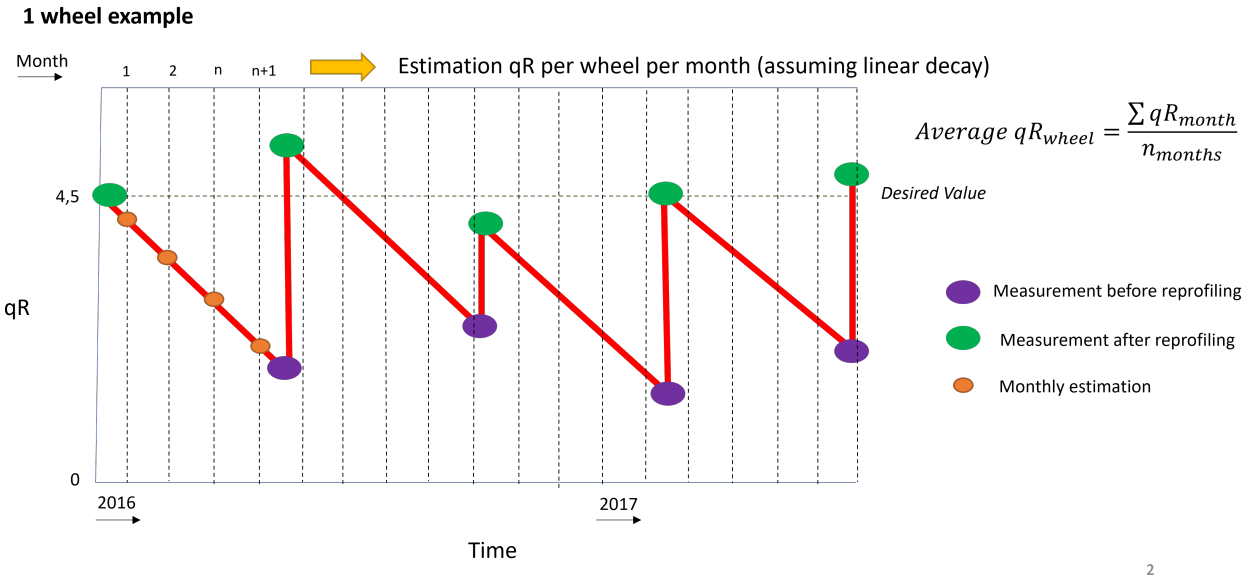


FIGURE 5.3: Example of the used method for one wheel.

manually. Therefore, the Python code checks for consistency and errors in the measurements. If the measurement is faulty, the code first tries to recover it and otherwise discards the wrong measurement.

The code loops over all measurements and determines the vehicle number, date, and qR measurements per measurement. The measurements are stored in a dictionary which is made during the code execution. The dictionary orders all the measurements per vehicle number. Per vehicle number, the measurements are ordered per wheel. After creating the dictionary, per vehicle number, per wheel of that specific vehicle, all before and after re-profiling measurements and the time intervals per re-profile session are considered. The decay rates per wheel between subsequent re-profile sessions are deduced by subtracting the before re-profile measurement from the after re-profile measurement from the previous session. The difference is then divided by the time difference between the subsequent sessions to obtain the qR decay rate per month. This decay rate is aggregated per wheel per vehicle type. The vehicle type could be deduced from the vehicle number.

Based on the measurements, also a wheel decay analysis was done, which is shown in Figure 5.3. An example is made for one (fictive) wheel during two years of the measurements in this figure. The qR measure in each month is simulated based on the qR measurements and the assumption of linear decay. The simulated qR measure per month is represented by the orange dots in Figure 5.3. Al those monthly qR values are aggregated per vehicle type and used to derive a network-wide distribution of qR measures.

5.3 Results

This section presents first the results of the qR distribution on the network, based on the monthly qR rates per wheel based on linear interpolation. Second, the qR decay rates aggregated per wheel are presented.

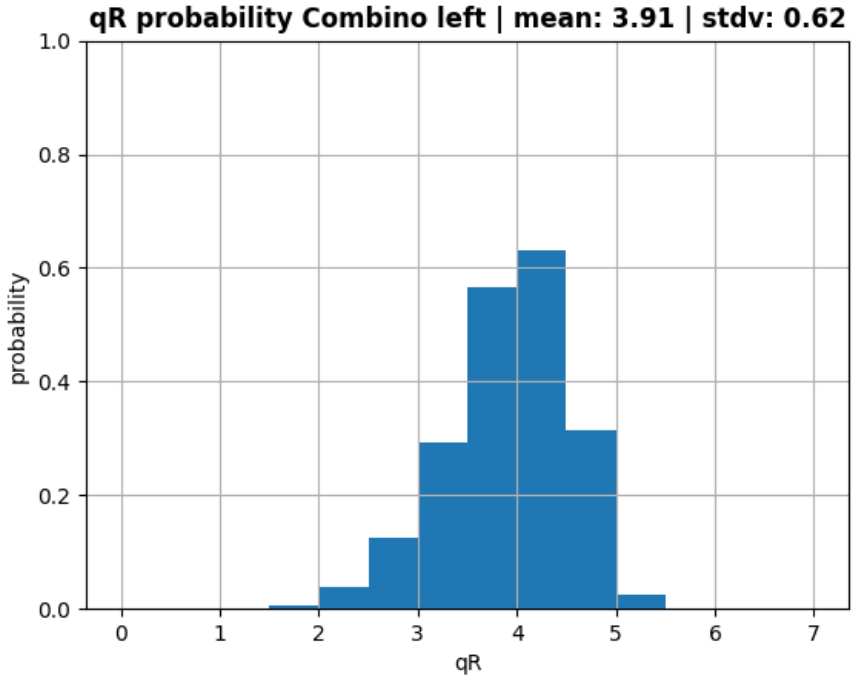


FIGURE 5.4: Derived qR probability distribution for the left wheels of the Combino.

5.3.1 Average qR on the network

Figure 5.4, Figure 5.5, Figure 5.6 and Figure 5.7 show the results of the simulated qR measure distribution over the network resulting from the linear interpolations; the results are aggregated per vehicle type per side. Figure 7.3 shows the wear category classification based on the qR range.

For both the BN and Combino trams, the left sides of the tram have lower qR decay rates than the right sides. It might be caused by the doors that are only at the right side for most concerned vehicles. A larger concentration of passengers weight could be concentrated on the right side, which increases the wear rates on the right side. (Deltarail, 2012) indeed concludes that the energy dissipation at the right side of the Combino trams might be higher because of asymmetric vehicle loading. Another cause could be that all turning loops at the route end-points are driven in an anti clockwise direction, which possibly enhances the wear on the trams' right-sided wheels. During the simulations (Chapter 6), it was indeed found that the right-sided flange endures more energy dissipation in tight curves.

The BN tram wheels were in overall better condition. Figure 5.4 and 5.5 do have a larger portion of wheels running with low qR, compared to Figure 5.6 and 5.7. The wheels fixed to an axle at the BN tram might increase the overall stiffness of suspension in comparison with the independent wheels of the newer Combino trams. This increased stiffness might be fortunate for the wheels, but it is more adverse for rail wear. During the simulations in Chapter 6, the curving behaviour of the CAF Urbos tram was simulated. This tram type has an increased suspension stiffness but also independent wheels. Indeed, this increased stiffness hurt rail wear.

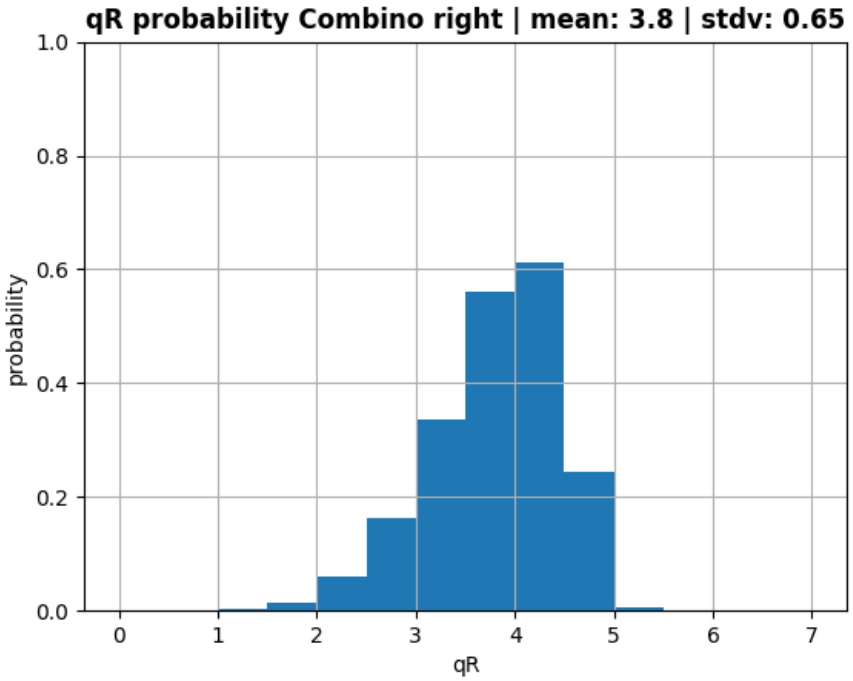


FIGURE 5.5: Derived qR probability distribution for the right wheels of the Combino.

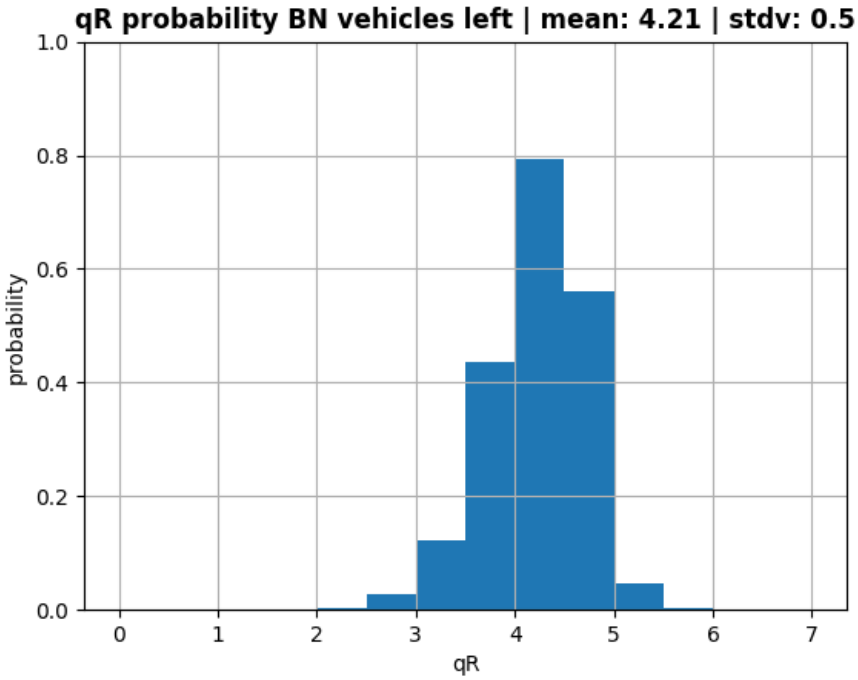


FIGURE 5.6: Derived qR probability distribution for the left wheels of the BN tram.

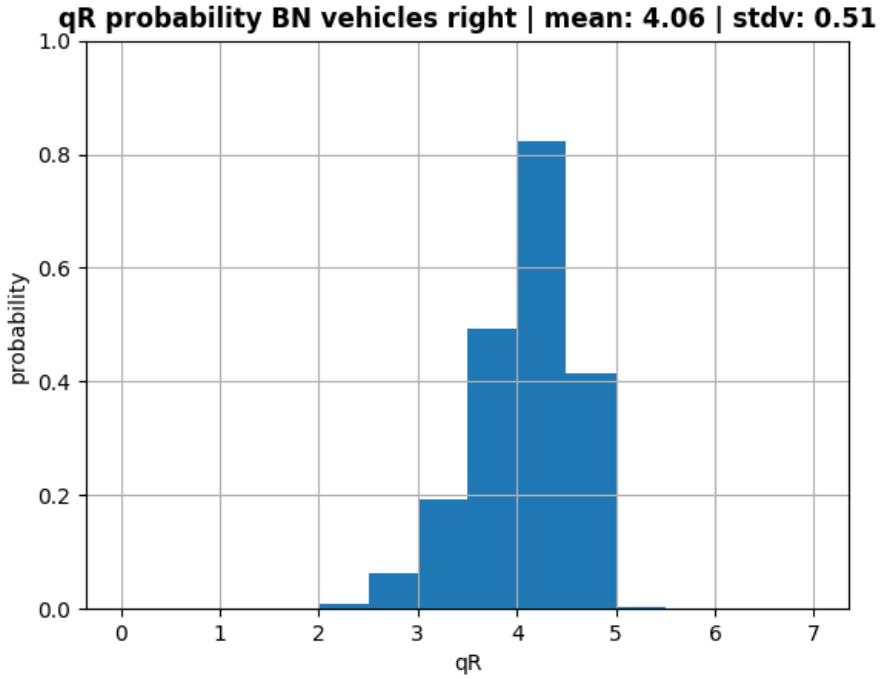


FIGURE 5.7: Derived qR probability distribution for the right wheels of the BN tram.

5.3.2 qR Decay per Wheel

Figure 5.8 shows the aggregated decay rates per wheel per vehicle type. Consult Figure 5.2 for the wear category ranges.

On both the BN and Combino trams, the first wheels stand out compared to the other wheels. This difference might be explained by the observation during the simulations (Chapter 6), which showed that the first wheels drive relatively much in flange contact, especially at tight curves. Also, the first wheels are the first ones that encounter a curve and have to steer, while the remainder of the tram is still pushing in the forward direction.

Again the BN trams seem to have performed better regarding qR decay, which can be a result from the more rigid BN trams. Also, the middle bogie of the Combino stands out in terms of qR decay. Furthermore, the decay rates at the rear wheels of the trams are higher. This increase might be caused by the over steering of the last bogie in tight curves. This phenomenon was observed during the simulations in Chapter 6.

5.4 Validity and Discussion

The measurements done by the machine are manually logged. Sometimes errors were encountered in the manually filled logfiles. It is reasonable to believe that some qR measurements also contain errors. It is difficult to derive the exact error rate. However, it is assumed that the number of considered measurements and the level of aggregation are both high enough to ensure accurate results.

It was too challenging to deduce wheel wear decay rates and distributions per specific curve or tram line since specific tram vehicles are not assigned to a particular line. As a result, an arbitrary vehicle could have driven over multiple lines in several weeks. Therefore,

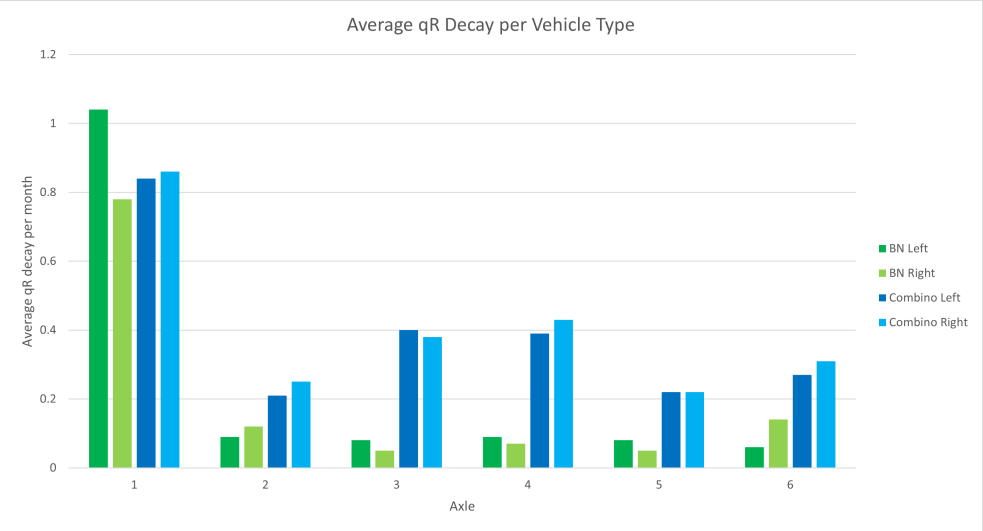


FIGURE 5.8: Average qR decay rate per wheel per vehicle type.

it was impossible to tailor decay rates to specific lines.

The assumption of linear decay might not be accurate. In Chapter 6 it was observed that worn wheels generate more energy dissipation. Therefore, a non-linear decline might be more feasible. It does not influence the average decay per wheel aggregation since the average decay would still have been calculated between two subsequent re-profiling sessions. However, the average qR distribution is expected to improve since the average state of the wheels will be better if an increasing decay rate over time is adopted.

Another issue concerns the decay rates per wheel, used in the aggregated results per wheel, which is used to verify simulations in Chapter 6. The aggregated results are based on a non-weighted average of the decay rates, which means that a decay rate measured over two months has an equal effect as a decay rate over e.g. five months. The average should be weighted by the time difference to obtain more sophisticated aggregated results. This issue does not affect the qR distribution over the network used in the energy estimation model (see (Chapter 7) since those monthly qR values are not dependent on the time interval between two subsequent wheel measurements.

The last issue concerns the wheel replacement of the tram done in the workshop. The flange angle could only be restored until the wheels reach the minimal diameter since part of the wheel diameter during the re-profiling is removed. The replacement of the wheels is not considered because no well-aligned data was available to include this in the analysis. It could lead to lower wear rates established by the research compared to reality when the wheels were replaced between the subsequent measurements.

Finally, more information could have been retrieved from this research. For example, the variety per specific vehicle could have been researched to assess if there are particular vehicles with very adverse decay rates, which might be a consequence of faulty assembly at the workshop. Also, the changes in average decay rate over time could have been researched to assess the effect of changing re-profiling policies or seasons. The analysis could have verified the hypothesis of more wear on the right side by only looking at bi-directional tram vehicles. The suggestions above were not undertaken since the results were not essential for the thesis research.

5.5 Conclusion

The first wheels seem to endure the most adverse wear effects, which is supported by the results of the simulations in Chapter 6. The general higher decay levels at the Combino trams than the BN tram stand out. This result might be an effect of the difference between the bogies of the Combino and BN trams, since Combino trams have independent mounted wheels and BN tram wheels share the same axle. The analysis results could be used to verify the simulation results and as input in the energy estimation model.

Chapter 6

Wear Simulation in Tramway Curves

This chapter describes the simulations performed to analyse trams' curving behaviour under different circumstances, e.g. different curve radii or velocities. The simulation results are analysed and form the basis for the energy estimation model. Appendix D elaborates on the method and models used in the simulations. This chapter focuses on the simulation setup and results.

6.1 Introduction

Simulations were performed at DEKRA rail. DEKRA already did the research for GVB about different subjects. For example, about the consequences of introducing a new tram type. The simulations were done with the VAMPIRE simulation package. It was very convenient that DEKRA already had cutting edge vehicle models of the tram types used by GVB. The vehicle models were not modified, no validation of the model's reliability was performed. However, model results were verified on consistency with the help of GVB tram maintenance engineers. The assumptions concerning the simulation model are further discussed in Chapter 8.

During the simulation, a tram drives over a predefined track. The simulation program calculates forces and displacements. The forces and displacements are used to derive the dissipated energy at the wheel-rail contact. In this case, energy estimation was chosen as a wear indicator, Chapter 2 describes and discusses this indicator. A further discussion on the accuracy and assumptions of this indicator can be found in Chapter 8.

The simulation process is divided into two phases: three curves and the parametric simulations. During the first phase, three existing curves on the network were simulated, and the results were assessed in detail. The second phase consisted of parametric simulations: over 600 fictive situations were simulated. During those simulations, the following parameters were analysed: curve radius, driving velocity, wheel profiles, rail profiles, vehicle loading and vehicle type. A Python code was made to analyse those parametric simulations.

6.2 Simulation Analysis: Three Curves

6.2.1 Introduction

Three curves of the tramway were analysed. Data on those three curves were gathered and included in the simulation model to resemble the actual situation. For two curves, some simulation variants e.g. increased tram loading or velocity, were considered. The aim of the three curves analysis was twofold. First, insight can be obtained in influential

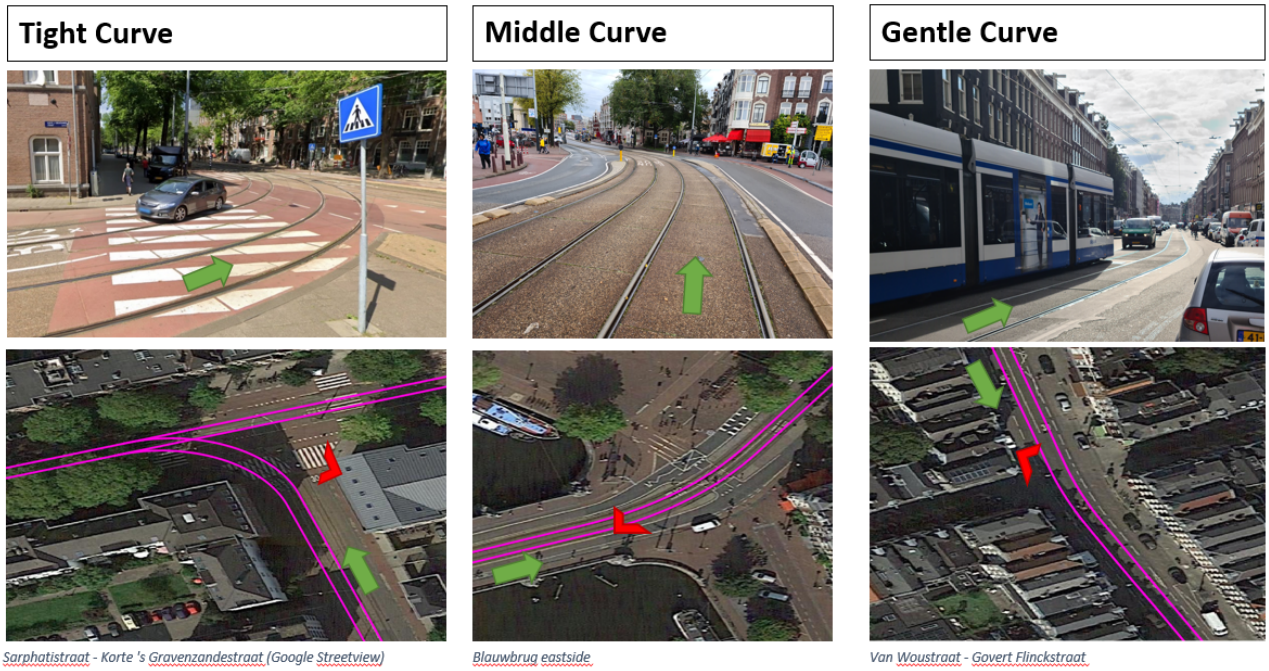


FIGURE 6.1: Footage of the 3 selected curves.

parameters, especially with the help of the simulation variants. This insight forms the basis for the setup of the parametric simulations because it can reveal the significance of parameters. The second aim of the three curves analysis is to verify the simulation model. The feasibility of the output is checked with the help of GVB employees and measurement results. This verification is essential since the 623 parametric simulations cannot all be verified in detail.

First, the details of the three chosen curves are given. Next, the simulations' results with the three curves are provided and verified. Furthermore, simulation variants based on the principle curve simulations are discussed.

6.2.2 Curve Description and Input Values

A tight, middle and gentle curve was selected. Figure 6.1 provide a visual impression from the three curves. All curves are located in the greater city centre and share the space with other traffic modalities. These specific curves were chosen since the quality of rail profile measurements by Autech was satisfying on these curves, important for the validity check.

Figure 6.2 provides the details per curve in table form. All curves were only passed by Siemens Combino's. From the velocity analysis, it followed that trams do not brake or accelerate on average on these curves. The average occupation of vehicles on these curves was less than 50%. Therefore, empty vehicle models were chosen. A simulation variant with a fully loaded tram was also performed for the tight curve. New wheel profiles were adopted, but a simulation variant was also made to assess the effect of worn wheels.

6.2.3 Results Three Curves Simulations

This subsection presents the results of the three principal curves simulations: the tight, middle and gentle curve simulations with the parameters approximating reality. The next sections provide the results of the simulation variants on those three curves. The result

Curve parameters:		
Tight	Middle	Gentle
Radius: 24m	Radius: 61m	Radius: 100m
Curve length: 26m	Curve length: 26m	Curve length: 26m
Railtype: 60R2 new	Railtype: 60R2 new	Railtype: 60R2 new
Steelsort: R200	Steelsort: R200	Steelsort: R200
Friction Flange: 0.15 (lubricated), rail: 0.32	Friction Flange: 0.15 (lubricated), rail: 0.32	Friction Flange: 0.15 (lubricated), rail: 0.32
Velocity: 7.2 kph	Velocity: 22 kph	Velocity: 21 kph
Tonnage: 5023 ton/day	Tonnage: 3809 ton/day	Tonnage: 3239 ton/day
Passages/day: 132	Passages/day: 100	Passages/day: 86
Vehicle: Siemens Combino	Vehicle: Siemens Combino	Vehicle: Siemens Combino
Vehicle load: empty	Vehicle load: empty	Vehicle load: empty
Wheel: Theoretical GVB Profile	Wheel: Theoretical GVB Profile	Wheel: Theoretical GVB Profile
No traction/braking	No traction/braking	No traction/braking

FIGURE 6.2: Input data for the principal simulations of the 3 curves.

of each simulation will be explained and verified. The results are aggregated by taking the average energy dissipation per wheel per contact surface along the curve. For more information on the post-processing process, consult Appendix D. The right rail refers to the outer rail, the left rail refers to the inner rail.

During the assessment of the simulation results, dissipated energy at the flange back was very rarely seen, while from practice, it is known it does occur. Because of the unclear effects of energy dissipation at the flange back, it was decided to limit the focus to the head of the rail. Therefore, the flange back is not taken into further account with the parametric simulations.

Tight Curve Simulation Results and Verification

Considering the aggregated results per wheel at the outer rail in Figure 6.3. Besides the first right wheel, the third right has short flange contact, and the other wheels mainly drive on the tread. The dissipated energy tends to be somewhat higher at the rear bogies, and the overall values are pretty high. When looking at the aggregated results of the inner rail in Figure 6.4, the second wheel makes many flange contact, which is logical for a curve in the left direction. The other wheels mainly stay on the tread. In this case, each bogie's first wheels show larger values than the rear wheels. The overall values are still relatively high, and no increase in dissipated energy on the rear bogie is visible at the inner side.

These results are further investigated by looking at the tram behaviour along the curve.

Figure 6.5 shows a schematic overview of the steering forces of the rail on the bogie. The front wheels have a clockwise angle of attack (AOA) on the rails. The small blue arrows are the steering forces of the rails on the wheels resulting from the angle of attack. These steering forces are transmitted via creep forces at the wheel-rail contact interface, resulting in energy dissipation.

The rear wheels do have a smaller anticlockwise angle of attack. This angle of attack is smaller since the angle of attack of the bogie, which is clockwise, compensates for the anti-clockwise angle of attack of the rear wheels. Therefore, fewer steering forces from the rails are generated, resulting in fewer creep forces and, thus, less energy dissipation at the rear wheels of the bogie in this theoretical situation.

Dependent on the stiffness of the primary suspension, the wheels could, in this case independently, make a yaw rotation to reduce the angle of attack. With a reduced angle of attack, the difference between the first and second wheels persist. With increased stiffness, the yaw rotation will be more minor, increasing the angle of attack and, therefore, the dissipated energy.

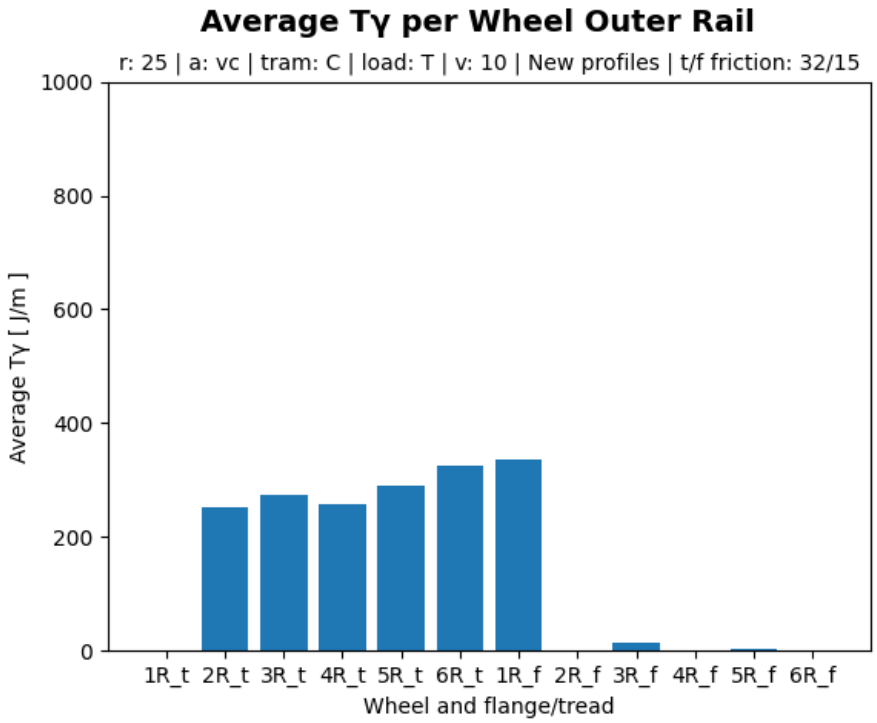


FIGURE 6.3: Aggregated results for the simulation at the outer rail representing a Combino negotiating a tight curve.

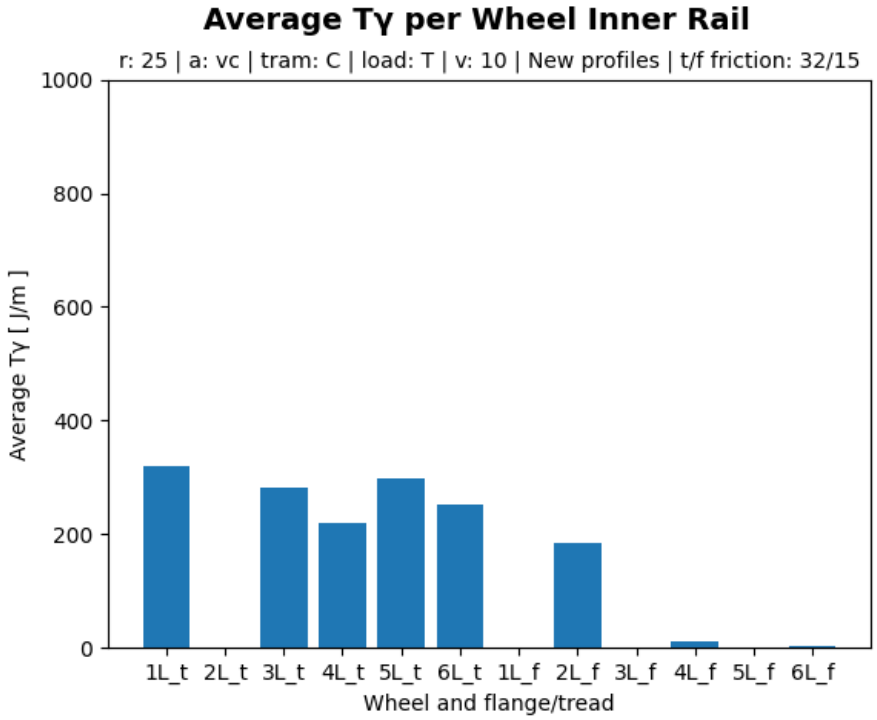


FIGURE 6.4: Aggregated results for the simulation at the inner rail representing a Combino negotiating a tight curve.

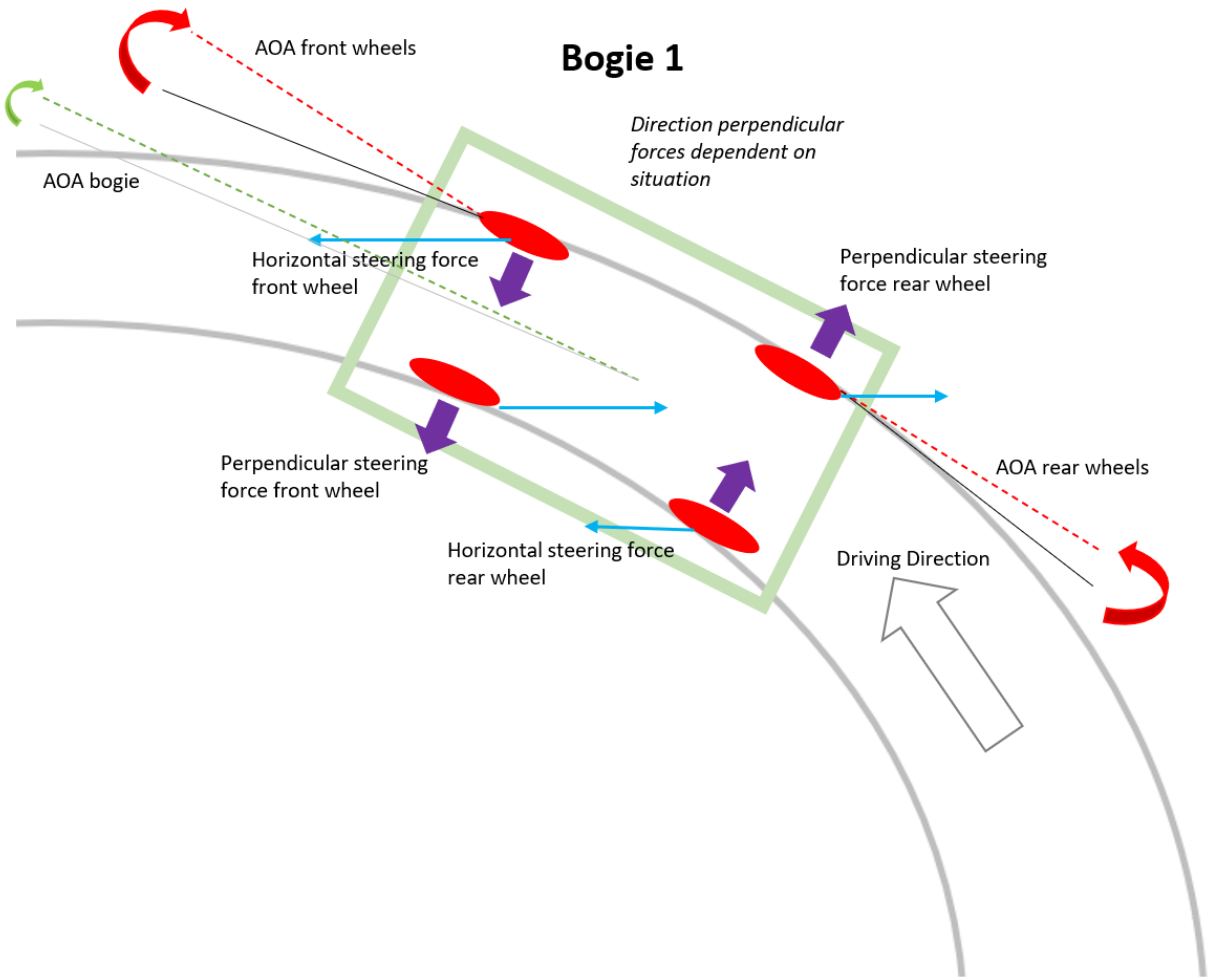


FIGURE 6.5: Schematic overview of the steering forces on bogie 1.

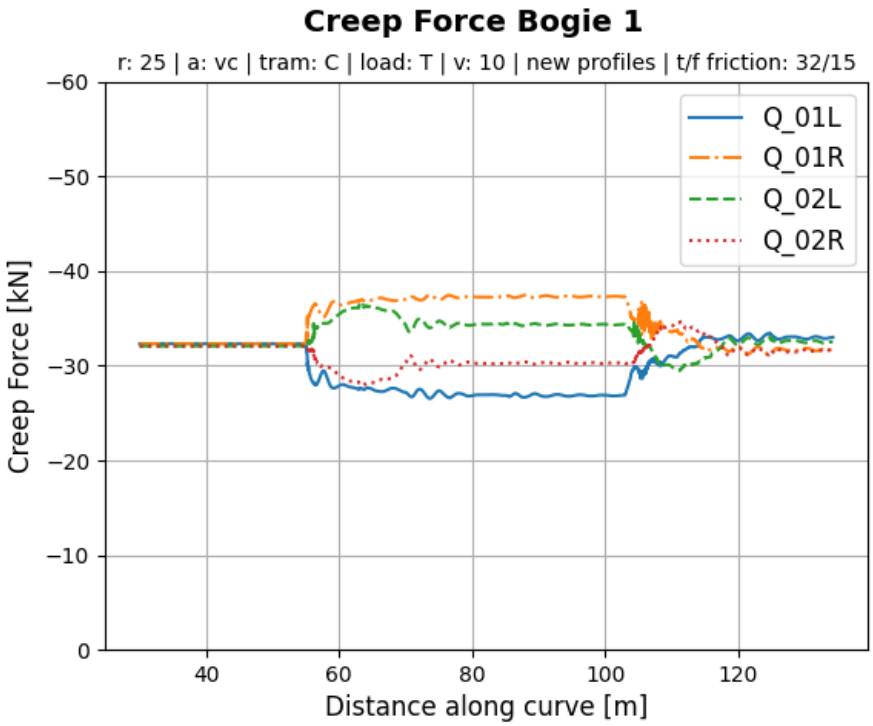


FIGURE 6.6: Creep forces at the first bogie, L = inner rail, R = outer rail.

The perpendicular steering forces, represented by thick arrows in Figure 6.5, are generated either by lateral tangential forces on the tread or by normal lateral forces on the flange-rail interface. Those perpendicular forces guide the bogie through the curve by limiting the lateral movement of the wheels. The magnitude and direction of the perpendicular forces are dependent on the situation. When the wheels are laterally displaced to the right the steering forces will point in the left direction in the running direction, as is the case in the figure.

The perpendicular steering force at the outer rail wheel could originate from the normal lateral force at the flange and the lateral creep force at the tread. This origin depends on the magnitude of lateral displacement of the wheel. The inner rail wheel at the front is most likely only to have lateral creep forces at the tread. With tram rails, it is possible to have normal forces from the contra rail. However, this is not taken into further account in this research. The perpendicular force at the rear wheels in the figure follows the same mechanism.

In figure 6.5 the wheels are assumed to be displaced to the left. The centrifugal force may overcompensate the lateral movement to the left at a higher velocity. In this case, the rear wheels are also laterally displaced to the right, and the guiding force will then point in the opposite direction. Also, the magnitude of the lateral displacements and the resulting forces and energy dissipation depends on the stiffness of the primary lateral suspension.

Figure 6.6 shows the creep forces at the four wheels of the first bogie. A constant creep force is present outside a curve, representing the friction at the wheel-rail contact and causing the tram to hold traction. The force generated by the curve on the first wheel on the inner rail is in the opposite direction, which causes the creep force to decrease. The creep force is increased for the first wheel on the outer rail. This same process but then mirrored is visible for the second wheels, the rear wheels of the bogies, since here, the

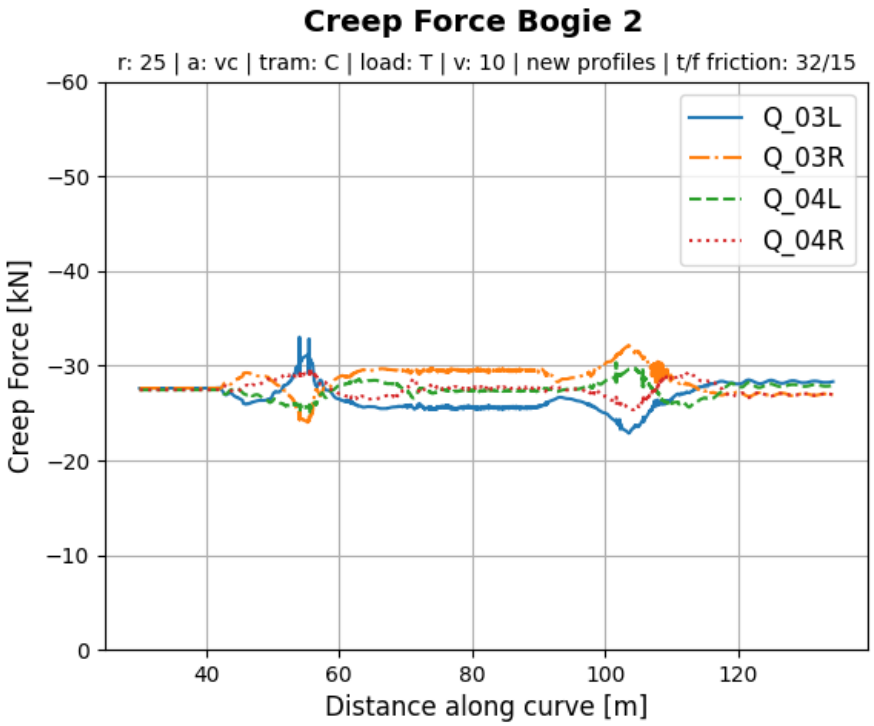


FIGURE 6.7: Creep forces at the second bogie, L = inner rail, R = outer rail.

angle of attack has a different sign. The magnitude of the creep force difference is lower since the angle of attack is smaller at the rear wheels of the bogie.

Figure 6.7 shows the creep forces at the second bogie. Compared with the first bogie, the rear wheel set seems only to have an angle of attack at the front and end of the curve. It is interesting to look closer at the sign of the angle of attack in Figure 6.7. Regarding the first wheels of the second bogie, the sign is swapped at the entrance of the curve. This swap means that the wheels over-steer to the left, which might be caused by the pull force of the front-driven bogie. The same is visible for the rear wheels of the second bogie. At the end of the curve, the rear wheels do have an angle of attack as in figure 6.5.

The angle of attack of the second bogie's front wheels is much smaller than the front wheels of the first bogie. This difference might be because the first bogie already steers the second bogie in the right direction, which could also explain why the rear wheels of the second bogie over-steer. Figure 6.8 shows the situation for bogie two during the stable curving phase in a schematic way. Although the second bogie is a trailer bogie, the creep forces do have the same sign as the first driven bogie. Still, the force is somewhat lower. According to the expectation, the creep force on the non driven bogie should have different signs; it is assumed that this is a result of the way the vehicle is simulated and that it will not have significant effects on the simulation outcomes.

Figure 6.9 shows the creep forces for the third bogie. It is interesting to notice that now the angle of attack of the rear wheels of the bogie is larger. Also, at both the rear and front, the sign of the angle of attack is swapped. This swap means that the bogie and wheels over-steer slightly to the left. The front part of the vehicle is already on the straight after the curve, pulling the part that is still negotiating in the left direction. Figure 6.10 shows this situation in a schematic way.

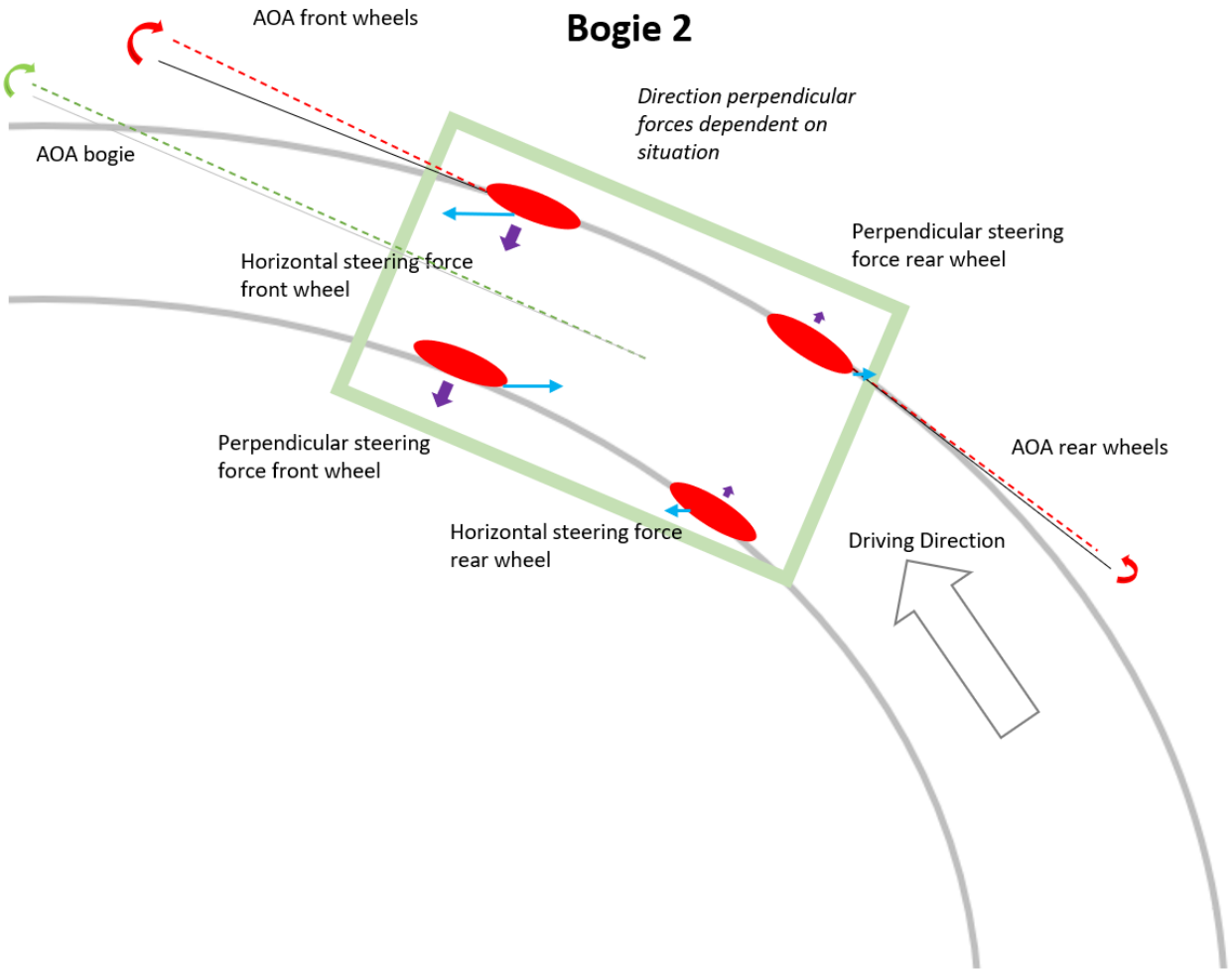


FIGURE 6.8: Schematic overview of the steering forces on bogie 2.

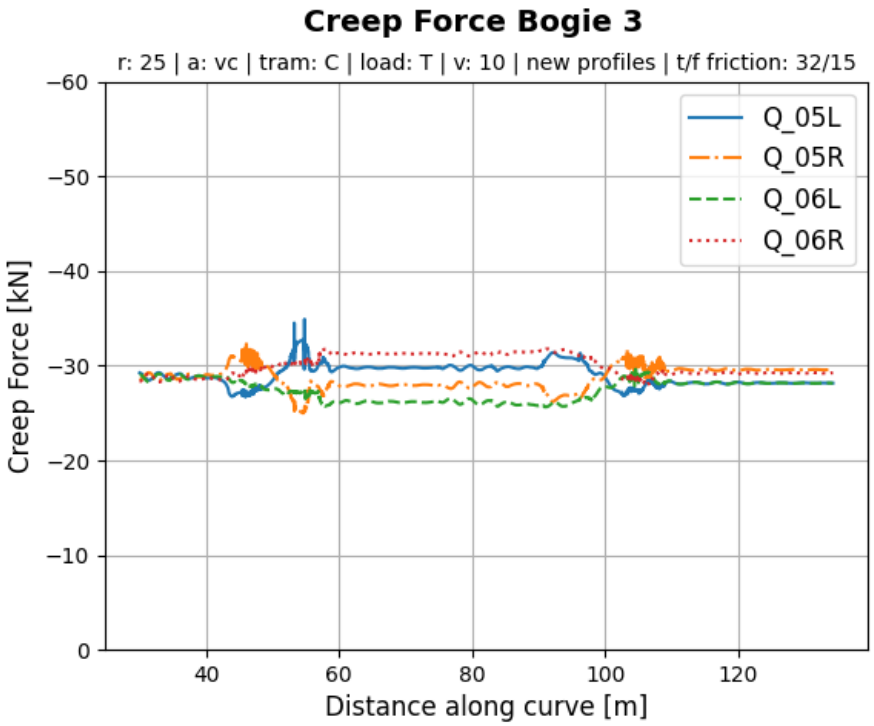


FIGURE 6.9: Creep forces at the third bogie, L = inner rail, R = outer rail.

According to the simulation, it is clear how the vehicle goes through the curve. Next, it is assessed how this behaviour is converted into dissipated energy.

Figure 6.11 and 6.12 show the dissipated energy along the curve for bogie 1. Because of the angle of attack and lateral displacement, the right front wheel and the left rear wheel make flange contact. The dissipated energy at the front right wheel is twice as high as the rear left wheel, which makes sense since the creep force resulting from the angle of attack is twice as high at the first wheels. However, this difference is not visible in the dissipated energy at the tread, the dissipated energy at the rear is somewhat lower but not 50%.

Figure 6.13 shows the dissipated energy along the curve for bogie 2. Only the tread is shown in this case since only short flange contact was made when leaving the curve. Remarkably, the dissipated energy values stay in the 300 J/m range, despite the smaller differences in creep forces. This observation is extraordinary for the rear wheels of the second bogie since the angle of attack was believed to be small.

Figure 6.14 shows a possible explanation for this occurrence. This figure is zoomed at the creep force plots of Figure 6.6 and 6.7. Although the differences in creep forces for the second bogie are lower, the alternation frequency of the creep force at the second bogie is higher, which points to a more unstable behaviour of the second bogie. This alternation could result from stick-slip behaviour on the tread, which results in a larger overall slip distance and more dissipated energy as would be expected when looking only at the creep force and angle of attack. The root cause why the first bogie does not show this behaviour during stable curving might be found in the stabilising effect of the flange contact.

The plots show a uniform distributed T_γ along the curve either at the flange or the tread. Therefore, it is concluded that averaging the T_γ over the curve length is feasible as an aggregation method. This relatively uniform distribution of energy dissipation along the curve is now verified by looking at the profile measurements of the concerned curve.

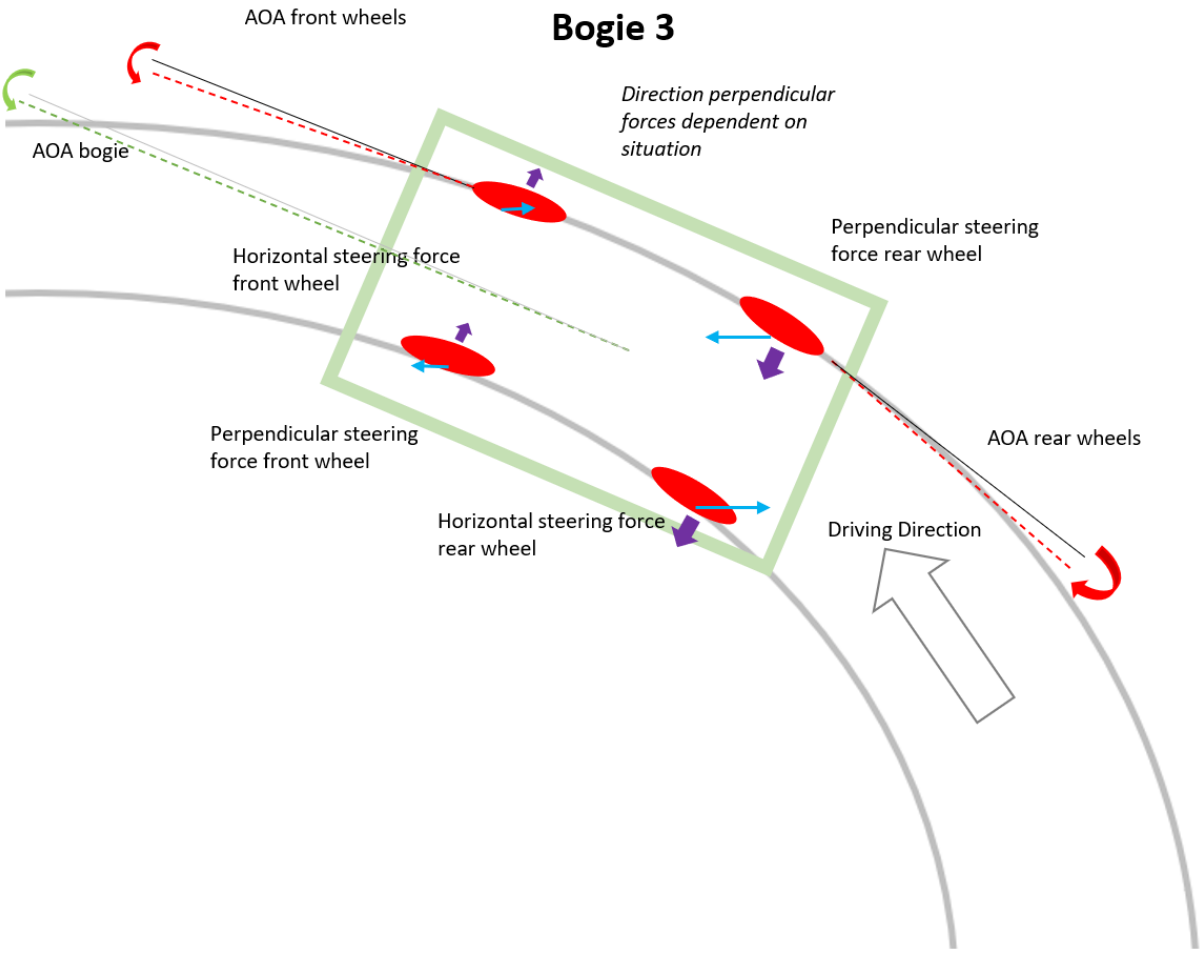


FIGURE 6.10: Schematic overview of the steering forces on bogie 3.

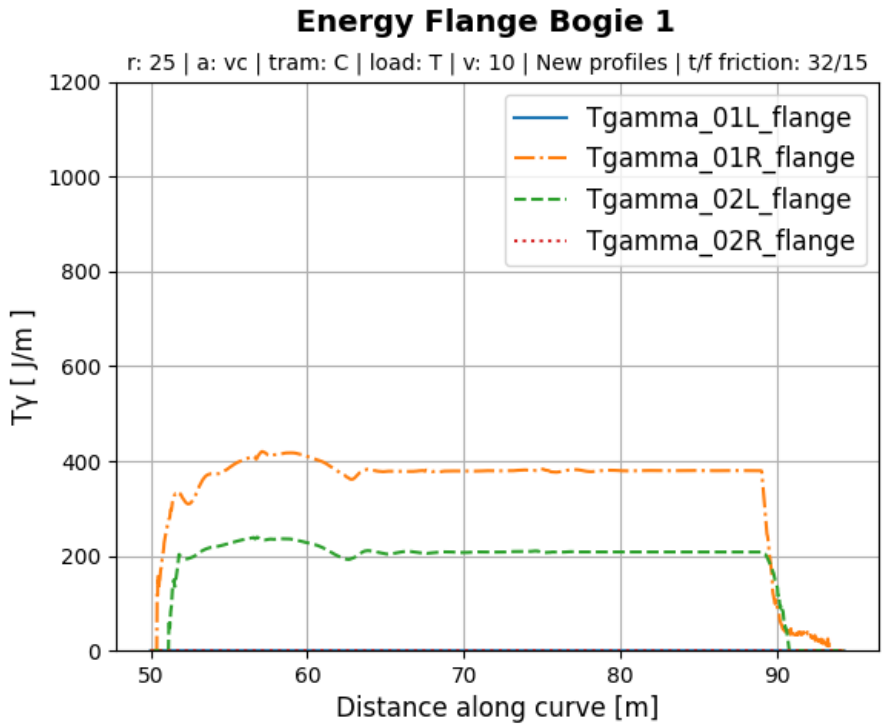


FIGURE 6.11: Energy dissipation on the flanges of the wheels of bogie 1. L = inner rail, R = outer rail.

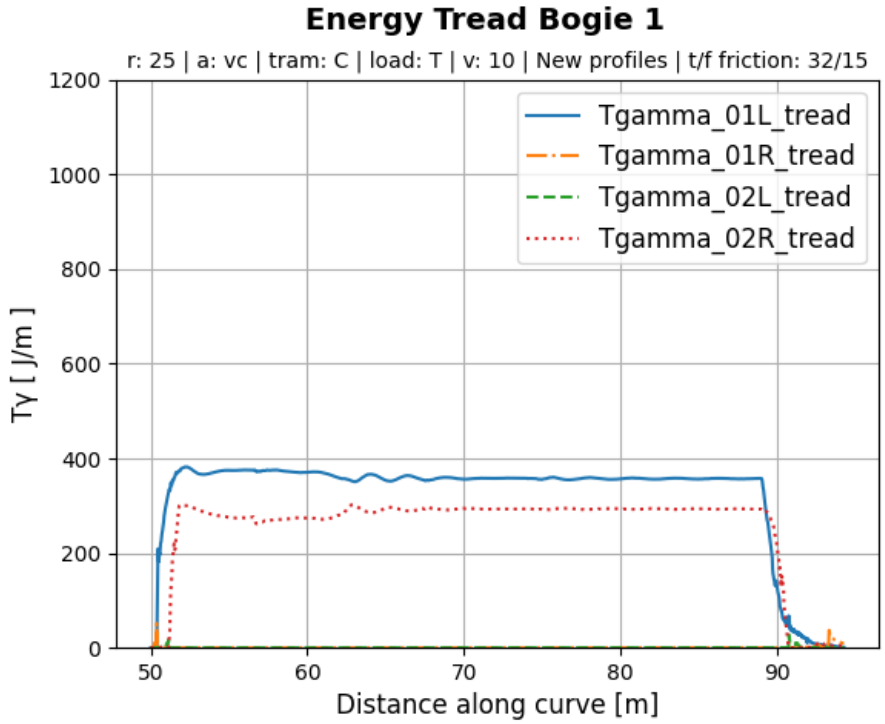


FIGURE 6.12: Energy dissipation on the treads of the wheels of bogie 1. L = inner rail, R = outer rail.

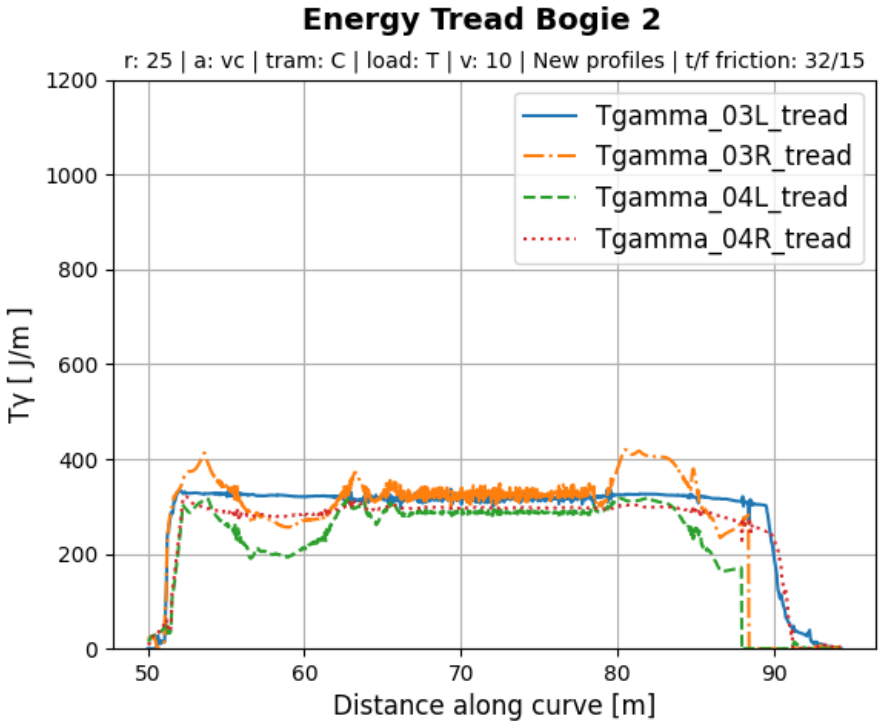


FIGURE 6.13: Energy dissipation on the treads of the wheels of bogie 2. L = inner rail, R = outer rail.

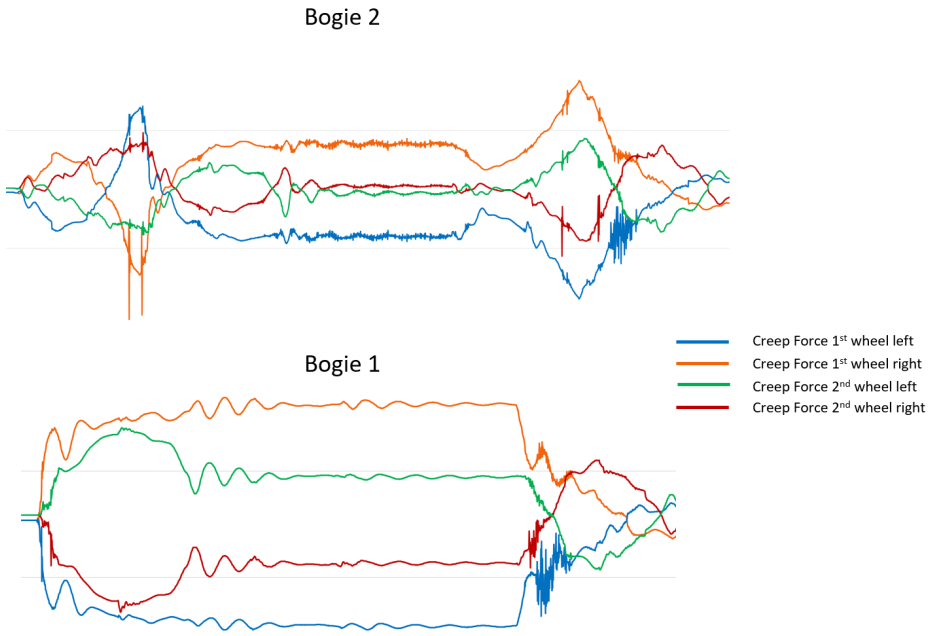


FIGURE 6.14: Zoomed in at the creep force along the curve from Figure 6.6 and 6.7.

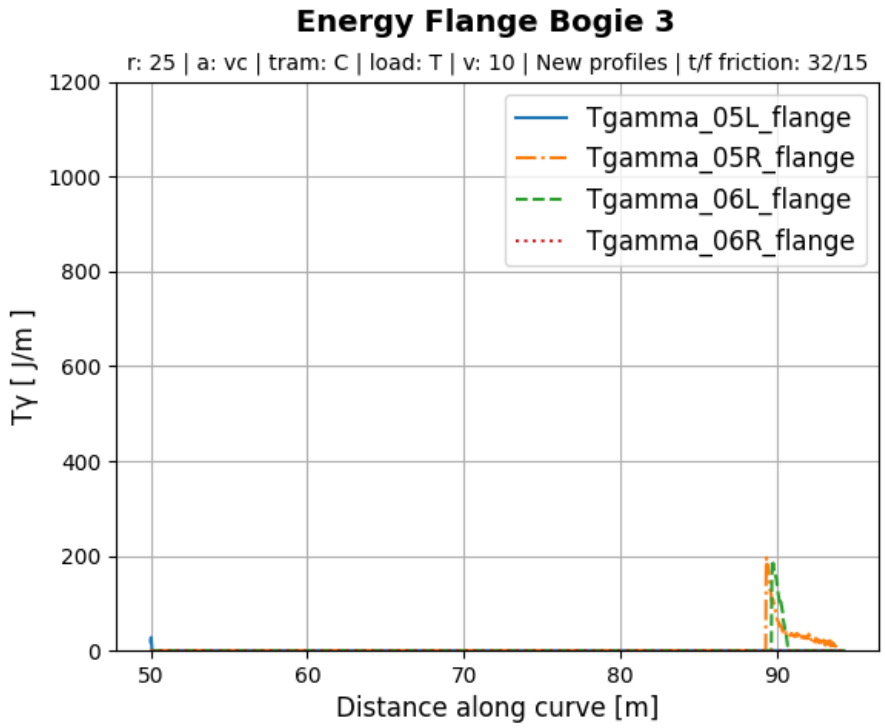


FIGURE 6.15: Energy dissipation on the flanges of the wheels of bogie 3. L = inner rail, R = outer rail.

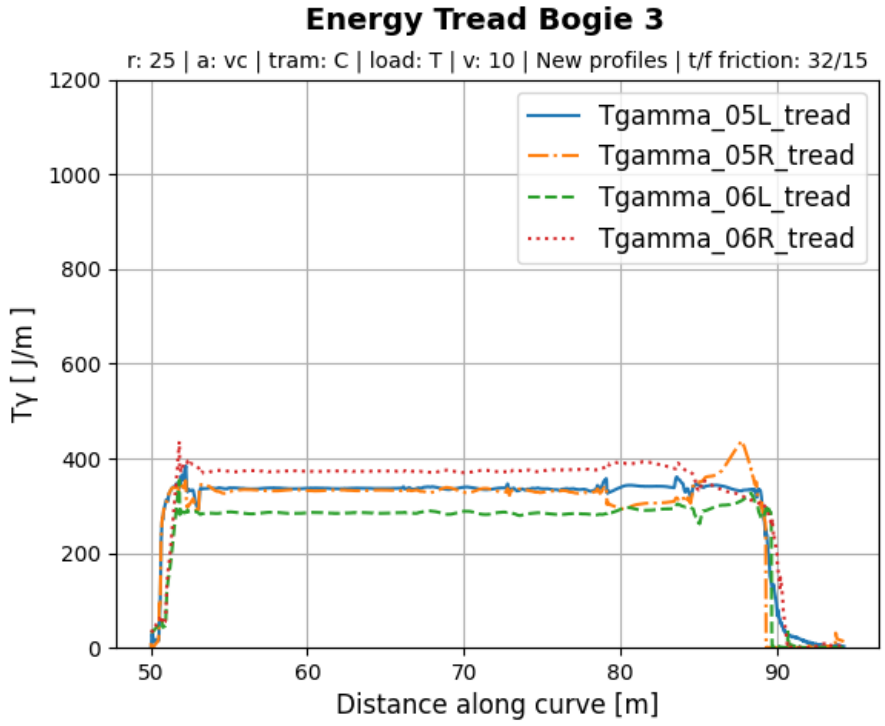


FIGURE 6.16: Energy dissipation on the tread of the wheels of bogie 3. L = inner rail, R = outer rail.

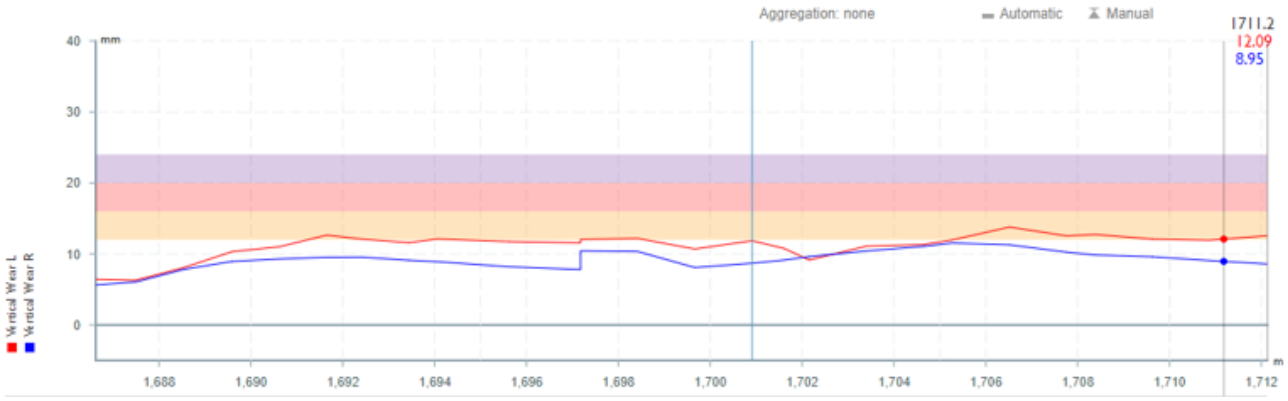


FIGURE 6.17: Measurement of the vertical wear along the outer curve at the 's Gravenzandestraat - Sarphatistraat intersection in 2020

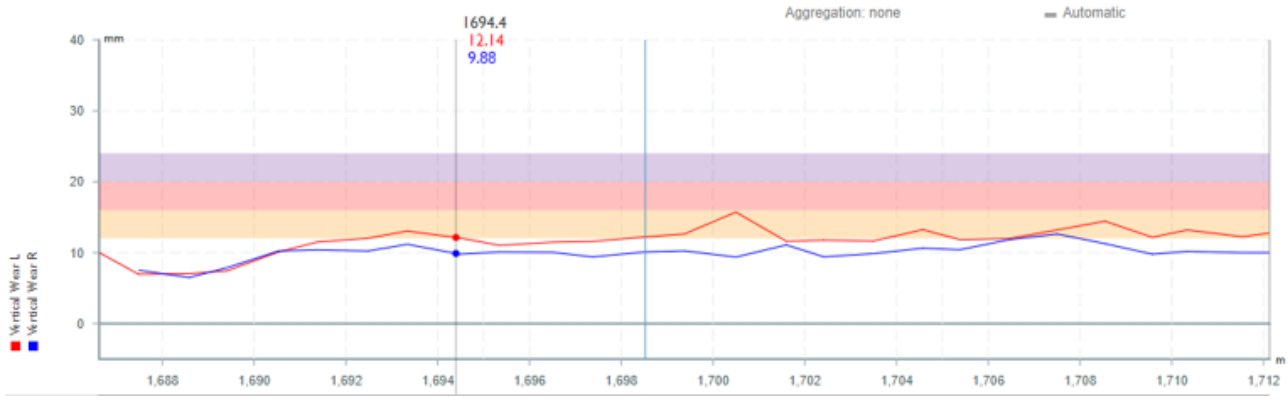


FIGURE 6.18: Measurement of the vertical wear along the outer curve at the 's Gravenzandestraat - Sarphatistraat intersection in 2021

Figure 6.17 and 6.18 show the measurement results of the concerned tight curve at the 's Gravenzandestraat/Sarphatistraat intersection for the years 2020 and 2021. The plot shows the vertical wear on both sides along the left curve in the driving direction. The cross-section at the right shows the measurement profile and indicates the horizontal wear.

Both measurements concluded that, indeed, the dissipated energy along the curve is uniformly distributed. The figures only show the distribution of the vertical wear, but it was verified that this uniform distribution also applies to horizontal wear. This profile measurement is not including that sometimes the rail is horizontally welded. If the outer rail is welded more often since it wears more, the horizontal wear at the inner rail could be deceptively more increased. Unfortunately, maintenance records with sufficient details are not available. When considering the wear rates according to the measurements, the following rates are found:

- Vertical wear left: 0.36 mm/year
- Horizontal wear left: *unknown*
- Vertical wear right: 1.51 mm/year
- Horizontal wear right: 0.31 mm/year

According to the simulations, this could be compared with the total dissipated energy per side per contact (flange/tread).

- Dissipated energy tread left: 1374 J/m
- Dissipated energy flange left: 198 J/m
- Dissipated energy tread right: 1400 J/m
- Dissipated energy flange right: 355 J/m

Now the ratio of wear per dissipated energy could be calculated in mm/year per J/m. Since those ratios would be relatively small, they are expressed in mm/year per kJ/m.

- Ratio vertical left: 0.26 (mm/year)/(kJ/m)
- Ratio horizontal left: *unknown*
- Ratio vertical right: 1.08 (mm/year)/(kJ/m)
- Ratio horizontal right: 0.87 (mm/year)/(kJ/m)

It is outstanding that the vertical ratio on the inner rail (left) is much higher than the outer rail. The following two curves could reveal if this is a pattern or just a coincidence in this particular curve.

The last verification step for this measurement concerns the aggregated T_γ distribution along with the wheels. For this step, the results of the wheel analysis are used (5. Those results are shown in Figure 6.19 and 6.20.

The measured wear patterns of the wheels could now be compared to the expected energy intake per wheel. However, the average intake per wheel per curve passage is only one half since there are two wheels per virtual axle. Since the flange decay is not tailored to one curve, no distinction could be made between the left and right sides. Because of this, the average wheel decay per axle based on the left and right sides was calculated first. Then, the expected energy intake per virtual axle from flange and tread contact was summed. The average flange decay is then divided by the expected energy intake per axle in kJ/m.

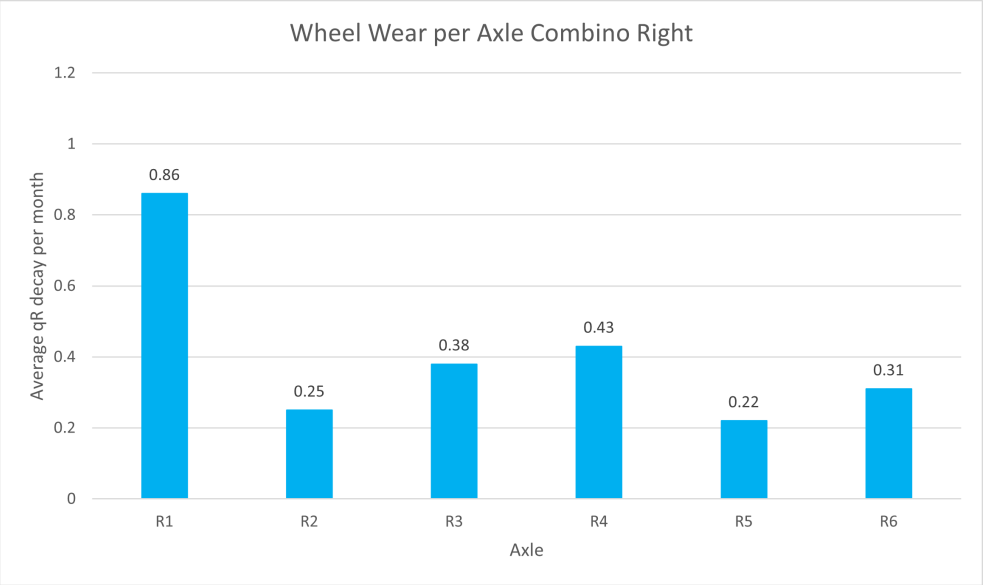


FIGURE 6.19: Average decay in flange angle per month for the right side of the Combino.

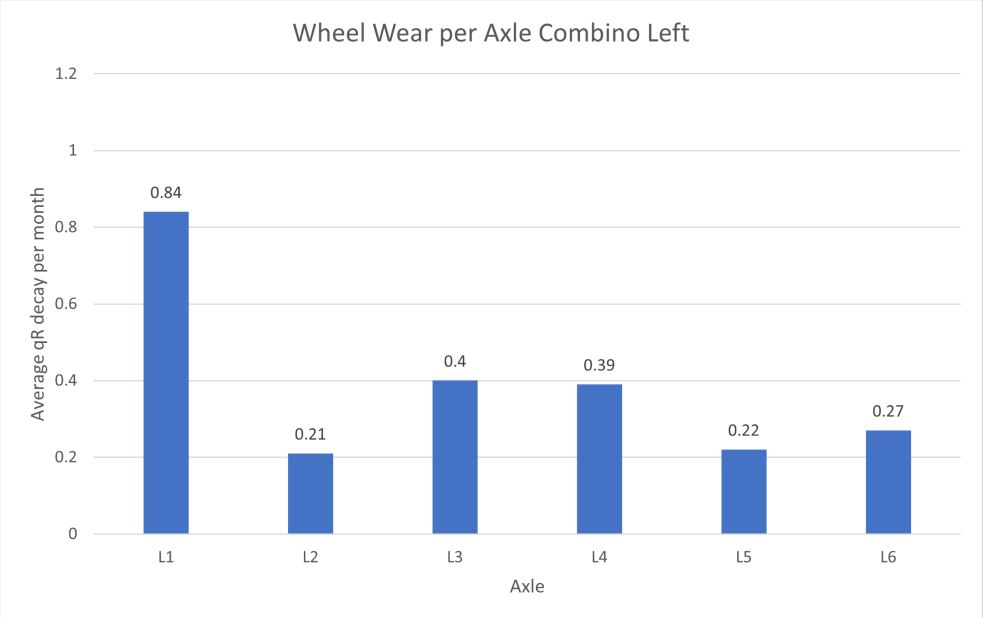


FIGURE 6.20: Average decay in flange angle per month for the left side of the Combino.

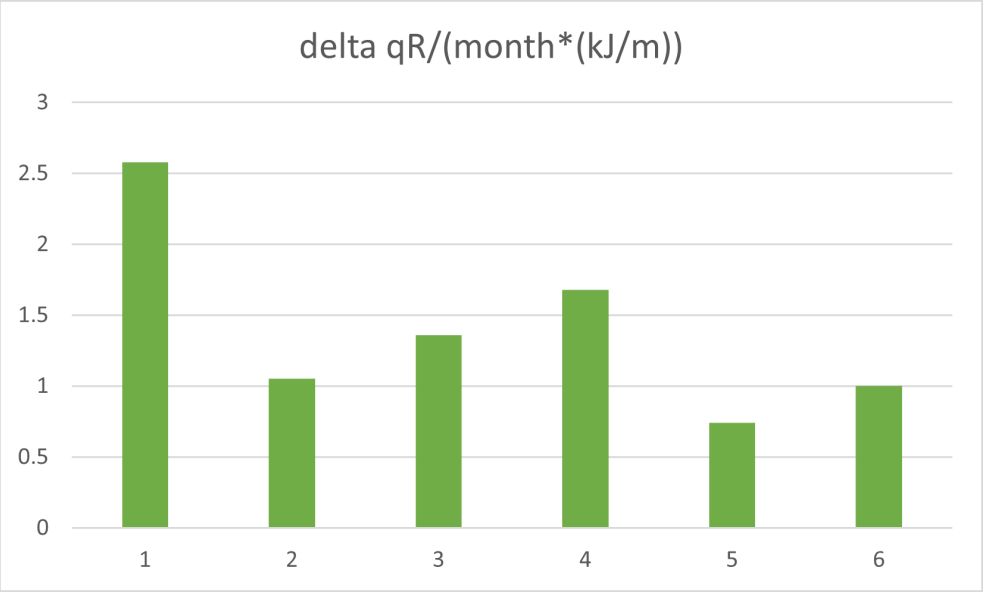


FIGURE 6.21: Average decay in flange angle per month per expected energy intake per wheel for the current curve: r25, v10, new profiles. y axis: decay per energy intake [delta qR/(month*(kJ/m))], x axis: axles.

Since no distinction between the left and right sides could be made from the flange decay measurements, the ratio is multiplied by 2 to obtain the ratio per wheel.

Figure 6.21 shows the results per virtual axle for this calculation. This graph is in a relative sense identical to the average flange decay per month per wheel. According to the simulations, this can be expected since the summed amount of dissipated energy per wheel did not differ that much. It has to be noted that this decay represents the whole network and not only the curve in consideration. Therefore, only based on those results no conclusion could be drawn about the validity of the aggregated distribution per wheel. Also, the relation between the dissipated energy and flange angle decay is unknown, complicating this issue. The flange contact may contribute to a larger relative extent to deterioration of flange angle. The high energy dissipation at the first wheels and the relative high qR decay on the first wheels support this hypothesis.

Next, the medium and gentle curves will be assessed. The result presentation and verification will be less detailed on these curves. Only essential differences in results and behaviour will be reported.

Medium Curve Simulation Results and Verification

Figure 6.22 and 6.23 present the aggregated results per wheel for the equivalent medium curve. The differences compared to the tight curve are shown. Now all outer first wheels of the bogies make flange contact. At the inner rail, the rear left wheels of the first and second bogie run the entire curve on the flange, while the rear left wheel of the last bogie mostly runs on the tread. The dissipated energy is more evenly distributed over the wheels than the tight curve. The aggregated sum of the T_γ equals 1404 J/m, while the sum of the tight curve was 3327 J/m. The amount of dissipated energy decreased by 58% on average, with a radius three times larger and a velocity two times higher.

The curve negotiation was different from the tight curve, as could already be expected from the aggregated results. The first bogie behaved comparably to the second bogie in

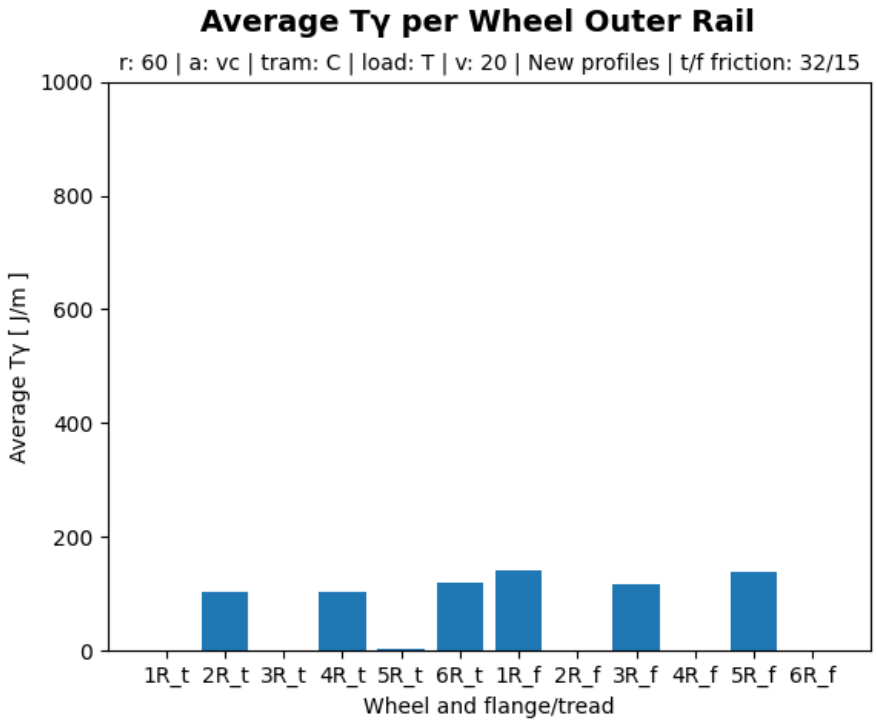


FIGURE 6.22: Aggregated results for the simulation at the outer rail representing a Combino negotiating a medium curve.

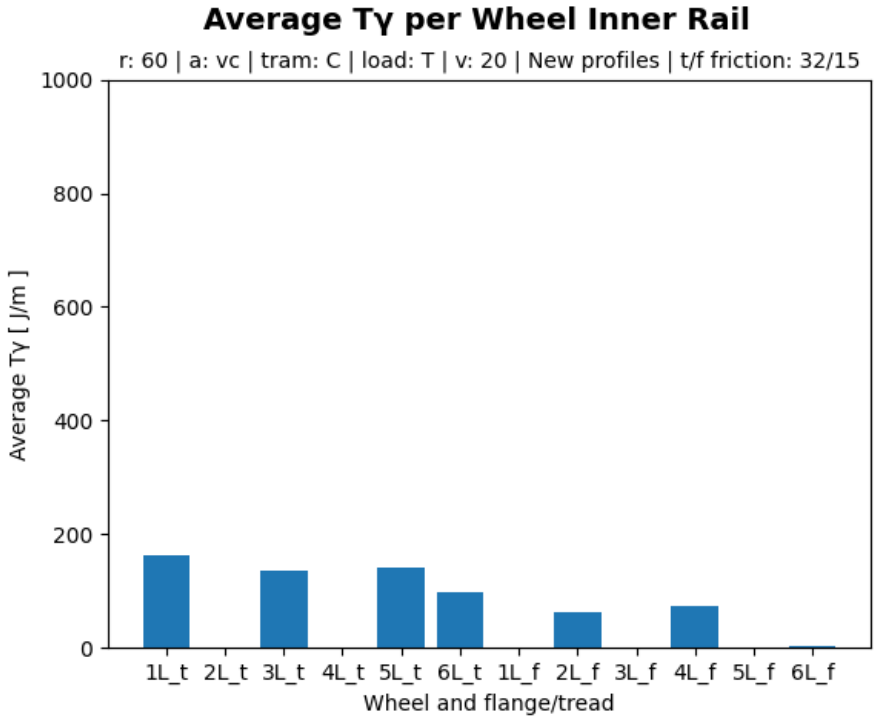


FIGURE 6.23: Aggregated results for the simulation at the inner rail representing a Combino negotiating a medium curve.

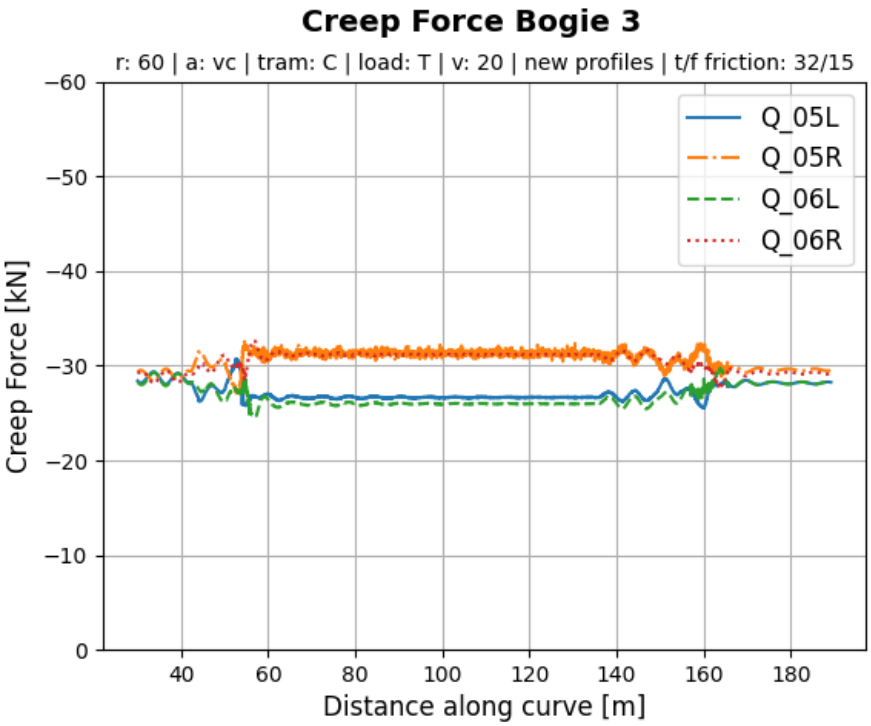


FIGURE 6.24: Creep forces of bogie 3 in the medium curve.

the tight curve, where the front wheels did have a clockwise angle of attack and the rear wheels did not have an angle of attack.

Figure 6.24 shows the creep forces for bogie 3, which was quite similar to the plot of bogie 2. Now, each bogie's rear and front-wheel have a clockwise angle of attack of the same magnitude. This difference is possible since the curvature is 2.4 times smaller than the tight curve. Figure 6.25 depicts the situation of bogie 2 and 3 schematically. Because of the smaller angle of attack and, in general, smooth creep lines, the overall curving behaviour seems to be more stable in this curve, which matches the expectations and dissipates less energy.

Again, the energy dissipation is distributed evenly along the curve, which complies with the profile measurements of this curve. The ratios for the wear per rate per energy, calculated with the profile measurements of 2020 and 2021, are as follows:

- Ratio vertical left: 1.02 (mm/year)/(kJ/m)
- Ratio horizontal left: 0.71 (mm/year)/(kJ/m)
- Ratio vertical right: 2.11 (mm/year)/(kJ/m)
- Ratio horizontal right: 0.71 (mm/year)/(kJ/m)

Those rates could now be compared with the rates of the tight curve which are presented again below:

- Ratio vertical left: 0.26 (mm/year)/(kJ/m)
- Ratio horizontal left: *unknown*
- Ratio vertical right: 1.08 (mm/year)/(kJ/m)
- Ratio horizontal right: 0.87 (mm/year)/(kJ/m)

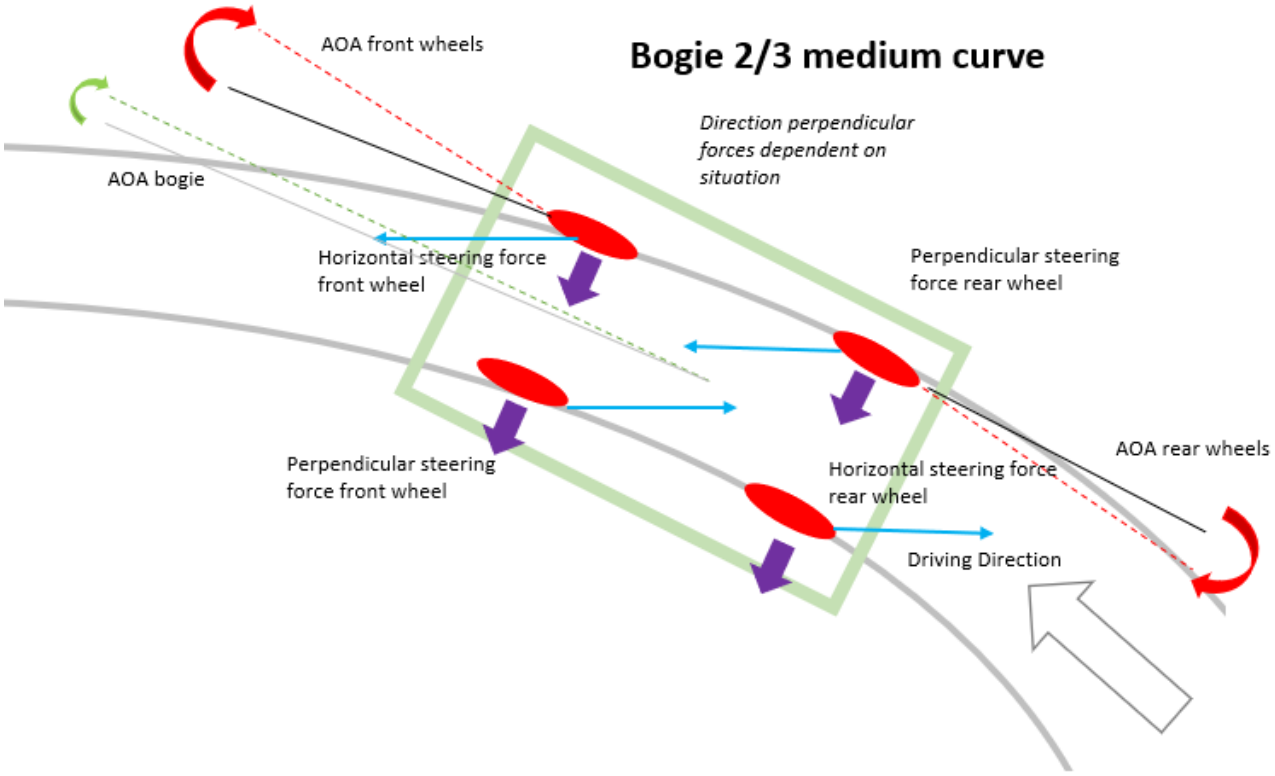


FIGURE 6.25: Schematic representation of bogie 2 and 3 at the middle curve.

However, the tonnage is not the same in both cases, thus the amount of dissipated energy per year taken by curves is not equal. According to the simulations, the comparisons could be simplified to mm/(J/m) units when it is multiplied with the total taken energy per curve. The number of passages per day on the tight curve is 132, which equals roughly 48180 passages per year. The total amount of passages per year for the middle curve equals approximately 36500.

The total amount of expected dissipated energy per year per side and tread/flange then equals:

Tight Curve

- Yearly dissipated energy tread left: 66.2 (MJ/m)/year
- Yearly dissipated energy flange left: 9.5 (MJ/m)/year
- Yearly dissipated energy tread right: 67.5 (MJ/m)/year
- Yearly dissipated energy flange right: 17.1 (MJ/m)/year

Middle Curve

- Yearly dissipated energy tread left: 19.7 (MJ/m)/year
- Yearly dissipated energy flange left: 5.1 (MJ/m)/year
- Yearly dissipated energy tread right: 11.9 (MJ/m)/year
- Yearly dissipated energy flange right: 14.5 (MJ/m)/year

A ratio could be made which in mm wear / dissipated energy since both values are yearly. It is expressed in mm/(GJ/m) (mm/($10^9 J/m$)).

Tight Curve

- Wear dissipation ratio vertical left: 5.44 mm/(GJ/m)
- Wear dissipation ratio horizontal left: *unknown*
- Wear dissipation ratio vertical right: 22.37 mm/(GJ/m)
- Wear dissipation ratio horizontal right: 18.13 mm/(GJ/m)

Middle Curve

- Wear dissipation ratio vertical left: 27.92 mm/(GJ/m)
- Wear dissipation ratio horizontal left: 19.61 mm/(GJ/m)
- Wear dissipation ratio vertical right: 57.98 mm/(GJ/m)
- Wear dissipation ratio horizontal right: 19.31 mm/(GJ/m)

Further research could help to understand the differences which emerge in those ratios. Based on those two curves, it is complex to make the correct interpretation since either the simulated energy by the model could be inaccurate, wear rates could vary in a non-linear way or unknown factors could have a significant role.

Regarding the tight and middle curves, the middle curve wears faster per energy dissipated than the tight curve. Especially on the right side, the tread tends to wear faster per expected energy compared to the flange. This difference could be because of underestimating the dissipated energy at the tread during flange contact. Then it makes sense that this effect occurs mainly at the right side since the amount of energy transferred in

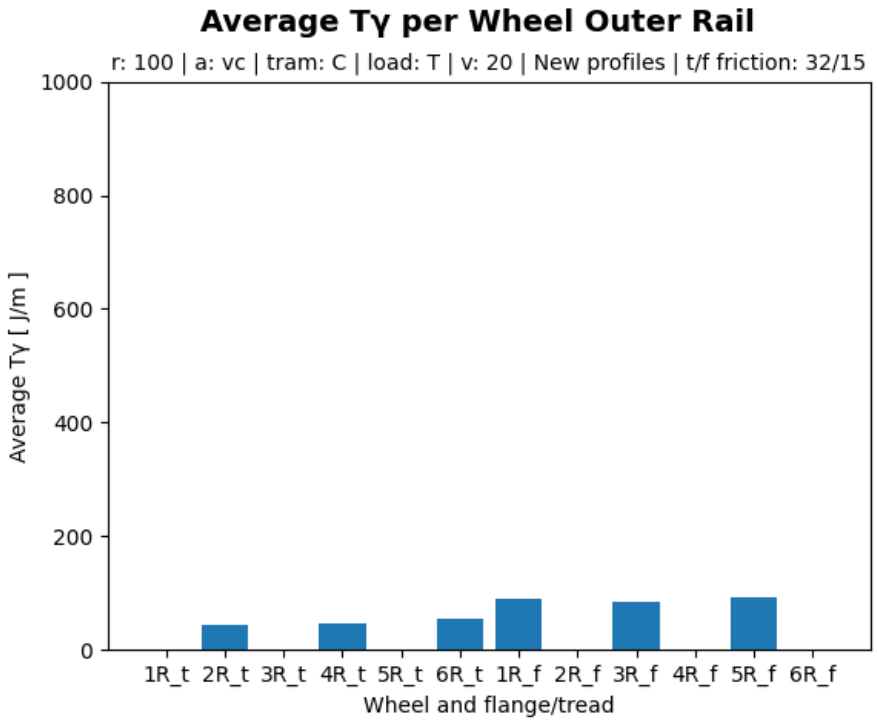


FIGURE 6.26: Aggregated results for the simulation at the outer rail representing a Combino negotiating a gentle curve.

the model via the flange is higher at the right side since it is the outer rail. However, the amount of two curves is too small to draw conclusions based on these results.

Gentle Curve Simulation Results and Verification

Figure 6.26 and 6.27 present the results of the equivalent simulations with the gentle curve. The right wheels at the front and left wheels at the rear of each bogie run in flange contact. Most energy dissipation occurs at the front wheels of each bogie. The total amount of dissipated energy equals 1166 J/m compared to 1404 J/m in the middle curve and 3327 J/m in the tight curve.

Taking the gentle curve as reference, the tight curve is 75% smaller and has 2161 J/m more dissipation, which equals 28.8 extra J/m per radius % decrease. The same calculation for the middle curve in relation to the gentle curve results in 6.0 extra J/m per radius % increase. This result means that the amount of dissipated energy increases non-linear with decreasing radius, even while the velocity at the tight curve was half the velocity at the middle and gentle curve.

The position of the first 2 bogies are equal to the position presented in figure 6.8, the last bogie behaves like the bogie in Figure 6.25. The overall magnitude of the creep force difference is small compared to the magnitude with the middle and especially the tight curve. This lower creep force translates into lower values of energy dissipation, which is also evenly distributed along the curve, and the measured wear is evenly distributed over the curve.

The calculated wear per dissipated energy values are as follows:

- Wear dissipation ratio vertical left: 4.95 mm/(GJ/m)

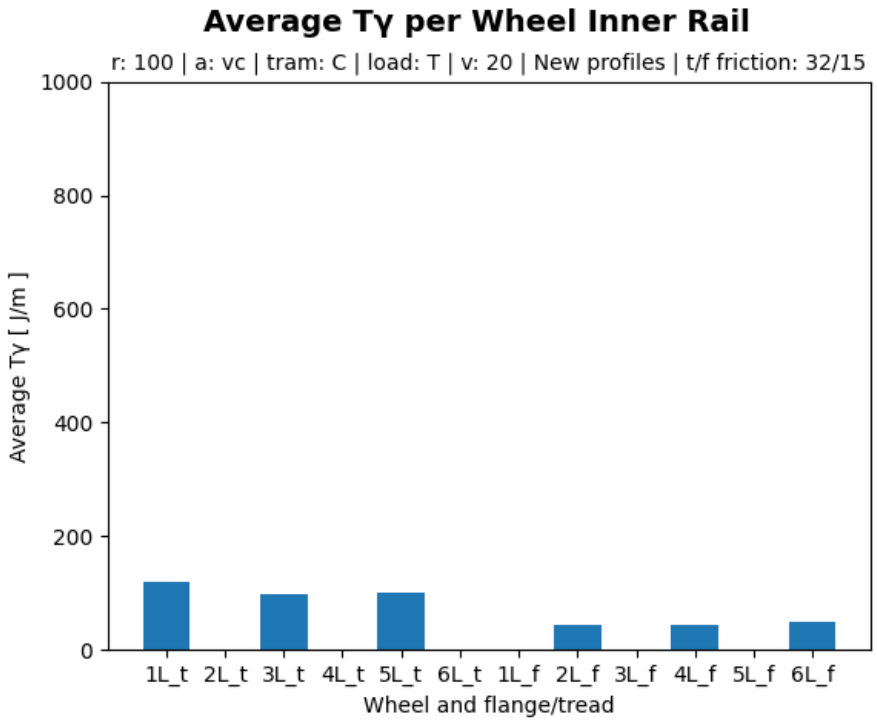


FIGURE 6.27: Aggregated results for the simulation at the inner rail representing a Combino negotiating a gentle curve.

- Wear dissipation ratio horizontal left: *unknown*
- Wear dissipation ratio vertical right: 53.19 mm/(GJ/m)
- Wear dissipation ratio horizontal right: 13.08 mm/(GJ/m)

Again, the amount of wear per estimated energy dissipation is outstanding high on the outer tread. This difference might be the model underestimates the amount of energy dissipated at the right tread. Because during flanging, the model assumes one point contact with new wheels. As a result, no energy dissipation is calculated at the tread during flanging. The amount of horizontal wear tends to be more in agreement with the tight and middle curve ratio's.

Next, some simulation variants will be presented based on the principal simulations with changed parameters.

6.2.4 Simulation Variants

Besides the three principal simulations based on the data from reality (6.2), also simulation variants were made to assess the behaviour of the model and results in different circumstances. Per variant, only the changed input compared to the principal simulation and changed outcomes compared to the principal simulations of the concerned curves will be mentioned. The following simulation variants were made:

Variants tight curve:

- braking
- loaded vehicle
- no flange lubrication

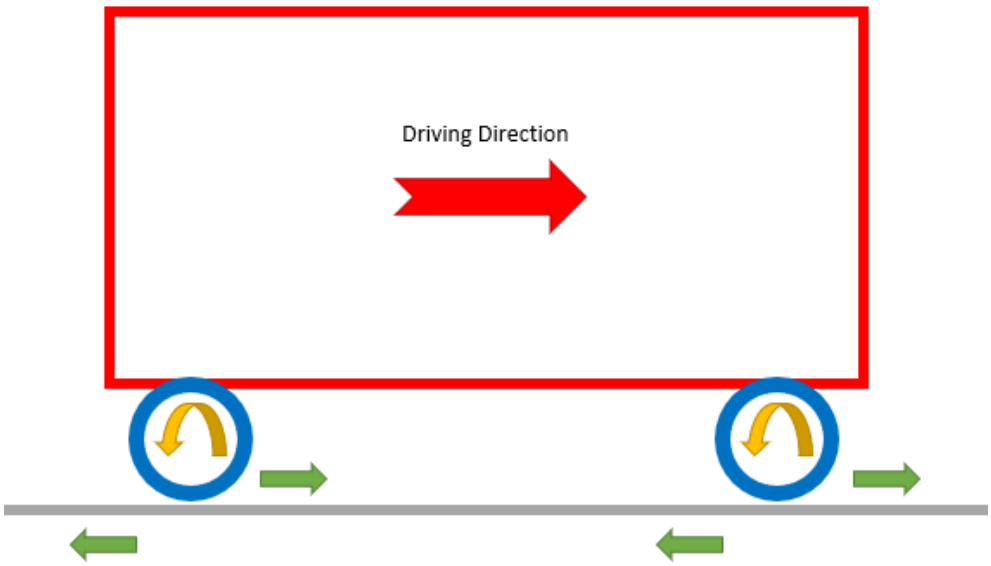


FIGURE 6.28: Tram vehicle and global wheel - rail contact forces, in yellow the extra pitch moment added to simulate the braking.

- worn wheels
- worn rails
- increased velocity
- CAF Urbos 100

Variants middle curve:

- settlement after bridge

Variants tight curve:

- no variants

The following parts describe each variant and the outcomes.

Braking

This simulation is a variant of the principal tight curve simulation. It is aimed to simulate the effect of braking while negotiating a curve. The simulation is performed by adding an extra pitch moment to each wheel to simulate the braking. This pitch moment was specified with an external force file added to the simulation. By iteration, a pitch moment was found that made the tram decelerate from 15 kph at the start of the curve to 5 kph at the end of the curve. Figure 6.28 shows in yellow the extra pitch moment added to all wheels to simulate the braking, the torque per wheel leading to the desired deceleration was -0.46 kNm.

The dissipated energy on the front bogie increased by approximately 3-4%. This percentage makes sense since a torque of -0.46 kNm will generate an extra creep force in the order of 1.5 kN, given a wheel diameter of 0.6 m. During negotiating in the principal simulation,

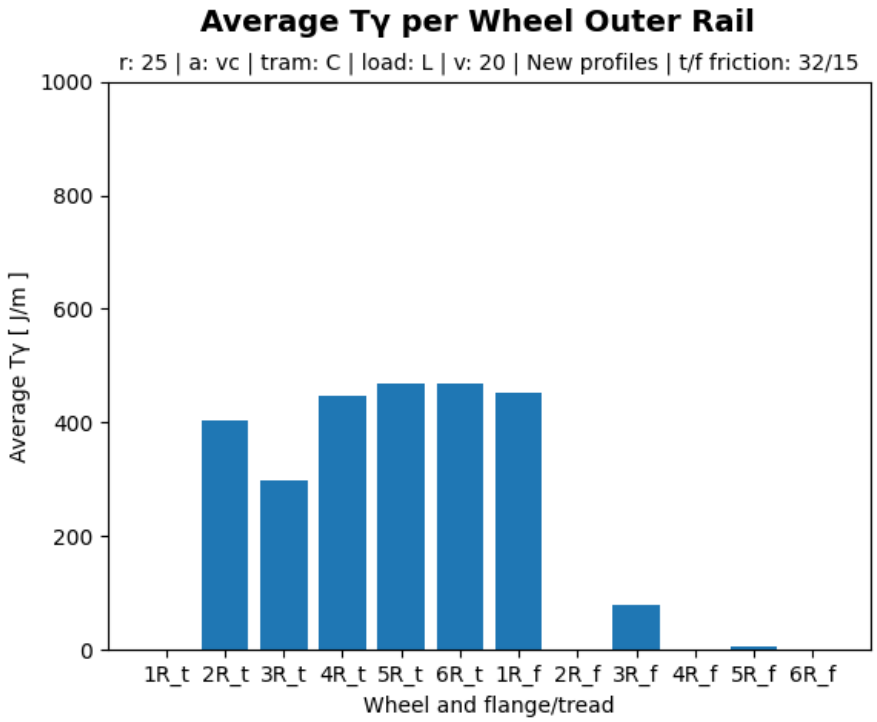


FIGURE 6.29: Aggregated results for the simulation at the outer rail representing a loaded Combino negotiating a tight curve.

the creep force was in the 27-37 kN range. An extra creep force of 1.5 kN would indeed increase creep force in the 5% range. Due to technical problems, the second and third bogie results could not be adequately recorded.

It was decided to not include the braking in the parametric simulations and the energy estimation model to limit the complexity and size. The braking was not included because of the relatively small increase of T_γ and the uncertainty regarding the model reliability of this complex matter. Furthermore, data about acceleration is made available with the velocity analysis in chapter 4, although the reliability of the acceleration estimation is considered premature. The velocity model should have given a more detailed and validated acceleration output to include acceleration in the energy estimation model.

Loaded Vehicle

Simulations with a loaded vehicle in the tight curve were performed to assess the effect of a loaded vehicle. Figure 6.29 and 6.30 show the results. The overall weight is expected to increase, which will adversely affect the amount of wear generation. However, the vehicle's centre of mass will be lower, decreasing the moment of the vehicle on the rails, which is expected to have a favourable effect on wear generation. The simulation was performed by selecting a vehicle model with all 55 seating places occupied. Also, a vehicle model was available with all standing places occupied, with four persons per square meter. The vehicle occupation analysis turned out that no track exists where the average occupation exceeds 55 persons per vehicle. Therefore, the loaded vehicle model with seating places occupied was selected.

The general distribution of aggregated T_γ on the outer rail was comparable to the principal simulation. The values of dissipated energy increased significantly at the tread. The increase at the tread was 40%, while the growth at the flange was about 10%. This increase

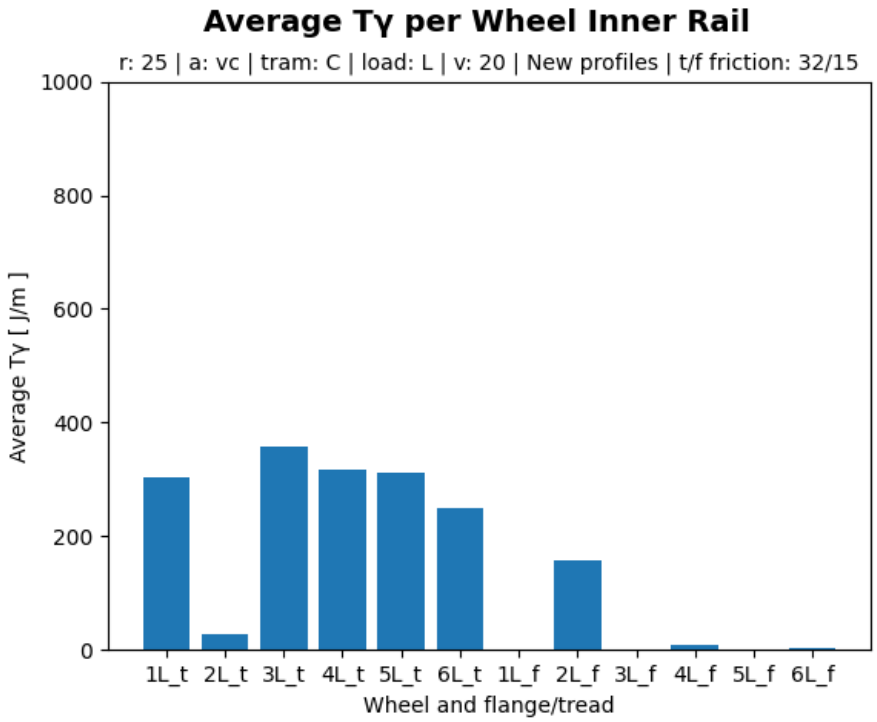


FIGURE 6.30: Aggregated results for the simulation at the inner rail representing a loaded Combino negotiating a tight curve.

makes sense since a rise in weight will mainly influence the vertical force transmission. At the inner rail also the general distribution was comparable with a significant increase of on average 60% at the inner rail tread.

The creep force plots did not change the overall curving behaviour from the principal case. The creep force on the straight was already 8 kN larger than an empty vehicle. The front wheels of the first bogie endured a more considerable creep force difference than the principal simulations, while the difference at the rear wheels of the first bogie was almost zero. This difference is possibly a result of a larger overall angle of attack of the bogie since more mass is pushing the bogie straight while it has to follow the curve. Also, the steady-state creep force at the other bogies increased since a more significant portion of tread contact is concentrated at the inner rail. The results suggest that the weight of the mass increased shifted to the inner rail, but further validation and analysis are needed.

The total dissipated energy per distance unit increased by 32%, while the mass only increases by approximately 10% when 55 passengers load the vehicle. The mass increase led to an increase of creep force difference in the 30-40% range, which is closer to the observed variations in the energy dissipation. Nevertheless, it was decided to include the vehicle loading in the energy estimation and parametric simulation. The model behaviour with loaded vehicles under different circumstances is investigated further, and accurate data on the average vehicle occupation enables inclusion it in the estimation model.

No Flange Lubrication

In the principal simulations, flange lubrication is assumed by choosing a friction coefficient of 0.15, while the friction coefficient on the tread is taken at 0.32. In practice, 50% of

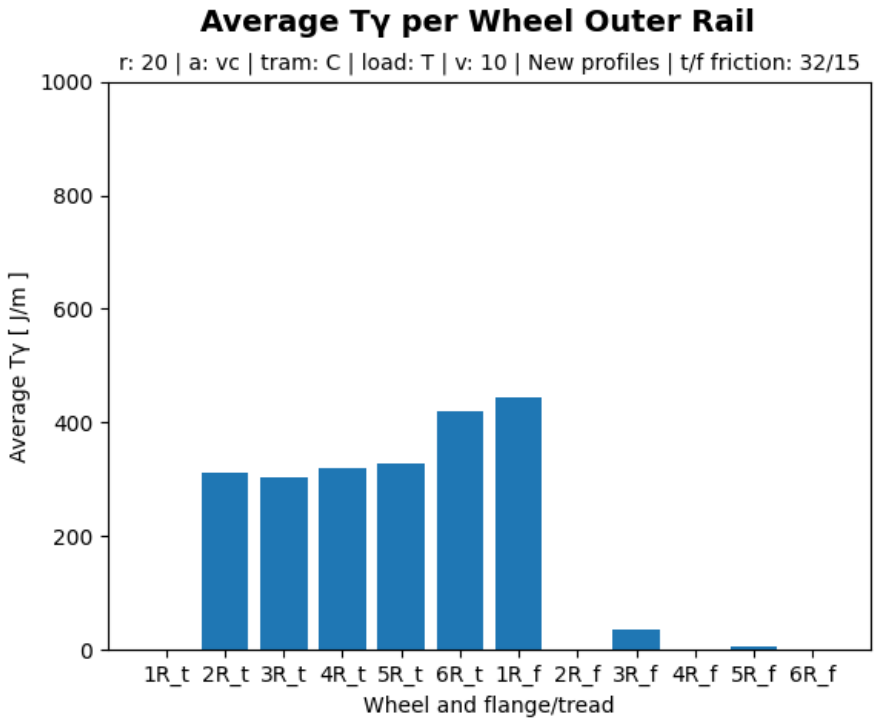


FIGURE 6.31: Aggregated results for the simulation at the outer rail representing a Combino negotiating a tight curve.

the trams have flange lubrication enabled and on some curves, especially near route endpoints, wayside lubrication devices are installed. It is assumed that the leftovers still lubricate the flanges at the non-lubricated vehicles from the trams with lubrication enabled. It is challenging to determine accurate friction coefficients for each situation. Therefore, the aim is to keep the coefficients constant as much as possible to compare differences when other parameters change. The simulation with an increased flange friction coefficient to 0.32 is intended to assess the model behaviour and sensibility for a changing friction coefficient.

The resulting increase in dissipated energy at the flange was proportional to the rise in the friction coefficient. An interesting change was observed at the second bogie, now the outer rail first wheel and inner rail rear wheel of the second bogie mostly negotiated in flange contact, compared to mostly tread contact in the principal case. The new flange contact at the second bogie suggests a change in running behaviour, which is remarkable since only a wheel-rail contact property changed.

It was decided to not include the altered friction in the parametric simulations because of the unknown reasons for this result and uncertainty about friction coefficients in general. Instead, the resulting mm/(GJ/m) from the energy estimation and measurement comparison per curve could be used to observe possible deviations at curves after the wayside lubrication devices.

Worn Wheels

The influence of worn wheels was only simulated with radius increments of 10 meters. Therefore, the simulation results with a curve radius of 20 meters are considered here. Figure 6.31 and 6.33 shows the reference aggregated energy dissipation per wheel for a curve with radius 20 m and new wheel profiles. Figure 6.32 and 6.34 show the simulation

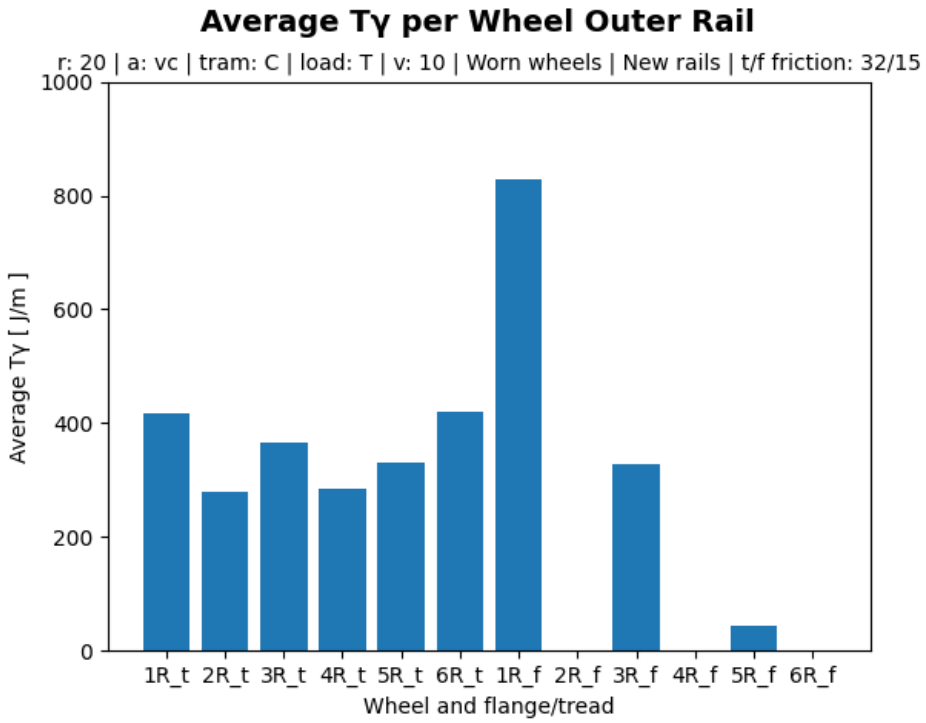


FIGURE 6.32: Aggregated results for the simulation at the outer rail representing a Combino with worn wheels negotiating a tight curve.

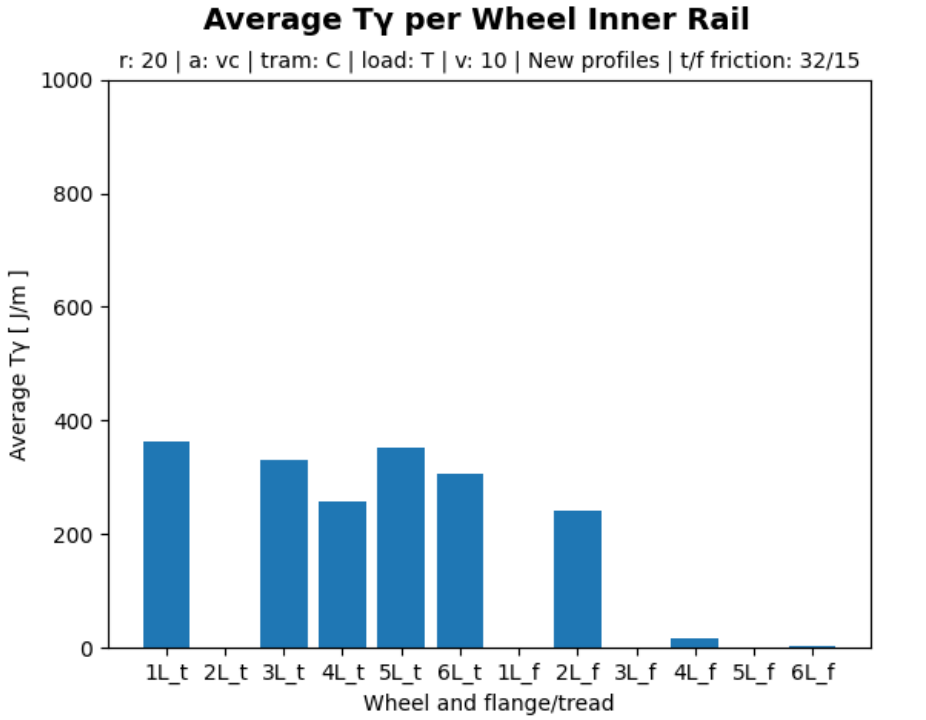


FIGURE 6.33: Aggregated results for the simulation at the inner rail representing a Combino negotiating a tight curve.

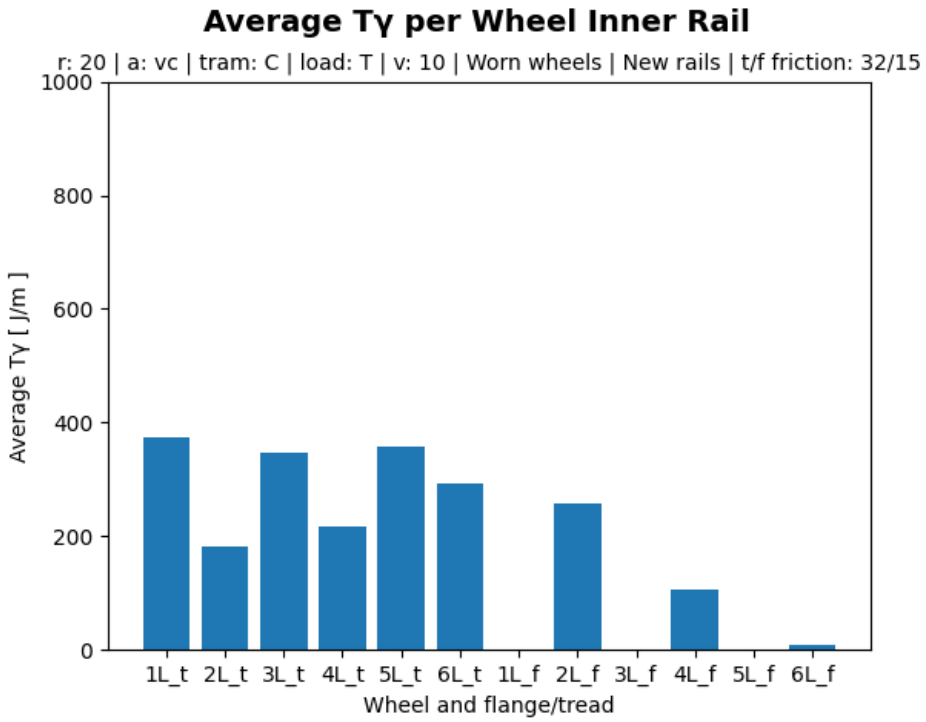


FIGURE 6.34: Aggregated results for the simulation at the inner rail representing a Combino with worn wheels negotiating a tight curve.

results with the worn wheel profiles. At the outer rail, the increase at the first wheel is striking, but the dissipation at the third wheel increases. For both the first and third wheel at the outer side, both tread and flange contact significantly influence this case.

The energy plots revealed that the first and third wheel at the outer side ran in two-point contact because of the increased flange steepness. The increase of energy dissipation is dramatic compared to the theoretical wheels. Still, it is believed that the simulation model underestimates the amount of dissipated energy at the tread with new wheels. Also, at the inner rail, the second and fourth wheels now run in two-point contact, confirmed by the energy plots. In all cases, the two-point contact lasted along the whole curve. The creep force plots did not show significant differences for this simulation variant.

The summed amount of energy dissipation in the reference case with radius 20 was 4040 J/m. With the worn wheels, the summed amount equals 5440 J/m. This sum equals an increase of 34%. Since the effect of worn wheels seems to be large and adverse, it was decided to further investigate the running behavior with worn wheels in the parametric simulations.

Worn Rails

Figure 6.35 and 6.36 show the simulation variants with the worn rail. This simulation is done with a curve radius of 20 meters. The reference results with new profiles could be found in Figure 6.31 and 6.33. The simulation had a worn rail model with horizontal wear of 3 mm at the outer side. At the outer rail, especially the third wheel endures higher dissipation at the tread. At the inner rail, the dissipation does not show major differences.

The energy plots only reveal two-point contact at short time intervals for the second wheel at the inner rail. The first wheel at the outer side runs the first 5 meters at the tread and

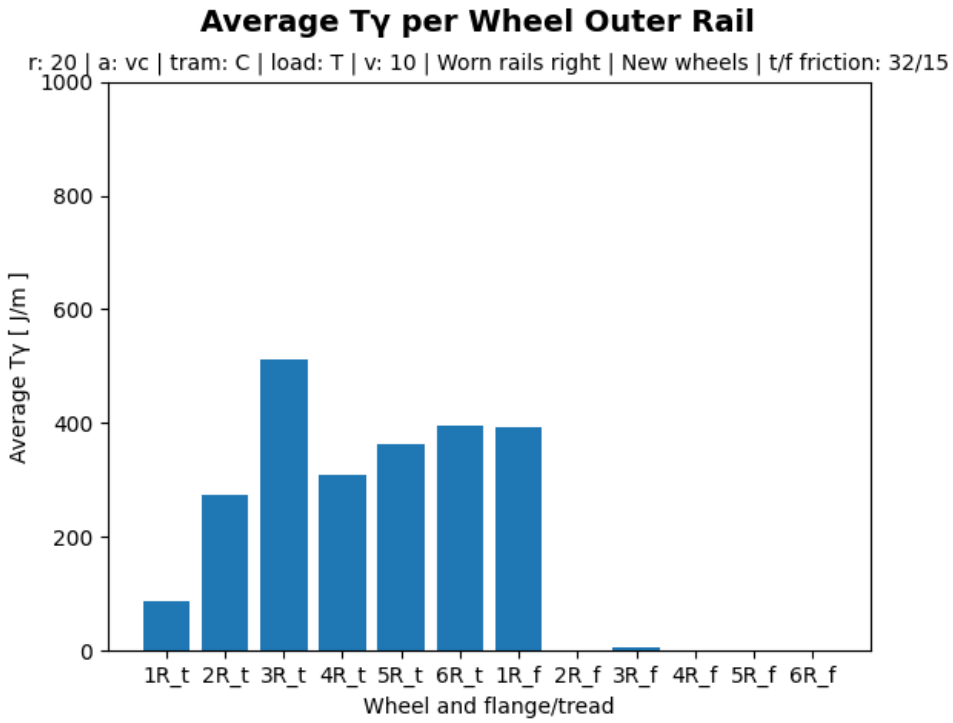


FIGURE 6.35: Aggregated results for the simulation at the outer rail representing a Combino with worn rails negotiating a tight curve.

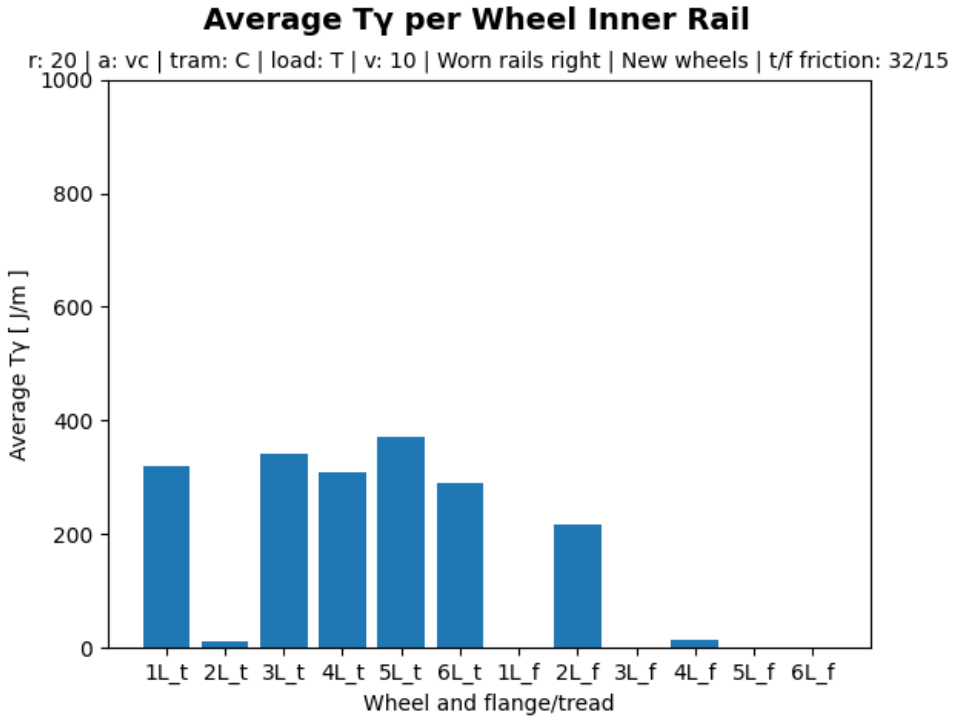


FIGURE 6.36: Aggregated results for the simulation at the inner rail representing a Combino with worn rails negotiating a tight curve.

then switches to flange contact for the remainder of the curve. The distance between the flange and side of the rail is increased on the outer side because of the rail wear. Therefore, the wheels must travel a more considerable distance on the tread in the lateral direction to make flange contact. The total energy dissipation increased by 5% compared to the reference case with a radius of 20 meters.

The simulation was also performed with a rail model with 3 mm wear on the inner rail, the aggregated T_γ results per wheel did not show significant differences in this case. Also, the summed average values from the wheels were equal to the reference case with radius 20 m.

The influence of worn rail is further investigated in the parametric simulations.

Increased Velocity

Another simulation variant was aimed to research the effect of larger velocities. The principal tight curve simulation (radius 25 meters) was adjusted from 10 to 20 kph. The summed average dissipated energy was 4359 J/m, compared to 3327 J/m in the case of a velocity of 10 kph, which is an increase of 31%. The distribution of dissipated energy over the wheels stays equal compared to the principal simulations. The increase was observed over all wheels. Only the third wheel at the outer sides has an increased dissipation at the flange at the expense of the tread.

The creep force plots showed that the angle of attack for all wheels now had the same sign. The increased velocity seems to push the vehicle more to the outer side and increases the yaw movement. The difference in creep forces between the outer and inner rail also increased towards more extensive yaw rotations.

The increased velocity is considered in the parametric simulations and the energy estimation model since the effects seem to be important. Accurate velocity data is made available by this research.

CAF Urbos 100

The principal tight curve simulation was also performed with an empty CAF Urbos 100 tram, the next generation of trams after the Siemens Combino trams. The distribution of dissipated energy along the wheels did not change except for the outer tread of the fifth wheel, where the dissipated energy increased disproportionally with the Urbos 100. The total dissipated energy per distance unit increased by 17% compared to the Siemens Combino under the same conditions. This increase in energy dissipation was expected since the suspension stiffness of the Urbos 100 is higher.

Since the increase of energy dissipation is significant, and the amount of Urbos 100 trams will increase in the future, the influence of the different tram types will be considered in the parametric simulations and the energy estimations.

Settlement After Bridge

A variant was made with a settlement after a bridge for the middle curve simulation. This phenomenon is commonly seen in Amsterdam: the ground settles over the years while the many bridges have a foundation on piles that do not settle at the same velocity. This mechanism results in a visible track settlement after the bridge, which adversely affects wear. A track file (see D) representing the middle curve was made with the height position

of the track following a sinusoidal curve, which represents the bridge and the settlement after the bridge.

The results showed that it is difficult to correctly model displacements and forces in the height direction; the model is optimised to capture lateral displacements. Alternatively, the wear per energy ratios based on the energy estimations could be checked at curves with settlements, to deduce any adverse effects of this phenomenon. In conclusion, this variant is not considered in the subsequent phases of the research.

6.3 Parametric Simulations

6.3.1 Introduction Parametric Simulations

This section presents the parametric simulations performed with the VAMPIRE software and the vehicle models of the Siemens Combino and CAF Urbos 100, made by DEKRA rail. The details concerning the simulation models and method can be found Appendix AppendixD.

The parametric simulation sets are chosen based on the results of the three curves analysis and the simulation variants. The outcomes of the parametric simulations will be the basis for the energy estimation model, this model estimates the energy per curve on the network based on curve specific parameters and the parametric simulation outcomes. Then the estimated energy will be compared to measured profile changes. The coverage of the results and verification of the parametric simulations will be more comprehensive than the tree curve analysis since it is assumed that the general model behaviour and accuracy are known now.

The subsection after this introductions lists which parameters were changed. Then, the extra post-processing steps compared to the three curve simulations are clarified in the following subsection. Finally, the results of the parametric simulations will be discussed.

6.3.2 Simulation Sets

In total, over 600 different simulations were done. Those simulations are fictitious situations where one parameter is changed to assess the influence. The main parameters which are changed in the parametric simulations:

- radius
- velocity
- vehicle loading
- new wheels / worn wheels
- vehicle type
- new rails / worn rails
- friction

All simulations do have a curve which is a quarter of a circle. The curve length does not influence the outcomes directly since the average energy dissipation (T_γ) per wheel per tread/flange is calculated. On every curve, zero cant is applied, which matches the situation in reality. The level of each curve is equal at all places. In other words, there are no height differences. This setting does not match reality, but it would make the process too

complex, and the model seemed to be less accurate when height differences were incorporated. Also, tram acceleration is not considered because the model accuracy was also not apparent, and it would make the number of required simulations too large. Unless mentioned otherwise, the used wheel profiles were new, and the used rail profiles were of the 60R2 type in a new state. Also, the tread friction was kept at 0.32 and the flange friction at 0.15. All fictive curves are going to the left in the driving direction. The difference between curves going to the right or the left was not assessed.

Basis per Simulation Set

Per set, the velocity was changed with increments of 10 kph, starting at 10 kph and ending at 40 kph. Per velocity, a separate simulation was performed per radius, which began at 20 meters and ended at 100 meters with a step increment of 10 meters. Speeds outside this range were rarely observed on curves with radii smaller than 100 meters, which followed from the velocity analysis (4. The velocity of 40 kph was only post-processed for curves with a radius of 50 meters or larger. This velocity was rarely observed at smaller curves.

Those basis of simulations is then run with the following models:

- Empty Combino, new rails and wheels
- Empty Urbos, new rails and wheels
- Loaded Combino, new rails and wheels, no 40 kph
- Loaded Urbos, new rails and wheels, no 40 kph
- Empty Combion, new rails and worn wheels
- Empty Urbos, new rails and worn wheels
- Empty Combino, worn rails 3 mm horizontally both sides, new wheels
- Empty Urbos, worn rails 3 mm horizontally both sides, new wheels
- Empty Combino, 3 mm wear horizontally left side, new wheels
- Empty Combino, 3 mm wear horizontally right side, new wheels
- Empty Combino, worn rails 3 mm horizontally both sides, worn wheels

A separate simulation set was performed to verify the results with changed friction. The results of this analysis were not taken into further consideration, since it would be difficult to input an altered friction per curve in the energy estimation model because of the uncertainty regarding the friction coefficient. However, the effects of modified friction on the model behaviour and wear are an interesting subject for further research.

Appendix D provides the post-processing method of the parametric simulations.

6.3.3 Parametric Simulation Results

This section is aimed to provide a general overview of the main results from the parametric simulations. Graphs are shown from the empty Combino with new profiles for all contacts and worn wheel profiles for contacts at the outer rail only.

Regarding the results for the flange at the outer rail, as shown in Figure 6.37, the summed amount of dissipated energy increases sharply at tight curves. The same is also the case for the tread, shown in Figure 6.38. The summed amount tends to increase exponentially

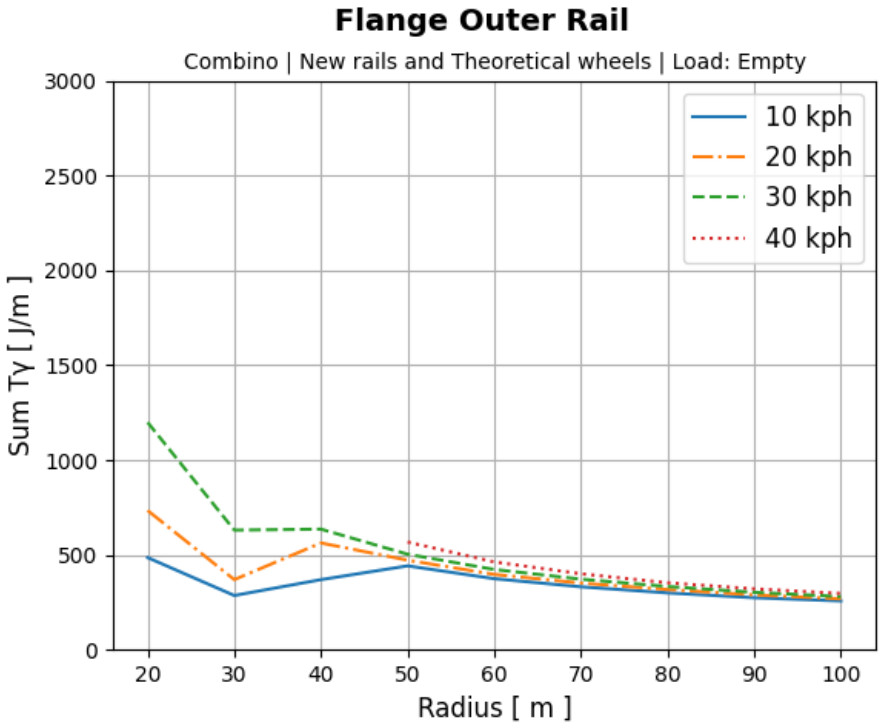


FIGURE 6.37: Aggregated results for an empty Combino outer rail flange.

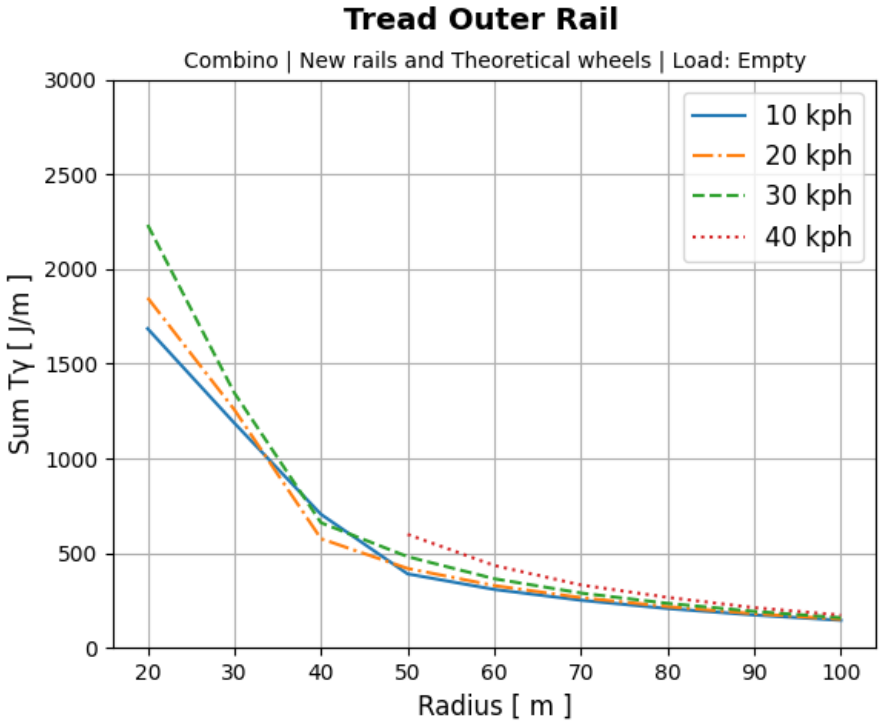


FIGURE 6.38: Aggregated results for an empty Combino outer rail tread.

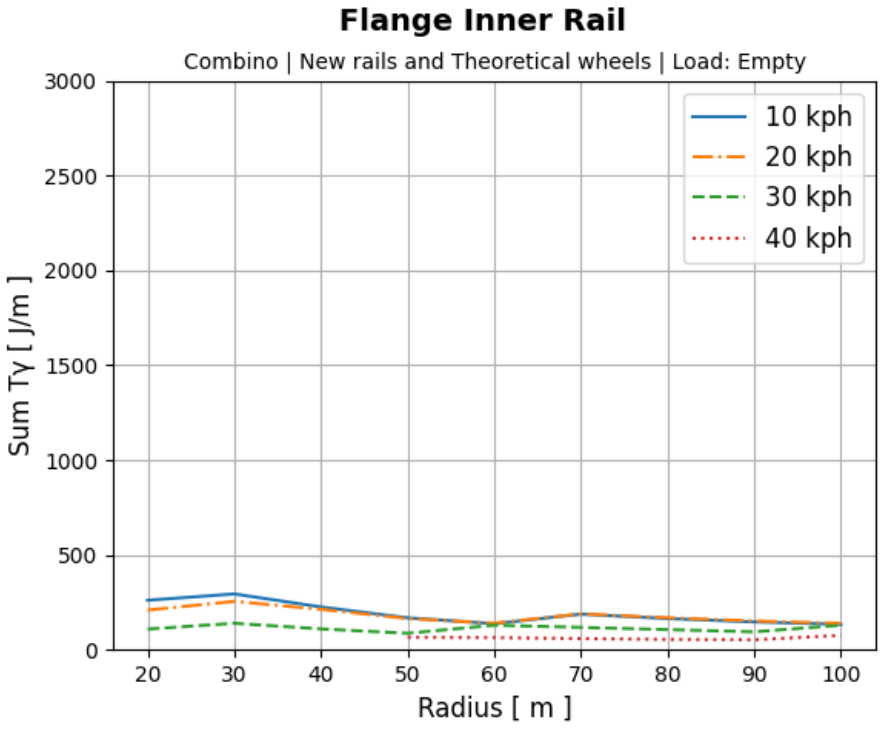


FIGURE 6.39: Aggregated results for an empty Combino inner rail flange.

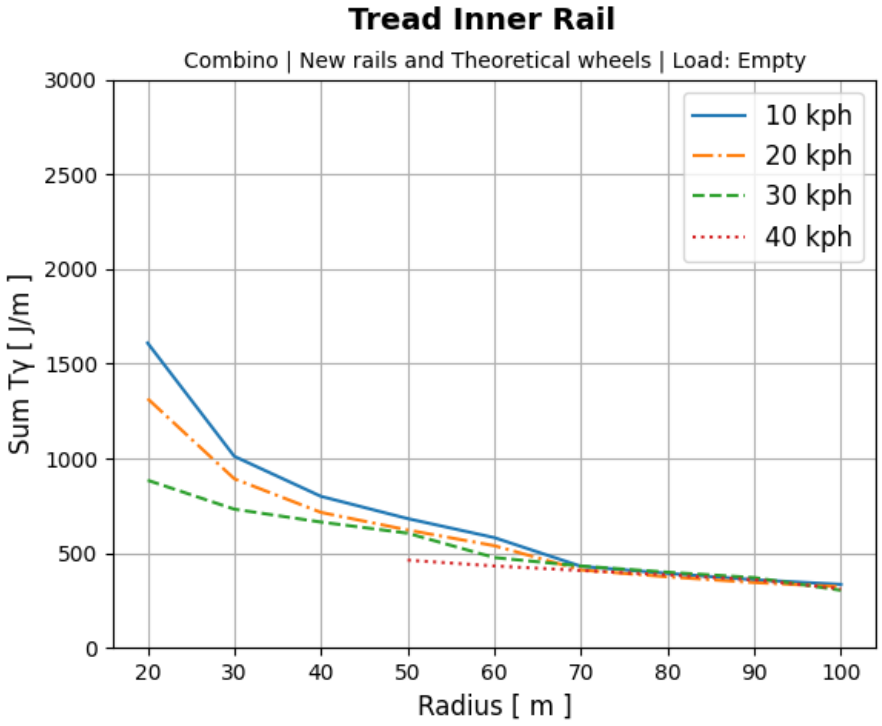


FIGURE 6.40: Aggregated results for an empty Combino inner rail tread.

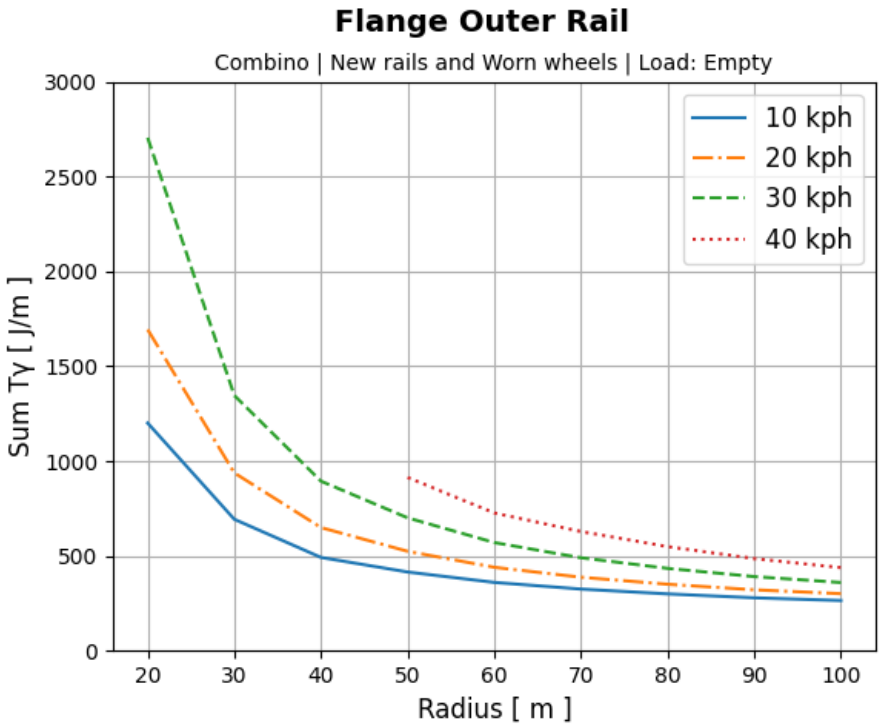


FIGURE 6.41: Aggregated results for an empty Combino with worn wheels outer rail flange.

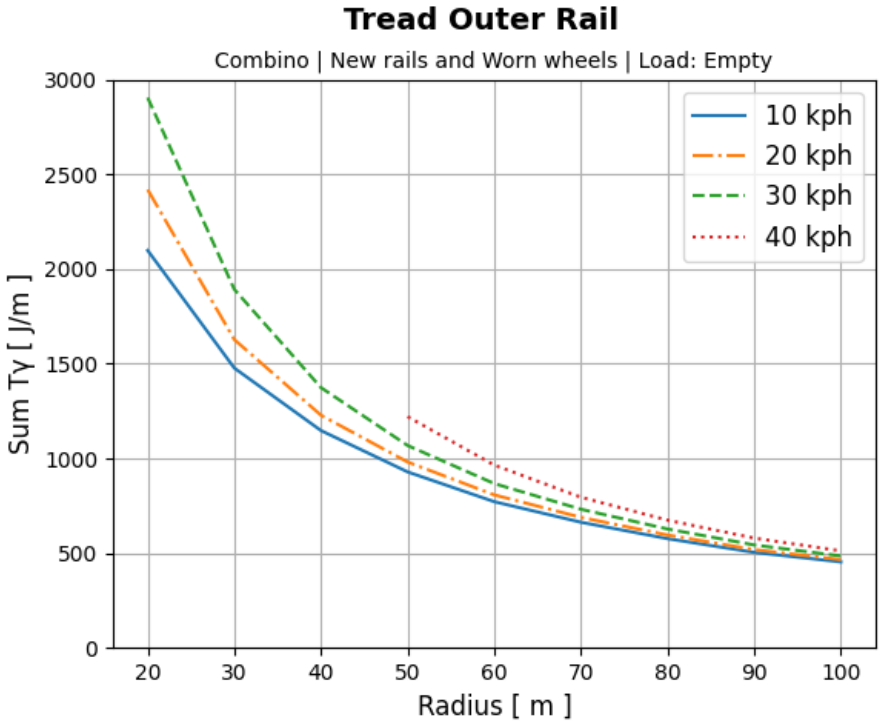


FIGURE 6.42: Aggregated results for an empty Combino with worn wheels outer rail tread.

at the tread when the curve radius decreases. Also, as curves become tighter, energy dissipation becomes more dependent on velocity, especially for the flange. At the inner rail, the velocity dependence is reversed. This difference makes sense since the forces will be more concentrated on the outer rail at larger velocities because of centrifugal effects.

In general, worn wheels tended to have the most adverse effects. Because of this, some graphs of the results with worn wheels are added. Regarding the other results not shown here, the increases were largely in accordance with the results obtained during the three curves analysis and its variants. Unfortunately, the simulation results with worn rails did not match the quality of the other cases. Mainly because of simulation that did not converge to an answer and did not give any results. Therefore, it was decided not to take the rails' wear degree into account in the energy estimation model.

6.4 Conclusion Simulations

With the help of the models and software already available at DEKRA, simulations were done to research which parameters are essential for the curving behaviour of trams. First, three existing curves on the network were analysed and verified. It turned out that the amount of dissipated energy increases exponentially when the curve radius decreases, according to the simulations. The amount of dissipated energy was evenly distributed along the curve, matching the rail profile measurements. No watertight validation of the results was possible because of the small number of curves and missing knowledge on maintenance history. However, preliminary results suggest that the model underestimates the amount of wear on the tread, especially the outer tread.

The simulation variants on the three curves revealed three parameters that had a significant adverse effect on wear: vehicle loading by passengers, increased velocity and increased flange steepness of the wheels. Another finding was the change in curving behaviour when the coefficient of friction was raised, which was against the expectations. It was tried to simulate the effect of acceleration and track settlements. It turned out to be quite complex to model this accurately. Therefore, those factors were not taken into further consideration.

Finally, over 600 parametric simulations were performed to capture the estimated amount of energy dissipation for most circumstances in practice. The parametric simulations simulated fictive quarter curves with stepwise increased radii and velocities. In addition, the following parameters were also changed: tram type, wear degree wheels and rails and vehicle loading. The parametric simulations with the worn rails were not satisfying. The other results are used as a basis for the energy estimation model.

Chapter 7

Energy Estimation Model

7.1 Introduction

This section provides essential information on the energy estimation model. After the specification of the main objectives of the model, a short model description is given and thereafter, the input and output of the model are specified.

7.1.1 Model Aim

Based on the parametric simulation results, the model aims to estimate dissipated energy (T_γ) values per curve on the whole network. The model estimates T_γ levels on four contact surfaces: the tread contact surfaces on both rails and the flange contact surfaces on both rails. Chapter 6 provides the physical meaning of dissipated energy expressed in T_γ.

The model estimates the total energy dissipation per contact surface during one *statistical tram passage*. This number is a weighted combination of all considered ways a tram could negotiate a curve based on the curve specific usage characteristics. Section 7.2 provides the method used to obtain the *statistical tram passage* energy dissipation values. Besides the dissipation of one passage, the model also determines the yearly total dissipation per contact surface, based on the number of tram passages. The annual amount of dissipated energy could be compared with the annual amount of measured volumetric wear.

The estimated energy dissipation per curve, combined with the volumetric wear per amount of dissipated energy, could be the basis for a future asset management model.

7.1.2 General Model Description

The parametric simulations, described in Chapter 6, provided tables containing T_γ estimations per radius per velocity. Those tables are available for both the Urbos and Combino trams in the loaded and unloaded state; also, tables are available for both vehicles in the unloaded state with worn wheels. The model searches per curve on the network the tabulated T_γ values which best represents the specific curve characteristics and usage parameters. Next, interpolation is made between the found tabulated T_γ values to obtain curve specific T_γ values. This process is repeated for each contact surface: the tread and flange at the outer and inner rail. The model is written in Python to perform this analysis at once for all 330 curves considered. Section 7.2 provides more information on the used methods.

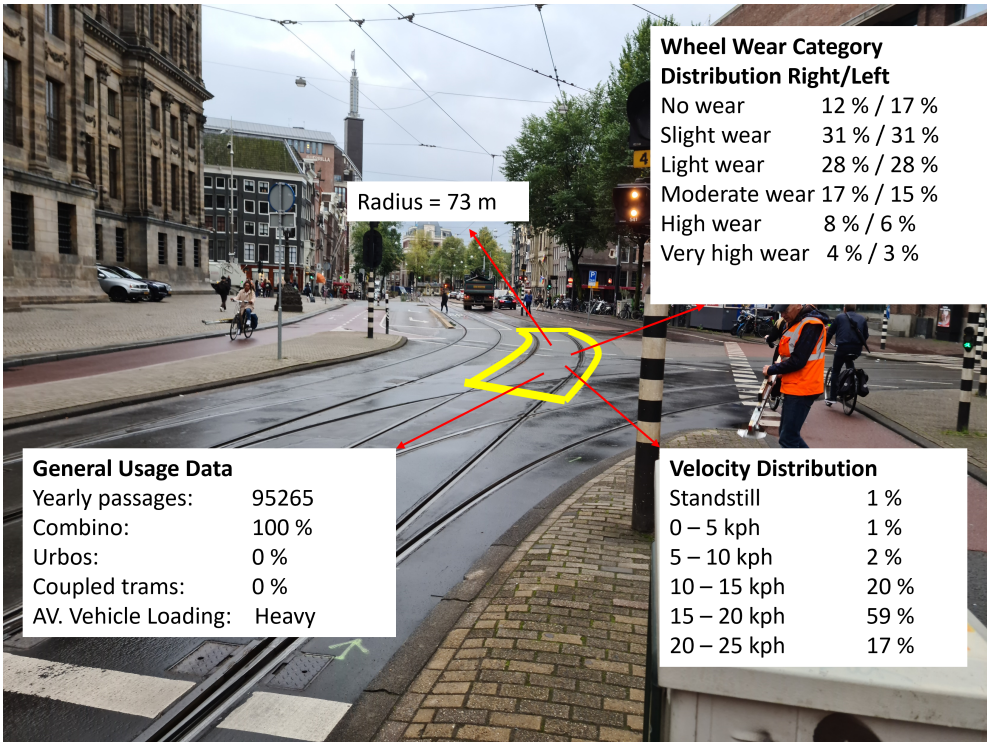


FIGURE 7.1: Input for the energy estimation model, general usage data taken from 23-09-2021, wheel wear data taken from tram wheel measurements from 2014 until 2020 (see Chapter 5), velocity data taken from 20-29 June 2021 (see Chapter 4).

7.1.3 Model Input Description

The model input could be separated into two categories: the tabulated T_γ values from the parametric simulations (see Chapter 6) and the curve specific input values. Figure 7.1 shows the curve specific input values for one example curve; this example curve will be used to guide the explanation of the model.

The parametric simulations only considered curve radii up to 100 m. The dependence on curve radius and velocity decreased with increasing radius, which is, for example, shown in Figure 7.6. Therefore, for curves with radii above 100 m, T_γ values were selected as if they were curves with radii of 100 m. The wheel wear distribution is derived based on wheel measurement data. Chapter 5 shows the used method for this derivation. The wear categories in the wheel wear distribution are based on the derived flange steepness (qR), Figure 7.3 shows the qR ranges per wheel wear category. The vehicle loading is taken into account with average vehicle occupation rates. No exact occupation rates could be demonstrated in this thesis because of confidentiality reasons.

7.1.4 Model Output Description

The model estimates the energy dissipation on the outer rail tread (HT), outer rail flange (HF), inner tread (LT) and inner flange (LF). The tread is the contact interface of the wheel band and the railhead, the flange is the interface of the wheel flange and the gauge side of the rail. The generated energy dissipation per contact surface is the sum of the expected energy dissipation of all six wheels. The model estimates the energy dissipation per *statistical passage* (SP), which is a weighted average based on the curve specific usage parameters. The 'detailed model description' provides the method to obtain the *statistical*

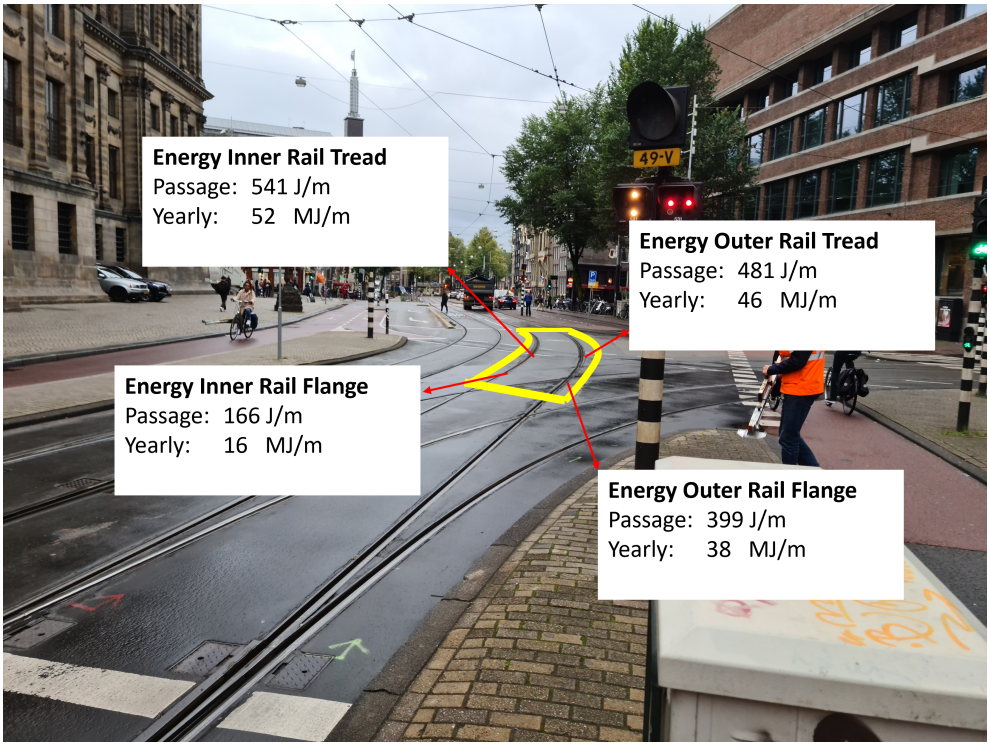


FIGURE 7.2: Output of the energy estimation model for one example curve.

passage T_γ values. The yearly energy intake (TW) is based on the *statistical passage* dissipation values, the yearly amount of tram passages and the amount of coupled trams. The abbreviation *TW* stands for 'Total Weight'. Figure 7.2 provides the output for the example curve used in this chapter.

7.2 Model Description

This section describes all the steps undertaken in the model to arrive at an energy estimation per curve based on the input values.

qR Range	Wear Category
> 4.5	No Wear
4.0 – 4.5	Slight Wear
3.5 – 4.0	Light Wear
3.0 – 3.5	Moderate Wear
2.5 – 3.0	High Wear
< 2.5	Very High Wear

FIGURE 7.3: Wheel wear categories, based on the steepness of the flange expressed in qR.

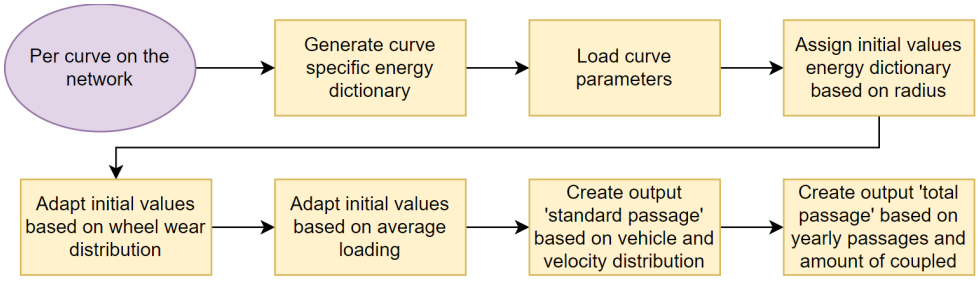


FIGURE 7.4: Flow chart of the energy estimation model.

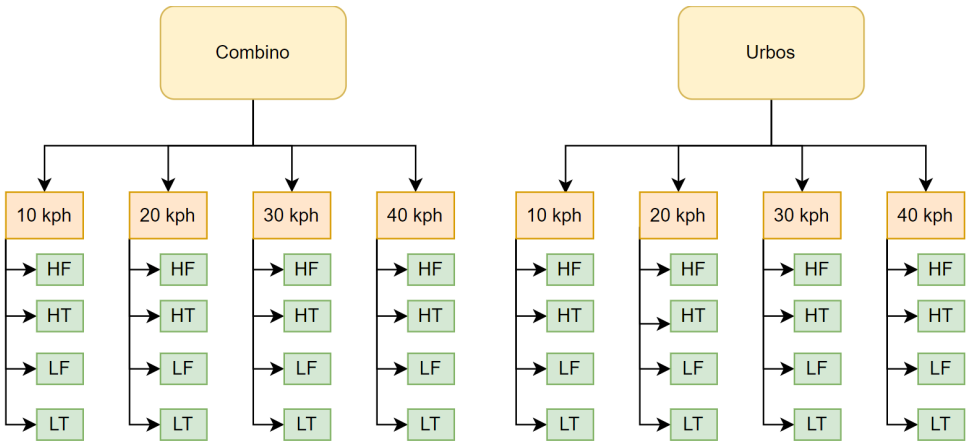


FIGURE 7.5: The T_γ dictionary which green boxes are filled per curve. H = outer rail, L = inner rail, F = Flange, T = Tread.

7.2.1 Introduction

The model executes itself in Python, where each curve is subsequently analyzed, following the steps shown in Figure 7.4. Per curve, a dictionary is generated which saves all T_γ values that belong to the different ways a tram could negotiate a specific curve. At first all T_γ values in the dictionary are equal to zero, the values are filled and adapted during the execution of the model. In the second step, the curve parameters specified under 'Model Input Description' are loaded for the specific curve. Next, the dictionary is filled with initial T_γ values based on the curve radius. Those initial values are then adapted for the wheel wear distribution, and after that, the dictionary is adapted for the average vehicle loading. Based on the vehicle type and velocity distribution, the model calculates a weighted average of the final T_γ values in the dictionary. Finally, the yearly energy dissipation is calculated based on the number of tram passages and coupled trams. The following subsections describe each step in more detail.

7.2.2 Energy Dictionary Generation

Figure 7.5 shows the T_γ dictionary which is generated per curve. Based on the curve radius, the green boxes are filled with initial T_γ values from the parametric simulations.

7.2.3 Loading of Curve Characteristics

The parameters taken into account are already described under 'Model Input Description'. It concerns the following parameters:

- Curve radius

- Vehicle distribution
- Velocity distribution
- Wheel wear distribution
- Average vehicle loading
- Yearly number of tram passages
- Share of coupled vehicles

The model takes each curve into account separately. The parameters are saved in comma-separated files (CSV) ordered per track number, each, e.g. curve, straight and switch, has its track number. Per curve specific information is obtained by selecting data in the CSV file which belongs to the track number of the curve in consideration.

7.2.4 Initial Energy Value Assignment

The initial values in the T_γ dictionary are filled based on the curve radius, Figure 7.5 shows the T_γ dictionary. The parametric simulations' tabulated T_γ values are available with a radius increment step of 10 m. During the filling of the initial values, tabulated T_γ values are obtained for the lower and upper radius divisible by 10. An interpolation between those values is made based on the actual curve radius, Figure 7.6 shows the interpolation. This process is repeated for each velocity taken into consideration (10 kph, 20 kph, 30 kph and 40 kph) for the empty Urbos and Combino vehicles with new wheels. In Chapter 4), it was found that velocities above 45 kph are rare on curves with a radius below 100m. In Chapter 6 it was found that the dependence on velocity vanishes on curves with a radius above 100 m. Therefore, only tabulated T_γ values of the before specified velocities are available. At higher velocities, the model assumes values belonging to a velocity of 40 kph.

7.2.5 Interpolation Based on Wheel Wear Distribution

The T_γ dictionary (Figure 7.5) is adapted for the measured wheel wear distribution which is derived in Chapter 5. The model can handle a different wheel wear distribution per curve, but it was only possible to derive a network-wide wheel wear distribution. Figure 7.7 shows the method used to include the wheel wear distribution for the example curve (Figure 7.1) for one green box of the T_γ dictionary. In this case, the outer rail tread of the Combino negotiating with 10 kph is taken as an example. The initial T_γ value in the dictionary for an empty Combino with new wheels was 250 J/m. The tabulated T_γ value for the empty Combino under the same circumstances with fully worn wheels is obtained for the two nearest radii divisible by 10. The same interpolation process as described in 'Initial Energy Value Assignment' (Figure 7.6) is now repeated for the empty Combino with fully worn wheels, resulting in a value of 650 J/m. Per wear category T_γ values are derived with linear interpolation, assuming a T_γ of 250 J/m for the lowest wear category and 650 J/m for the highest wear category. In Figure 7.5 those interpolated values are represented by red dots. The weighted average of those interpolated values is calculated based on the measured wheel wear weight distribution. Finally, the green box in the dictionary is updated with the new T_γ value which now includes the wheel wear distribution.

7.2.6 Interpolation Based on Average Loading

The T_γ dictionary (Figure 7.5) is adapted for the average vehicle loading after the adaption for the wheel wear distribution. This order was chosen since it was found in Chapter 6 that wheel wear has a more profound influence on the curving behaviour than vehicle loading.

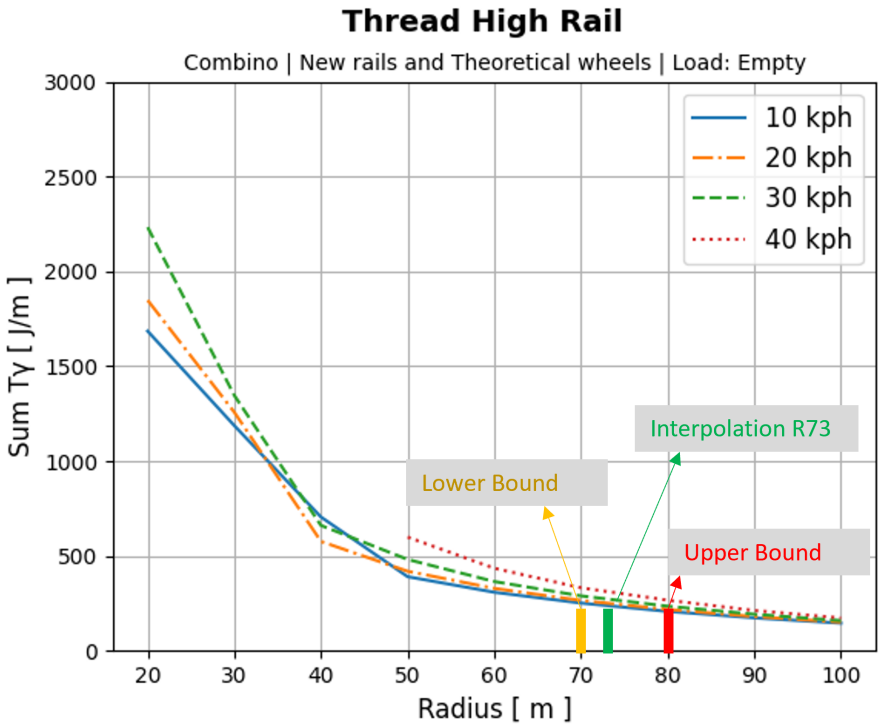


FIGURE 7.6: Initial T_γ value selection using interpolation based on the curve radius.

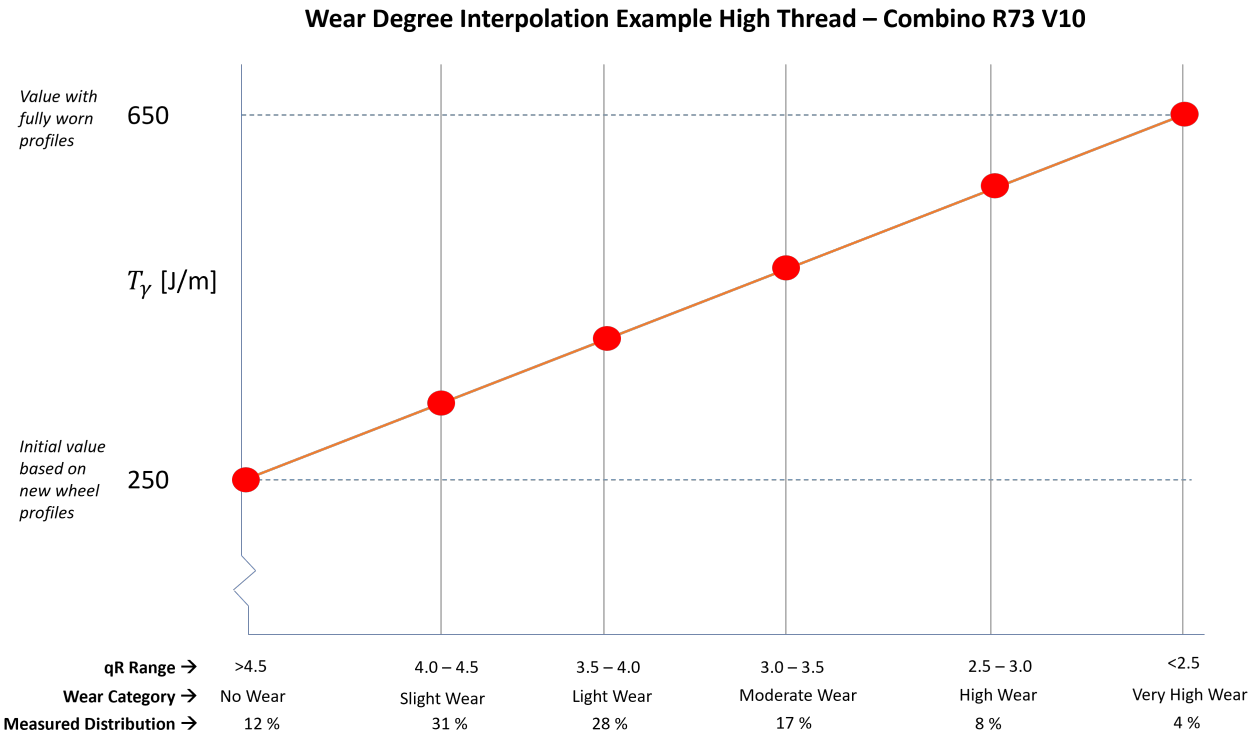


FIGURE 7.7: T_γ interpolation per wheel wear category.

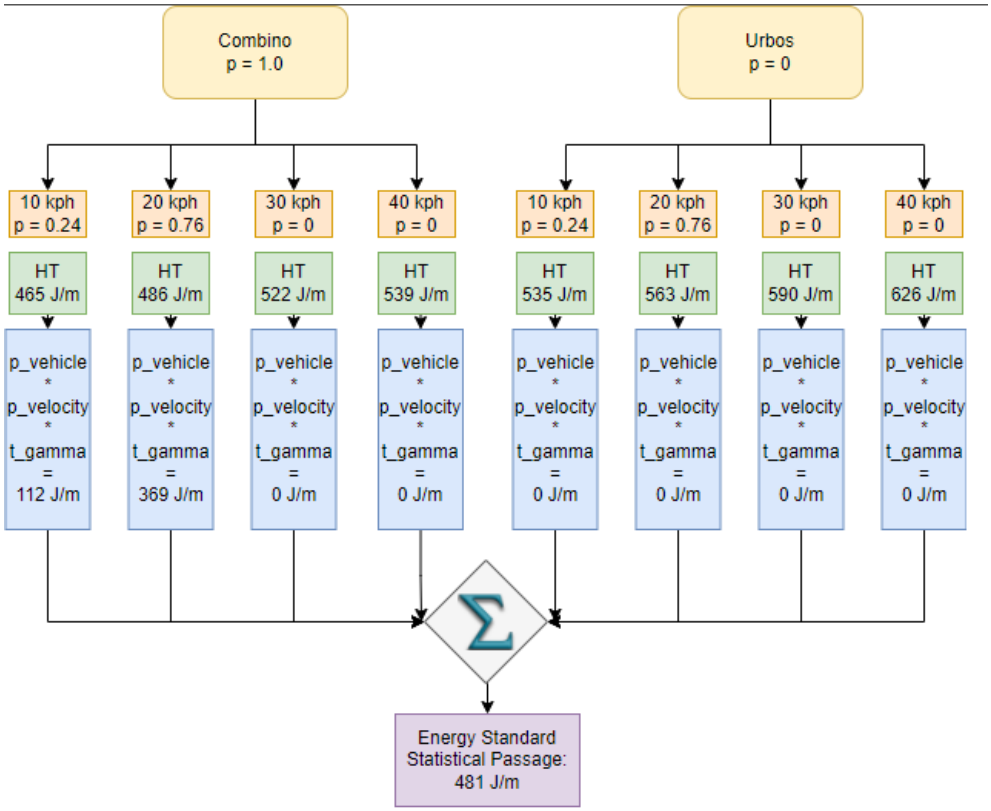


FIGURE 7.8: T_γ factoring to arrive at a statistical passage value. HT = tread at outer rail.

For each green box in the T_γ dictionary, matching tabulated values for a loaded vehicle are obtained and interpolated based on the curve radius. The relative change in T_γ compared to the empty vehicle with new wheels is then calculated. After that, the T_γ values in the dictionary already adapted for wheel wear are factored for the average loading. The factor is based on a linear interpolation between the loaded and empty case.

7.2.7 Factoring Based on Vehicle and Velocity Distribution

Figure 7.8 provides an example of the T_γ values for all green *HT* (Outer Tread) boxes in the T_γ dictionary for the example curve (Figure 7.1). Those values are corrected for the wheel wear distribution and average vehicle loading. The energy of a standard statistical passage (SP) at the outer rail tread in the example curve is determined by averaging all the green boxes belonging to the outer tread in the T_γ dictionary. The averaging is weighted based on the observed vehicle type and velocity distribution determined in Chapter 4.

7.2.8 Yearly Dissipated Energy Calculation

The yearly dissipated energy (TW = Total Weight) is calculated by multiplying the statistical passage T_γ (SP) per contact surface with the annual number of vehicle passages, factored by the amount of coupled vehicles. This calculation results in a yearly expected energy dissipation per contact surface.

Category	T_γ SP [J/m]	T_γ TW [MJ/m]	Color
Light	< 200	< 20	
Moderate	200 - 500	20 - 50	
High	500 -1000	50 - 100	
Very High	> 1000	> 100	

FIGURE 7.9: Energy dissipation categories for one statistical tram passage (SP) and the yearly amount of energy intake (TW). The colours are used in the figures which show the energy estimations on the map.

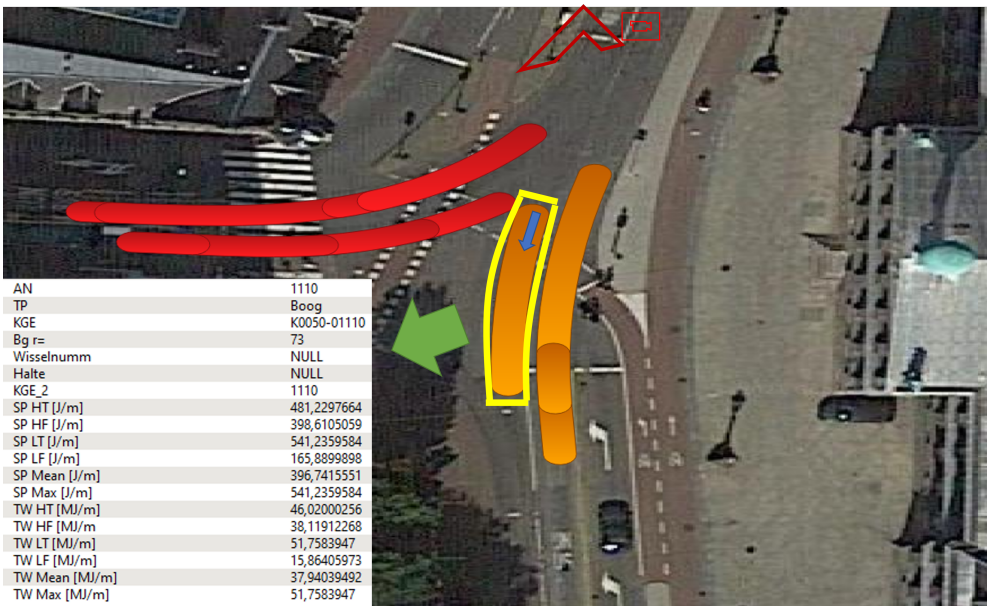


FIGURE 7.10: Example of the energy dissipation estimation model output, for curve 1110 at the Nieuwezijds Voorburgwal - Raadhuisstraat intersection. See Figure 7.9 for the color references. H = outer rail, L = inner rail, F = Flange, T = Tread.

7.3 Results

This section provides a short impression of the results from the energy estimation model.

7.3.1 Result Examples

In this subsection, an impression of the results is given. Figure 7.9 shows the T_γ output categories and the used colours per category on the map. The results for the example curve are shown in Figure 7.10. The model calculates these results for each curve on the network at once, this is shown in Figure 7.11 for a part of the city.

7.3.2 Energy Estimation

The results were in line with the expected output of the model. As expected, the T_γ levels at the statistical passages are most dependent on the curve radius. The yearly T_γ values show a wider variety over the network since those depend on vehicle passages and coupled trams. However, also at quiet lines in the suburbs on tight curves, the calculated yearly energy dissipation levels could be high to very high. No large differences were observed for the amount of dissipated energy at the outer rail flange and tread at both sides;

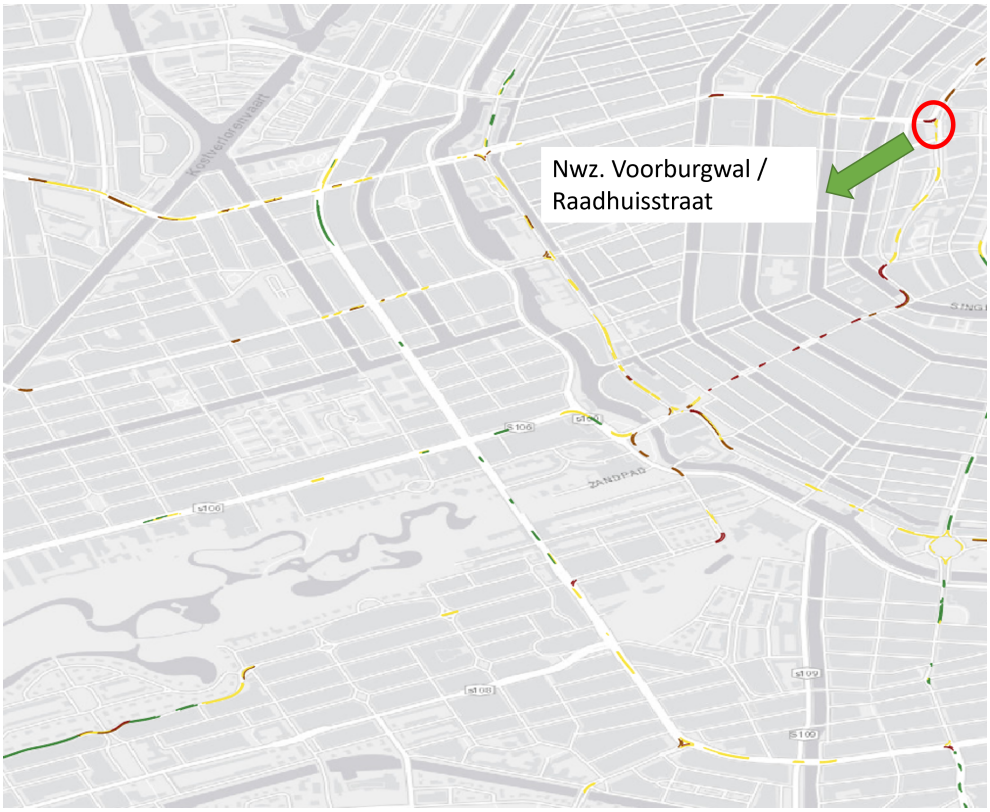


FIGURE 7.11: Example overview of the network wide yearly expected energy dissipation values in curves. See Figure 7.9 for the color references.

the inner rail flange's energy dissipation was relatively low. Besides the inner rail flange, all T_γ values for the statistical passages were at least moderate.

7.4 Comparison Energy Estimation with Profile Measurements

This section compares the estimated energy and measured wear for four curves. The number of curves is too small to consider as model validation. Still, it could give an impression of the possible comparison method. Two tight and two curves with larger radii were selected across the city. The energy dissipation at the treads is linked to vertical wear in the profile measurements, while the horizontal wear is related to the energy dissipation at the flanges. Figure 7.12 provides the legend of the velocities per point. Those velocities are shown in the comparison figures since they could help understand comparison results.

7.4.1 Curve 1 - Verbindingsdam/Ertskade

Figure 7.13 shows the comparison of curve 1: the inner rail tread and outer rail flange wear faster than expected, the inner rail flange has the minor wear indeed but not as small as expected. From the longitudinal rail measurement graphs, it could be deduced that the curve definition does not exactly match with the wear zone along the curve. Therefore, the wear rates are expected to be higher in reality. This error does not change the disproportion between the observed wear and estimated energy at the different contact surfaces.

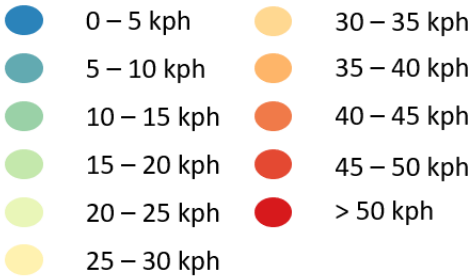


FIGURE 7.12: Legend of the velocities per trackpoint, resulting from the analysis described in Chapter 4

Curve 1 - Verbindingsdam / Ertskade

Curve Information	Inner curve
Number	33030
Radius	25 m
Yearly Passages	41610
Combino	100 %
Urbos	0 %
Coupled trams	0 %
AV. Vehicle Loading	Light

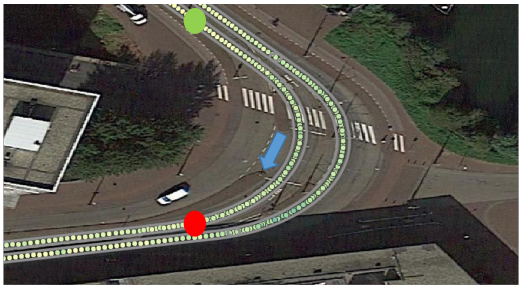
Velocity Distribution	Inner curve
Standstill	0 %
0 – 5 kph	2 %
5 – 10 kph	2 %
10 – 15 kph	7 %
15 – 20 kph	46 %
20 – 25 kph	36 %
25 – 30 kph	6 %
30 – 35 kph	1 %
35 – 40 kph	0 %
40 – 45 kph	0 %
45 – 50 kph	0 %

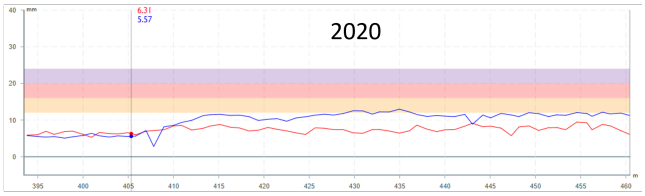
Passage Dissipation [J/m]	Inner curve
Outer rail tread	1920
Outer rail flange	1007
Inner rail tread	1243
Inner rail flange	246

Yearly Dissipation [MJ/m]	Inner curve
Outer rail tread	82,0
Outer rail flange	43,0
Inner rail tread	53,1
Inner rail flange	10,5

Wear Rates [mm/y]	Inner curve
Outer rail tread	0,28
Outer rail flange	0,39
Inner rail tread	0,53
Inner rail flange	0,12

mm/(GJ/m)	Inner curve
Outer rail tread	3,41
Outer rail flange	9,07
Inner rail tread	9,98
Inner rail flange	11,43





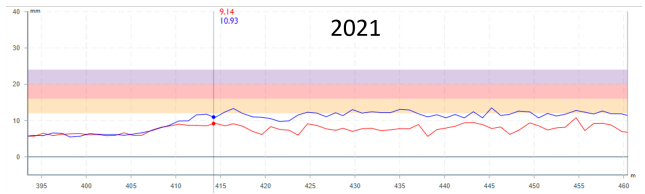


FIGURE 7.13: Example validation of curve 33030. Green = start, red = end. Velocity legend: Figure 7.12. The profile measurements along the curve show the vertical wear in mm (left = red, right = blue).

Curve 2 - J. Evertsenstraat / J. Tooropstraat

Curve Information	Inner curve
Number	50170
Radius	26 m
Yearly Passages	48910
Combino	100 %
Urbos	0 %
Coupled trams	0 %
AV. Vehicle Loading	Heavy

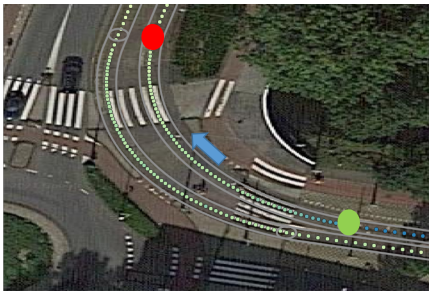
Velocity Distribution	Inner curve
Standstill	8 %
0 – 5 kph	4 %
5 – 10 kph	12 %
10 – 15 kph	32 %
15 – 20 kph	34 %
20 – 25 kph	9 %
25 – 30 kph	0 %
30 – 35 kph	0 %
35 – 40 kph	0 %
40 – 45 kph	0 %
45 – 50 kph	0 %

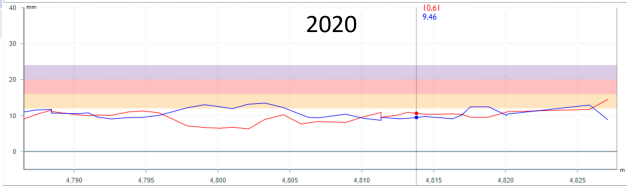
Passage Dissipation [J/m]	Inner curve
Outer rail tread	1965
Outer rail flange	844
Inner rail tread	1462
Inner rail flange	306

Yearly Dissipation [MJ/m]	Inner curve
Outer rail tread	96,8
Outer rail flange	41,6
Inner rail tread	72,0
Inner rail flange	15,1

Wear Rates [mm/y]	Inner curve
Outer rail tread	0,37
Outer rail flange	0,2
Inner rail tread	0,18
Inner rail flange	0,3

mm/(GJ/m)	Inner curve
Outer rail tread	3,82
Outer rail flange	4,81
Inner rail tread	2,50
Inner rail flange	19,87





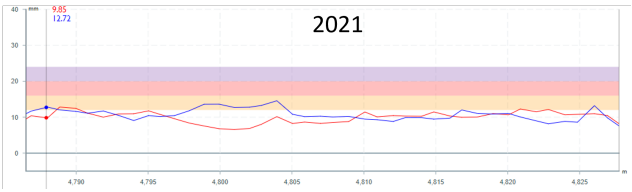


FIGURE 7.14: Example validation of curve 48910. Green = start, red = end. Velocity legend: Figure 7.12. The profile measurements along the curve show the vertical wear in mm (left = red, right = blue).

7.4.2 Curve 2 - J. Evertsenstraat/J.Tooropstraat

Figure 7.14 shows the comparison of curve 2: the inner rail tread wears a bit slower than expected while the inner rail flange wears much faster than expected. It is unclear why such differences between the energy estimation and profile measurements occur since they seem to be of good quality for this curve.

7.4.3 Comparison Curve 1 and Curve 2

In curve 1 the outer rail flange is expected to wear faster than in curve 2, since trams drive faster on curve 1. This difference is visible, but the wear difference is considerably larger than the difference in the energy estimation. This disproportion is shown in the difference in wear per dissipated energy at the outer rail flanges in both curves. The inner rail tread on curve 2 is expected to wear faster than curve 1 because of the lower velocity on curve 2. However, this was not the case in curve 2. On the contrary, in curve 2 the outer rail tread suffered more wear than expected. In both cases, the inner rail flange wears faster than expected by the energy estimation model.

In conclusion, the measured wear in curve 1 and 2 is not in proportion to the amount of estimated energy. It might be the case that some relations are not linear while those relations are assumed as linear in this validation. For example, this could be the case for the wear increase at the outer rail flange with increasing velocity.

7.4.4 Curve 3 - Raadhuisstraat/Nwz. Voorburgwal

Figure 7.15 shows the comparison for curve 3, the example curve of this chapter with a larger radius compared to the previous two curves. The outer rail tread wears faster than

Curve 3 - Raadhuisstraat / Nwz. Voorburgwal

Curve Information	Outer curve
Number	1110
Radius	73 m
Yearly Passages	95265
Combino	100 %
Urbos	0 %
Coupled trams	0 %
AV. Vehicle Loading	Heavy

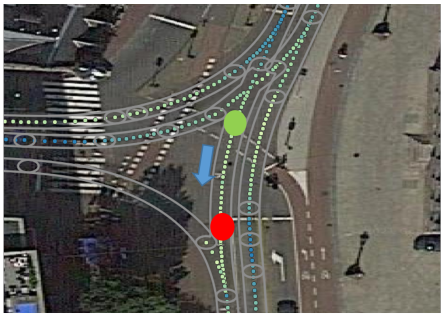
Velocity Distribution	Outer curve
Standstill	1 %
0 – 5 kph	1 %
5 – 10 kph	2 %
10 – 15 kph	20 %
15 – 20 kph	59 %
20 – 25 kph	17 %
25 – 30 kph	0 %
30 – 35 kph	0 %
35 – 40 kph	0 %
40 – 45 kph	0 %
45 – 50 kph	0 %

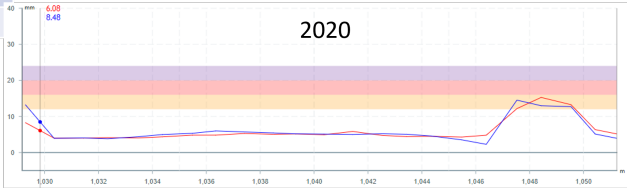
Passage Dissipation [J/m]	Outer curve
Outer rail tread	481
Outer rail flange	399
Inner rail tread	541
Inner rail flange	166

Yearly Dissipation [MJ/m]	Outer curve
Outer rail tread	46,0
Outer rail flange	38,1
Inner rail tread	51,8
Inner rail flange	15,9

Wear Rates [mm/y]	Outer curve
Outer rail tread	1,65
Outer rail flange	0,88
Inner rail tread	0,92
Inner rail flange	0,16

mm/(GJ/m)	Outer curve
Outer rail tread	35,87
Outer rail flange	23,10
Inner rail tread	17,76
Inner rail flange	10,06





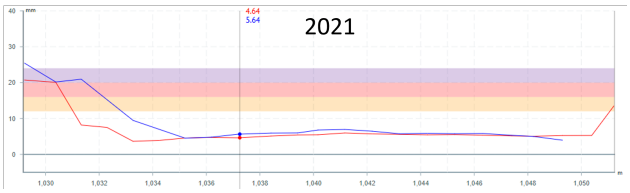


FIGURE 7.15: Example validation of curve 1110. Green = start, red = end. Velocity legend: Figure 7.12. The profile measurements along the curve show the vertical wear in mm (left = red, right = blue).

expected at this curve. However, from the longitudinal graphs in Figure 7.15, the suspicion arises that the rail measurements at this curve might be inaccurate.

7.4.5 Curve 4 - W. de Zwijgerlaan/A. de Ruijterweg

Figure 7.16 shows the comparison for curve 4: the wear rates at the treads are higher than expected, especially on the outer rail tread. On the contrary, the inner rail flange wears slower than anticipated.

7.4.6 Comparison Curve 3 and Curve 4

The wear at curve 4 was expected to be lower because of the larger radius. While this was the case for the flanges, the treads had higher wear rates on curve 4 compared to curve 3. It might be the case that the combination of a more significant overall velocity and a more considerable amount of Urbos vehicles on curve 4 had a more substantial influence than expected.

7.4.7 Comparison All Curves

Figure 7.17 shows a scatter plot of the yearly expended energy dissipation and wear for the four selected curves. The 4 curves were selected because of the relative high qualitative profile measurements. No correlation was found for the Ertskade and Tooropstraat curves. The other two curves have a low correlation between estimations and measurements. It is remarkable both curves with larger radii have higher wear rates, especially at the outer rail tread, compared to the curves with smaller radii. Possibly the model overestimates wear in tight curves, or underestimates wear in gentle curves. At the tight curves, the inner rail flanges had more wear than the expectations, while the inner rail flanges had less wear at

Curve 4 - W. De Zwijgerlaan / A. de Ruijterweg

Curve Information	Outer curve
Number	43790
Radius	100 m
Yearly Passages	86505
Combino	73 %
Urbos	27 %
Coupled trams	0 %
AV. Vehicle Loading	Heavy

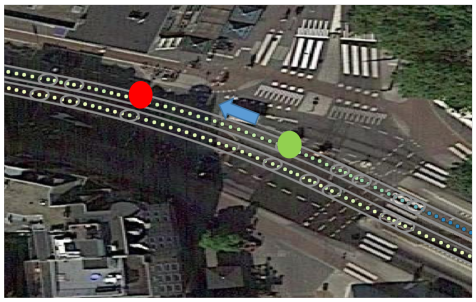
Velocity Distribution	Outer curve
Standstill	0 %
0 – 5 kph	2 %
5 – 10 kph	3 %
10 – 15 kph	20 %
15 – 20 kph	39 %
20 – 25 kph	33 %
25 – 30 kph	3 %
30 – 35 kph	0 %
35 – 40 kph	0 %
40 – 45 kph	0 %
45 – 50 kph	0 %

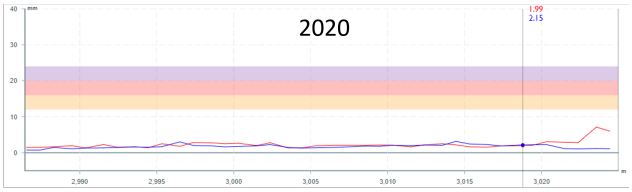
Passage Dissipation [J/m]	Outer curve
Outer rail tread	318
Outer rail flange	327
Inner rail tread	430
Inner rail flange	116

Yearly Dissipation [MJ/m]	Outer curve
Outer rail tread	27,9
Outer rail flange	28,7
Inner rail tread	37,7
Inner rail flange	10,2

Wear Rates [mm/y]	Outer curve
Outer rail tread	1,86
Outer rail flange	0,58
Inner rail tread	1,69
Inner rail flange	0,03

mm/(GJ/m)	Outer curve
Outer rail tread	66,67
Outer rail flange	20,21
Inner rail tread	44,83
Inner rail flange	2,94





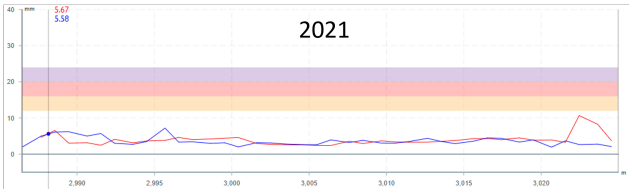


FIGURE 7.16: Example validation of curve 43790. Green = start, red = end. Velocity legend: Figure 7.12. The profile measurements along the curve show the vertical wear in mm (left = red, right = blue).

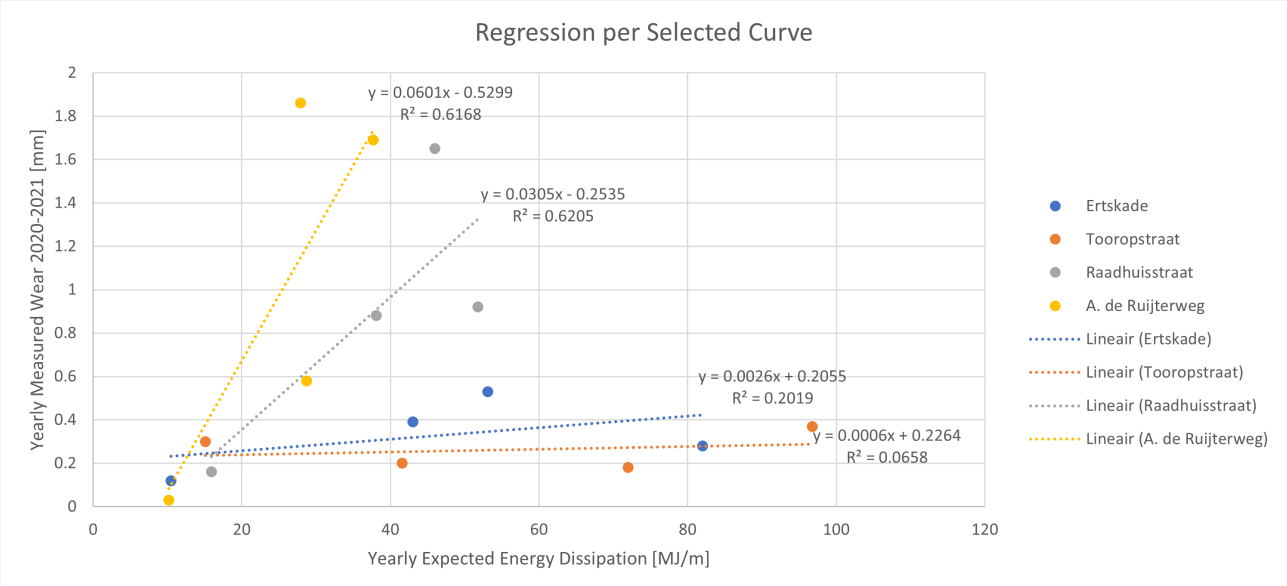


FIGURE 7.17: Comparison yearly expected energy dissipation and measured wear for the 4 selected curves.

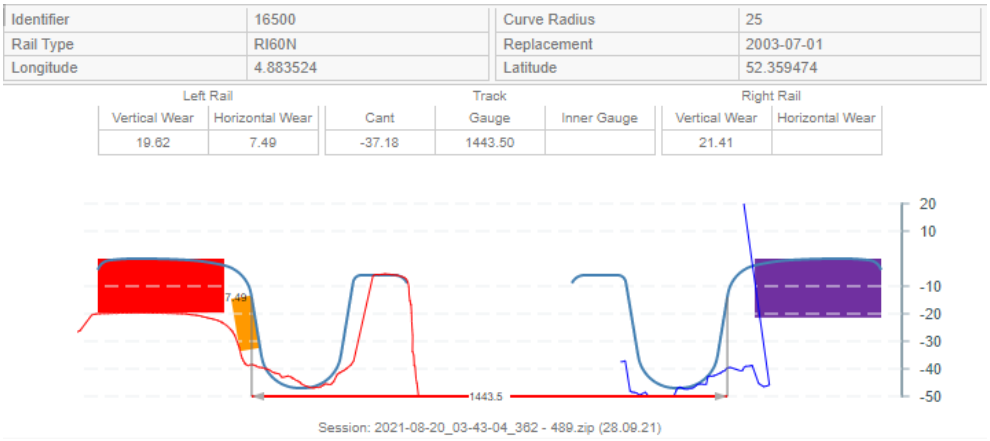


FIGURE 7.18: Example of extreme worn rail (left) and faulty rail profile measurements (right).

the larger curves than expected. Therefore, it is not expected measurement error causes these unexpected deviations.

Based on these results, it is not possible to derive general wear coefficients link T_γ estimations to volumetric wear. Wear is non-linear related to energy dissipation. Further research could identify curves that show identical patterns in wear behaviour related to energy estimation. Based on this future research, specific characteristics per group of curves might be isolated, declaring the observed differences. It would also be interesting to assess regression patterns per curve over consecutive years. In this thesis, the estimations and measurements are further compared with a larger group of curves in the next section.

7.4.8 Comparison with Large Group of Curves

The wear measurements and energy estimation were compared for a set of about 200 curves. A large group of curves could not be compared because no measurements were available for both 2020 and 2021. Also, many curves had negative wear values measured over both years. This negative wear can occur because of rail maintenance, extreme vertical wear or inaccurate measurements. An example of the two latter issues is shown in Figure 7.18. In 7.18, the two identical blue lines on both sides represent the original rail profile. The red line shows the measured profile on the left rail. The rail could expand horizontally because of vertical wear, resulting in negative horizontal wear. It is evident from the right side of Figure 7.18 this measurement was not successful.

The comparison analysis was coded in Python. First, wear rates were calculated by subtracting the wear measured mid-2020 from that measured mid-2021. Negative wear values were not further considered. Wear rates were separated into horizontal and vertical wear for both rails. Then, the energy estimations were compared with those measurements based on the curve direction (left curve or right curve). Vertical wear was compared with energy estimations at the tread contact, horizontal wear with the flange contact.

All comparison results can be found in Annex **??**. This section uses the comparison results for the outer rail tread as an example. Figure 7.19 provides the comparison results in a scatter plot for the outer rail tread. In this case, the annual estimated T_γ [MJ/m] was compared to the measured annual wear [mm]. The curve radius was shown because, in section 7.4.7, more correlation was observed at curves with larger radii. However, from 7.19, such a dependence on curve radius is not visible anymore. Overall, the correlation between annual estimated wear and energy dissipation is not present at a satisfying degree.

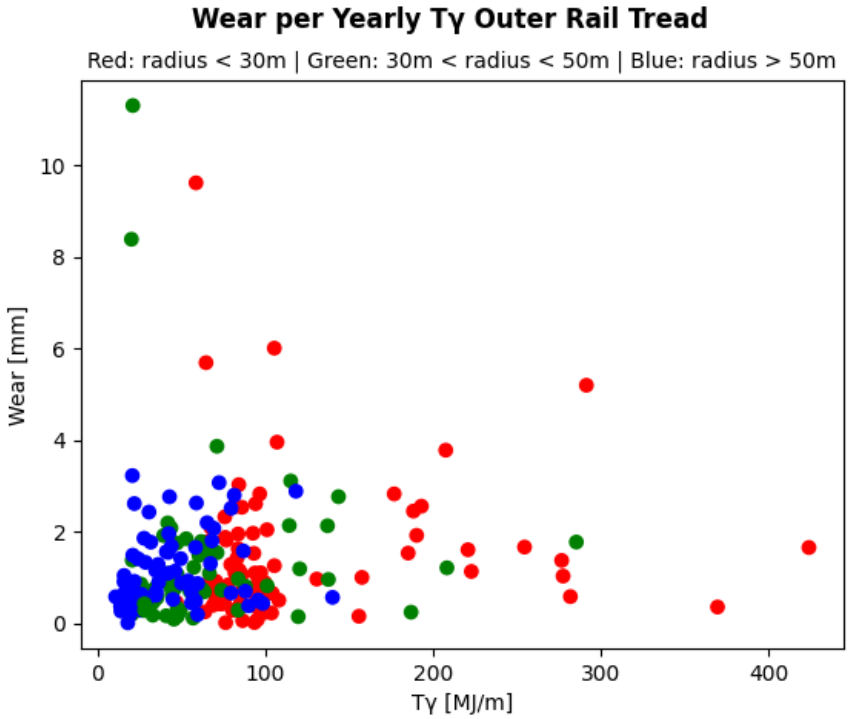


FIGURE 7.19: Scatter plot of the yearly estimated energy dissipation and measured wear of the outer rail tread.

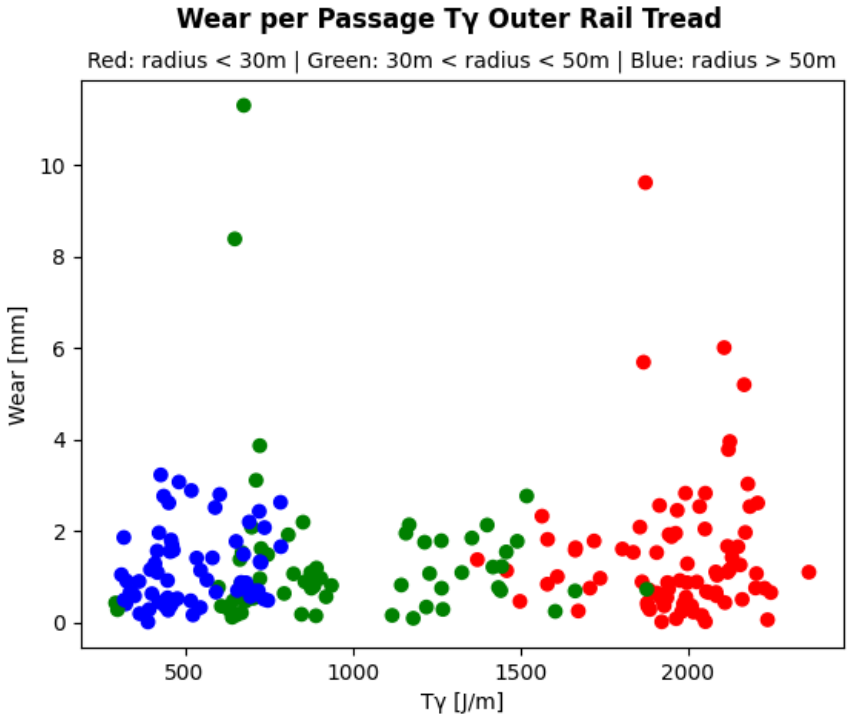


FIGURE 7.20: Scatter plot of the estimated energy per passage and yearly measured wear of the outer rail tread.

Another comparison was made between the annual wear [mm] and summed energy dissipation per statistical tram passage [J/m]. Again, results for the outer rail tread are shown in Figure 7.20. Also, no clear correlation was observed between the model estimation and profile measurements in this case.

This comparison showed it is not possible to derive a general coefficient of *wear per energy dissipation*, neither when single passages values or curve radii are taken into account. Assumptions made during the process or faulty profile measurements might cause this issue. The discussion in Chapter 8 elaborates on these assumptions.

7.5 Conclusion

Estimating energy dissipation based on the parametric simulations was done for the whole network. While the model results were consistent, the comparison with profile measurements turned out to be more challenging. It was too challenging to derive an average wear per energy dissipation ratio (mm/(GJ/m)) since those values varied largely per curve and contact surface. Perhaps the relationship between the energy dissipation and volumetric wear is not linear and, therefore, not obtainable by simply dividing the observed wear and estimated energy. This difficulty could already be expected from the literature review and background information in Chapter 2. More factors should be included in the energy estimation model to increase the model reliability. These factors could be, e.g. material hardness, rail irregularities or rail lubrication. Isolation of curves with high wear rates compared to the expectation could be isolated to research whether shared characteristics exist in this group.

Chapter 8

Conclusion and Discussion

8.1 Conclusion

The main goal of this research was to develop a wear prediction model for tramway curves. Based on data and simulation results, such a model was created. Energy dissipation (J/m) was used as a wear indicator. Verification of the model output showed an agreement between the expected energy dissipation per curve and simulation results. However, estimating volumetric wear per curve based on the estimated energy per curve was challenging.

The research started with the literature review and background information assessment. A scientific basis is available for modelling wheel-rail contact, railway vehicles, and dynamical responses due to curve negotiation. This basis is mainly tailored to heavy rail, not much research and information were found on tram railways specifically. The focus in the literature on heavy rail makes it more challenging to establish a proper model for tram curving behaviour, since tight curves commonly seen at tram infrastructure are rare at heavy rail infrastructure. As part of a topic of future research, the numerical, physical, and hybrid models to research a variety of problems in the heavy railways, are a basis for the modelling approach required for tram railways.

Since GVB wants to use the model for the asset management of the tram network, the energy estimation model needs data from the tramway. Fortunately, much data was available at GVB, which was used to simulate the actual situation on the network. The availability of network characteristics, track measurement data, and usage data was excellent. However, the availability of maintenance data was insufficient for inclusion in the research. Track characteristics and usage data are sufficient to model the curving process, but measured wear rates are needed to validate the results. The profile measurements do not provide exact wear rates since track maintenance could also affect the track profiles. Wear measurements did not have the same quality in the whole network. For instance, there are evident failures in the measurement signals at some locations. The available data at GVB is ill aligned since it is all obtained at different departments from different database systems. It took much effort to align all data so the model could easily retrieve it per curve.

The velocity analysis suggested that most trams mainly comply with the speed limits. However, the majority of trams exceed the maximum permitted speed limit at some specific tight curves. This could play a role in the wear observed at those particular tight curves. It seems that the broader curve layout is essential for speed limit compliance. Curves not part of a junction with other traffic and curves with long straight adjacent stretches are more prone to speed limit violations.

The wheel analysis performed with the wheel re-profile measurement resulted in some insight that could be used to optimise the tram fleet asset management. It turned out that the first wheel has more significant qR decay rates and that the Combino trams underperform compared to the old BN trams. The results of the wheel analysis were used to validate the simulations and as input for the energy estimation model. The simulations showed that flange contact mainly occurs at the wheels on the first axle. Therefore, flanging has a relatively significant effect on qR decay, given this comparison between simulations and wheel analysis. The wheel analysis agrees with simulations for the first wheel in relation to the other wheels. However, less agreement was observed in the decay rate distribution and simulation results over the remainder of the wheels.

The simulation results showed an exponential increase of energy dissipation when the curve radius decreased. Also, the velocity dependence increased exponentially with decreasing curve radius. At the outer rail, the effect was adverse with increasing velocity and vice versa on the inner rail. At a radius of 100 m, the velocity dependence vanished, and the radius dependence was only very low. Worn wheels did have the most significant adverse effect on simulation results, especially combined with increased velocities at tight curves. The tram vehicles' passenger loading and suspension stiffness also played a considerable role in resulting energy dissipation, with an overall adverse effect with increased levels. The impact of the wear degree of the rails on curving behaviour was also considerable. The influence was, however, not always harmful. In general, it turned out to be challenging to obtain accurate simulation results with worn rails. The difficulty lay in the simulation model, which often failed to deliver results when a worn rail profile was used. Often, model failure was the violation of the wheel-rail contact boundaries. Then, the model assumes the vehicle is derailed. In practice, the vehicle runs on the street hardening in such a case. This effect could be included in a future version of the simulation model, to improve outcomes with altered rail geometry.

An energy estimation model was made, which combined the simulation results, track characteristics and usage data per curve on the network. The vehicle type distribution, velocity distribution, tonnage, average vehicle loading, and tramway-wide wheel wear distribution were taken into account in the energy estimation model. To validate the results of the model, three different approaches were considered. The first one was an interview with tramway maintenance experts. They were shown a complete set of energy predictions (T_γ) over the whole tramway. The experts indicated the general trends agree with observed wear on the tramway.

The second approach for validating the results was selecting four different curves. This second validation approach compared energy estimations, curve characteristics, and wear measurements. Two out of the four curves with relatively large radii showed a correlation between energy estimations and wear measurements. The other two curves with smaller radii showed lower wear rates than the expectations. A final attempt was made to obtain more clarity on the model validity with an approach purely based on data. From 200 curves on the tramway, estimation results of energy dissipation were compared with wear measurements. It was too challenging to deduce a general wear coefficient that directly relates energy dissipation to wear for all curves at once. Analysing the ageing process per particular curve is a more promising method for a reliable wear prediction. A significant challenge appeared when including wear measurements in the comparison, as the quality of the measurements varies per location. For instance, some sites show apparent errors in the signals. Negative wear values were observed in a significant amount of cases. Severe vertical wear, structural changes, maintenance or measurement errors can cause this negative wear. Further research could be tailored to improve track profile measurements.

Given the results in this thesis, the methodology can be incorporated as part of the asset management decision support for tramways. Further research is needed to evaluate the effect of the nonlinearities in the rail wear process. A finite element modelling or other advanced method is required to capture scenarios with more complex dynamics and characteristics of the tram/rail. It appears that each curve has unique features and dynamics, for which continuous monitoring and a tailored physical model are required.

8.2 Recommendations

From the conclusion, the following recommendations were derived.

(1) It is recommended that GVB rank the curves using both the developed model and wear measurements. Curves with significant deviations in both rankings could be subject to further investigation to uncover critical parameters which might cause increased wear. Those parameters could then be included in the estimation model for improvement. For example, the Autech measurements also have the corrugation levels per curve. The possible influence of rail corrugation could be researched by comparing wear rates and corrugation levels per curve.

(2) Instead of the energy dissipation in Joule per meter, another wear indicator could be chosen. For example, the power dissipation in work per second could be calculated. The power dissipation is equal to the summed energy dissipation times the velocity. It could then be verified if the alternative wear indicator is in better agreement with profile measurements. Further explanation on *power dissipation* could be found in section 2.1.6 in Chapter 2.

(3A) The asset management at GVB could be optimised by improving the asset's database. The already existent SAP database with track characteristics could be expanded with: wear rates, maintenance records, usage data and actual wear vs expectations. This could provide a better overview of the state of the overall infrastructure, which will help decision making regarding budget allocation and maintenance planning. Furthermore, when data indicates the condition of an asset is deteriorating faster than expected, interventions could be made earlier and more adequate.

(3B) In reference to recommendation 3A, the interface and usability of SAP could be either improved, or a new asset database could be developed. This could enhance the inclusion of maintenance data in the asset database. E.g., maintenance personnel could then directly enter maintenance data and information in the database via a wearable device (tablet, smartphone).

(3C) In reference to recommendation 3A, such an improvement does not need to be limited to the track. Also, switches, catenary and electrical systems could be included in an improved database.

(4) The velocity analysis shows a set of curves where the majority of trams drive too fast. Those curves could be analysed to assess possible causes for the speed limit violations. Research under tram drivers could clarify the main reasons for overspeeding. Measures according to the outcomes of such research could then be taken. Ultimately a GPS based vehicle speed limit could be enforced on those curves.

(5) Wheel re-profiling could be optimised by condition-based decision making regarding vehicle selection for re-profiling. Instead of a fixed time interval, trams could be sent to the re-profiling machine based on wheel measurements at the tram depots. If severely worn wheels are re-profiled faster, the average wheel wear degree on the tramway decreases.

This has a beneficial effect on both wheel and rail, since simulation results indicated worn wheels result in a considerable increase of energy dissipation at the wheel-rail contact. Furthermore, it could also overcome trams that are sent too early to the re-profiling machine. The costs savings related to wear prevention can be higher than the acquisition costs of a wheel measurement device. New sensing technologies allow fast screening of wheels.

(6) The wheel measurement data indicated increased decay rates of the front tram wheels. Possibly this could be considered during re-profiling, for example, by creating a relatively thicker flange for the first wheels. Alternatively, the hardness of the first wheels relative to the other wheels could be increased. This is expected to equal the wheel condition of the 12 tram wheels on average, which increases the cost-effectiveness of the wheel re-profile policy. Furthermore, it could decrease the average wear degree of the first wheels, which lowers the amount of expected wear in curves.

8.3 Discussion

Regarding the velocity analysis, faster trams have fewer records per unit distance. This decreases the measured average velocity per track number and track point with a fixed length. The resulting decrease is expected to be minor because of the relatively low speeds, e.g. if 50 per cent of the trams would drive 20 kph and the other 50 per cent 30 kph, the calculated average velocity per stretch would be 24 kph. In reality, it would be 25 kph. A velocity based compensation factor can compensate trams providing fewer data points due to higher speeds.

For the wheel analysis, non-linear qR decays could be assumed to improve the accuracy of the qR distribution on the tramway. The wheel analysis could be deepened by considering changes in qR decay over time to assess effects of, e.g., seasonal effects or wheel re-profiling policy changes. Furthermore, it is possible to evaluate decay rates per vehicle to identify vehicles with above average decay rates. This is not done in the current research but could be the subject of further investigation.

The energy estimation results for selected curves were consistent with the simulation model results. Unfortunately, including these energy estimations in the wear prediction tool was not straightforward. It was too challenging to establish a general relation between energy estimations and wear rates. The energy dissipation could be an inaccurate wear indicator since energy dissipation, and wear are two different measures. Another reason for the lack of alignment between measurements and estimations could be an inaccurate energy estimation. This is challenging to validate since energy dissipation is hard to measure in practice. Causes for an inaccurate energy estimation could lay in assumptions made in the simulation model, energy estimation model and wear measurement post-processing. Those assumptions are elaborated on in the following paragraphs.

Many assumptions made during modelling could cause the observed deviations. For example, the theory based on creepages assumes non-complex surfaces. In practice, the railhead often has a degree of irregularities, influencing the wear rates. Furthermore, the simulation model also used Kalker's wheel-rail contact model to calculate energy dissipation at the (sliding) flange contact. A more suitable wheel-rail contact model should be explored, since the flange does not satisfy the half-space assumption and mostly suffers from sliding contact instead of rolling contact. The influence of these factors could be researched with FEM analysis in further research. The last issue regarding the used

wheel-rail contact theory for the simulations concerns the material hardness. In the simulation, the Poisson and Youngs modulus of the rail is taken into account. However, these parameters describe the material on a global scale. Since wear in wheel-rail contact is a local effect, estimating the material hardness can lead to better results.

The energy estimation model is based on the dissipated energy per unit distance. However, this parameter does not consider factors that influence wear, for example, the influence of the rail temperature, which varies between -20 and +60 degrees Celsius. The effect of flange lubrication is partially taken into account by decreasing the friction coefficient at the rail flange contact from 0.3 to 0.15. However, this only changes the model's wheel-rail contact forces and related energy dissipation. Further analysis should be considered to study the influence of the chemical composition of the lubricant in the wear since that is not part of the energy dissipation definition. Also, the impact of dirt and debris on track wear could be assessed in further research.

Other assumptions which might cause deviations might lay in the assumptions and limitations of the available vehicle models. This is particularly important in the case of the modelling of bogies with independent wheels. Also, the low floor of the Siemens Combino and Urbos 100 tram vehicles deviates from conventional heavy rail vehicles. Possibly the dynamic effects related to the low floor need more consideration. The traction in the available vehicle models is simulated per side of the driven bogies, which is accurate to reality. However, traction control was not taken into account to, e.g., stretch the vehicle a bit. Traction control could also influence curve negotiation and therefore wear.

Rail maintenance was not included in the wear rate analysis from profile measurements. During grinding, rail material is removed, measured as wear but caused by maintenance. Since only a little bit of material is cleared (0.1 mm), it was assumed to be no significant factor. During welding, the original profile is restored. Especially in curves that are welded frequently (more than once a year), wear rates could be deceptively low. This might explain some deviations but only regarding horizontal wear.

When comparing the energy estimations and measurements, horizontal wear was directly coupled to dissipation at the flange contact and vertical wear to the tread contact. It might be expected that flange contact is the most significant contributor to horizontal wear. However, this is still an assumption since it is not proven by an e.g. FEM analysis. This topic is an interesting subject of further research. Vertical wear does not influence the horizontal wear measurement directly since the horizontal wear is measured at a fixed point of 14 mm below the original height of the rail. However, severe vertical wear might laterally expand the railhead, reducing horizontal wear.

Another issue concerns the energy estimation model. The model provided estimations of the energy dissipation on all curves on the network based on the VAMPIRE simulations. However, only the 60R2 grooved rail model was used during the simulations. Although this rail profile is dominant on the tramway, running behaviour on, e.g. Vignole rail, might differ, resulting in different energy estimations.

Also, the comparison method which divides annual wear and energy, used in Chapter 6 and 7 should be improved because it is incorrect to assume a linear relationship between wear and total energy dissipation. The non-linear effect on the wear of different energy dissipation values per tram passage could be considered in further research.

Appendix A

Tram Network Characterization

A.1 Overview

This section provides an overview of the tram network in Amsterdam. More details can be found in the following paragraphs.

The city of Amsterdam is one of the largest cities in the Netherlands: the municipality has 870 thousand inhabitants (2021), the continuously urbanized area where Amsterdam is part of consists of nearly 1.2 million inhabitants (CBS, 2021). The city is built upon a former swamp area, which results in the weak subsoil. As a result, most infrastructure is built at ground level or above the ground, although some tunnels exist.

The city centre is old en dense, characterized by many canals and tight streets. Moving out of the city center, the built environment becomes gradually less dense, resulting in more space for infrastructure and traffic.

Amsterdam's standard gauge tram network connects most parts of the city, providing a frequent and dense connection between different parts of the city. The public transport network consists not solely of the tram network. Bus, ferry, metro and train services complete the public transportation network. As shown in Figure A.1, the city centre contains the densest and older tram network. In many cases, tram vehicles share the space with other traffic in the city centre. Amsterdam New-West, Amstelveen and Diemen are served by tram lines separated from other traffic in most cases. Also, the distance between subsequent stations is more extensive, enabling higher velocities.

Schiphol Airport, Bijlmer and Amsterdam North are only served by other transport modalities. GVB, the public transport operator in Amsterdam, had four tram depots, from which one also has a workshop for periodic maintenance. The second and largest workshop could be found in Diemen, where extensive maintenance on both tram and metro vehicles is performed. GVB also has its track workshop where track parts are customized, and maintenance actions are coordinated.

A.2 Rolling Stock

The tram network is fully served by tram vehicles: 70-80% is operated by the Siemens Combino tram. The remainder is done by the CAF Urbos 100 tram, which gradually came into service in 2021, replacing an older tram generation phased out during the same period.

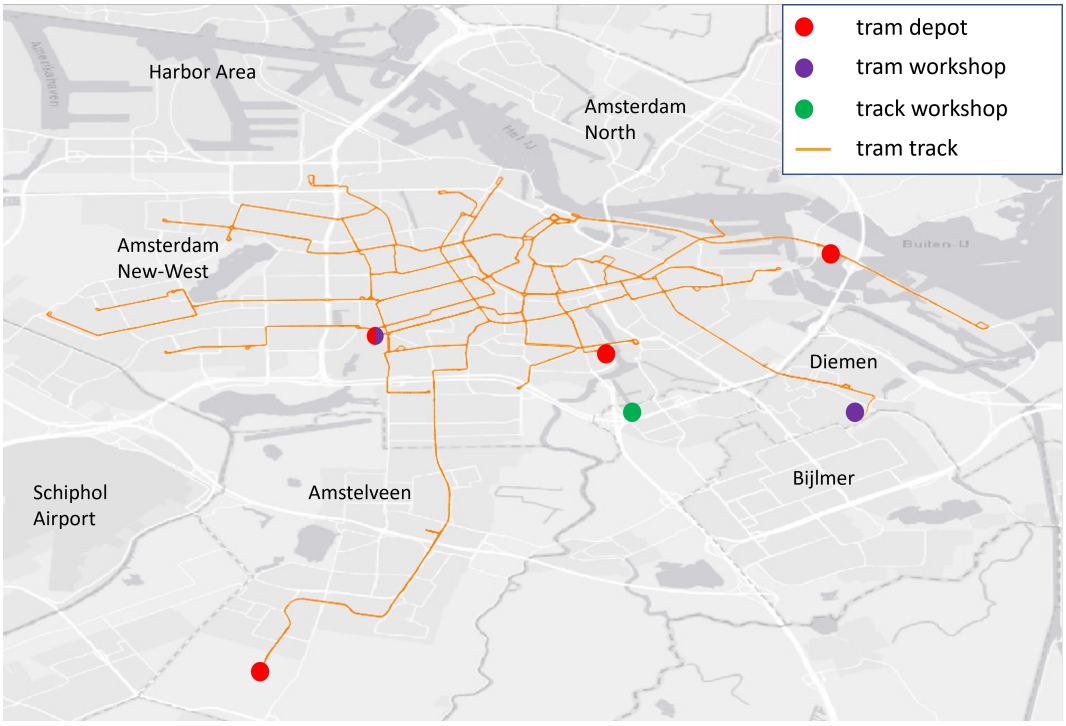


FIGURE A.1: Overview of the tram tracks, -depots and -workshops in Amsterdam.

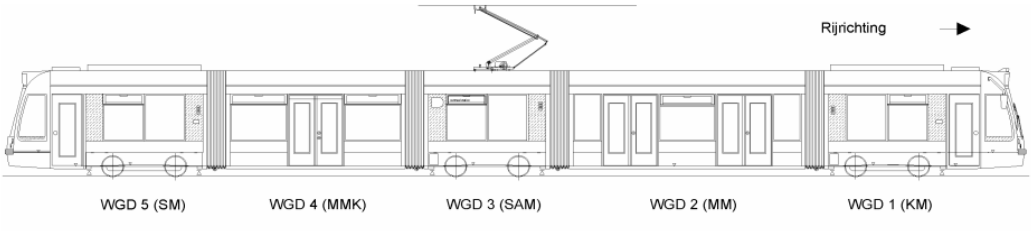


FIGURE A.2: Technical drawing of the Siemens Combino for Amsterdam Siemens, 2007.

A.2.1 Siemens Combino

The Siemens Combino is the primary tram vehicle used on the network in Amsterdam. In total, 155 low floor vehicles of this type were built by Siemens-Düwag between 2001 and 2004. The majority of vehicles are suitable for one direction only. Some have a full control panel on both sides to be compatible with lines without a turning loop at the end. It is possible to couple multiple vehicles to each other to increase capacity. Within GVB the one direction tram is referred to as '13G' (13th tram generation) and the two direction tram as '14G'.

As shown in Figure A.2, the quadruple articulated tram has three boogies attached to the 1st, 3rd and 5th carriage. Two engines, one per side, drive the boogies on the rear and front. This setup means that the wheels per driven boogie per side are electrically coupled. The wheels do not share a joint axle. As a result, the wheels could turn independently of the wheel on the other side in the longitudinal direction (DeltaRail, 2012).

The vehicle's empty weight is 36 ton, the engine power is 4 times 100 kW, and the maximum velocity is 70 kph. The vehicle is equipped with slide and slip protection and has a



(A) A Siemens Combino at line 14 in Amsterdam Simons, 2019.



(B) A CAF Urbos in GVB livery at line 5 at the Marnixstraat/Rozengracht intersection (Martin, 2021).

FIGURE A.3: Tram vehicles used at the tram network in Amsterdam.

length of 29 meters. The total number of seats equal 52 of 59 (depending on one direction only or two direction suitability) and 125 standing places. The independently bearing wheels do have a rubber suspension between the wheel and wheel band, the *as new* wheel diameter is 600 mm, and the maximum worn diameter is 520 mm when replacement of the wheel band is needed. The vertical stiffness of the primary suspension is 2.4 kN/mm, and the horizontal stiffness of the primary suspension is 3.4 kN/mm per wheel, the horizontal stiffness of the secondary suspension per wheel 0.5 kN/mm (DEKRA, 2020). Those stiffness values change over time or during maintenance. In general, the older suspension becomes stiffer. Figure A.3a shows a picture of a Siemens Combino on line 14 in Amsterdam.

A.2.2 CAF Urbos 100

The CAF Urbos 100 tram is a new low-floor tram vehicle that gradually came into service in 2021. In total, 63 vehicles will join the tram fleet of 155 Siemens Combino trams. CAF has been building the tram vehicles for Amsterdam since 2019, and the last one is scheduled to be finished in 2022. All trams have a full control panel at both sides, making turning loops at the end of lines no longer necessary. It is possible to couple vehicles to each other to increase capacity. Within GVB the vehicle is referred to as '15G' (15th tram generation). The maximum velocity of these vehicles is 70 kph, which is equal to the Siemens Combino.

Figure A.3b shows a picture of the CAF Urbos tram in GVB livery. The quadruple articulated tram has three boogies attached to the 1st, 3rd and 5th carriage. The front and rear boogies are driven. In contrast to the Combino, all four wheels per driven bogie are driven by a separate engine. Also, each wheel has individual bearings, which prevents longitudinal slip during curve negotiation. The vehicle's empty weight is equal to 43 tons, which is an increase of 19% compared to the Siemens Combino. The vehicle length equals 30 meters, and the capacity is similar to 50 seats and 125 standing places. The wheels do have rubber suspension and a *as new* diameter of 600 mm.

A.3 Public Transport Network Amsterdam

The urban public transport system of greater Amsterdam contains train, metro, tram, bus and ferry services. Figure A.4 shows the tram- and metro network, and the main train stations.



FIGURE A.4: Simplified overview of the urban public transport network of greater Amsterdam.



(A) Typical lay-out in the city center, Rembrandtplein.



(B) Typical lay-out in the greater city center, Surinameplein.

FIGURE A.5: Typical tram track lay-outs in the larger city center.

The urban tram network provides a good connection between nearly all places in the greater city centre, roughly within the highway A10 ring, south of the IJ river. It consists of a dense network of lines, served by (single) Combino and Urbos 100 vehicles which often has to drive at small streets with tight curves, cross canals over old bridges and share space with other traffic. During the day, lines are served between 6 and 12 minutes. Figure A.5a and A.5b show some typical track layouts for the greater city centre, especially the rails encased in asphalt is very common. Also, plates instead of asphalt are used very often.

Amsterdam New-West and Diemen are also severed by urban tram lines that branch out of the city centre. Outside the greater city centre, the tram tracks lay separately from other traffic with more space between subsequent stations. This layout increases overall velocity, and the characteristics tend to go more to lines 25 and 26, which will be explained in more detail. Figure A.6 shows tram 13 at the Jan van Galenstraat, with a typical track layout for outside the greater city centre.



FIGURE A.6: GVB Combino op lijn 13 bij de halte Jan van Galenstraat (Eelco, 2021).

All tough lines 25 and 26 are part of the tram network. The characteristics of those lines tend to be an intermediate between metro and tram. No shared space with other traffic, increased distance between stops, and higher overall velocities.

Line 25 from Amstelveen to the South station used to be a *light* metro line, served by smaller metro vehicles, all tough till the centre of Amstelveen the track was and is still shared with the urban tram line 5. Recently the line has undergone extensive renovation and is now only suitable for trams. In practice, the new CAF Urbos 100 trams are exclusively used, often in coupled formation, while velocities in between stops reach 50-70 kph. Line 25 will be extended to Uithoorn, a village south of Amstelveen.

Line 26 runs from IJburg to central station and runs isolated from other lines. Only Siemens Combino trams are used on this line, often in coupled formation. Also, this line will probably be extended in the future to accommodate further expansion of the IJburg district. Both lines run at a frequency of about 6-10 minutes during daytime. Figure A.7 and A.8 show respectively line 25 and 26 with their usual track layout and vehicle composition.

While the greater city centre and outside districts/places IJburg, Nieuw-West, Amstelveen and Diemen are primarily connected by tram. Amsterdam Bijlmer and North are connected by metro to the other parts of the city. In the case of Amsterdam North also ferries over the IJ river, and buses play an important role. The metro also provides a ring line around the greater city centre, while tram lines cross the greater city centre. This ring line is not finished between Amsterdam Sloterdijk and Central station. However, frequent train services between both stations provide an alternative.

Nowadays, Schiphol Airport is connected by train and bus services. In the future, the airport might also obtain a connection by metro. Besides rail vehicles, many lines in the city



FIGURE A.7: To coupled Urbos trams on line 25, here the line was being tested after the renovation (Dubbelman, 2020).



FIGURE A.8: Two coupled Siemens Combino's at line 26 (EenRailSpotter, 2020).

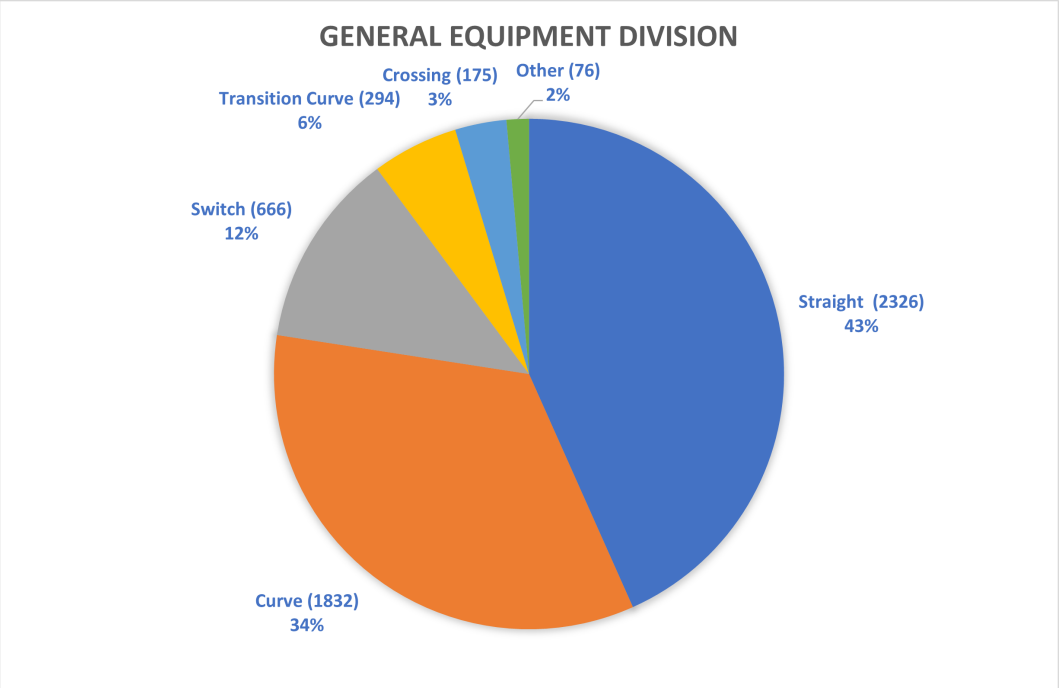


FIGURE A.9: Equipment division on the network, numbers between parenthesis are the number of equipment objects per category.

are served by buses. Some of these high-frequency bus lines also run to neighbouring towns. Figure A.4 also shows the intercity train stations.

A.4 Infrastructure Characteristics

This section provides an overview of some infrastructure characteristics of the tram network in Amsterdam. In this section characteristics are shown for the network in general and for tight curves (radius < 30m). The data used for the diagrams and maps used originates from February 2021.

Figure A.9 shows the general equipment division of the tram network, the units in parenthesis are amounts; e.g. the network consists of 1832 curves. From the picture, it is clear that curves form a significant part of the network composition, 24% of all curves is tight (radius < 30m), as shown in Figure A.10. Figure A.11 shows the age of the track since it was renewed or newly built. The vast majority of the tracks are renewed in the past 30 years, some parts are 30-40 years old and older than that is very rare.

Figure A.12 and figure A.13 show the last renewal year categories in relation to each other for both the whole network and tight curves. The majority of the network is not older than 20 years, and the vast majority is not older than 30 years. Tight curves are not renewed earlier or later than other parts of the network. Figure A.14 reveals the location of tight curves. Tight curves are positioned at the red dots on the tram network (black). As shown, most tight curves at located at junctions. Those junctions primary exist in the city centre but could also be found at other places.

Figure A.15 and A.16 shows the usage by other traffic of the tram tracks. This usage by other traffic appears mostly in the greater city centre where cars, bikes, scooters, etc., also drive at the tram tracks. Also, often the tracks are only shared with buses and taxis (called

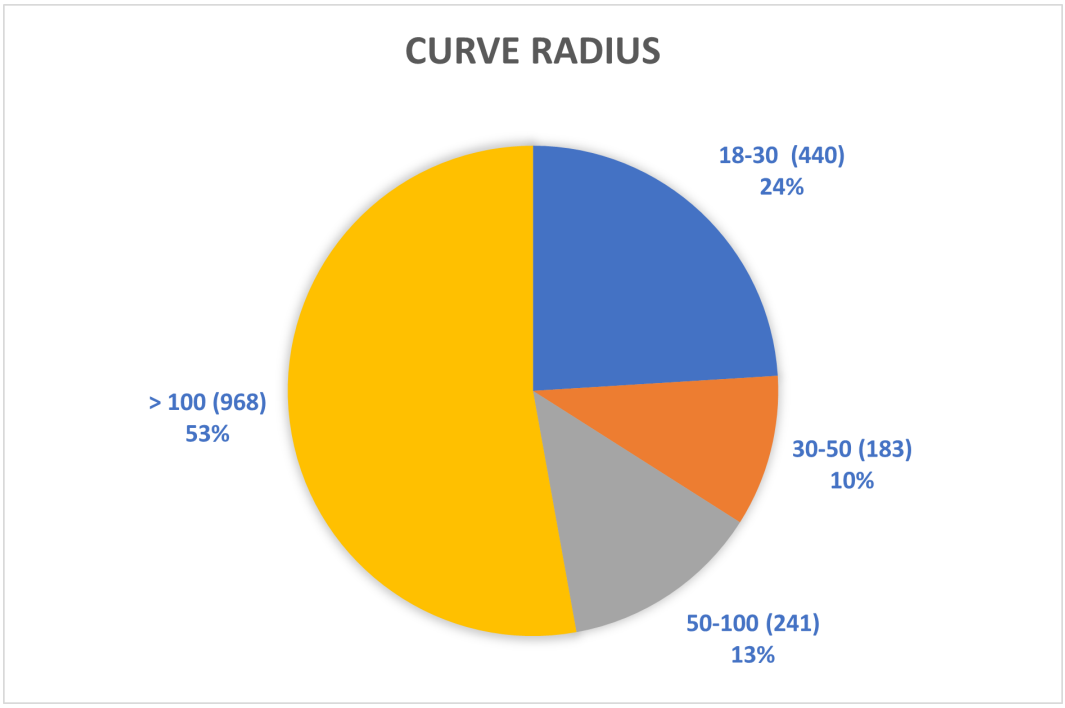


FIGURE A.10: Curve radius distribution [m].

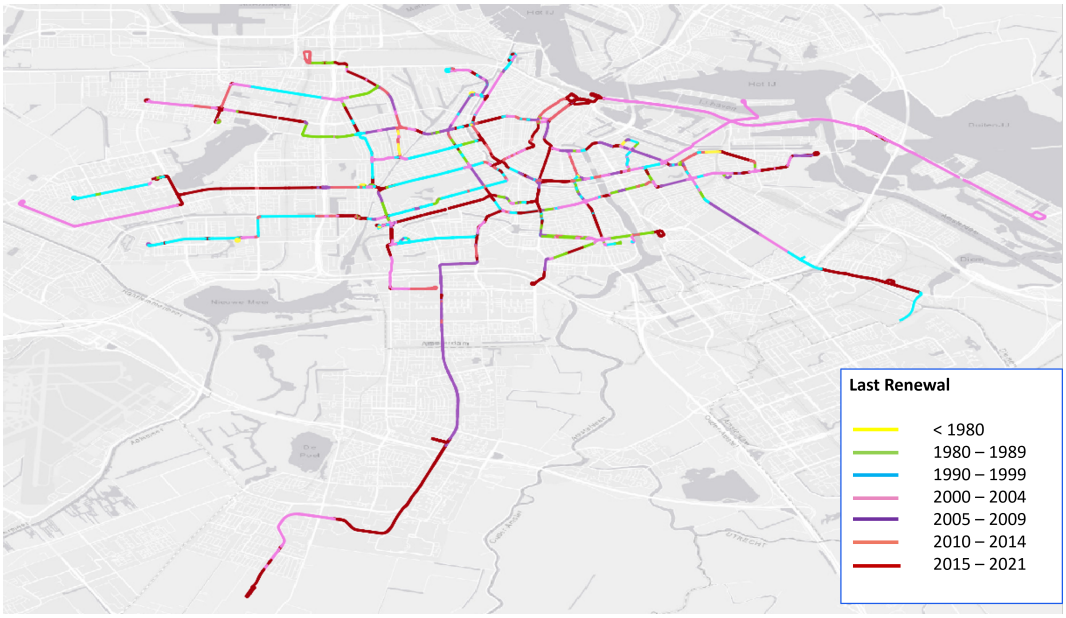


FIGURE A.11: Last track renewal year.

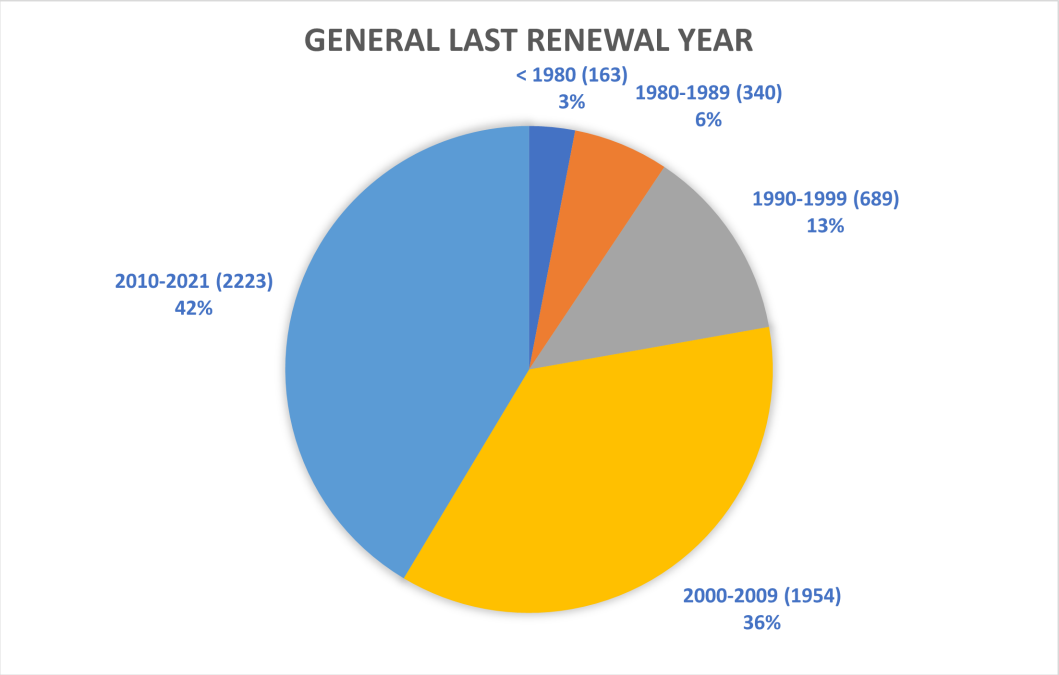


FIGURE A.12: General last renewal year of parts on the tram network.

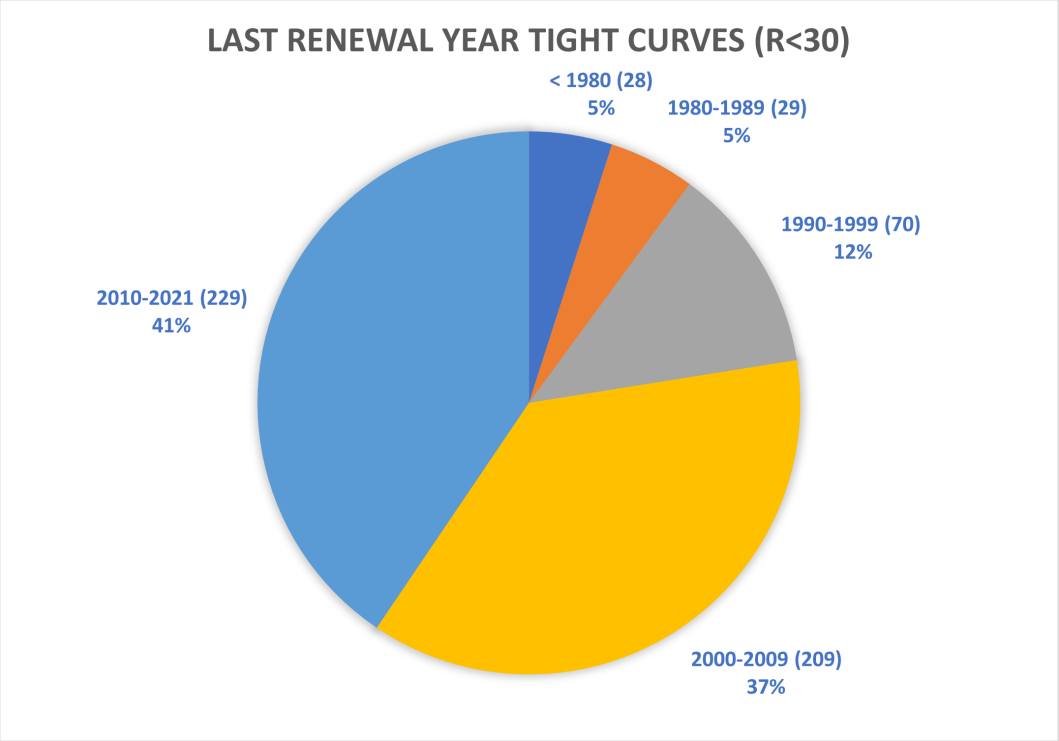


FIGURE A.13: Last renewal year of tight curves (radius < 30 meter).

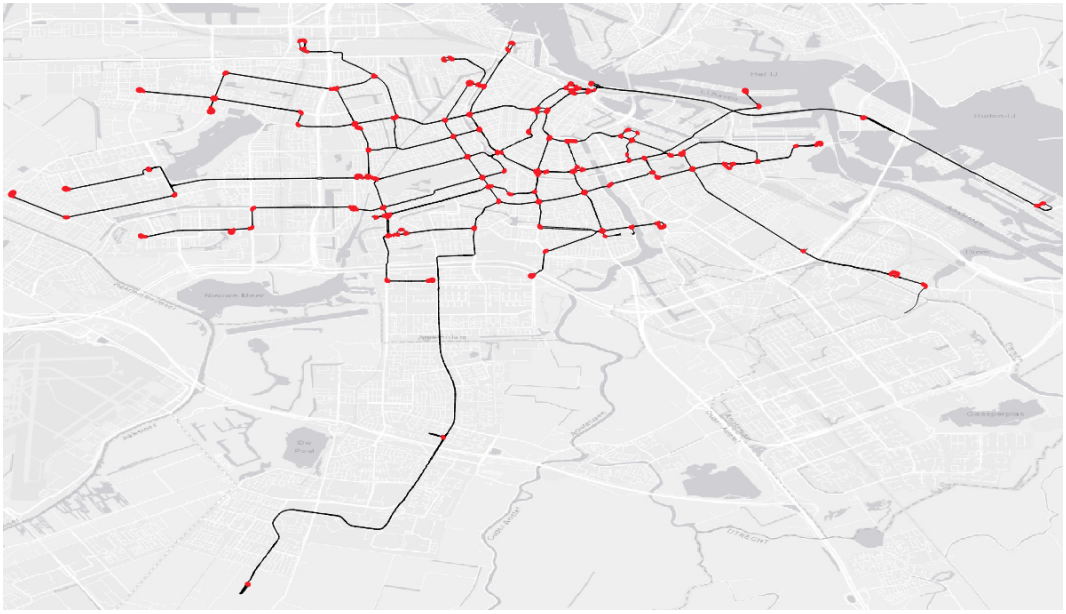


FIGURE A.14: Location of tight curves (radius < 30 meter).

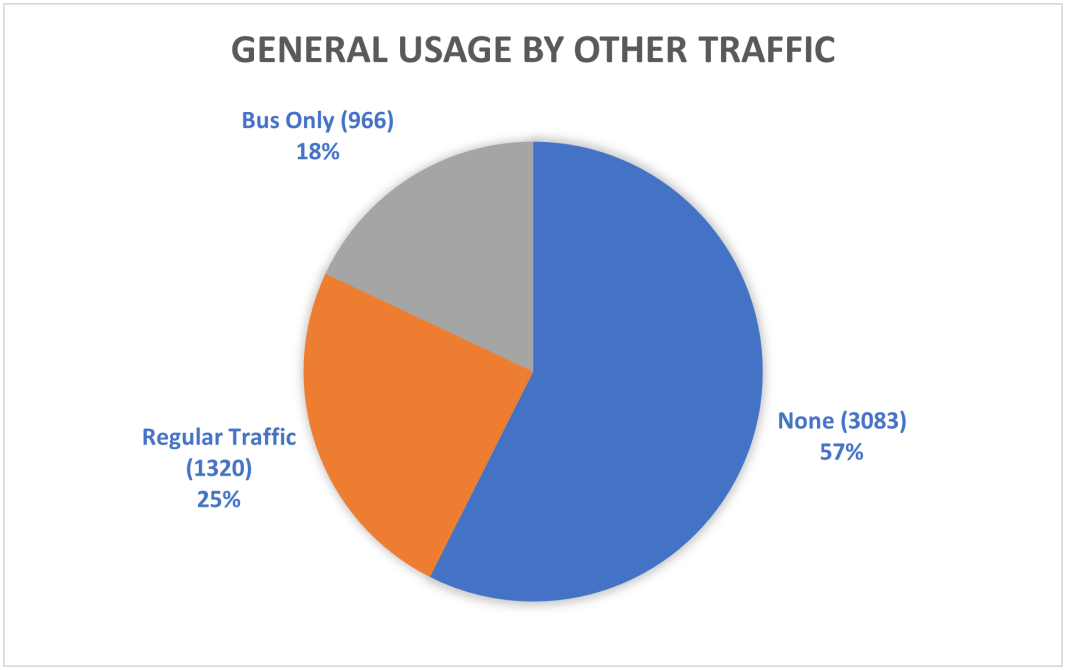


FIGURE A.15: General usage by other traffic.

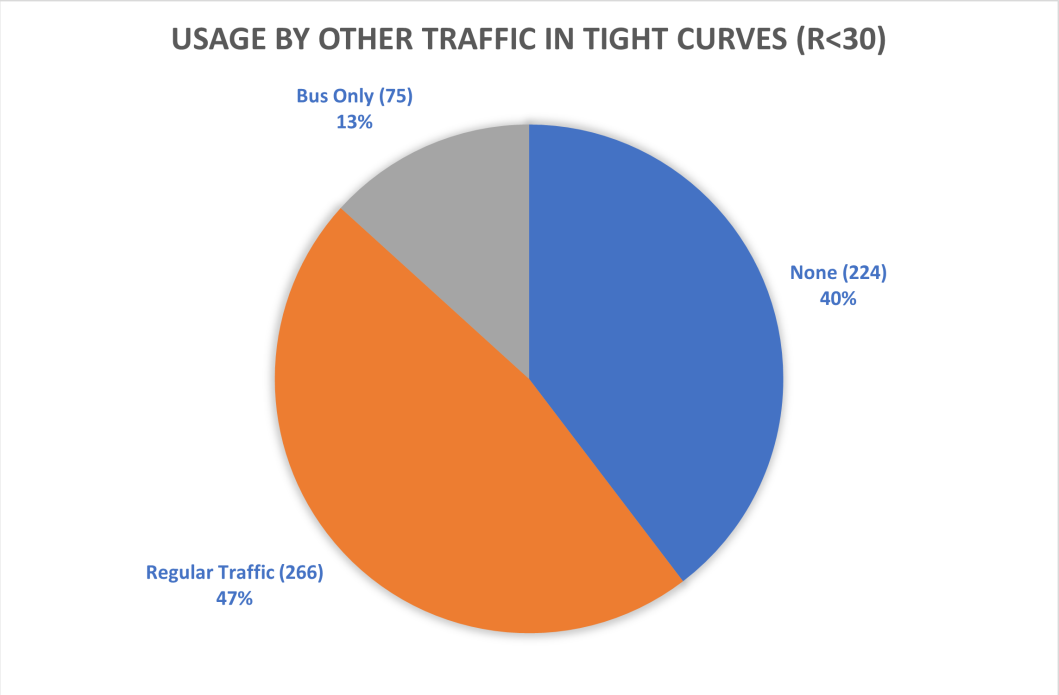


FIGURE A.16: Usage by other traffic tight curves only (radius < 30 meter).

'bus only' in the graph). It appears that tight curves are more often than average located in places where regular traffic is allowed to drive.

Figure A.17, A.18, A.19, A.20, A.21, A.22, A.23 and A.24 show the used rail type, steel sort, rail fastening and hardening for both the network in general and tight curves (radius < 30 meter)

Regarding the rail type, 78% consists of 60R2 groove rail, in curves (85%) and tight curves (90%) this percentage is even higher. The other rail types are mostly found at older track segments. The used steel sort is in the vast majority of cases R200. In comparison, on the Dutch heavy rail network, R260 is the most usage steel sort (Prorail, 2010). There is a wide range of rail fastening systems. Sleepers can only be used when the tram has a monopoly on space. VKB fastening systems, where the rails are mounted with clamps to the track base, is more often seen at newer track segments.

The rail and filling material (often concrete) are separated by an encasement, sealed with rubber to overcome water intrusion. In the case of a rigid fastening system, the rails are fixed by the filling material. Note that the rails are also mounted with clamps to the sleepers in the case of sleepers. Regarding hardening type, asphalt, plates, concrete, and stones enable the usage by other traffic. Therefore it is no surprise that these dominate the hardening type of tight curves. Ballast end sleepers are used together most of the time, which is the conventional heavy rail superstructure.

A.5 Network Usage

Figure A.25, A.26 and A.27 show the network usage. Especially the amount of tram passengers per track segment is important since it will play an important role in estimating wear rates. Also, the tram loading is of interest since a loaded tram alters the weight and

the centre of mass, which alters the rolling behaviour of the tram vehicle. The usage characteristics in these figures are only relative since the absolute values are not representative because of COVID19 related measures. The research used data from September 2021, which was not affected at a large extent by COVID19 measures.

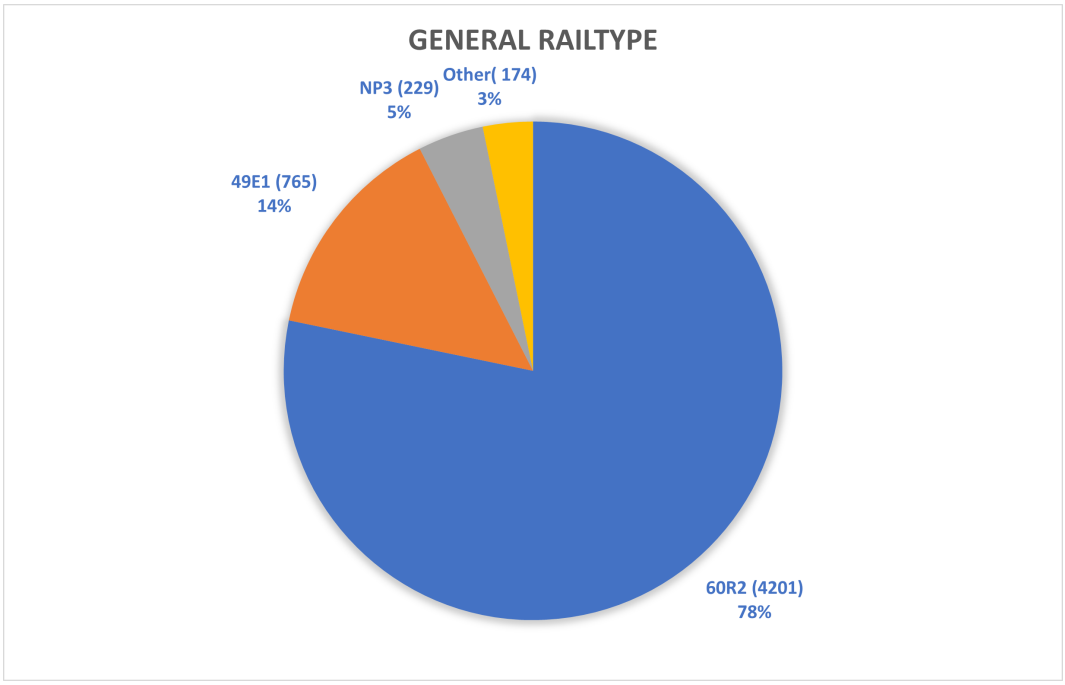


FIGURE A.17: General railtype.

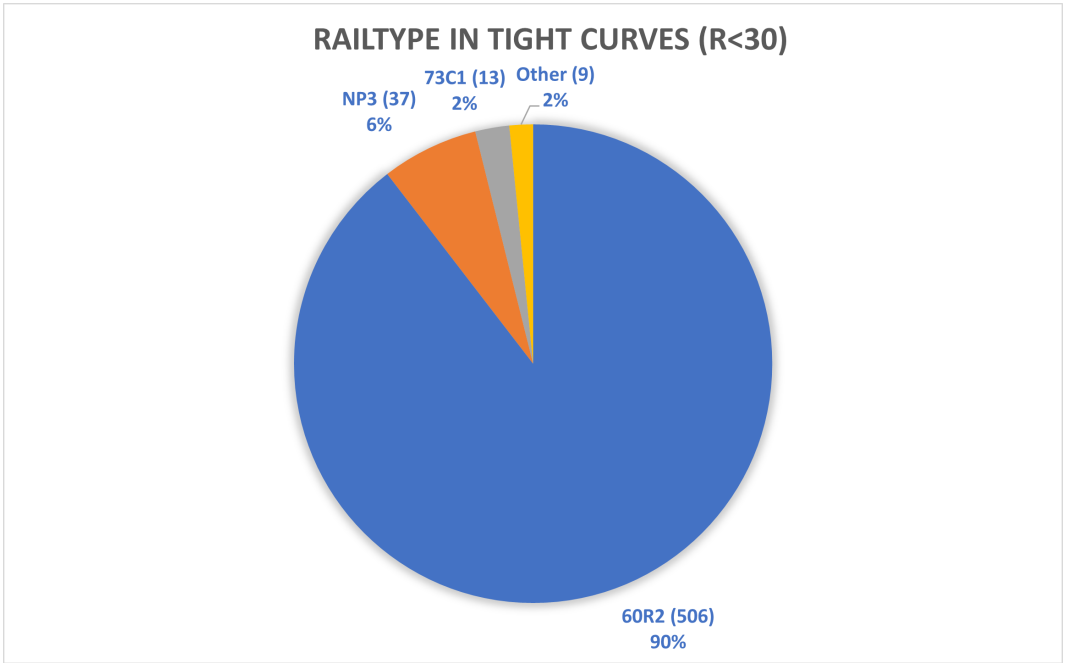


FIGURE A.18: Tight curves railtype.

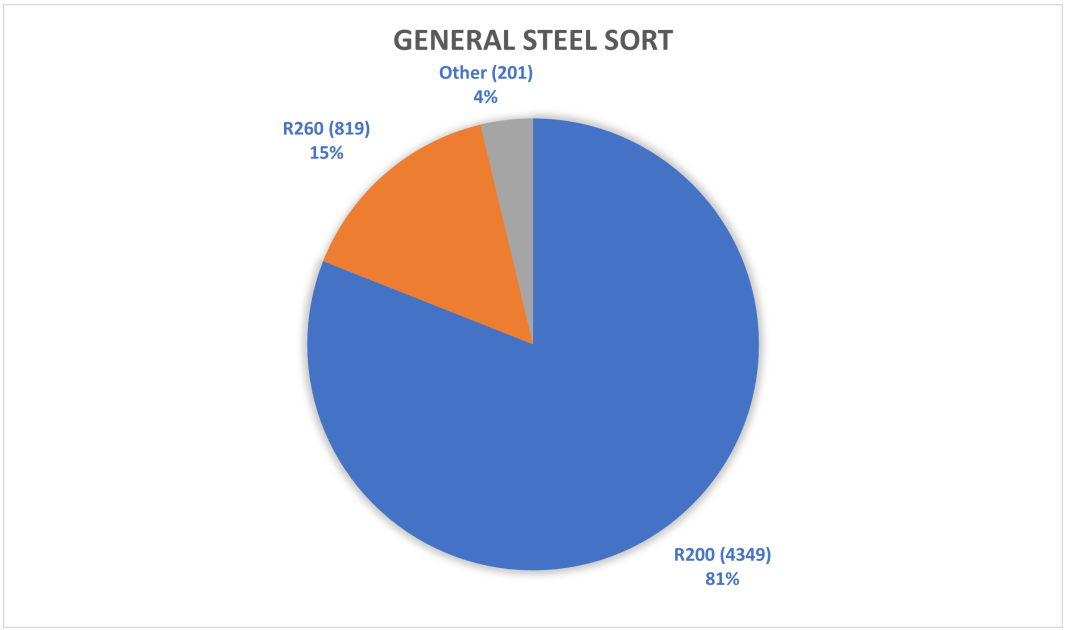


FIGURE A.19: General steel sort.

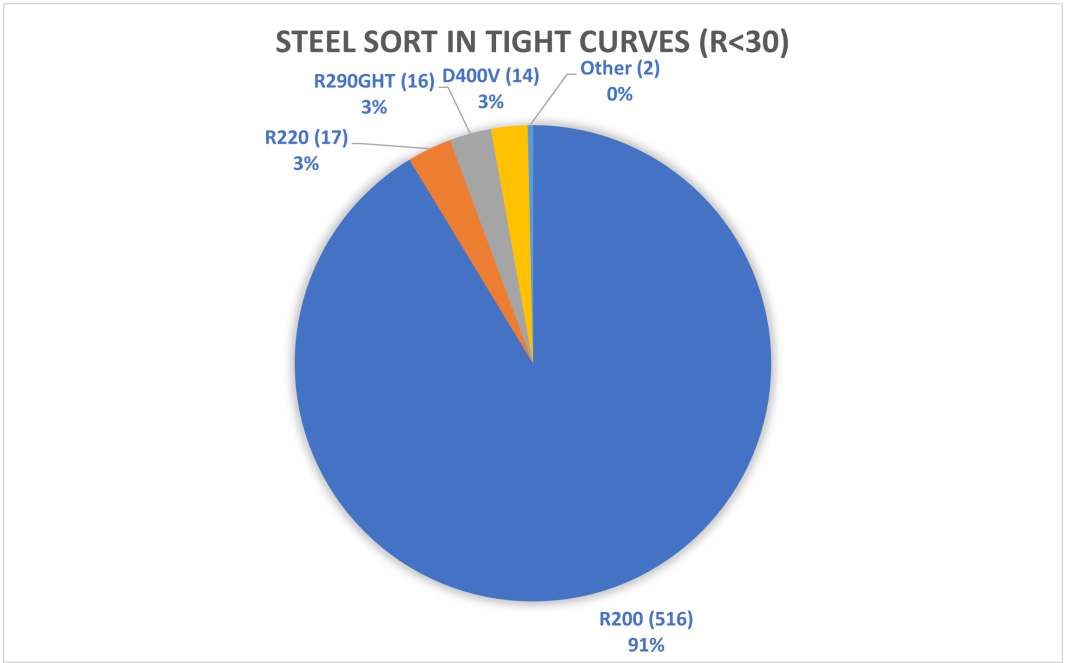


FIGURE A.20: Tight curves steel sort.

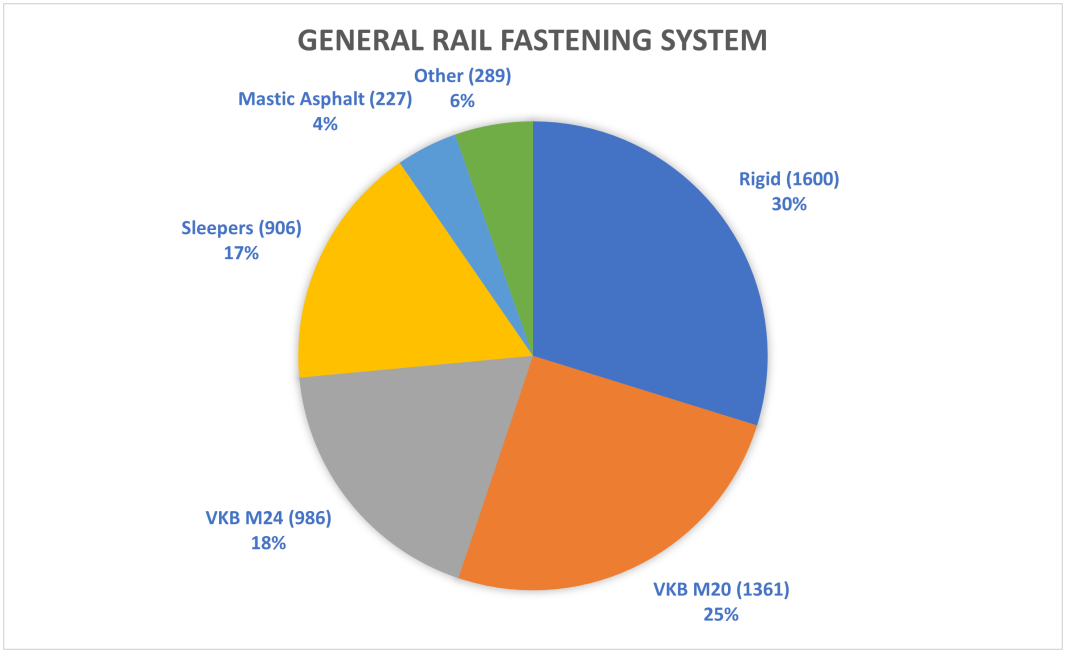


FIGURE A.21: General rail fastening system.

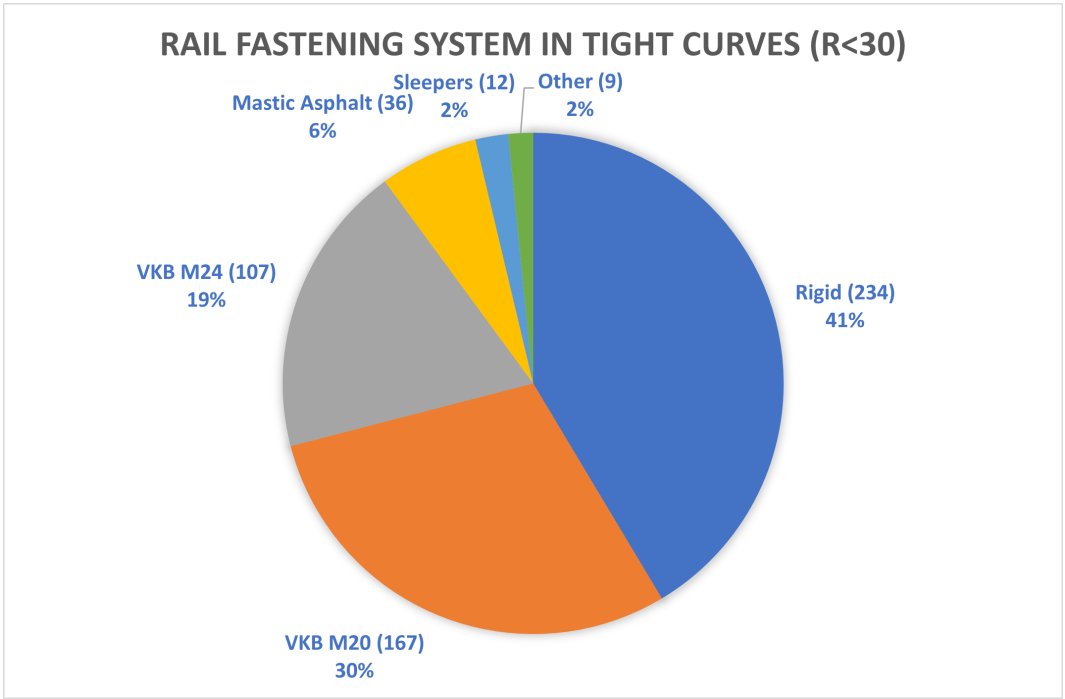


FIGURE A.22: Tight curves rail fastening system.

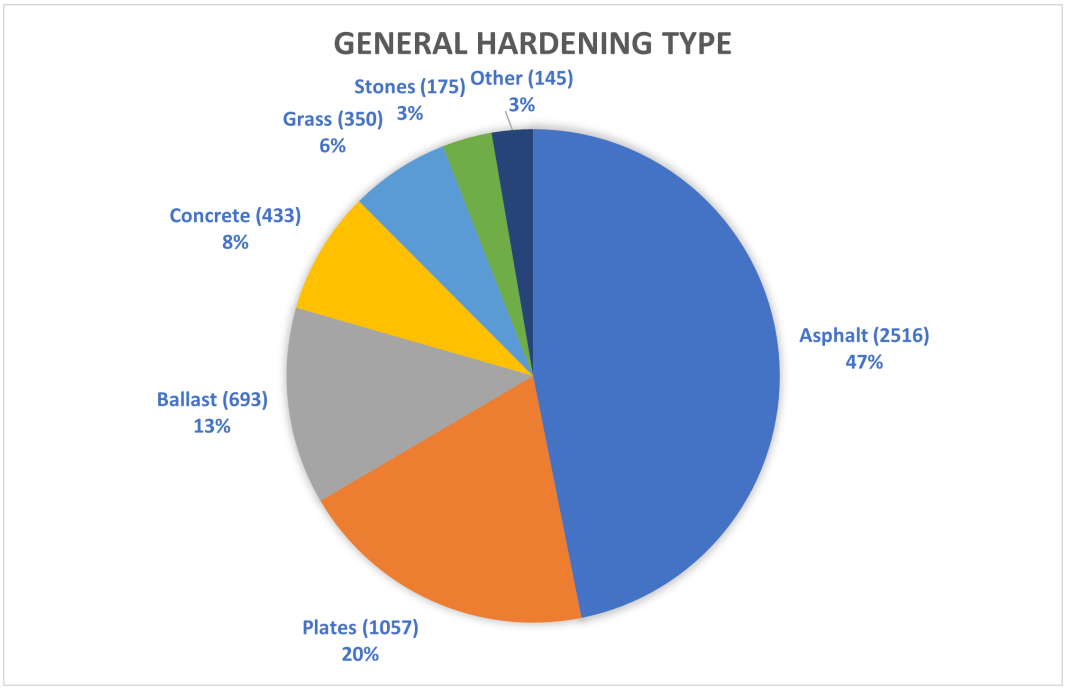


FIGURE A.23: General hardening type.

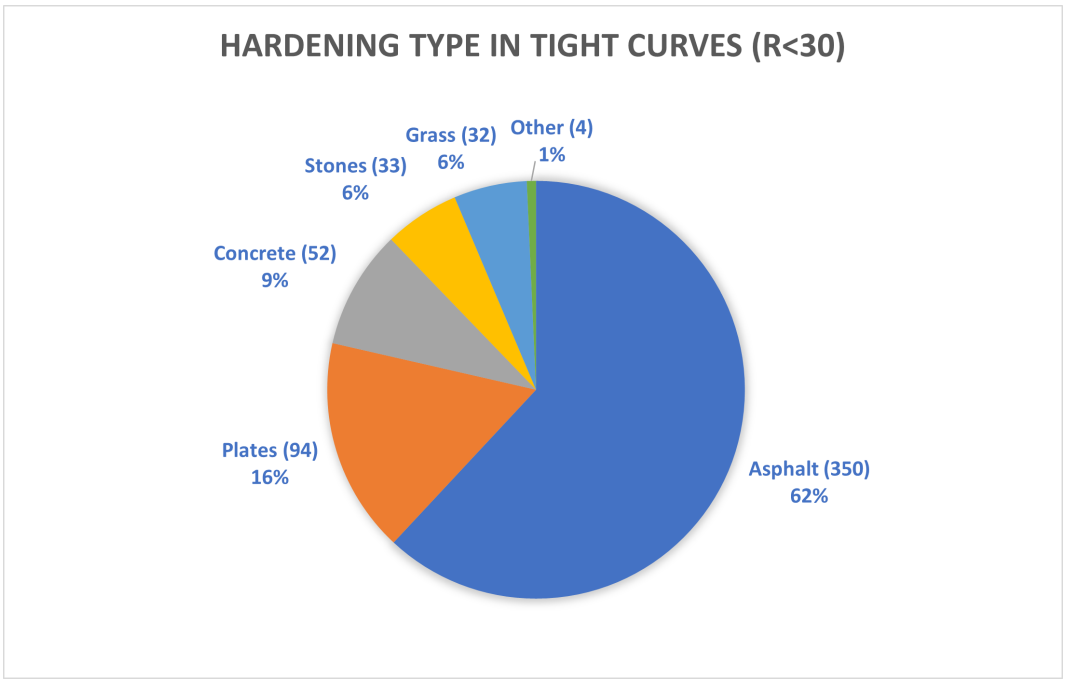


FIGURE A.24: Tight curves hardening type.

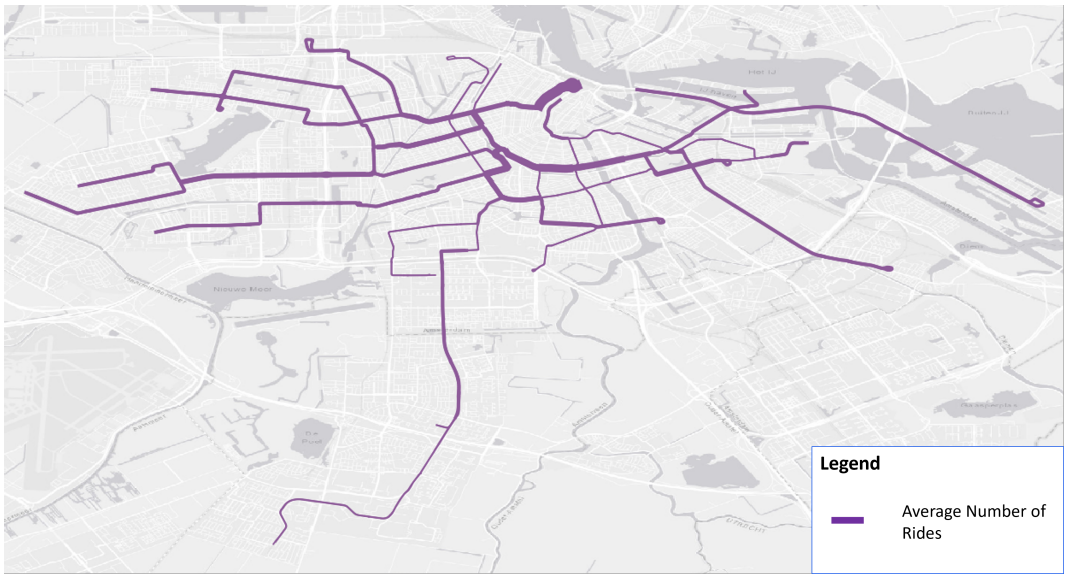


FIGURE A.25: Tram passages per track segment.

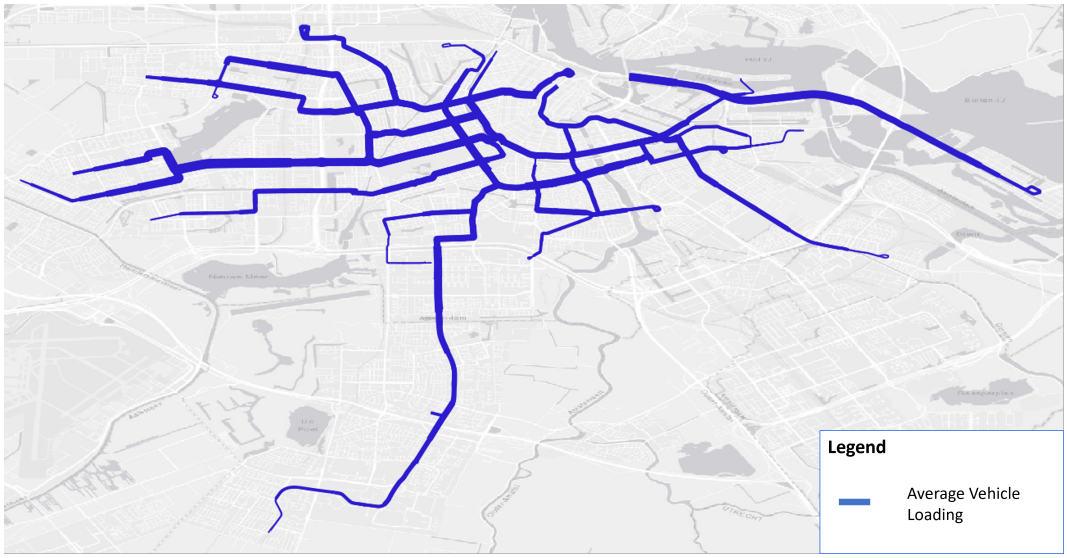


FIGURE A.26: Average loading per vehicle per track segment.

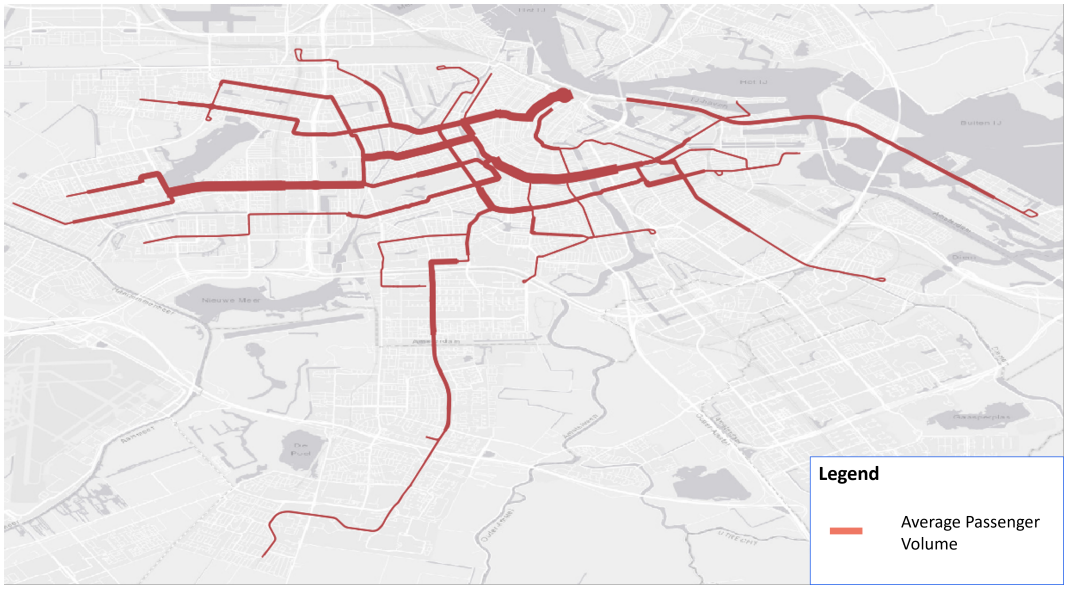


FIGURE A.27: Total volume of passengers per track segment.

Appendix B

Comparison Measurements and Estimation Results

This appendix shows the comparison between measurements and energy estimations from about 200 curves. The comparison is described and commented in 7.

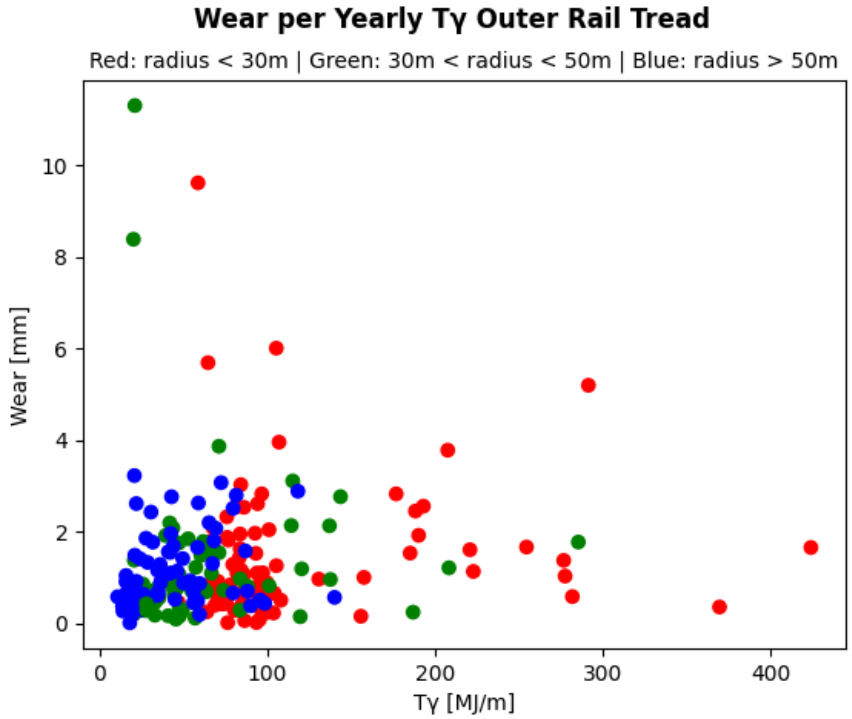


FIGURE B.1: Scatter plot of the yearly estimated energy dissipation and measured wear of the outer rail tread.

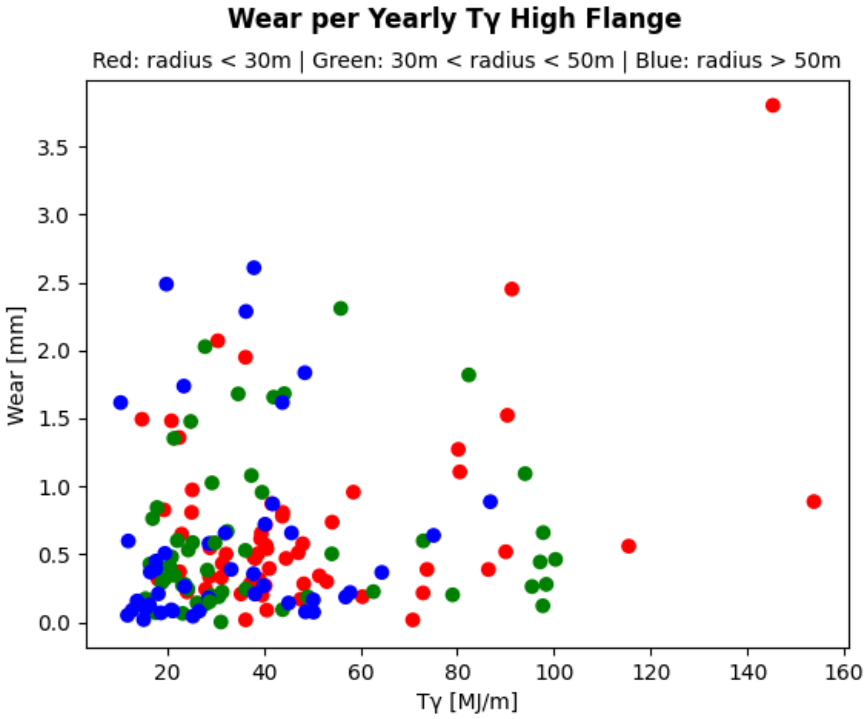


FIGURE B.2: Scatter plot of the yearly estimated energy dissipation and measured wear of the outer rail flange.

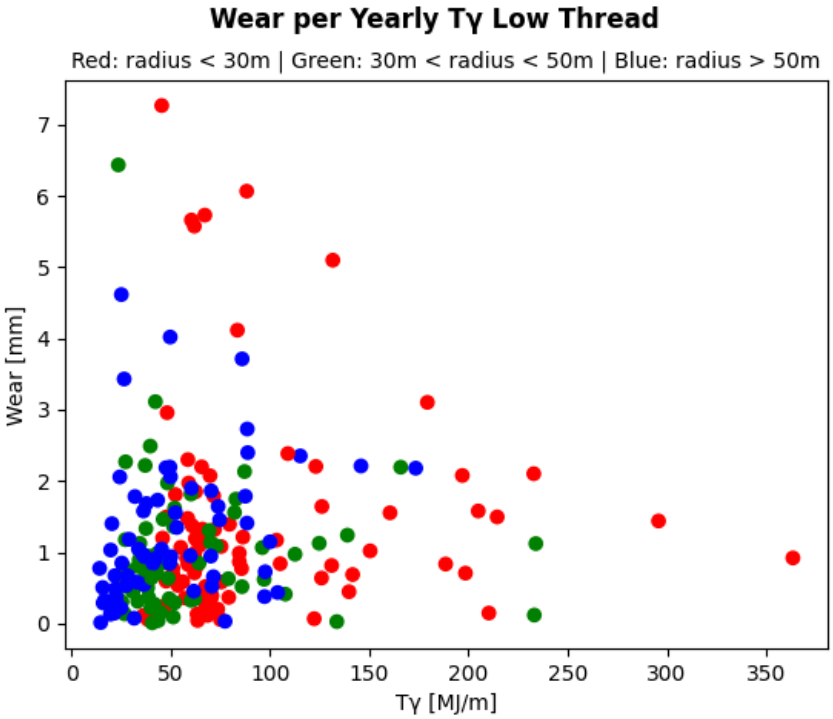


FIGURE B.3: Scatter plot of the yearly estimated energy dissipation and measured wear of the inner rail tread.

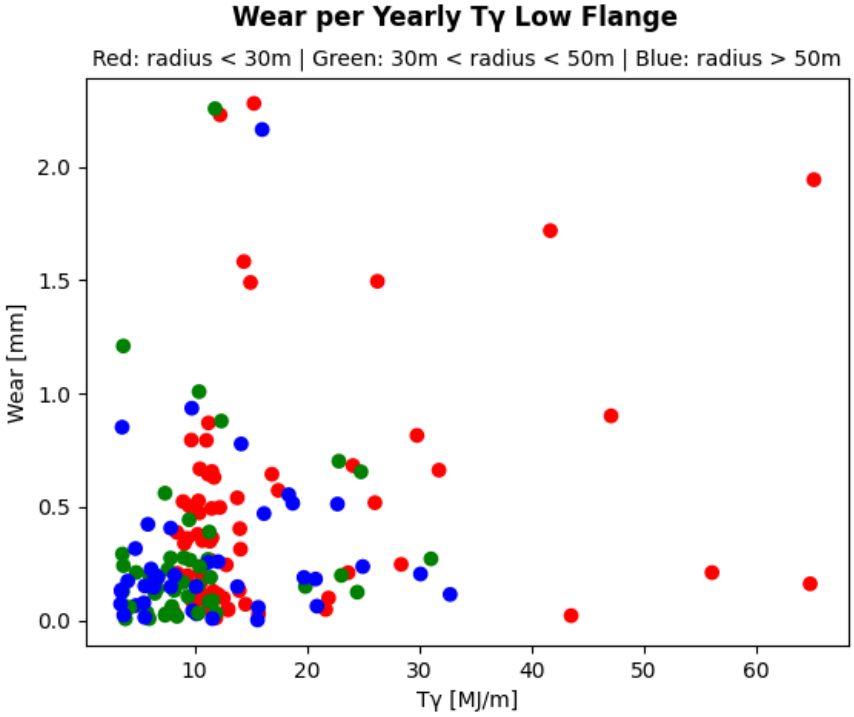


FIGURE B.4: Scatter plot of the yearly estimated energy dissipation and measured wear of the inner flange.

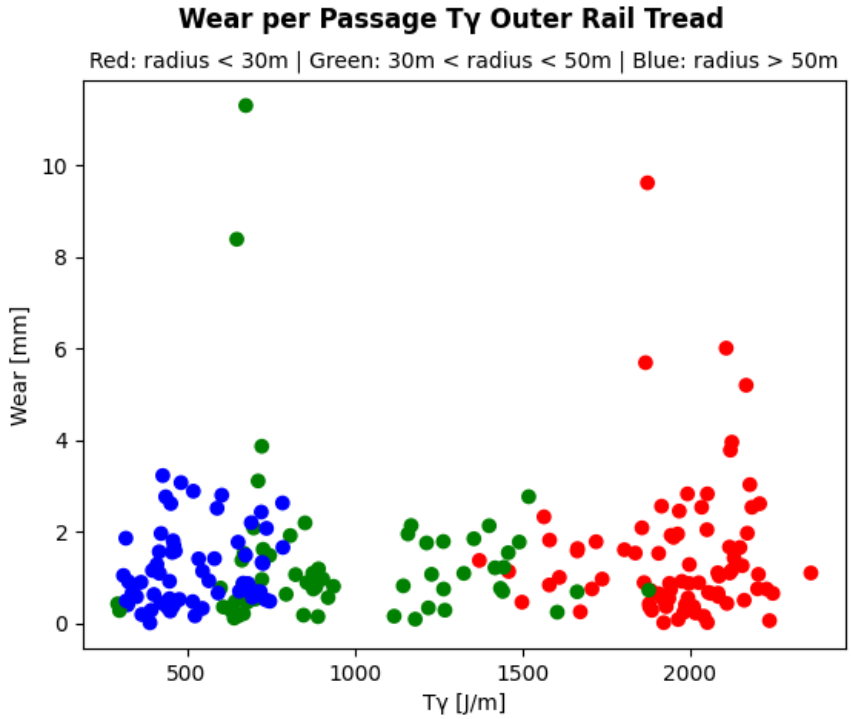


FIGURE B.5: Scatter plot of the estimated energy per passage and yearly measured wear of the outer rail tread.

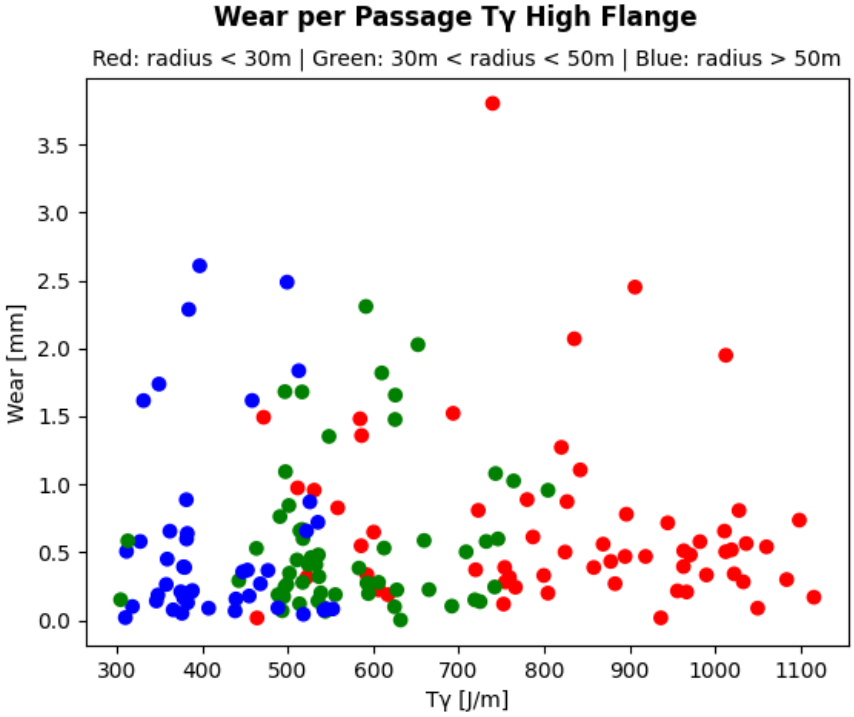


FIGURE B.6: Scatter plot of the estimated energy per passage and yearly measured wear of the outer rail flange.

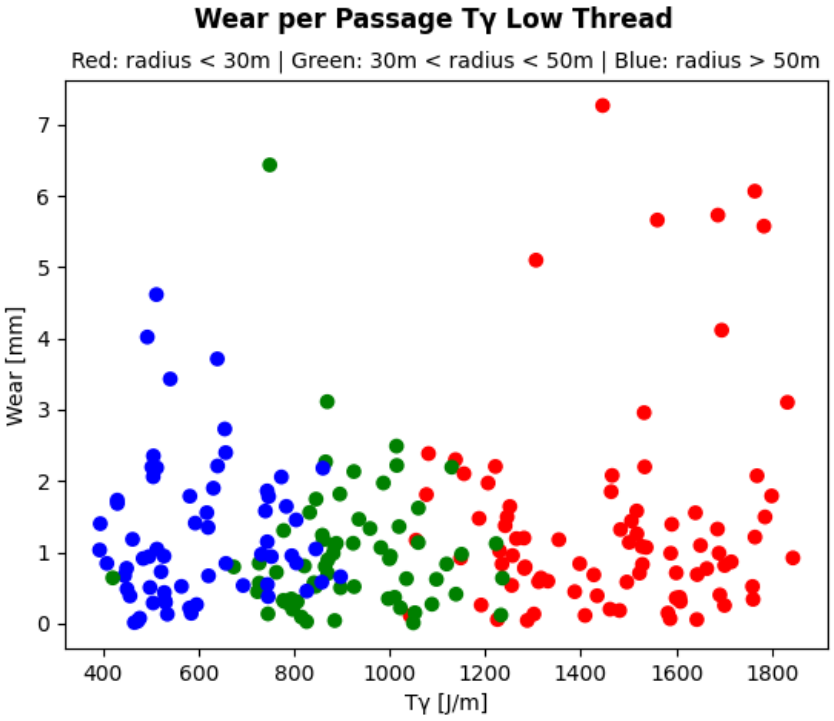


FIGURE B.7: Scatter plot of the estimated energy per passage and yearly measured wear of the inner rail tread.

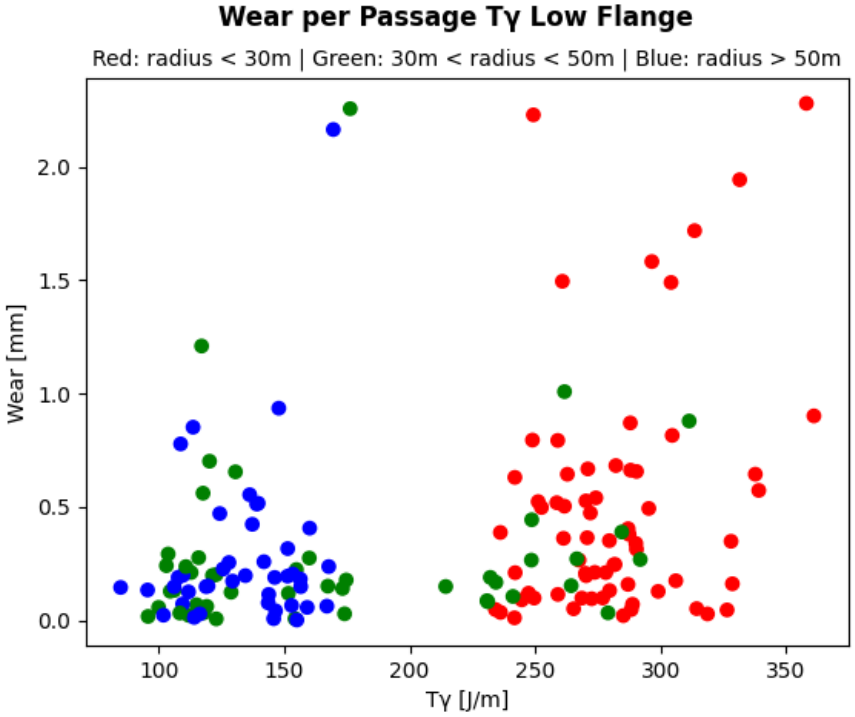


FIGURE B.8: Scatter plot of the estimated energy per passage and yearly measured wear of the inner rail flange.

Appendix C

Velocity Coupling Model Description

C.1 Introduction to the Velocity Coupling Method

The method aims to couple velocity log data sent by tram vehicles to track segments and determine a one-meter accurate average velocity along the track. This method gives insight into the velocity distribution per curve, straight, crossing and switch, and driving behaviour of the tram. With this information, we can answer questions such as *at what point do trams start to brake or accelerate? Do tram drivers of coupled trams accelerate later to account for the rear vehicle, which is still negotiating a curve?* The answers to those questions could help to understand the occurrence of excessive rail wear. The coupling process consists of Steps 1, 2A, 2B, 3 and 4: loading and process input data; determine route and trackpoints; couple nearest valid trackpoint; velocity per tracknumber analysis and export data. These steps will be elaborated in detail in this appendix. It was chosen only to analyze track segments used in regular passenger operation to fasten the analysis. First, some basic terms used to explain the process are explained.

C.1.1 Tracknumbers

Each track part has its number in GVB administration to track information like steel type, rail sort and curve radius. In this Appendix, those numbers are called tracknumbers, Figure C.1 shows an example of the tracknumber division. All velocity loggings are aggregated per tracknumber to create velocity distributions per tracknumber.

C.1.2 Trackpoints

Trackpoints are created by separating the track centerlines per meter along straights, and with a smaller interval along curves, each tram logging is coupled to the nearest trackpoint on the route. This coupling enables velocity analysis with an accuracy of 1 meter,

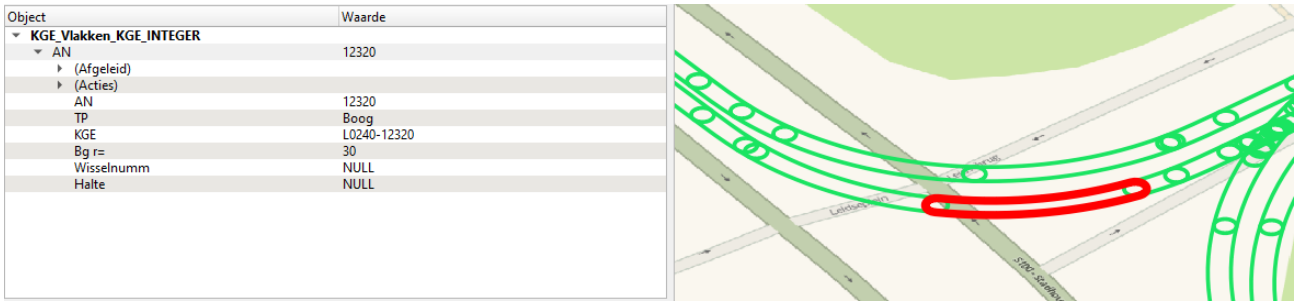


FIGURE C.1: Each piece of track has its own tracknumber, on the left the tracknumber ('AN') is visible for the curve part encircled in red.

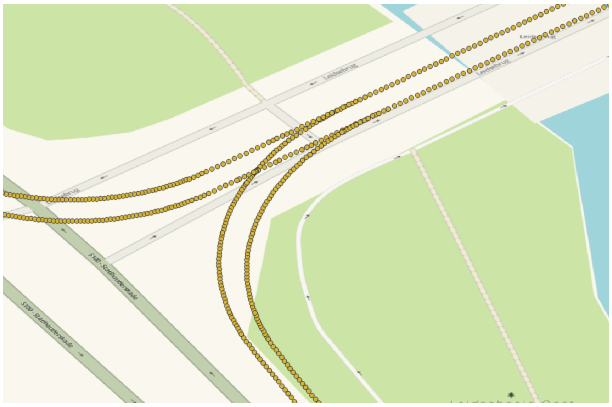


FIGURE C.2: Trackpoints used in the velocity analysis.

Object	Waarde
KGE_Punten_WGS84_C	
AN	12320
(Afgeleid)	
(Acties)	
AN	12320
X	4,8803110547
Y	52,362888146
Z	0
M	0

FIGURE C.3: Data attached to each trackpoint.

provided sufficient loggings are available per trackpoint. Figure C.2 shows an example of how each track is divided into points, Figure C.3 shows the available info per trackpoint: the tracknumber where it belongs to (AN) and the coordinates (WGS84 reference).

C.1.3 Routecodes

The tram network consists of multiple different tram lines. Those lines could intersect at some points or share the same tracks. Therefore, it is impossible to determine where a tram was driving only using the coordinates. To solve this, the analysis uses routecodes assigned to specific routes in specific directions.

C.2 General Description of the Analyzing Process

As stated in the introduction of this chapter, in essence, 6 million geometrical points need to be coupled to the nearest point out of a set of 273000 trackpoints, to analyze one week of data. The method was coded in Python. The Python code first determines the coupling conditions and then the nearest valid point based on the log- and track points coordinates. This method assumes no significant error since the distances will be calculated using coordinates not larger than 100 meters. The resulting code is made such that GVB employees could use the code in the future to analyze velocity distributions in a different week. When the routes or network has been changed, the trackpoints and tracknumbers on the route should be updated first. The code also includes a file check functionality to read and check input data before running the whole code since the input file with tram loggings is too large to open in, e.g. Microsoft Excel. When the code is run with PyPy PyPy, 2021, an alternative way of running Python code that increases velocity significantly, it takes 12-14 hours to couple 6 million loggings, which is around one week of data, on a 2.5 GHz CPU. QGIS is used to plot the output of the code on the map, which results in immediate insight into driven velocities at the tram network.

C.3 Step 1 : Loading of Input Data

Per input data category needed for the analysis, the data itself and the loading process are described. Figure C.4 shows this step in a flow chart.

C.3.1 General Input: Grid and Day Range

The general input consists of the reference coordinate and the desired day range, which should be included in the analysis.

A virtual square grid is created with the reference points in the lower-left corner and the upper right point 1/2 longitudinal line to the right, and 1/2 latitudinal line upwards. The grid size is about 30*30 meters (1/2000 of the distance between a longitudinal or latitudinal line with the WGS84 reference system). This grid is needed to spatially group the trackpoints and loggings to consider only trackpoints in the vicinity of the log location.

C.3.2 Tram Logdata

The tram log data contains tram loggings which include the following information: logtime, coordinates, velocity and vehicle number. The speed is directly reported from the vehicle. The coordinates are based on the position of the front cab of the tram (cab in driving direction). Figure C.5 shows the result of loading all loggings of ten days directly in QGIS, the locations are mostly accurate since most loggings lay close to the track lines. However, it was not feasible to perform a spatial coupling with those loggings directly in QGIS since the number of spatial points which should be coupled was too large. During the data loading process, first, the completeness of the input file is checked. When columns are missing or not recognized, the code will terminate and output the missing data. After this first check, the data is sorted and added to the internal database structure of the code. Next, the coordinates of each logging are checked with the reference coordinates (see General Input: Grid and Day Range in this section). When coordinates fall outside the predefined grid, the log is considered faulty and excluded from further analysis. Also, when a logging falls outside the specified day range, it is excluded from further investigation at this point. For the loggings that are still left after this step for each one, it is determined to which grid it belongs. The grid id (xxx,yyy) is then assigned to each logging.

C.3.3 Tram Routedata

The tram routedata is used to determine for each vehicle at which line it was running in which direction for any point in time. Every time a tram is *set* for a new run, e.g. at the start of the day or a turning point of the line, it sends a notification that includes the time, current route code and vehicle number.

During loading, the routedata is first checked for completeness. If everything is in order, per vehicle a routelist is created based on the route start notifications. The routelist contains the routecode and the time of notification. It assumed this routecode stays valid till a new route start notification is sent or 2 hours after the notification. In normal circumstances, none of the routes takes over 2 hours to complete for a vehicle. Tram loggings sent outside a valid timeframe are assumed to be no part of any route in normal passenger operation and therefore neglected in the analysis.

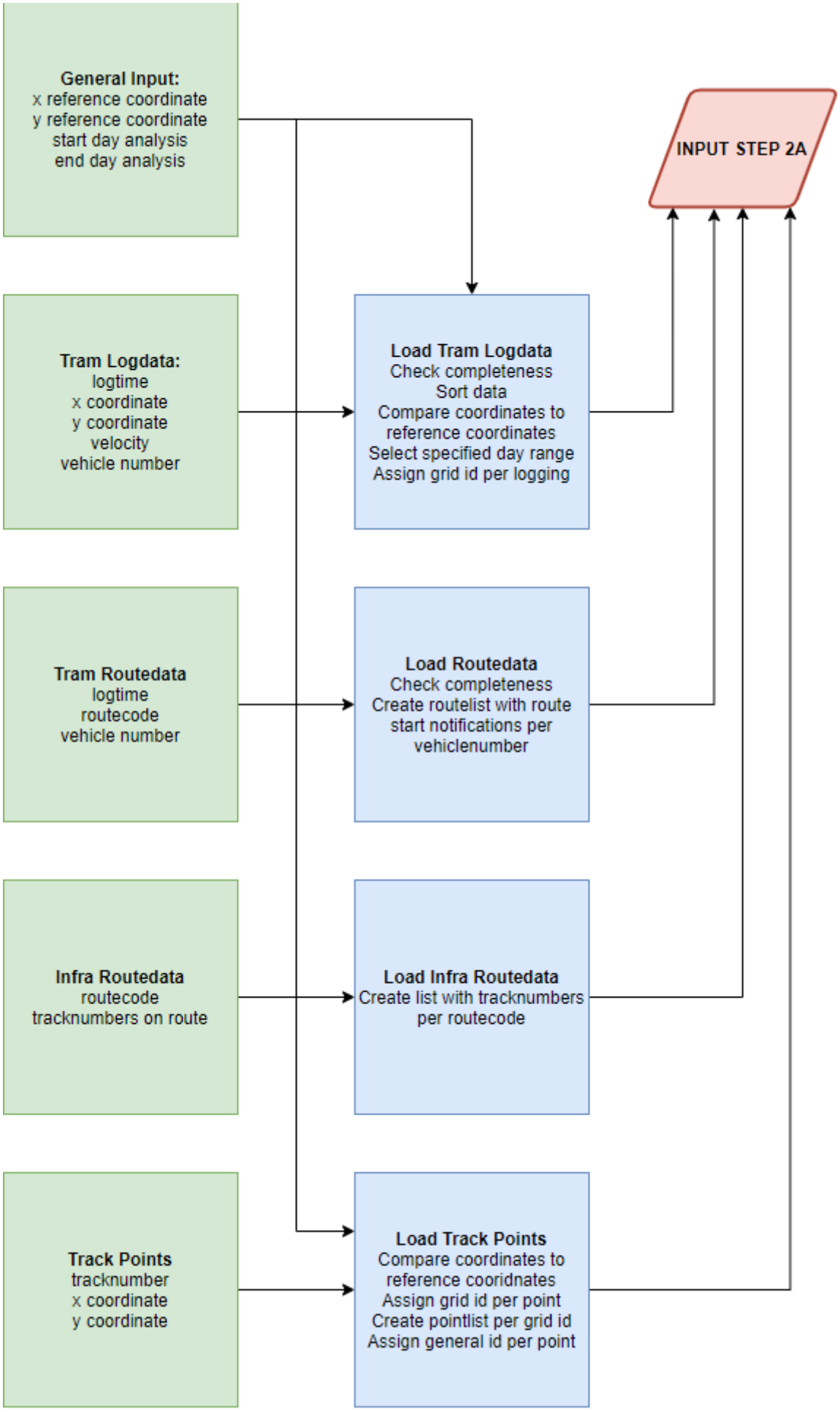


FIGURE C.4: Step 1 of the analyzing process: loading of input data.



FIGURE C.5: Velocity loggings, directly plotted in QGIS.

C.3.4 Infra Routedata

This database links routecodes to a specific set of tracknumbers. This database is created in QGIS, by spatially combining tracknumbers and routecodes.

C.3.5 Track Points

In essence, the track is divided per meter or less in points. These points also serve as input for the analysis, the info attached to each point is the tracknumber where it belongs to and the coordinates. While loading each trackpoint is compared to the reference coordinates, trackpoints outside the grid are neglected; the remaining trackpoints are assigned to a grid and the grid id (xxx,yyy) is assigned to each track point. Besides a grid id a point also obtains a unique id to keep track of each trackpoint. This makes it possible to make per grid a list of trackpoints located into that grid.

C.4 Step 2A: Determine Route and Trackpoints

In Step 2A the route of the tram is determined. With the help of the coordinates of the logging and the link to the routecodes and tracknumbers, it is possible to derive which tracknumbers where on the route and in the vicinity of the tram at the time of the logging. Figure C.6 shows the flow chart of this process: each single tram logging undergoes this process. Furthermore, the process could be separated in two parallel branches: to obtain the route at which the tram was driving and to obtain trackpoints in the vicinity of the logging. The two branches are explained respectively below.

C.4.1 Obtain Route

During the loading of the routedata, routelists where already created per vehicle. Since a logging also contains the vehicle number, it is straightforward to select the routelist belonging to that routelist/vehicle. The only job to be done by this step is to choose which routecode was valid at the logtime. This is perfomed by calculating the time differences between the logtime and the time of each route start notification on the routelist. The

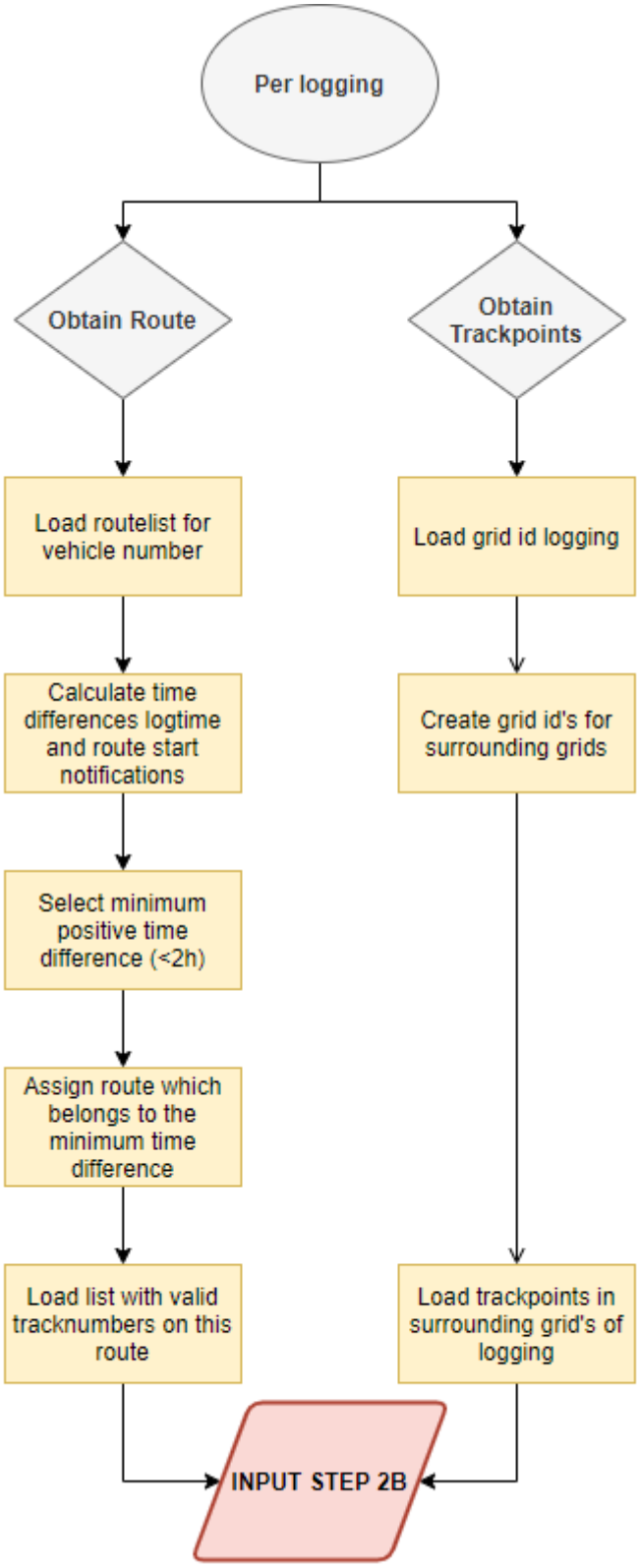


FIGURE C.6: Step 2A of the analyzing process: determine the tram route.

minimum positive time difference is selected, smaller than 2 hours. If no time difference remains, the logging is rejected from further analysis since it is then assumed the tram was in regular passenger operation. The Python code traces which route belongs to each time difference. Therefore, when a time difference is selected, the routecode could be directly assigned to logging. When the routecode is known, a list of tracknumbers for that specific route could be loaded from the Infra Routedata (explained under Step 1).

C.4.2 Obtain Trackpoints

To reduce the running time, a list of trackpoints in the vicinity per tram logging is made before the distance to each trackpoint is calculated. This is based on the grid id assigned to the logging. During loading of the trackpoints a list of trackpoints was created per grid id. The trackpointlist of the logging grid id and adjacent grids (inclusive grids that only share a corner). The pointlists of the adjacent grids are also loaded since otherwise loggings close to the grid border would have a search offset. As a result, the search field to tracpoints per logging is a square of around 90 by 90 meter, the logging itself is always located in the inner 30 by 30 meter square.

C.5 Step 2B: Obtain Nearest Valid Trackpoint

Step 2B is a continuation of Step 2A. The flowchart is visible in Figure C.7. At first, each trackpoint in the vicinity of the logging, determined in Step 2A, is considered: per trackpoint the tracknumber is compared with the tracknumbers on the current tram route, given the Step 2A. If the tracknumber of a trackpoint in the vicinity matches with a tracknumber on the current route, the trackpoint is valid. If the tracknumber is valid, the geometrical distance between the trackpoint and logging is calculated using the coordinates. Since the maximum possible distance would be 60 meters, it was assumed this method results in sufficiently accurate distances.

The minimum distance is selected after calculating the distances for each trackpoint per logging. The Python code tracks the trackpoint which belongs to each distance. At this point is possible to assign the closest trackpoint to the log location given the tram route. Since typically 5-20 loggings are coupled per trackpoint, the average velocity per trackpoint is assumed to by reasonably accurate.

The velocities per trackpoint are aggregated per tracknumber and submitted to Step 3 for the analysis per tracknumber. Separately the mean velocities and standard deviation per trackpoint are calculated and this information is directly submitted to Step 4: the output step.

C.6 Step 3: Velocity per Trackpoint Analysis

Per trackpoint a velocity analysis is done, which could be separated into two branches (see Figure C.8): the analysis of the average acceleration per tracknumber and a statistical analysis where a velocity distribution is made per tracknumber. Those two branches will be explained separately below.

C.6.1 Acceleration Analysis

The acceleration analysis was done to approach the average acceleration per tracknumber. Since braking and accelerating also dissipate a certain amount of energy in the track,

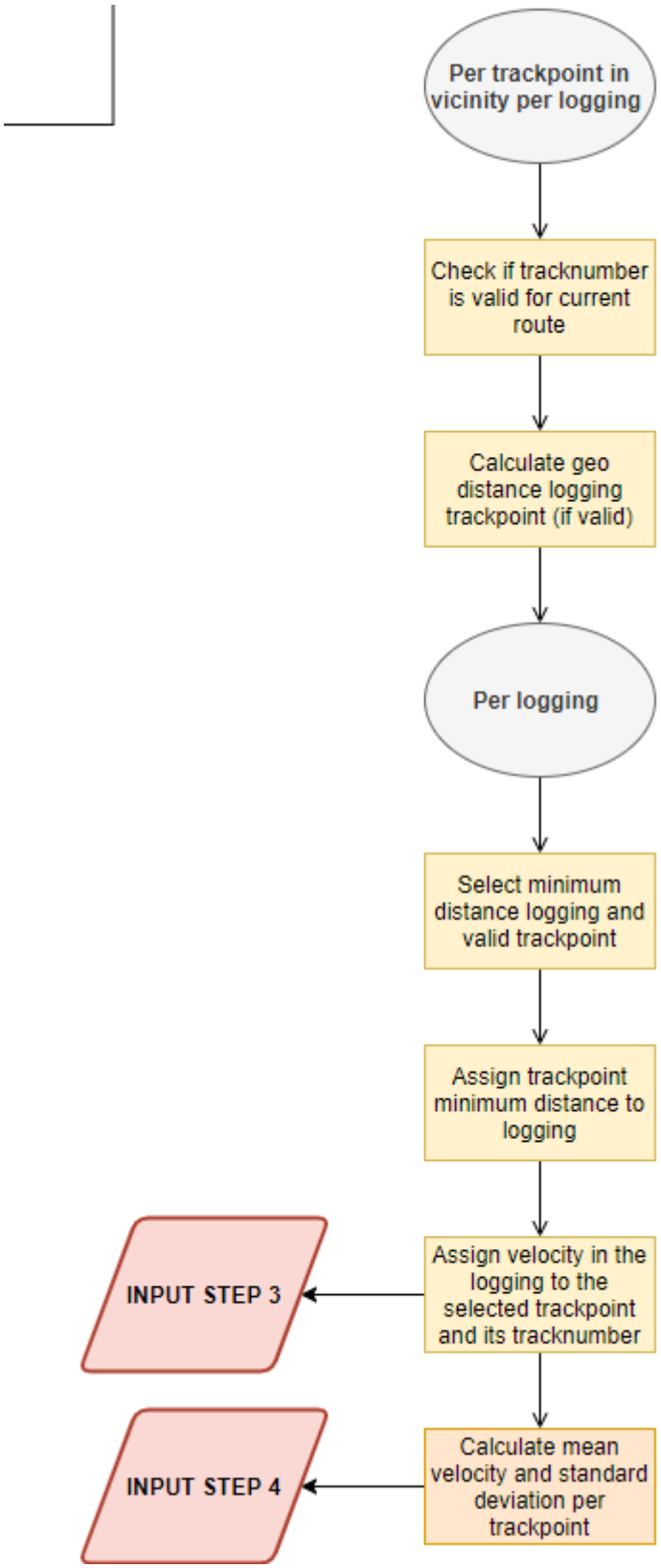


FIGURE C.7: Step 2B of the analyzing process: determine the nearest valid trackpoint.

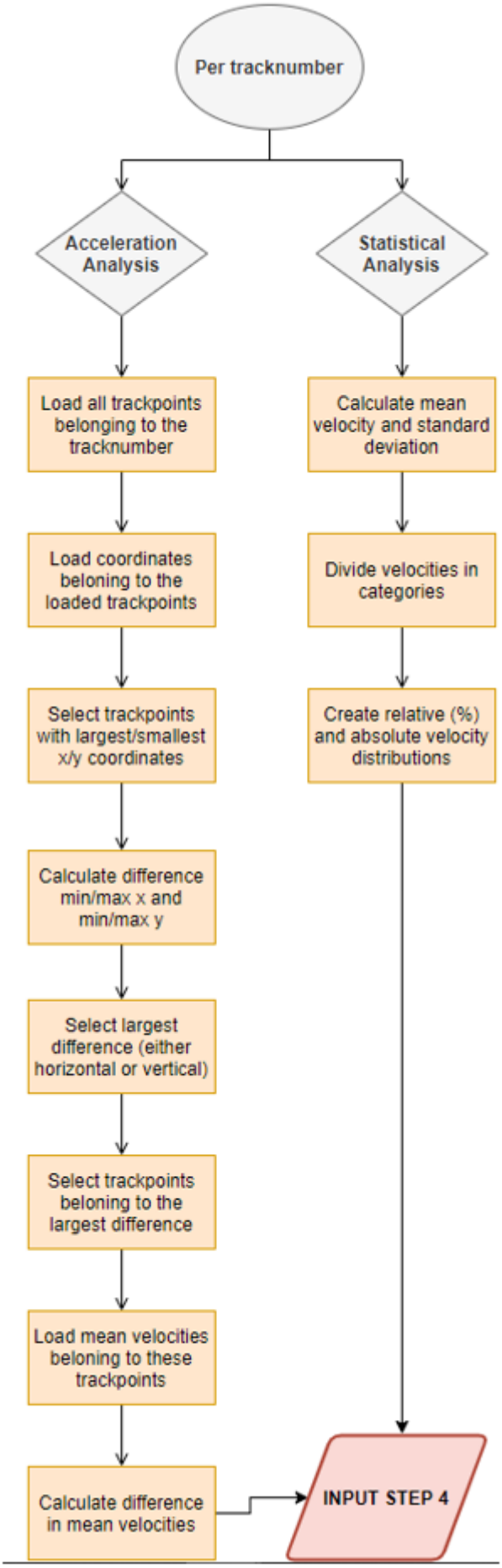


FIGURE C.8: Step 3 of the analyzing process: velocity per trackpoint analysis.

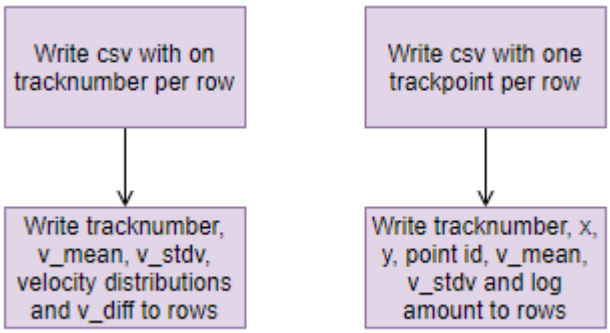


FIGURE C.9: Step 4 of the analyzing process: output.

the influences of this could be researched. It was not possible to make a difference between braking and accelerating since it was too challenging. In essence, the result of the acceleration analysis is the difference between the average velocities on the first and last trackpoint, per tracknumber.

The following steps were undertaken in the acceleration analysis: per tracknumber all points (incl. coordinates) which belong to that specific tracknumber are loaded. The trackpoint with the largest and smallest x and y coordinates are loaded. Next, the differences between the minimum and maximum x and y are calculated. The largest, either horizontal or vertical distance is selected. It is assumed the outer trackpoints on this largest distance will be the outer edges of the tracknumber. The trackpoints belonging to this largest distance are selected, and the difference in mean velocities is calculated and assigned to the tracknumber. This is an input for the output Step 4. This process is repeated for every tracknumber in the Python code.

C.6.2 Statistical Analysis per Tracknumber

Per tracknumber all trackpoints belonging to that trackpoint are gathered and all velocities belonging to those trackpoints are loaded. First, the mean velocity and standard deviation in velocity per tracknumber is calculated. All velocities are then assigned to categories starting at 0.0 kph (standstill) and then per interval of 5 kph (0-5, 5-10 kph etc.) until 65-70 kph. Distributions are created per velocity category in relative (%) and absolute terms (amount of logging's per category). Since a small number of loggings could be mismatched because of GPS offset, velocity categories with less than 20 loggings assigned are not assumed to be accurate. In theory, those loggings could likely originate from e.g. a straight after the curve. When more than 20 loggings are assigned to a velocity category, which is the case in the vast majority of cases, it is assumed those velocities are driven in reality on that specific tracknumber. It is deemed to be unlikely that >20 loggings will be all GPS offset, given the validation results and average log coordinate offset (see validation section in this chapter).

This process is repeated for every tracknumber in the Python code and submitted to the output Step 4.

C.7 Step 4: Output

The output of the velocity analysis consists of two CSV files: One file with per tracknumber the average velocity, standard deviation, average acceleration and the velocity distributions. The other file contains per trackpoint the coordinates, point id, average velocity, standard deviation and amount of coupled loggings. The output file containing the tracknumbers is used in the energy estimation. These results could also be plotted in GIS, by relating the tracknumbers to a shapefile containing the tracks and tracknumbers. The output file with trackpoint is used for detailed analysis at specific curves. It is, for example, possible to assess differences in tram driving behaviour. The velocities per trackpoint could be directly loaded and plotted in GIS, since it contains the coordinates. Figure C.9 shows the process in the flow diagram.

Appendix D

Simulation Method and Models

This section describes the VAMPIRE software, simulation models and integration method. Annex A contains a description of the parameters of both tram vehicle models used in the simulations. Further details on the simulation vehicles models are not discussed for confidentiality reasons.

D.1 VAMPIRE Software

VAMPIRE is a simulation software developed by Resonate Group limited and its predecessors: AEA Technology Rail and British Rail Research. The software is based on research into rail vehicle dynamics and wheel-rail interaction. It is a package of multiple analysis tools to assess the dynamics of railway vehicles under different circumstances. For example, two other wheel profiles could be simulated to check performance differences in running behaviour and energy dissipation. The basis for the simulation is a mathematical mass-spring system or multi-body model which resembles the railway vehicle. The vehicle's multi-body model is a combined set of smaller models. The most important models are the wheel models, axles, suspension models, dampers, bushes, connections and position of masses. The simulation also needs track and wheel-rail contact models besides the vehicle model. The simulation models are discussed in the 'Simulation Models' subsection.

Input files form the basis of every model in the program. The simulations are controlled with run files. The desired models and simulation parameters should be specified in those run files. Command files could be created that define replaceable parameters in runfiles; which allows running a batch of simulations with varied parameters. All information regarding the simulation software is based on the manual for the VAMPIRE program (RGL, 2018).

D.2 Simulation Models

Three main models were used in the simulation: vehicle models, wheel-rail contact models and track models. Wheel-rail contact models consist of the wheel and rail geometry and the possible positions of the wheel on the rail. Track models define the length, radii and cant. The vehicle, wheel-rail and track models are further explained in the following subsections.

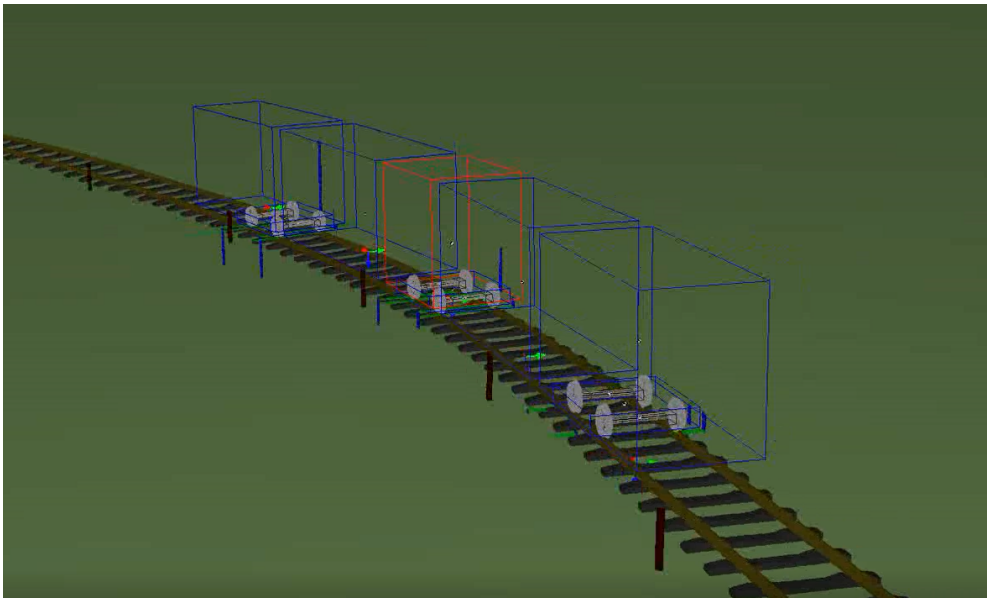


FIGURE D.1: Siemens Combino vehicle model.

Vehicle Models

Two vehicle models are used in the simulations: the Siemens Combino and the CAF Urbos 100; Annex A provides further vehicle information. The most important parts of the vehicle model are the suspension systems and distances between the different masses. The stiffness of the primary suspension plays a vital role in the dynamics of the trams and, as a result, the forces and dissipated energy at the wheel/rail contact. The suspension stiffness of the considered vehicles is known from the factory and processed into the model. Suspension values will change over time or could be different after maintenance. Tram experts at the GVB assured that this change would be within 10% limits in most cases; therefore, modification of suspension stiffness is not further considered in the simulations.

A Combino model during the simulation is visible in Figure D.1. This picture might be confusing since an axle connects the wheels while both trams have independent wheelsets. In the vehicle models, it is specified that each wheel could rotate independently from the other. The axle is a visual representation. The models were available in loaded and empty condition. The loaded condition assumed that all 55 seating places were occupied. In reality, the wheels of the trams do have rubber suspensions. This was not taken into account in the used vehicle models. The application of rubber suspension in vehicle models and the effect on simulation results, is a topic for further investigation. The vehicle models contain other simplifications: connections are modelled by springs and dampers. In reality, the geometry and physical implications are more complex. Especially the global vehicle behaviour in the longitudinal direction is simplified.

D.2.1 Wheel-rail Contact Models

Figure D.2, D.3 and D.4 show the geometrical wheels for three different geometries (new rail new wheel, new rail worn wheel, and worn rail new wheel). The wheels could move in the lateral direction about the track, which shifts the contact area, which results in adjusted stress distribution. The contact area could be either on the tread or on the flange.

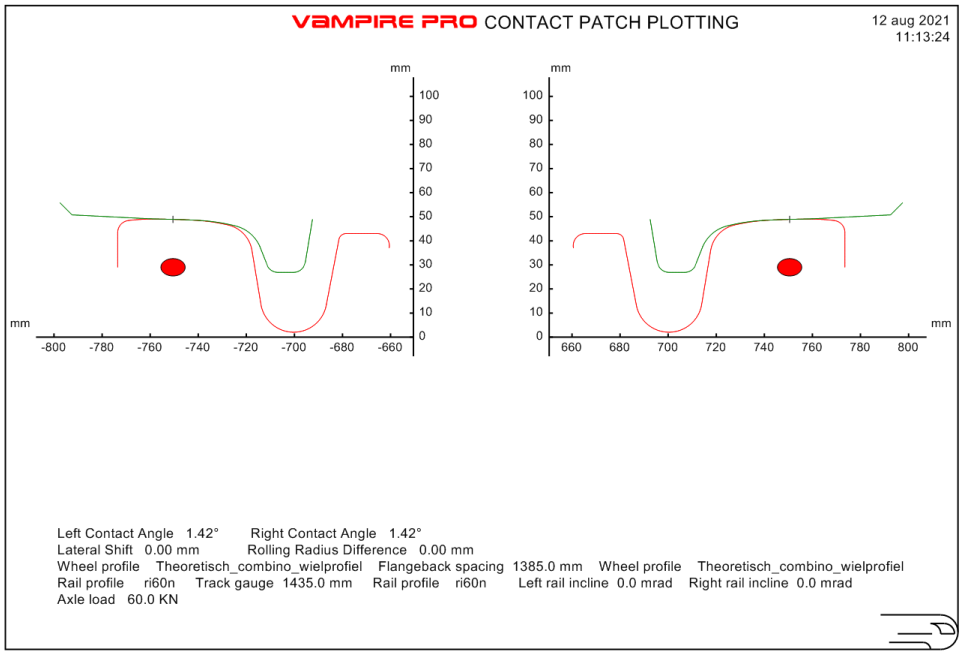


FIGURE D.2: Wheel-rail contact model with new 60R2 rails and new wheels. The red line represents the rail profile, green line is the wheel profile and the red ellipse is the contact patch (Hertzian model).

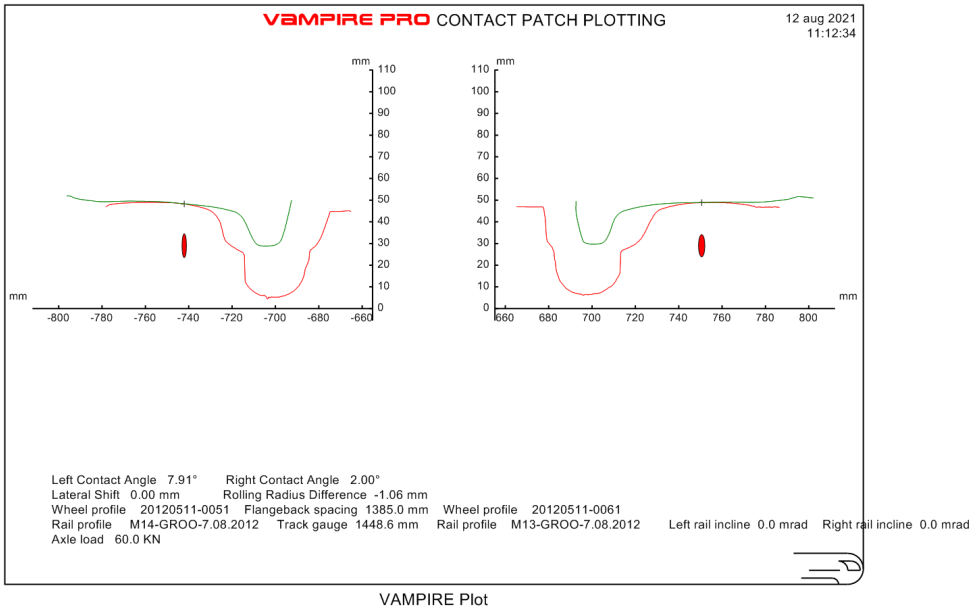


FIGURE D.3: Wheel-rail contact model with worn rails and new wheels. The red line represents the rail profile, green line is the wheel profile and the red ellipse is the contact patch (Hertzian model).

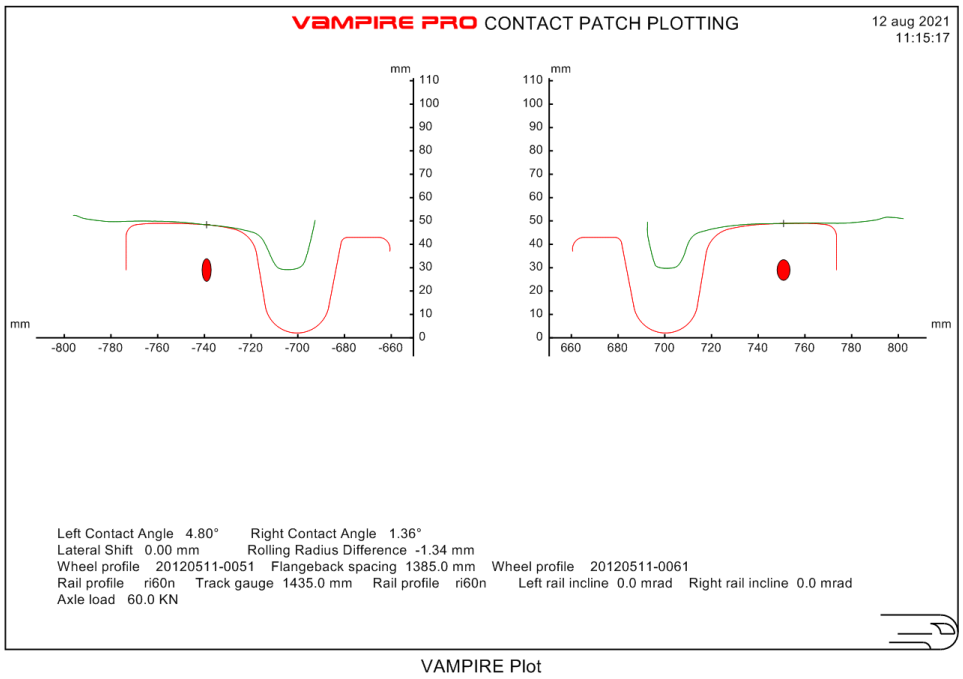


FIGURE D.4: Wheel-rail contact model with new 60R2 rails and worn wheels. The red line represents the rail profile, green line is the wheel profile and the red ellipse is the contact patch (Hertzian model).

Flange contact occurs when the wheels can not move further in the lateral direction. When the wheels are shifted further, it will climb on the rail and eventually derail.

During two-point contact, both the flange and the tread contact the rail. Simulation results only showed two-point contact when worn wheels were selected. The contact point is only at the flange during flange contact with new wheels. In this case, the wheel is virtually lifted off the rail, and all vertical forces go through the flange contact area. The flange contact area has an angle of about 77 degrees. This would imply that the total vertical force is transmitted from the wheel to the rail under an angle of 77 degrees. No evidence was found that this is indeed the case with new wheels. Therefore, the simulation model could underestimate the dissipated energy at the tread during flange contact and overestimate the dissipated energy at the flange. Different geometrical wheel and rail profiles were used in the simulations: new wheels, worn wheels, new 60R2 rails and worn rails. The wheel and rail profile could be chosen independently in the wheel-rail contact model. The GVB has one standard wheel profile, on the contrary, multiple rail profiles are in use but 90% in tight curves is 60R2 rails. Therefore, it was chosen not further to research the influence of a different rail profile and only simulate 60R2 rail profiles. The worn rail profile is deduced from measurements. Non of the worn rail profiles will be precisely the same in reality. For simplicity, three worn rail profiles were chosen, resembling a geometrical state often seen in reality.

During the simulation, the creepages at the wheel/rail contact are calculated at each time step. Then, the forces resulting from those creepages are determined. The creepages are the relative sliding velocities at the contact surface in different directions. The contact forces are determined using Kalker's non-linear theory based on those creepages and the friction coefficient. Those contact forces are then the input for the displacements and resulting creepages at the next time step. The interested reader can consult (Ayasse and Chollet, 2006) or (J.J.Kalker, 1967) for more information on Kalker's contact theory.

The influence of changing the friction coefficient on the simulation output was verified. Finally, the friction coefficient was set to 0.32 for the tread and 0.15 for the flange because it is assumed the flanges are lubricated. In reality, only half of the trams do have flange lubrication enabled. It is assumed that this lubrication will be on the rail when other trams pass. The values of the friction coefficients are the same ones DEKRA used in previous research for GVB. Therefore, the contact force and the dissipated energy were linear dependent on the used friction factor.

At sharp curves at low speed, the running behaviour of the vehicle changed with an altered friction factor. An increased friction factor of the flange resulted in more flange contact. It was expected a modified friction factor would change contact forces but not running behaviour. The origin and correctness of these cases are unclear, so further investigation is needed to explain them.

The friction factor is expected to vary between places and time, as it depends on material contact characteristics (wheel and rail), weather conditions, and other substances on the rails. Therefore, it was not possible to establish friction coefficients per curve that are proved to match reality. Since the friction factors are kept the same in the simulations, it is still possible to compare the dissipated energy output between different simulations to identify factors that cause an increase in dissipated energy.

D.2.2 Track Models

The track model determines the general layout of the track. The precise rail geometry is defined in the wheel-rail contact model described previously. The most critical parameters for the track models are the curvature, length and cant. During the simulations, the curvature is changed according to the desired radius. No transitional curves are added since those are not present in most cases at the tram network. The length is adapted to the desired curve length; in the parametric simulations, a quarter of a circle. Zero or only slight cant (1-3 cm) is applied on the urban tram network. In the vast majority of cases, there is a cant deficiency. Because of this, no cant was added in the simulation since the amount of cant per curve is also unknown. Each curve in the simulation has a 50 meter long straight before and after the curve, the straight before the curve functions as warm up for the simulation. The track after the curve is needed since the front of the tram needs to drive further to allow the last bogie to fully negotiate the curve. At last, it is essential to mention that each curve in the simulation goes towards the left in the driving direction.

The results for the right rail are sampled as outer rail, and the results for the left rail are sampled as inner rail. It makes the output generic and usable for curves going to the right in the driving direction. The vehicle models are symmetrical, with the centre of gravity of each passenger car in the middle. This simplification reduces the complexity, but it also reduces the accuracy. When people are standing, a Combino is asymmetrically loaded to the right. (Deltarail, 2012) concludes that the asymmetrical loading of a Combino increases the energy dissipation on the right side. This factor is not taken into further consideration in this research. After running the simulation, it is possible to watch a demonstration video where the tram runs over the track to verify if the track layout and general behaviour is according to the expectations.

D.3 Integration Method

The following input is needed for this simulation: velocity, calculation distance, number of timesteps, track file, wheel-rail contact file and the vehicle file. It is optional to add a

force file that inputs specified forces on specified model parts. The calculation distance was set equal to the distance of the track in the trackfile. Output values were later gathered from the start until the end of the curve to leave out the 'warm up' and 'cool down' track stretches. An integration time step of 0.00005 seconds was used for 20, 30 and 40 kph and a timestep of 0.0001 seconds for 10 kph. This larger step was chosen because of the lower velocity to reduce simulation times. Larger timesteps would lead to instabilities in the integration process during the simulation. Results of different timesteps were compared. No significant differences occurred if the timestep was made smaller than the used timesteps. At very high velocities in tight curves or worn rails at one side, the wheels sometimes violated the spatial boundary in the wheel-rail contact model in the lateral direction. This could be interpreted as a vehicle derailment, but in reality, it is also possible the vehicle drives on the hardening with the flange still in the rail. In both cases, the simulation did not reach a correct output, which was no problem in the case of very high velocities in tight curves since those velocities are not driven in reality.

The simulation starts by defining a minimum selection of degrees of freedom based on the supplied vehicle model. The six known translational and rotational degrees of freedom are available per mass. A pitch rotation degree of freedom for the axleboxes is added for the wheelsets. Only degrees of freedom containing a suspension element is selected. VAMPIRE assumes small yaw and pitch rotations to simplify and speed up the simulation regarding the rotational degrees of freedom. By assuming small rotations in those directions, the three rotations could define a unique orientation of the masses, which would be otherwise more complex. The assumption is valid since a guided rail system is modelled. However, in the case of this research, tight curves are modelled with small vehicles. Therefore, local axis is defined per vehicle part to keep small yaw angles.

The first step of the calculation is the development of a linear stiffness matrix for the vehicle and its suspension elements. With this matrix, a static load analysis is performed. No friction elements are considered in this calculation since it is assumed that friction does not influence loads when the model is in static equilibrium. When the static equilibrium is known, responses are calculated per timestep. The main timestep loop calculates forces in all the suspension elements based on the displacements and velocities per mass, resulting from the previous timestep. Those are zero at the first timestep. At this moment also optional external forces could be included from the force file, which should be specified per degree of freedom and time interval. In this research, external forces were only used by simulating a braking vehicle. The position of the wheelset needs to be determined relative to the track per timestep. This is done with 7th order polynomials for lateral position and yaw angle; the longitudinal position is calculated with linear interpolation. Those displacements of the wheelsets are then used to determine the wheel-rail contact forces, according to the wheel-rail contact definition described previously. The accelerations of the masses resulting from the summed force per degree of freedom are obtained as follows: by dividing the forces by the mass at translational degrees of freedom or inertia at rotational degrees of freedom. Then, the accelerations are integrated to determine the velocities and displacements of the input for the next timestep. At the end of each timestep, the desired output data defined by the user is assembled.

D.4 Post Processing Method

In further analysis, the used simulation output is the dissipated energy per unit distance. The dissipated energy is the creep force and creepage product and is often denoted as T_γ. This multiplication is done for the longitudinal, lateral, and spin creepage in the current

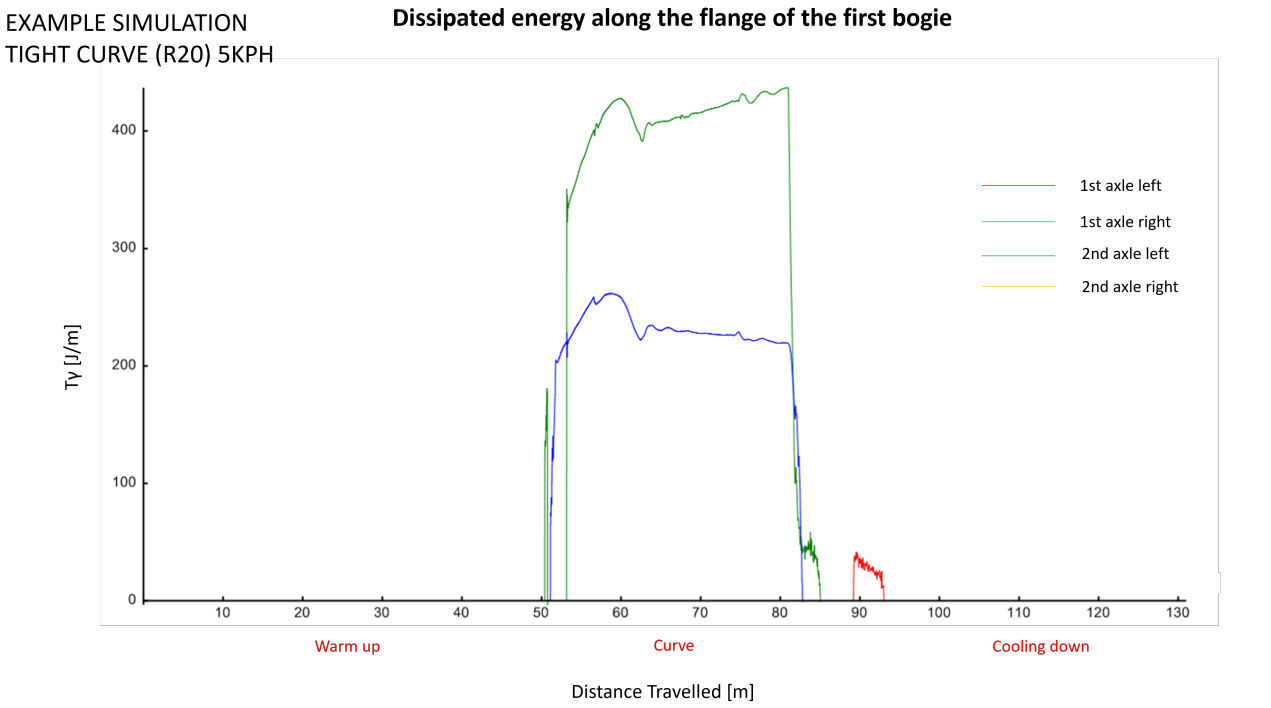


FIGURE D.5: Dissipated energy at the wheels of the first bogie at the flange contact surface.

simulation. By adding the dissipated energy per unit distance for all three creepages, a measure is obtained for the total dissipated energy per unit distance in wheel-rail contact. An elaboration on the wheel-rail contact theory, including creepage formulas, could be found in (Ayasse and Chollet, 2006) and Chapter 2.

Figure D.5 and D.6 show the results of an example simulation of a Combino traversing a tight curve at very low speed. This example is used to explain the post-processing method. The x-axis shows the travelled distance of the front of the tram. The y-axis shows the dissipated energy in J/m. This example considers only the first bogie. For example, the '1st axle left' is the energy dissipated at the tread of the left wheel on the first axle.

From figure D.5 it is shown that the right wheel on the 1st axle is in continuous flange contact with relatively high energy dissipation. In this case, the right wheel is the outer rail since all curves are simulated to the left in the driving direction. According to this simulation, a tight curve results in abrasive wear on the flange of the first outer rail wheel despite the low velocity. After the 50 meter in a straight track, the first outer rail wheel enters the curve, makes flange contact, loses it for a few meters, and negotiates the remainder of the curve in continuous flange contact. Then, when considering Figure D.6, the first outer rail wheel only has tread contact when it loosed flange contact. This observation is important since it could be deduced that no two-point contact occurred in this case. As a result, all the normal force would be transferred via the flange contact when the flange makes contact with the rail. However, when the flange is in contact, also the tread is expected to remain in contact. This reduces the amount of normal force and creep force at the flange, at the expense of the tread. Therefore, it is expected the energy expended at the flange is overestimated, while the energy at the tread is underestimated. Since the exact degree of under- and overestimation is unknown, no correction was made for this issue.

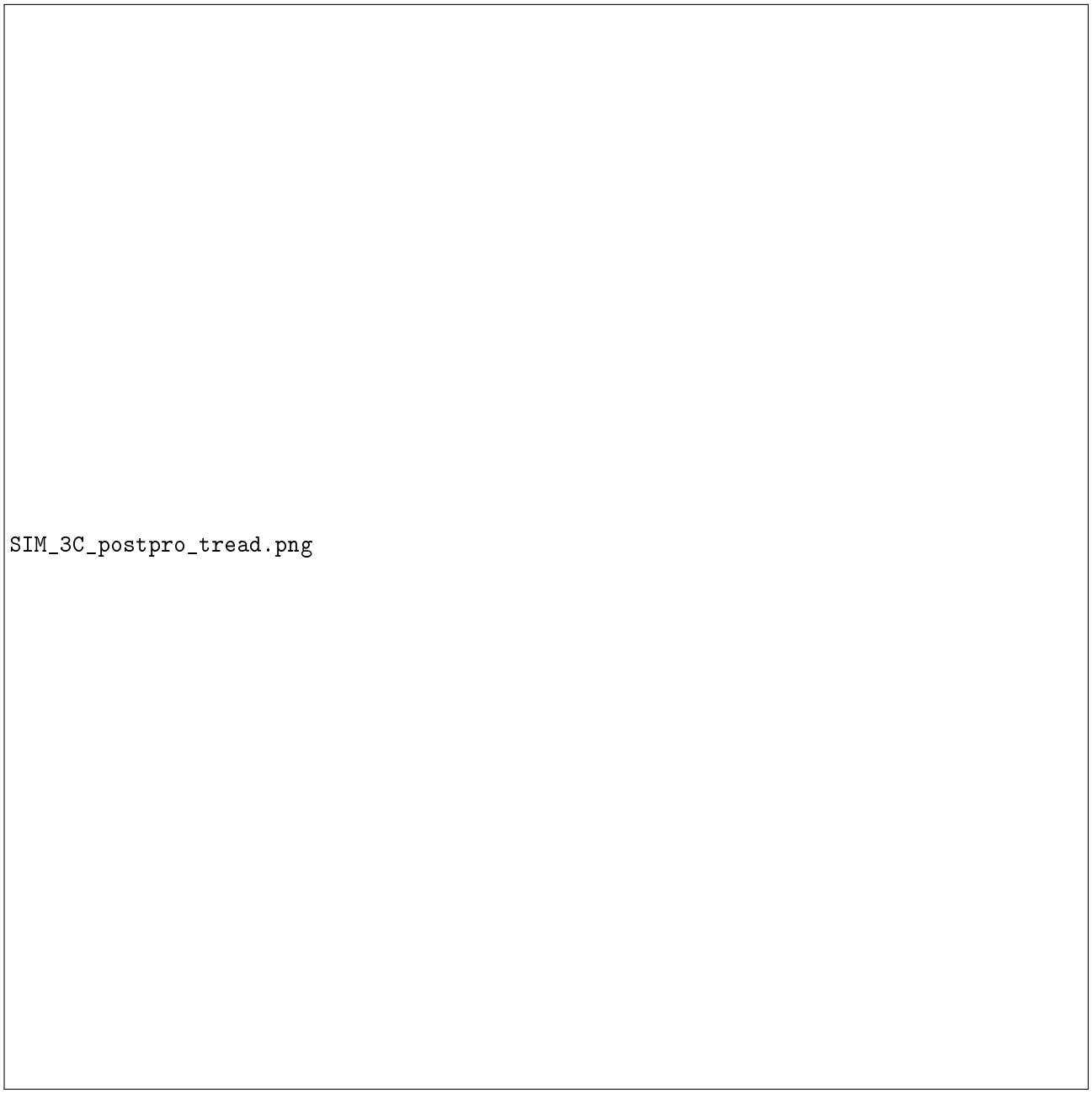


FIGURE D.6: Dissipated energy at the wheels of the first bogie at the tread contact surface.

The left wheel on the second axle, the inner rail, will also make flange contact because of the tightness of the curve and the low velocity. However, the energy dissipation is only half of the dissipation at the outer side. This is explainable since the outer rail has to steer the tram the right way, which results in higher energy dissipation. The flange of the 1st wheel on the inner rail makes quick and small flange contact after the curve. This is expected to occur because of longitudinal tram dynamics since the back is still in the curve. Looking at the dissipated energy at the tread, shown in Figure D.6, the energy dissipation is also relatively high. In line with the expectations, only the inner rail first and high second wheel are in continuous tread contact, since the other wheels are in continuous flange contact.

The post-processing of this data is done by taking the average energy dissipation per wheel per contact phase during the curve. In the example of Figure D.5 and D.6, the energy dissipation of the 1st outer rail wheel would be just below 400 J/m at the flange and quit low but non zero at the tread. This method was chosen since it best represents the 'wear load' per curve. It was assumed that short high pulses of dissipation along a short stretch, like the tread of the first outer rail wheel, are less critical than high dissipation with a long distance along the curve.

D.4.1 Post Processing Method Parametric Simulations

The initial post-processing of the simulations resulted in the average T_γ per wheel per flange/tread. For the parametric simulations analysis, the result is aggregated over the left and right side per flange/tread. This was done to reduce the complexity of the analysis and the energy estimation model. Furthermore, the profile measurements are also only available per left and right rail in horizontal and vertical directions.

The main choice during this step was to either sum the average T_γ per wheel per side per flange/tread, taking the average of the average T_γ per wheel or just taking the wheel with the maximum T_γ. Summation would give a pure average T_γ per unit distance intake when a tram negotiates a curve, the best way to capture all the average energy input in a curve per passage. A disadvantage of this method is the loss of the original T_γ values, which will make it more difficult to couple certain T_γ thresholds to increased wear when the energy estimation is compared with rail profile measurements. Taking the wheel with the maximum T_γ would preserve the original values; however, after reviewing the parametric simulation results with the 'maximum (T_γ)' method, this post-processing method was discarded.

The main reason to discard the *maximum* T_γ method was the following observed phenomenon: at low speeds, the first wheels of the bogies tends to have the highest energy dissipation values. When the velocity also increases the second wheels *lean* more into the outer rail, which causes the dissipated energy to spread over the two wheels per bogie. In this case, the maximum T_γ at increasing velocity decreases, while the total T_γ still increases. Therefore, this method would not properly measure the average energy intake per unit distance along the curve per passage. To retain the original values, the average T_γ over the average T_γ values per wheel could be taken. However, especially at the flanges, often one or two out of six wheels do have a high value and the other T_γ values are zero; taking the average T_γ would then still jeopardize the original T_γ values.

Therefore, it was decided to take the sum of the average T_γ values per wheel. It is believed that this method conserves the total average T_γ intake per unit distance in the best manner. In general the T_γ was quit equally distributed along the curve length, as a result, the average T_γ per wheel is in general close to the actual simulated T_γ per unit distance since it does not deviate that much along the curve.

The post-processing code is written in Python, which can simultaneously process all parametric simulations. If it still turns out to be desirable to obtain maximum or average T_γ values, only a setting in the code needs to be changed to get those results immediately. The Python code that processes the raw simulation data to produce the resulting graphs creates files that can be directly read by the post-processing code, which sums the T_γ over the wheels. Also, this post-processing code produces files that can be directly read by the energy estimation model, which estimates the energy dissipation for every curve on the network. The coding was needed because of the large number of simulations and curves to be analyzed. It also provides much flexibility in the analysis process since results could be obtained directly when a post-processing step changes or the raw data changes.

Parametric Simulation Post Processing Code Description

The code first reads the files generated by the code that analyses the raw data. Each simulation has a CSV file that contains the average T_γ per wheel per tread/flange. The name of each file contains the parameter settings of each simulation. This also enables the user to find results files quickly. An example file name is given:

F02003100001 vc 00 CT 20 08 32 15 r0 01

The *F* is only a marker that it is a parametric (fictive) simulation file which the code should consider.

The first block before the separator contains information on the track file. The first three digits mark the curve radius, 20 meters in this case. The second three digits denote the curve length, 31 meters in this case. The third three digits mark the cant, which is always zero in this series of parametric simulations. The last two digits of the first block are used to number the track files, in case two-track files with the same properties needs to be separated.

The second and third blocks are used to mark the used force file. In this case, *vç* means *velocity constant* which means that no external forcing file was used in this case. No acceleration was taken into account in the parametric simulations. If any force file was used, the letters could mark the kind of acceleration (dc = braking, ac = accelerating). The number after the letter then should refer to an auxiliary file, which specifies the details per force file number.

The remainder of the file name specifies some simulation details: *C* stands for Combino, *T* stands for *tangent* which means empty vehicle (no passengers). The two digits after the *CT* block mark the velocity, in this case, 20 kph. Then, *08* is the wheel-rail contact file number that was used. The code needs an auxiliary file to translate the wheel-rail contact file numbers. Then *32* stands for the head contact friction and *15* for the flange contact friction. *r0* is not used by the code, but just for user convenience, it marks that this simulation at worn rails and new wheels. In the case of new rails and worn wheels, it would be *0w*. The last two digits of the file name distinguish between different simulations with the same input.

Per batch simulation in VAMPIRE, a coded routine automatically gives the raw data result file this file name, based on the simulation input. The Python post-processing code, which processes the raw data, gives its output files the same name to preserve the simulation information.

The code stores all the simulation aggregated results in an internal directory with the file name as key for the results of each simulation. It then sums per simulation the T_γ values

over all wheels per side per flange/tread. The resulting files for the energy estimation code with the summed values per simulation are exported under the same file name.

Bibliography

Ahac, M. and S. Lakušić (2017). *Track Gauge Degradation Modelling on Small Urban Rail Networks: Zagreb Tram System Case Study*.

Amontons, G. (1699). "De la resistance cause'e dans les machines". In: *Mem l'Acedemie*, pp. 257–282.

Arman (2021). *GVB Combino tram*. URL: https://3dwarehouse.sketchup.com/model/a37cb92d-6667-42a1-8fe3-5ee7d7fd13a5/GVB-Combino-tram?hl=nl.

Ayasse, J. and H. Chollet (2006). *Handbook of Railway Vehicle Dynamics*.

Bolton, P.J. and P. Clayton (1984). "ROLLING-SLIDING WEAR DAMAGE IN RAIL AND TYRE STEELS". In: *Wear* 93, pp. 145–165.

Burstow, M. (2003). "Whole Life Rail Model Application and Development for RSSB – Development of an RCF Damage Parameter". In: *AEATR report*.

Carter, F. (1926). "On the action of a locomotive driving wheel". In: *Proceedings of the Royal Society* 112.760.

CBS (2021). *Inwoners per Gemeente*. URL: https://www.cbs.nl/nl-nl/visualisaties/dashboard-bevolking/regionaal/inwoners.

Coulomb, C. (1773). "Sur une application des regles de maximis minimis a quelques problemes de statique, relatifs a I' architecture". In: *Memoires de Mathematique de Physique, presentes a I' Academie* 7, pp. 343–382.

Crosbee, D., P.D. Allen, and R. Carroll (2017). "A combined numerical/experimental prediction method for urban railway vibration". In: *J Rail and Rapid Transit* 23.5, pp. 578–597.

DEKRA (2020). *Invoering trammaterieel 15G - gevolgen voor de onderhoudsbehoefte van de railinfra [confidential]*.

Deltarail (2012). *Railslijtage in bogen van het tramnet te Amsterdam [confidential]*.

DeltaRail (2012). *Railslijtage in bogen van het tramnet te Amsterdam [confidential]*.

Dubbelman, G. (2020). *Primeur: 15G tram op zuidelijk deel Amstelveenlijn*. URL: https://amstelveenlijn.nl/nieuws/2020/primeur-15g-tram-op-zuidelijk-deel-amstelveenlijn/.

Eelco (2021). *GVB Combino op lijn 13 bij de Jan van Galenstraat*. URL: https://trams.fandom.com/nl/wiki/Jan_van_Galenstraat_(west).

EenRailSpotter (2020). *GVB Combino 13G 2148*. URL: https://treinposities.nl/foto/48414.

G. Alarcón N. Burgelman, J. Meza A. Toro Z. Li. (2015). "The influence of rail lubrication on energy dissipation in the wheel/rail contact: A comparison of simulation results with field measurements". In: *Wear* 330-331, pp. 533–539.

Group, Agico (2021). *Grooved Rail*. URL: http://www.rail-fastener.com/grooved-rail.html.

GVB (2021). *Jaarverslag 2020*. URL: https://jaarverslag.gvb.nl/.

Hertz, H. (1882). "Über die Berührung fester elastischer Körper und Über die Härte". In: *Verein zur Beförderung des Gewerbefleisses*, pp. 449–463.

Higgins, C. and X. Liu (2018). "Modeling of track geometry degradation and decisions on safety and maintenance: A literature review and possible future research directions". In: *J Rail and Rapid Transit* 232.5, pp. 1385–1397.

J.J.Kalker (1967). *On the Rolling Contact of Two Elastic Bodies in the Presence of Dry Friction.*

Kasraei, A., J.A. Zakeri, and A. Bakhtiaryi (2020). "Optimal track geometry maintenance limits using machine learning: A case study". In: *J Rail and Rapid Transit.*

K.L.Johnson (1985). *Contact mechanics.*

Kouroussis, G., O. Verlinden, and C. Conti (2010). "On the interest of integrating vehicle dynamics for the ground propagation of vibrations: the case of urban railway traffic". In: *Vehicle System Dynamics* 48.12, pp. 1553–1571.

Kouroussis, G., K.E. Vogiatzis, and D.P. Connolly (2017). "A combined numerical/experimental prediction method for urban railway vibration". In: *Soil Dynamics and Earthquake Engineering* 97, pp. 377–386.

Martin (2021). *GVB 15G-tram 3046.* URL: https://busposities.nl/foto/42599.

Melo, A.L.O. et al. (2020). "Methods to Monitor and Evaluate the Deterioration of Track and Its Components in a Railway In-Service: A Systemic Review". In: *Frontiers in Built Environment* 6.118.

Periard, F.J. (1998). *Wheel-Rail Noise Generation Curve Squealing by Trams.*

Prorail (2010). *CO2 ketenanalyse spoorstaven.*

PyPy (2021). *What is PyPy?* URL: https://doc.pypy.org/en/latest/introduction.html.

RGL (2018). *VAMPIRE Pro V6.60 (Resonate Group Limited) [confidential].*

Shevtsov, I.Y. (2008). *Wheel/Rail Interface Optimisation.*

Siemens (2007). *Onderdelen catalogus Amsterdam [confidential].*

– (2016). "Wheel sets or independently rotating wheels - from theory to practice". In.

Simons, P. (2019). *Lijn 14.* URL: https://ppsimons.com/2019/02/22/lijn-14/.

Soleimanmeigouni, I. et al. (2020). "Investigation of the effect of the inspection intervals on the track geometry condition". In: *Structure and Infrastructure Engineering* 16.8, pp. 1138–1146.

Trading, Gummi (2021). *Isolation of Grooved Rails and Cross-section.* URL: http://www.gummipraha.cz/en/259-isolation-of-grooved-rails-and-cross-section.

Łuczak, B. et al. (2020). "Numerical algoritm for predicting wheel flange wear in trams - Validation on a curved track". In: *J Rail and Rapid Transit* 234.10, pp. 1156–1169.

Vincent, N. et al. (2006). "Curve squeal of urban rolling stock—Part 1: State of the art and field measurements". In: *Journal of Sound and Vibration* 293, pp. 691–700.

Vinko, A. (2016a). "Monitoring and condition assessment of tramway track using in-service vehicle". In: *Pollack Periodica* 11.3, pp. 73–82.

– (2016b). "Monitoring and condition assessment of tramway tracks in the aspect of deterioration rate". In.

Vinko, A. and P. Bocz (2018). "Experimental Investigation on Condition Monitoring Opportunities of Tramway Tracks". In: *Periodica Polytechnica Civil Engineering* 62.1, pp. 180–190.

Wegdam, J. (n.d.). *Tool development for manual inspections of crossing geometry.*

Weston, P. et al. (2015). "Perspectives on railway track geometry condition monitoring from in-service railway vehicles". In: *International Journal of Vehicle Mechanics and Mobility* 53.7, pp. 1063–1091.

Williams, J.A. (1999). "Wear modelling: analytical, computational and mapping: a continuum mechanics approach". In: *Wear.*

Xie, W. et al. (2018). “Decision support tool based on multi-source data analysis for the tram wheel-rail interface”. In: *Preprints, 15th IFAC Symposium on Control in Transportation Systems June 6-8, 2018. Savona, Italy*.

Yang, Z. (2020). *Lecture Slides - CIE4873 Lecture 6*.